Damage Propagation and Detection using Nonlinear Elastic Wave Spectroscopy in Aerospace Structures

Ginzburg, Dmitri

Award date:
2016

Awarding institution:
University of Bath

Damage Propagation and Detection using Nonlinear Elastic Wave Spectroscopy in Aerospace Structures

Dmitri Ginzburg

A thesis submitted for the degree of Doctor of Philosophy

University of Bath
Department of Mechanical Engineering

March 2016

Abstract

The sustainable future of aerospace industry in large part relies on two factors: (i) development of advanced damage tolerant materials and (ii) the ability to detect and evaluate defects at very early stages of component service life. The use of laminated composite materials, such as carbon fibre reinforced plastics (CFRP), has had a significant contribution to reducing airframe weight while improving passenger safety and comfort. However, it is well known that these materials exhibit poor resistance to impact damage caused by foreign objects. Inspired by the naturally occurring impact resistant structures, the first part of this work has shown that enhanced damage tolerance can be achieved with standard CFRP layers by creatively arranging them into bio-inspired configurations. Through an extensive numerical modelling study supported by the experimental results, a further insight into the possibilities that these structures can offer in terms of damage resistance was attained.

The second part of this PhD work focused on developing a range of nonlinear nondestructive evaluation techniques that are sensitive to the early signs of material degradation. A range of defect types in metallic and composite structures has been considered, such as fatigue cracks, impact damage and disbonds in adhesively bonded components typical in aerospace industry. Furthermore, throughout this work, an advanced explicit finite element analysis (FEA) software code LS-DYNA® has been used for modelling the nonlinear effects associated with the propagation of elastic waves in damaged solid media.

Acknowledgments

My sincere gratitude is to my supervisor, Prof Michele Meo, whose guidance and support have enabled me to carry out this research and develop an understanding of the subject.

I would like to extend my deepest appreciation to my parents, my brother, and my wife, Amanda, for their love, support and patience.

The work presented herein has been performed as part of ALAMSA project supported and funded by the European Union (EU) in the 7th framework programme (FP7) for research and technological development. I would like to express my gratitude to the colleagues who collaborated on the project: Dr Gian-Piero Malfense Fierro for jointly carrying out the experimental work presented in Chapter 5.1.2, 5.2.4, 5.3.4-0 and 5.3.8-5.3.9; Daniele Calla for performing the experimental work presented in Chapter 5.2.5; Dr Francesco Ciampa for developing the mathematical procedure presented in Chapter 5.1.3.1 and for the derivation of the nonlinear flexural waves in plates provided in Chapter 5.4.2.2; and all the Italian community that I had pleasure working alongside with over the past several years.

List of Abbreviations

AE	Acoustic emission
ASTM	American Society of Testing and Materials
AWG	Aerospace Working Group
BSI	British Standards Institute
BVID	Barely Visible Impact Damage
CAA	Civil Aviation Authority
CAI	Compression After Impact
CDM	Continuum Damage Mechanics
CLPT	Classical Laminated Plates Theory
CFRP	Carbon fibre reinforced plastic
CT	Computer tomography
CZM	Cohesive Zone Models
DCB	Double Cantilever Beam
ESL	Equivalent Single-Layer
FAA	Federal Aviation Administration
FE	Finite element
FEA	Finite element analysis
FEM	Finite element method
FFT	Fast Fourier-transform
FOD	Foreign object damage
FRP	Fibre reinforced polymer or plastic
HF	High frequency
HMEU	Hysteretic mesoscopic elastic units
HVI	High velocity impact
ICAO	International Civil Aviation Organization
IR	Impact region or infrared (depending on context)
ISS	Interlaminar shear stresses
KE	Kinetic energy
LDR	Local defect resonance
LDV	Laser-Doppler vibrometer

LEO	Low Earth Orbit
LF	Low frequency
LG	Luxemburg-Gorky
LS	Lamination scheme
LVI	Low Velocity Impact
MCT	Multiresolution Continuum Theory
NEWM	Nonlinear elastic wave modulation
NEWS	Nonlinear elastic wave spectroscopy
NIM	Nonlinear imaging
NFLS	Normal failure stress
NRUS	Nonlinear resonant ultrasound spectroscopy
NWMS	Nonlinear wave modulation spectroscopy
PM	Preisach-Mayergoyz
POD	Probability of detection
PVD	Principle of virtual displacement
RT	Radiographic testing
SAW	Surface acoustic waves
SEM	Scanning electron microscopes
SFEM	Spectral finite element method
SFLS	Shear failure stress
SH	Shear Horizontal
SHM	Structural Health Monitoring
SLJ	Single lap joint
TOF	Time of flight
TSA	Thermoelastic stress analysis
TTU	Through transmission ultrasonic
UMAT	User Defined Material
VCCT	Virtual Crack Closer Technique
XFEM	Extended Finite Element Method

List of Symbols

Q_0	Amplitude of the excitation force
ω	Angular frequency
$\varphi_I(\mathbf{X})$	Approximation functions for the enrichment in XFEM
α	attenuation coefficient
$[D]$	Bending stiffness matrix
D	Bending/flexural rigidity of the plate
[B]	Bending-extensional coupling stiffness matrix
$\mathbf{L}_\mathrm{e}$	Boolean connectivity matrix
Γ_e	Boundary of finite elements
Γ_e^c	Boundary of the cohesive element
L_e	Characteristic element dimension
μ_k	Coefficient of kinetic friction assuming dry and clean surfaces
$\mathbf{u}$	Column vector of nodal displacements
$\widetilde{\mathbf{C}}$	Components of a second-rank tensor in the 6D space
η_{crack}	Crack loss factor
G_{IIc}	Critical energy release rate for mode II fracture
ϖ	Damage variable associated with a particular elastic property
λ	Damping coefficient
k	Denotes the thermal conductivity
ρ	Density
χ	Displacement
u_0, v_0, w_0	Displacements along the (x, y, z,) coordinate directions
$\mathbf{u}(\mathbf{X})$	Displacements at a material point $\mathbf{X}$
$\mathbf{u}_I$	Displacements at the nodal degrees of freedom
Ω_e	Domain of finite elements
E	Elastic modulus
Q_0	Excitation amplitude
$[A]$	Extensional stiffness matrix
$\varepsilon_{xx}^{(1)}, \varepsilon_{yy}^{(1)}, \gamma_{xy}^{(1)}$	Flexural (bending) strains
G_c	Fracture toughness
f	Frequency
ΔT	Temperature gradient

$\mathbf{F}^{ext}$	External forces vector
$\boldsymbol{C}$	Heat capacity matrix
$\mathbf{F}^{int}$	Internal forces vector
∇	Gradient operator
$\mathbf{E}$	Green-Lagrange strain
c_g	Group velocity
$\mathbf{q}$	Heat flux vector
ω_{max}	Highest natural frequency of the system
V_i	Impact velocity
x_0	Initial (at time of first contact) displacement (assumed zero)
E_0	Initial kinetic energy or initial elastic moduli corresponding to the undamaged response of the material
v_0	Initial velocity (prior to impact)
$\mathbf{X}$	Lagrangian (material) coordinates
C_0	Linear elastic modulus
$\mathbf{M}$	Lumped mass matrix
m	Mass or material softening parameter governing the stress-strain response of the damaged lamina
V_s	Material speed of sound
$\mathbf{B}$	Matrix of spatial derivatives of shape functions
P_{max}	Maximum force during impact
$\varepsilon_{xx}^{(0)}, \varepsilon_{yy}^{(0)}, \gamma_{xy}^{(0)}$	Membrane strains
$\ddot{\mathbf{u}}$	Nodal accelerations vector
q^{NL}	Nonlinear force term which can be a sum of quadratic and cubic terms
c_{ph}	Phase velocity
$\{\bar{Q}_{ij}\}$	Plane stress reduced stiffnesses
ν	Poisson's ratio
$\ddot{\mathbf{u}}$	Second time derivative of the global displacement vector
δ^F	Separation at failure
N_I	Shape functions
m_1	Shear coupling coefficient
τ	Shear stress
c_p	Specific heat of a material

$\mathbf{K}$	Stiffness matrix in Kelvin notation
$\mathbf{C}$	Stiffness matrix in Voigt notation
$\mathrm{U_e}$	Strain energy
$\mathrm{U_s}$	Strain energy
$\dot{\varepsilon}$	Strain rate
S_{aT}	Strength with subscripts indicating the direction and failure mode
$\tilde{\boldsymbol{\sigma}}^{(i)}$	Stress eigentensors
$\Delta\sigma_k^m$	Stress increment in the principle material direction
$\boldsymbol{\sigma}$	Stress tensor
m	Structural mass
ΔT_k	Temperature increment at a current simulation step k
$\otimes$	Tensor or dyadic product
$\mathbf{k}$	Thermal conductivity tensor
Δt	Time increment or time step
t	Time or laminate thickness depending on the context
ε_k^m	Total element strain components in principle material directions
$\bar{\mathbf{t}}_e$	Traction forces vector acting on the standard finite element
W_0	Transverse (out-of-plane) displacement
$\{\varepsilon^0\}$	Vector containing the membrane and bending strains
$\mathbf{b}$	Vector of body forces
$\{N\}$	Vector of force resultants
{M}	Vector of moment resultants
$\mathbf{t}_\mathrm{x}$	Vector of surface tractions
$\mathbf{f}$	Vector of the body forces per unit volume
α_T	Vector of thermal expansion coefficients
$\mathbf{t}^c$	vector of traction forces per unit area in the element coordinate system
v	Velocity or displacement along y coordinate depending on the context
$\delta\mathrm{u}$	Virtual displacement
$\delta\dot{\mathrm{u}}$	Virtual velocity
k	Wave number
λ	Wavelength
ε_y	Yield strain

Table of Contents

Table of Figures

1 Introduction

1.1 Background and Motivation

New technologies are fuelling the effort to advance the renewable energy enabling development of commercially viable spacecraft and airliners that leave a smaller carbon footprint. Owing to their high specific strength (strength to mass ratio), laminated composite materials, especially fibre reinforced polymer or plastic (FRP), has been increasingly contributing to this effort. In the aerospace industry, the use of carbon fibre reinforced plastic (CFRP) has been instrumental in driving the improvement in passenger comfort (e.g. allowing higher cabin pressure), reducing overall weight (and hence increasing fuel burn savings), reducing lifecycle cost and environmental impact. Since late 1980s, A320 featured 15% of CFRP by mass; this proportion is 25% in A380 and 50%+ in the latest generation of aircraft such as Boeing 787 and Airbus A350 with the ratio set to increase in the future designs [1]. Evidently, this signifies a shift from the use of FRP laminates in secondary structural components (e.g. fairings, landing gear doors, interior panels etc.) to mission critical primary structural components (e.g. outer wing, fuselage, spars) as shown in Figure 1.1. Therefore, as the use of the laminated composite materials goes through this transition, the objectives of the analysis must be expanded to include: (i) an accurate assessment of local regions especially prone to damage and (ii) predicting an acoustic response of the structure in its damaged state in order to aid an effective Structural Health Monitoring (SHM) when in service. This study aims to contribute to both of these objectives.

Figure 1.1: Airbus A350XWB materials used by weight; reproduced from [1].

1.1.1 Composite Materials and Damage Tolerance

Composite materials constitute a combination of materials that are arranged or mixed together in order to attain specific structural properties that are superior to the properties exhibited by the individual constituents. These individual components are not merged or dissolved within a composite. Instead, they are grouped together in a layered fashion and form a laminate. A typical layer, which is also referred to as lamina or ply, of an advanced laminated composite material consists of fibrous material (e.g. carbon fibre, fibreglass, Kevlar® etc.) embedded in a thermosetting resin[1] matrix. The plies are stacked together at various orientation angles in order to achieve the desired structural properties such as strength, stiffness and dimensional stability[2]. In the aerospace industry, the ply angles are usually constrained to 0°, 45°, 90° with infrequent use of 30° and 60° ones. This is primarily due to a potentially increased manufacturing effort that would arise in managing a large number of ply orientations. However, there is evidence from naturally occurring structures that suggests that composite materials with layers arranged in a *helicoidal*[3] stacking sequence exhibit enhanced damage resistance during repetitive impact events. Driven by this evidence, the first part of this thesis explores the energy absorption capabilities of composite laminates with helicoidal stacking sequences and their potential use in applications where *damage tolerance* is required.

In general, there are two approaches in aircraft design – *safe life* and *damage tolerance*. The former philosophy requires that the components are designed in such a way that a damage grows slowly enough that no defect would reach a critical level that may compromise the safety of the structure and ultimately the passengers during the service life of the aircraft. This naturally leads to a very conservative design. In damage tolerant philosophy, which is characteristic to modern aircraft design, the damage grows at such a rate that it can be detected and repaired/replaced before a catastrophic failure can develop. In an aircraft structure, damage may be caused by a number of factors such as fatigue accumulated during service or by foreign object damage (FOD). FOD can be typically described as physical damage that is caused by the object that is not a deliberate part of the vehicle design (hence *foreign* object) which may or may not lead to the degraded performance or safety characteristics of the vehicle. Examples of foreign FOD include debris, rocks, ice build-up on the wings, lightning strike, hail and birdstrikes. One of the most famous occurrences of birdstrike took place in 2009 when an Airbus A320 made an unpowered emergency landing in the Hudson River following multiple birdstrikes which caused both engines to fail. Although rarely fatal (at least to the aircraft and

[1] Resin is a generic term used to define a polymer such as epoxy which is a structural adhesive.
[2] Dimensional stability is a measure of the linear dimensional change which results from thermal exposure.
[3] Helicoidal stacking sequence implies a composite laminate created by rotating each ply (layer) by a small angle relative to each other when staking these layers during manufacturing, with the final arrangement resembling a helix – see Figure 4.8(c-e) of Chapter 4 Section 4.3.1 for clarity.

the passengers), birdstrikes are recognised as an ever increasing threat to aviation safety. Some visual examples of the consequences of such event are shown in Figure 1.2.

(a) – (reporduced from [2]) (b) – (reproduced from [3])

Figure 1.2: (a) A flock of starlings fly straight into the path of the Boeing 737 airliner as it lifts off at 200mph – engine damage was reported and the aircraft landed safely after circling for 45 minutes [2]; (b) A Boeing 757 struck a bird at 4600 feet during the climb following take-off with aircraft landing safely at the destination airport where a large dent in the radome was revealed; aircraft was out of service for 24 hours with repair costs over $30,000 [3].

In the UK, there were over 2,500 birdstrikes to civil aircraft reported to the Civil Aviation Authority (CAA) in 2013 alone [4], while the number of such incidents as recorded by the Federal Aviation Administration (FAA) in the United States was just over 13,500 in 2014 [3]. As the total number of aircrafts and flights is only increasing year by year, the statistics show that the frequency of the birdstrikes are set to grow accordingly. This leads to a requirement of FOD tolerant airframe and engine design. Laminated composites materials may assist in reducing the effects of FOD and prevent catastrophic failure by absorbing the impact energy via mechanisms not typical to metals.

Damage tolerance approach in aircraft design has important implications in improving the overall efficiency and reducing the environmental footprint as it leads to reducing weight without compromising safety. International Civil Aviation Organization (ICAO) sets out the minimum safety and environmental requirements for civil aircraft to be allowed to fly. In order to meet the environmental challenges that are facing our planet, these standards are becoming ever more stringent, meaning that each new aircraft generation is required to be quieter and cleaner. As part of an international effort to secure a sustainable future, ICAO imposed a long term goal (2026) to reduce the CO_2 and NO_x (oxides of nitrogen) engine emissions by 60% compared to the average levels produced by airliners manufactured up to 2005 [5]. This goal may be achieved through a range of improvements in various subsystems, weight reduction, aerodynamic efficiency and engine fuel efficiency. As mentioned earlier, the use of CFRP has already been contributing to weight reduction and therefore increasing

the overall efficiency. However, it may not have been used to its full potential yet. Interestingly, in aerospace industry, the safety factors not exceeding 1.5 are typical for design of various wing and fuselage structures made of metal alloys, whereas a number of 2.0 is usually considered for the components made of laminated composite materials [6]. This means that composite components are intentionally designed in rather conservative manner in order to account for uncertainties associated with their behaviour during a considerably long and cyclic life of an aircraft. This is primarily because the behaviour of metals is very well understood and practically tested, while even with the extensive research effort over the past decades the same cannot be stated about composites. Intrinsically complex and nonlinear nature of deformation, damage propagation and failure mechanics in composite laminates significantly impedes and complicates the analysis and design process, while physical full-scale and subscale testing of aircraft components during a range of conditions is time consuming and expensive and presents difficulties in obtaining the reliable data. Hence, alternative means of evaluation that are able to predict the dynamic response of the composite structures are needed. With the growing capabilities and availability of high power computing, numerical modelling and simulations are being increasingly used to design laminated composite structures for damage tolerance while reducing time to market.

Evidently, a smarter and more effective use of composite materials is needed in order to address the engineering challenges mentioned above. As part of this effort, the first half of this thesis focuses on studying the impact response of CFRP laminated plates with nonstandard, *helicoidal* stacking sequences through a range of simulated and experimentally conducted Low Velocity Impact (LVI) events. LVI is a well-established method for testing composite structures where the impact is typically taking place perpendicular to the plate which is the weakest, least stiff and non-reinforced direction and therefore leads to a larger damage extent. This method has been extensively used by researchers and industry alike as it mimics a very likely scenario of a hardware tool being dropped on the composite component during production or servicing and other types of FOD occurring during manufacturing or service life. The contact force, indentation, and extent of internal damage can be quantitatively analysed as the result of LVI testing which can be used to assist the effective design of composite structures. This in turn may play an important role in enhancing damage tolerance capabilities of passenger aircraft while allowing weight savings critical for compliance with the stringent environmental requirements.

1.1.2 Nondestructive Testing and Evaluation (NDT/NDE)

As explained previously, there are a number of real life situations where LVI events may occur and result in impact damage. While metals can absorb the impact energy by deforming plastically (in irreversible or permanent manner), which can be typically detected visually as dents in the structure, laminated composite materials usually exhibit internal damage during LVI scenarios leaving little to virtually no externally visible trace of the impact taking place. The extent of internal damage caused by LVI may be considerably more significant and detrimental to structural integrity than can be visually observed. This phenomenon constitutes a class of damage known as Barely Visible Impact Damage (BVID) which requires a use of specialised SHM techniques called Nondestructive Testing (NDT[4]) and Nondestructive Evaluation (NDE[5]) which enables appropriate detection and evaluation of such damage. As can be glimpsed from its name, NDT refers to testing without the destruction of or damage to the material being tested and generally involves the determination of the type, size, location and orientation of damage or flaws in the medium being tested. The commonly used techniques include visual inspection, ultrasonic testing, X-ray inspection, thermography and electrical/magnetic methods. Over the past several decades, these techniques have expanded significantly and are regularly used in virtually all major engineering industries – in transportation for inspection of railways, aircraft and helicopter parts; in civil engineering for inspection of bridges and buildings; and in energy sector for inspection of oil/gas pipes and wind turbine blades to name a few examples. The NDT/NDE methods are well-established for metal parts, whereas in the field of composites, they are still a very active field of research. In metals, fatigue is one of the prevailing damage types. However, there are considerably more defect types that composite materials are susceptible to such as porosity and delamination to name a few. Porosity can be a result of inadequate tooling, poor resin mixing, incorrect layup and curing procedure. Delamination is a separation of adjacent layers and is a typical consequence of impact damage. The major defects arising in composite parts can be summarised as follows:

Material Manufacturing Flaws:	**Assembly Faults:**	**In-service Damage:**
Delamination	Impact Damage (e.g. tool drop)	Impact Damage (e.g. FOD)
Debonding	Surface scratches/tears	Lighting strike
Porosity	Bonding faults	Water ingress
Resin poor/rich regions	Fastener errors	Fatigue
Fibre waviness	Layup errors	
Fibre fracture		

Table 1-1: main defect types and causes in composite components.

[4] Nondestructive testing can be synonymously referred to as nondestructive inspection or examination.

[5] Some authors make a distinction between the abbreviations NDT and NDE, in that NDT is merely a technique used for flaw detection, whereas NDE refers to a more quantitative analysis aimed at determining the size, orientation and sometimes consequences of such defects. In the context of this thesis, no real difference is implied and the terms NDT and NDE are often used interchangeably.

Detection and evaluation of defects and damage at early stages in service life of an aircraft are central to the damage tolerant design philosophy. The concept is demonstrated in Figure 1.3 by schematically plotting the growing damage size against time.

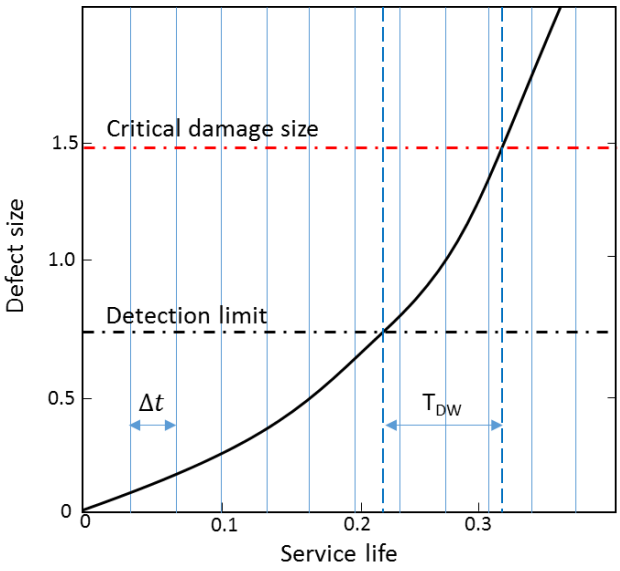

Figure 1.3: inspection windows in damage tolerant design.

In order to ensure safety, the time between inspections (Δt) must be less than $T_{DW}/(N+1)$, where T_{DW} is the time between the defect being detectable and becoming critical, and N is the number of inspections required to be certain of detection. Thus, increasing the sensitivity and reliability of NDT/NDE techniques can ultimately result in lower detection limits and increased inspection intervals or reduced structural weight by allowing the damage to grow at a higher rate with reduced critical size. A range of NDT/NDE techniques can be successfully utilised depending on the composition, dimensions of the part, damage type of interest, accuracy required etc. However, the most powerful and by far the most frequently used NDT techniques are linear ultrasonic methods as they allow directly relating the characteristics (e.g. wave speed, amplitude, phase etc.) of the propagating ultrasonic wave to the material properties or location and size of the flaws/damage. These techniques are effective in detecting well-developed defects, such as open cracks and delaminations, but are less sensitive to distributed micro-cracks and low level material degradation. Nonlinear ultrasonic NDE has a potential to overcome this limitation by looking at the frequency content of the received signal which differs from the input one in presence of discontinuities (e.g. cracks, voids, inclusions, delaminations) in the medium. Indeed, material failure is typically preceded by a nonlinear mechanical behaviour that manifests prior to significant plastic deformation or visible material degradation, which explains the increasing attention from the SHM/NDT research community on the nonlinear ultrasonic methods [7]. Therefore, a major part of this thesis was dedicated to developing and advancing the class of nonlinear NDT techniques referred to as nonlinear elastic wave spectroscopy (NEWS) methods which can offer high sensitivity to defect/damage detection at the early stages, improving the efficiency and safety of air travel.

1.2 Objectives

The primary objectives for this PhD work can be broadly outlined as follows:

1. Extending the damage tolerance of CFRP laminates through the study of helicoidal composites.
    a. Review the numerical methodologies and currently available simulation tools for analysing transient response of complex lamination sequences under dynamic load.
    b. Examine the response of helicoidal composites under low velocity impact (LVI) and assess their residual strength through a range of experimental-numerical studies.
2. Enhancement of NEWS and nonlinear imaging (NIM) techniques.
    a. Review the linear and nonlinear NDT/NDE techniques and the numerical methods used for numerical modelling of elastic wave propagation in defect-free and damaged structures.
    b. Develop a range of experimental and numerical approaches that can be applied to study nonlinear elastic wave effects in solid structures, containing low level damage, such as fatigue cracks, BVID and disbonds, in both metallic and laminated composite materials.

Furthermore, the objectives included the dissemination of the outcomes of the research to the relevant project partners and stakeholders as well as writing journal and conference papers.

1.3 Approach

The twofold objective of this work means that two literature review chapters were required. However, it will be shown that the concepts introduced in one are relevant in the other and vice versa. The first half of the thesis focused on studying the structural response and possible benefits of *bio-inspired* laminates for extending damage tolerance of laminated composite materials, while the second part aimed at developing the experimental and numerical nonlinear acousto-ultrasonic methods for evaluation of structural damage. CFRP and aluminium were considered as primary materials during the investigations, although, the presented methods can be generally applied to other isotropic and generally anisotropic structures.

The first part involved drawing inspiration from examples of natural body armour found in certain animals that exhibit remarkable resistance to impact damage. Several elements of these bio-structures such as helicoidal arrangements were adopted to laminated composite materials (CFRP) to assess a potential for increasing the damage tolerance capabilities of aerospace components. This was preformed via experimental (e.g. LVI testing) and numerical studies (i.e. FEA) provided in Chapter 4. The choice of the numerical and analytical methods was driven by the review of the relevant state-of-the-art techniques which are discussed in Chapter 2 of the literature review.

The second part of this work aimed at developing novel methodologies for defect and damage detection in aerospace materials using nonlinear class of NDT techniques due to their superior sensitivity to low level damage. A number of typical aerospace components were considered including composite stiffener panels and adhesively bonded joints. The experimental approach involved the use of piezoelectric transducers along with the thermal and Laser-Doppler vibrometer imaging in order to interrogate the structure and capture its thermal and mechanical response. Moreover, numerical studies were carried out simulating various structural states by means of modal and wave propagation analyses using a commercial FEA code. The devised numerical and experimental methods are given in Chapter 5, while the corresponding literature review is provided in Chapter 3.

Throughout this work, a commercial FEA solver LS-DYNA® was used for various analysis types due to its unsurpassed computational efficiency and capabilities that will be further addressed later in the thesis.

The outline of the thesis followed by the original publications is provided next.

1.4 Thesis Outline

Chapter 2 provides some fundamental theory and reviews the literature in the field of damage mechanics and impact energy absorption of composite materials.

Chapter 3 reviews various NDT/NDE techniques including linear ultrasound and NEWS methods along with the underlying theoretical concepts.

Chapter 4 starts with a further literature review of impact resistant materials and composite laminates drawing inspiration from a number of examples found in nature. Subsequently, the experimental and numerical studies involving bio-inspired laminates are provided.

Chapter 5 proposes and evaluates a range of NEWS-based methods for effective NDT/NDE of aircraft components containing fatigue cracks, BVIDs and disbonds. Furthermore, numerical techniques for modelling nonlinear elastic wave phenomena in isotropic and anisotropic structures are presented.

Chapter 6 summarises the work carried out and provides suggestions for future work.

1.5 Publications

D. Ginzburg, and M. Meo. "Damage tolerance of bio-inspired helicoidal composites under low velocity impact." *Manuscript submitted to the Journal of Composite Materials,* 2016

D. Ginzburg, F. Ciampa, and M. Meo. "Nondestructive evaluation based on generation of subharmonic frequencies in single lap adhesive Joints." *Manuscript submitted to the journal NDT & E International,* 2016

G.P. Malfense Fierro, D. Ginzburg, F. Ciampa, M. Meo. "Nonlinear thermosonics and laser vibrometry for barely visible impact damage of a composite stiffener panel." *SPIE Smart Structures and Materials+ Nondestructive Evaluation and Health Monitoring*. International Society for Optics and Photonics, 2016.

G.P. Malfense Fierro, F. Ciampa, D. Ginzburg, E. Onder, and M. Meo. "Nonlinear ultrasound modelling and validation of fatigue damage." *Journal of Sound and Vibration,* 2015.

2 Composite Damage Modelling Techniques

This chapter provides a comprehensive literature review starting with the explanation of the fundamental failure modes, energy absorption capabilities and testing methods used for the mechanical evaluation of laminated composite structures. This is followed by the analytical theories that are used to analyse the deformation and stress state of such materials. The numerical methods and fracture modelling techniques that can be employed in order to simulate the behaviour of composite structures under complex loading conditions are introduced next. However, before embarking on the discussion of the failure mechanics and numerical modelling of composite laminates, a reader is encouraged to refer to Appendix A in order to get acquainted with some standard terminology and notations associated with the field of composites.

It is important to note that no attempt is made here to cover all significant theory and publications. This is simply not feasible, as for example, at the time of writing of this thesis, a simple search on *Google Scholar* for '*Composite Damage Modelling*' returns over 250,000 publications.

Therefore, in this work, a descriptive discussion is presented with selected references which are cited to deliver evidence and sources for further reading on specific points related to this study.

2.1 Failure Mechanics of Composite Laminates

In general, an advanced material is required to be both strong and tough. However, strength and toughness are usually competing and sometimes exclusive characteristics. Strength is the ability of a material to withstand loads without deforming in plastic manner or fracturing/rapturing and it can also be defined as the maximum stress at failure. Toughness, which is an important property in crashworthiness analysis, is the ability of a material to absorb energy (e.g. during impact) without fracturing – it can be defined as the area under the stress-strain curve. Crashworthiness is defined as the ability of a structure to absorb impact energy in a non-fatal (to the structure and/or its contents) manner. An ideal energy absorbing material should be strong and ductile in order to deform plastically at high stress and strain until failure. As explained earlier, unlike metals, composite laminates and their constituents are not sufficiently ductile to deform plastically to the extent typical for metal alloys. FRPs dissipate internal strain energy primarily by crack growth and fracturing at the microstructural level in the fibre-matrix interface and as planes of weakness between the plies at the macroscopic level. This creates large amounts of new surface area resisting further deformation via internal friction. The design challenge is to facilitate controlled fracturing and fragmentation that allows a composite structure to undergo a large deformation while carrying the design loads. An effective composite

design promotes a controlled failure in a progressive manner. The progressive failure behaviour of a general composite laminate under an arbitrary load may be broadly divided into the following four sequential stages (see Figure 2.1):

1. *Undamaged state* – no matrix or fibre damage, elastic region
2. *Damage initiation* – onset of matrix cracking but fibres are intact
3. *Damage progression* – substantial matrix failure with some fibre fracture leads to reduction in load carrying capacity
4. *Final (catastrophic) failure* – substantial fibre breakup leads to laminate failure with low post failure stress

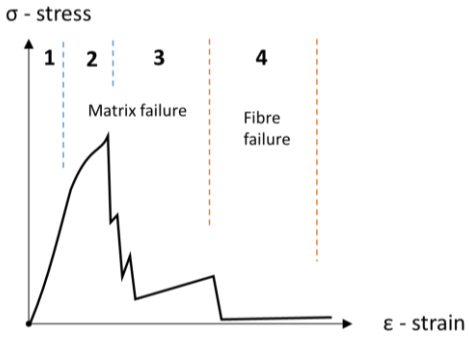

Figure 2.1: generalised damage states in a typical composite material.

As seen in Figure 2.1, the damage progression of composite laminates is dominated by matrix failure until ultimate failure by fibre fracture. Generally, the structural response is highly dependent on the relative brittleness and ductility of the fibres and the matrix among other factors such as a lamination scheme. Composite laminates utilising advanced resins such as *Bismaleimides* (BMI), which are significantly tougher than a typical epoxy resin, may exhibit some degree of plasticity characterised by a smoother progressive failure and larger area under the stress strain curve. The loading conditions also play an important role. In certain scenarios such as *high velocity impact* (HVI), the transition from stage 2 to stage 4 may not practically exist as both the matrix and the fibres fail simultaneously, and therefore, the graph in Figure 2.1 would look differently. Moreover, the relative stiffness of fibres also plays an important role in the overall performance limit of a composite. Figure 2.2 summarises the damage progression typical during a fatigue life of laminated FRP composites.

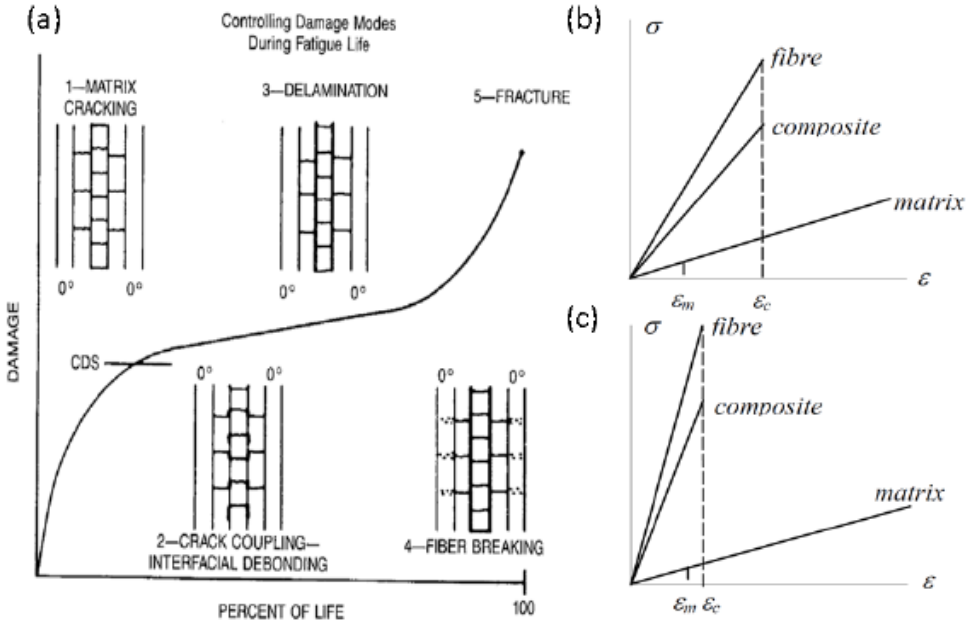

Figure 2.2: (a) fatigue damage development in composite laminates, (b) stress-strain curves for laminates with low stiffness fibres and (c) high stiffness fibres; reproduced from [8].

The aforementioned damage modes lead to a diversity of energy absorption mechanisms which can be exploited in certain applications such as crush resistance [9]. Generally, the energy absorbing capacity of FRP laminates depends on a multitude of factors such as the elastic and strength properties of the constituents as well as the loading direction to name a few. A chart shown in Figure 2.3 helps summarise these factors.

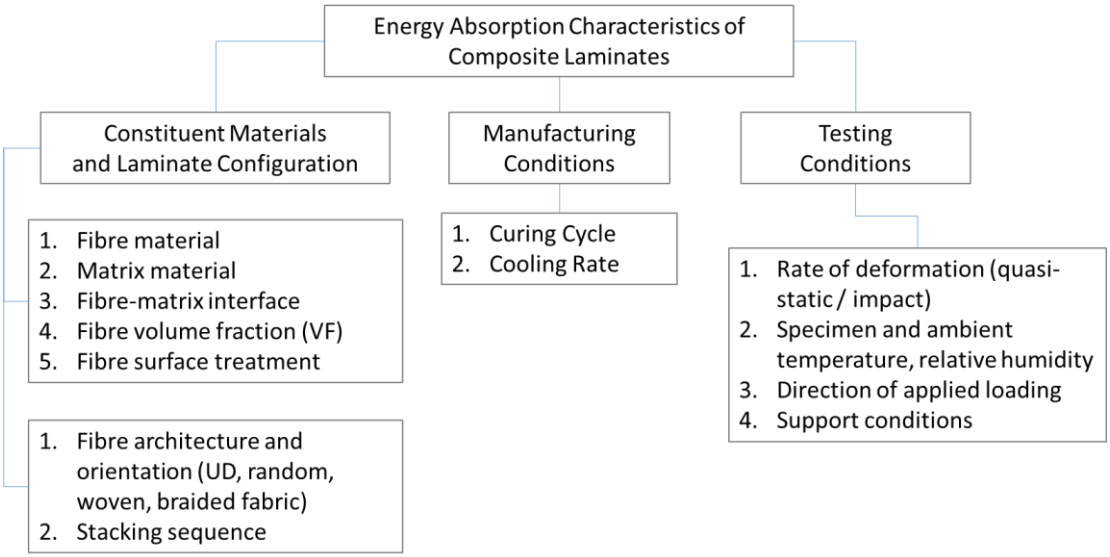

Figure 2.3: factors affecting the energy absorption characteristics of composite laminates.

The failure mechanics of fibre-reinforced laminates have been well understood through an extensive research and analysis using optical and scanning electron microscopes (SEM) and includes matrix cracking, interfacial debonding, delamination, fibre pull-out and fibre fracture [10, 11].

The mechanics of various failure modes of fibre-reinforced laminated composite materials can be generally explained from the perspective of classical fracture mechanics which states that a crack may propagate in a medium in three ways shown in Figure 2.4.

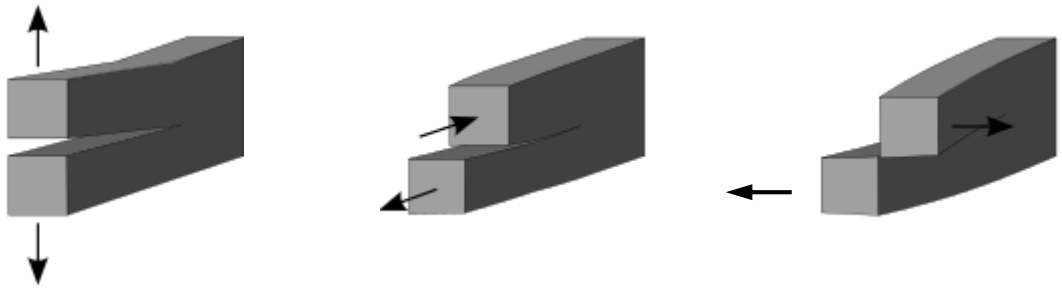

(a) – Mode I - Opening (b) – Mode II – In-plane shear/ sliding (c) – Mode III – out-of-plane shear / tearing

Figure 2.4: classical fracture modes of materials.

In a real world scenario, a crack or damage rarely propagates in pure mode I, II or III but as a combination of them which leads to a term *mixed mode fracture*. The energy released during advancement of a crack arises from the release of the elastic strain in the material. Given a fracture mode, a quantity called *strain energy release rate* (J/m^2) can be estimated for a specific material.

$$G = \frac{\partial U_e}{\partial A} - \frac{\partial U_s}{\partial A}, \qquad \textbf{(2.1)}$$

where U_e is external work and U_s is the strain energy and therefore ($U_e - U_s$) is the energy dissipated during fracture; A is the crack area or crack length for 2D analysis. G is frequently used for analysis of onset and growth of delamination and is considered to be independent of geometry and applied load; it is used in certain failure criteria - if the level of the strain energy release rate (G) reaches a certain value termed *critical energy release rate* (G_c – also known as *fracture toughness*) a fracture is said to take place. A vast number of studies focused on determining the fracture toughness of composite laminates for a particular mode (e.g. G_{Ic}, G_{IIc}) and the relationships between the modes [12, 13]. Experimentally, the fracture toughness can be estimated by means of Double Cantilever Beam (DCB) [14] or 3 Point Bending (3PB) [13] testing, while numerically, it can be calculated via Virtual Crack Closer Technique [15] (VCCT - more on this approach in Section 2.6.2). In a general composite laminate, mode-I fracture can initiate and propagate in two planes resulting in the flaws that are typically parallel to the fibre direction and are called *inter-* and *intra-* laminar cracking. The difference between them is graphically shown in Figure 2.5. Interlaminar damage such as *delamination* is defined as a discontinuity in the X-Y plane between two adjacent plies or laminae, whereas intralaminar crack is a discontinuity in the Z-X plane (through a lamina).

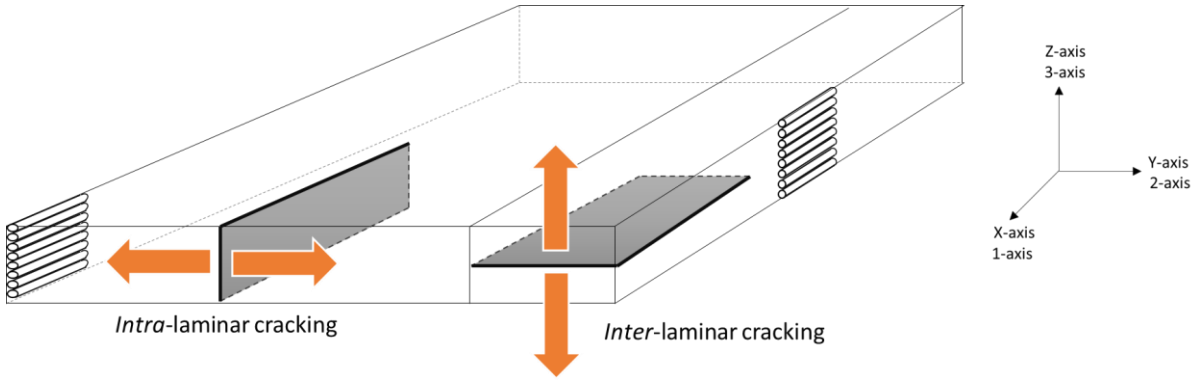

Figure 2.5: a schematic representation of interlaminar and intralaminar damage in a laminated composite plate.

Delaminations and intralaminar cracks often arise concurrently within a composite structure, as observed in LVI damage [16] and fatigue loading [17, 18]. Delamination or interlaminar damage is one of the prevailing and most important failure mechanisms of the laminated materials. It is generally characterised by debonding of the resin or fracture within the resin or reinforcement and leads to a separation of layers or plies. It can occur due to a number of reasons such as physical impact or poor processing during manufacturing which leads to structural discontinuities which in turn result in interlaminar stresses. Internal matrix cracks and porosity can act as precursors for the delamination to initiate in the laminate. Figure 2.6 schematically shows several delamination related defects that may arise during production.

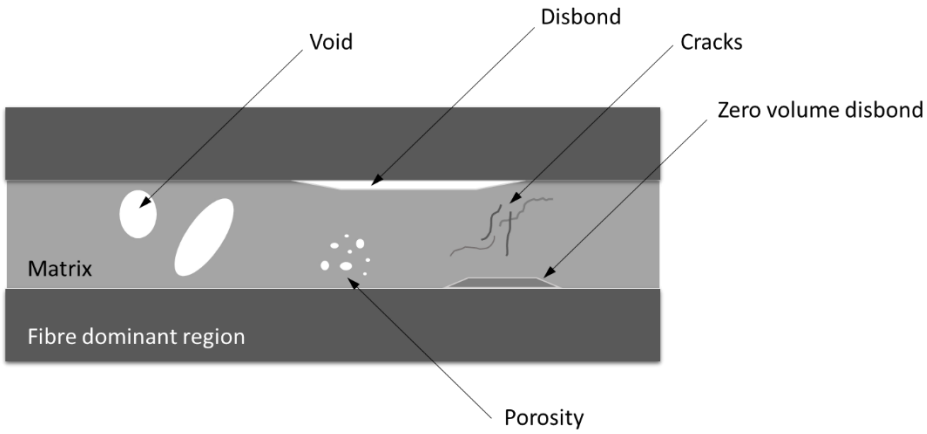

Figure 2.6: typical defects during manufacturing of laminated composite materials.

Intralaminar cracking is also an important energy absorption mechanism as it can act as a delamination migration pathway between adjacent interfaces as well as a boundary that constrains delamination growth [16]. Figure 2.7 presents an actual image captured using optical microscope of a damaged composite with several intra-laminar cracks and delaminations arising from fatigue damage [18].

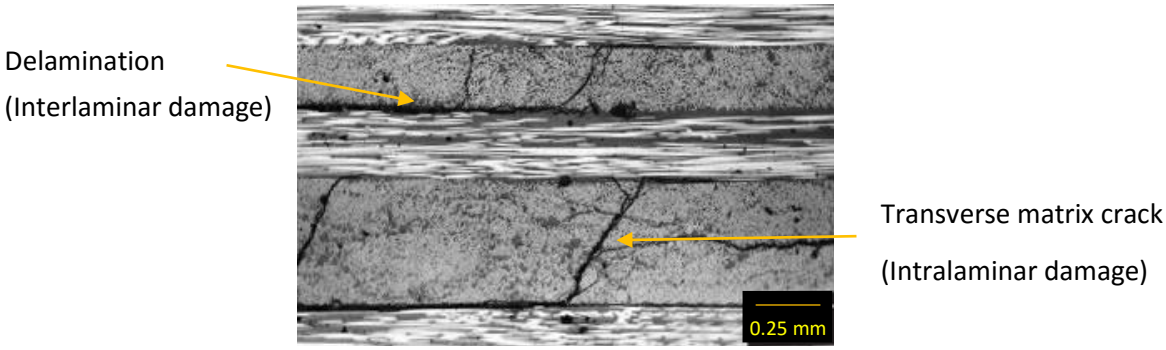

Figure 2.7: micro-photographs of a cross-section of a CFRP plate subjected to fatigue loading [18].

As evident from Figure 2.7, fracturing of a composite material involves not merely the breakup of load bearing fibres and the weaker matrix but also a complex combination of cracks developing along these interfaces. These complex energy-absorbing mechanisms increase the overall toughness of composites having important implications in terms of dealing with fatigue damage. Fatigue is one of the most common causes of catastrophic failure in metallic structures as plastic deformation is a key contributor; relatively small forces are required in order for crack front to propagate by plastic deformation at the tip due to local stress concentrations and as a result of cyclically applied load, the damage accumulates and ultimately leads to failure. In laminated composite materials, fatigue damage manifests itself as intra-laminar cracks and interlaminar damage (see Figure 2.7) which occur as the earliest fractures modes during repeated loading. Fibre fracture typically constitutes the most critical damaged state characterised by substantially reduced stiffness of the composite material. In fact, carbon fibres make little direct contribution to the overall toughness. On the contrary, the use of metallic fibres can make a significant contribution to the work of fracture. Angle-ply carbon/epoxy composite laminates develop many micro inter-laminar and transverse cracks following exposure to alternate loading which in fact increases the tensile strength (compared to unfatigued laminate) as the driving fracturing force is shared among these micro defects. This effect is called toughening or ware-in phenomenon [19]. The toughing mechanism may be understood more specifically by examining a propagation of a crack in an idealised situation of a single fibre embedded in a matrix considered by Cook and Gordon [20] (see Figure 2.8).

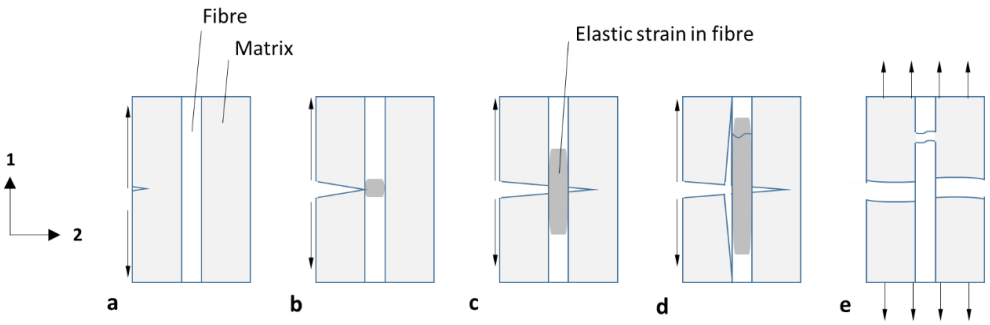

Figure 2.8: idealised crack propagation in matrix (adopted from [20]).

There exists a longitudinal stress σ_1, which is parallel to the applied load which is concentrated at the tip of the crack, and a significant transverse stress σ_2, which acts in the direction of the crack propagation. This transverse stress causes the crack to propagate until it encounters the stiff fibre which restricts further opening of the matrix crack. However, as the transverse stress concentration become more significant, the debonding may occur at the fibre/matrix interface resulting in the relative sliding between the matrix and the elastically extending fibre until the fibre breaks. When this occurs, the stored elastic energy is released and the fibre advances to regain the contact with the matrix. Therefore, the fractured fibre bridges the crack and the energy can be dissipated by the friction at the interface. For subsequent crack opening to take place, the fibre must either break in the middle of the matrix crack or it must be pulled out of the matrix.

This behaviour is not just hypothetical but is representative of what happens in an actual composite laminate and has a net effect of raising the overall toughness. Therefore, it may be stated that while UD CFRPs are not less susceptible to cyclic damage than metals, fatigue is less problematic in case of the UD CFRP because it does not significantly increase the probability of catastrophic failure developing in components manufactured from it. This does not necessarily apply to laminates with 2D woven carbon fibre reinforcement as the stress concentrations at crossover fabric locations lead to premature failure [18]. Weaving reduces overall toughness due to crimp interaction which tends to inhibit the Cook-Gordon toughening mechanism. However, Harris et al. [21] reported that woven composites retain their toughness when subjected to repetitive impacts in contract to the CFRP laminates comprised of UD layers which tend to lose their toughness after the initial impact.

2.2 Testing Methods

Generally, the testing of materials is aimed at acquiring the understanding of their physical characteristics such elastic properties and/or evaluating the state of materials in terms of structural health. Both of these aspects are considered in this study. Indeed, over the past decades, an array of *destructive* and *nondestructive* inspection techniques have been devised in order to detect the presence, determine the location and extent of damage or flaws in a material. Destructive testing involves cutting several sections at different locations and orientations from a given specimen, which are then examined using micrographs, SEM and similar optical methods. FRPs are typically cut using a diamond lapidary saw with a water spray to minimise the local heating. Another destructive technique called *deplying* entails chemical treatment of a composite laminate which successively allows to separate the plies with incurring minimum damage due to the procedure itself. Subsequently, the extent of delaminations and matrix cracks can be examined under an optical microscope. However,

the use of destructive techniques is usually confined to specific material research applications in a laboratory environment. In most practical cases, it is not feasible or desirable to alter a given composite structure (e.g. aircraft components in service) in the course of inspection. A broad and interdisciplinary field of NDT/NDE deals with such requirements. Section 3.2 of the thesis discusses various NDT techniques applicable to laminated composite materials.

As explained earlier, the failure modes of composite laminates are much more diverse than those of homogeneous isotropic materials such as metals and depend on a loading direction which leads to a requirement for specialised inspection and physical testing techniques. Although, it is possible to calculate some of the equivalent elastic properties of the laminate from the constitutive properties of fibre and polymer matrix using micro-mechanical theory, it is usually insufficient and impossible to obtain all of the required properties analytically. Over the past decades, a number of internationally accepted methods have been devised by standards organisations such as American Society of Testing and Materials (ASTM), British Standards Institute (BSI) and the International Organisation for Standardisation (ISO). They enable consistently measuring the elastic and strength properties of UD and woven composite laminates through a multitude of coupon testing. Moreover, by physically testing composite coupons, a further insight beyond of what can be understood from the constituent behaviour can be gained about the static and dynamic response of fibre-matrix interaction in a fabricated condition. The testing methods can be broadly divided into quasi-static and dynamic or impact testing.

2.2.1 Quasi-Static

In quasi-static testing, the test specimen is subjected to loading at a monotonic rate (constant speed). The strain rate in such experiments does not usually exceed 0.01 mm^{-1} [22]. This may not be a true representation of a real world case for a composite component that is expected to exhibit high rate of deformation such as experienced during some FOD events. This is because virtually all mechanical parameters of real world materials depend on the rate or speed they are being deformed at. This in turn affects the energy absorption capabilities. However, quasi-static testing is considered as an acceptable method for determining the elastic and strength characteristics of structures designed for carrying static loads as well as low to intermediate dynamic loads such as the conditions experienced during LVI events. In addition, quasi-static testing has an advantage in being relatively easy and inexpensive to setup and control.

An international standard ASTM D3039/D3039M [22] presents a standard coupon testing methodology for measuring tensile properties of polymer matrix composite materials, while the

mechanical characteristics of composite laminates associated with resistance to shear deformation may be experimentally estimated using ASTM D5379/D5379M [23]. The coupon testing involves a flat strip of material with a constant rectangular cross section being mounted using the grips of a mechanical testing machine which monotonically loads the specimen in the desired direction (e.g. tension) while recording the force. The maximum force before failure is used to determine an ultimate tensile strength. During the procedure, strain is recorded with strain gauges or displacement transducers in order to determine the stress-strain response of the material. Longitudinal tensile failure is typically characterised by brittle fracture of fibres, fibre-pull-out and fibre/matrix debonding.

Most composites are much weaker in the transverse direction with failure controlled by rupture or plastic flow of matrix. Shear strength of the composite laminates is of special importance as delamination occurs due to high interlaminar shear stresses (ISS) which tend to be high at the free edges of the laminate. The interlaminar shear strength (τ_{IL}) of polymer matrix composite material can be evaluated by means of 3PB test following the procedure outlined in ASTM D2344/D2344M [24]. A typical setup for this test is schematically depicted in Figure 2.9.

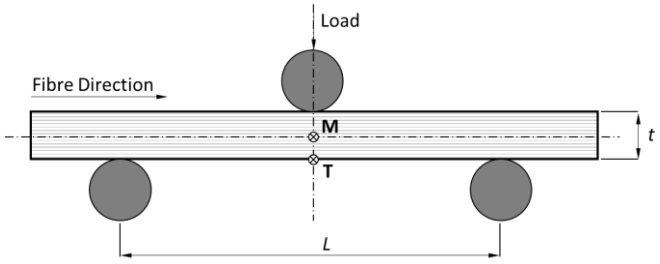

Figure 2.9: a schematic view of 3 point bending (3PM) testing.

Whether a laminate will fail due to reaching the maximum shear stress (τ_{IL}), which occurs at the mid-plane point labelled '**M**', or by reaching the maximum tensile stress (σ_T), which occurs at a point labelled '**T**' on the outer surface, depends on the span-to-depth ratio (*L/t*). Equating the stresses at point '**M**' and point '**T**', a relationship for the critical span-to-depth ratio (L/t) required for the specimen to fail in interlaminar shear at the neutral plane can be derived as follows:

$$\frac{L}{t} < \frac{\sigma_T}{2\tau_{IL}}. \qquad \textbf{(2.2)}$$

A typical CFRP laminate with σ_T of 1.5 GPa and τ_{IL} of 50 MPa will fail due to interlaminar shear failure at $L/t < 15$. For short beam testing, a typical span-to-depth ratio of 5 is used.

A procedure similar to that of the tensile and shear testing can be followed to determine the compressive properties of a laminate - ASTM D3410/D3410M [25] outlines such a method. Typical longitudinal compressive failure modes include microbuckling of fibres in shear or extensional mode and shear failure of fibres without buckling. Fibre reinforced components subjected to compressive

load can also fail in the ways termed *crushing* modes. Although there is no standardised procedure for it, crush failure is sometimes considered as a whole separate class of failure modes especially in automotive industry [26]. Several global crush failure modes of a composite specimen under compressive load are presented in Figure 2.10.

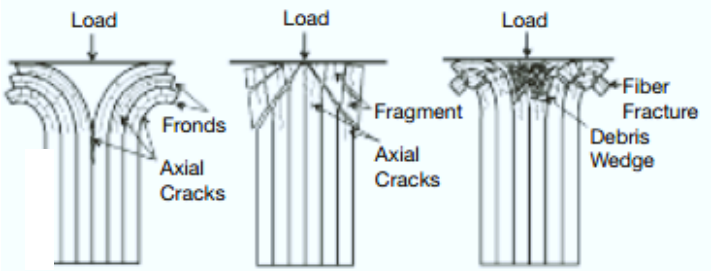

(a) Fibre splaying (b) Fragmentation (c) Brittle fracture

Figure 2.10: typical crash failure modes [27].

Another type of a quasi-static test called Compression After Impact (CAI) is typical in aerospace industry and is performed according to ASTM D7137/D7137M [28]. It is usually carried out after LVI testing in order to determine the residual compression strength of multidirectional polymer matrix composite laminate plates that have been damaged by impact. The residual tensile strength is less affected by the LVI than the compressive strength with reductions on the order of over 60% typical for BVID [29]. Delamination produced by a LVI test causes the laminate to divide into *sub-laminates* having lower bending stiffness than the original composite plate which makes the sub-laminates and the overall laminate less resistant to *buckling*. Figure 2.11 shows the difference between several buckling modes typical for delaminated beams and plates.

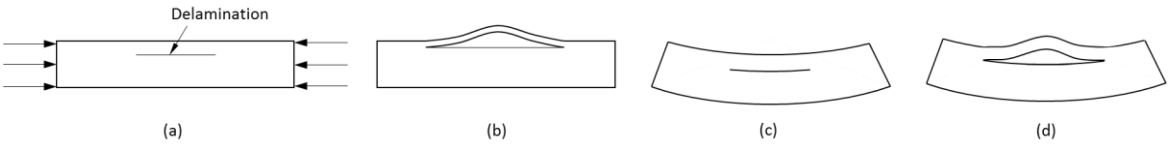

Figure 2.11: a schematic example of a composite plate subjected to axial compressive loading characterised by (a) stable compression without buckling (b) local (sub-laminate) instability (buckling) (c) global buckling (d) local-global (mixed mode) buckling.

The compressive loading of a partially delaminated specimen can exhibit *global buckling* and/or *local instability*/buckling [30]. The occurrence of the global plate buckling inhibits a consistent assessment of the post-impact residual strength of a composite. The presence of metallic anti-buckling guides used in CAI testing helps to support the specimen preventing the global buckling while allowing the local instabilities to take place at sub-laminate level by gradually applying an in-plane compressive load to a damaged rectangular specimen fixed at its base which essentially crushes the sample. The associated strength parameters such as maximum load and compressive strength are recorded. These properties provide guidance regarding damage tolerance capabilities of the composite structure

taking into account material parameters, thickness, stacking sequence etc. However, it is important to note that significant variability and differences in the relationship between pre-existing damage state and the residual strength may result because damage tolerance of composite structures highly depends on the component geometry, stiffness, support conditions and the damage distribution with its associated modes.

2.2.2 Impact

While quasi-static testing allows to evaluate the discrete material properties of composite laminates under virtually static conditions, impact testing enables to assess their overall performance under a sudden load application which may be a closer representation of a real world scenario. The initial impact velocity of the striker decreases as the specimen absorbs the impact energy by elastic / plastic deformation and material failure modes. The energy of the impact can be trivially stated as the kinetic energy, $E = \frac{1}{2}mv^2$, where m is the mass of the striker/impactor and v is its velocity during the initial contact. Evidently, it is possible to have high velocity, low mass and low velocity, high mass strike that yields the same impact energy. However, they would not yield the same response in terms of structural damage, contact force and energy absorption. An important implication of impact testing is that the deformation takes place at a higher rate than during quasi-static one and virtually all material properties are affected by this rate. In other words, impact testing accounts for stress or strain rate sensitivity of a material. The strain rate, which can be stated as $\dot{\varepsilon} = d\varepsilon/dt$, has units of s^{-1} and is a measure of a deformation change with time. The material properties start to depart from their quasi-static values at around 10^{-1} to 10^{2} s^{-1} which is considered a medium strain rate at which the inertial forces and mechanical resonance of the structure start to become significant and should be considered in the analysis. At higher rates, the stress and strain state of the test specimen starts to become influenced by the propagation of the stress wave through the material [31]. Figure 2.12 helps put the various regimes of the strain rate into context.

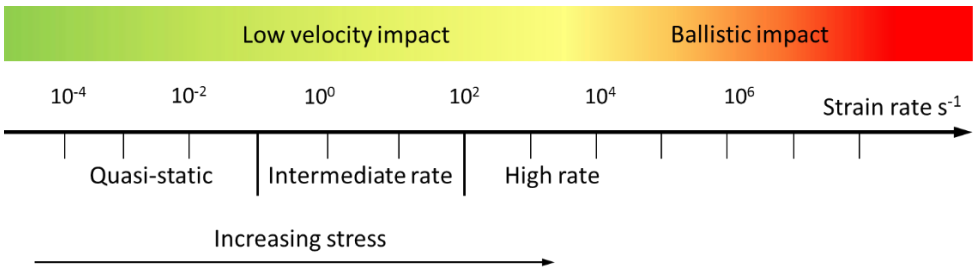

Figure 2.12: classification of strain rate regimes (adopted from [31]).

Due to the importance of the strain rate sensitivity, the impact testing is broadly divided into low velocity (large mass), intermediate velocity, high velocity (small mass) and hyper velocity regimes.

2.2.2.1 Low Velocity Impact (LVI)

In airline industry, LVI events can typically manifest themselves as tool drops during maintenance or collision with ground vehicles during servicing of an aircraft. During LVI, the contact interval is sufficiently long for the entire structure to respond by flexure and shear modes, whereas the high velocity impact is characterised by a very short duration allowing little time for the structure to respond globally and the damage is typically confined locally to the point of impact. A vast amount of research has been conducted over the past few decades in the domain of LVI on laminated composite plates and several review papers are available on the matter [29, 32, 33]. Cantwell and Morton [32] classified the impact velocity characteristic to LVI events to be below 10 m/s, whereas Liu and Malvern [34] proposed to classify the impact type based on the incurred damage. Other authors [30, 35] suggested that LVI should be generally characterised as the impact event resulting in a stress state of a target material which is not significantly affected by the through-the-thickness stress wave. In order to assess if the impact problem is a stress-wave-dominated or an LVI event, the following model based on a uniform strain state in the material region immediately under the striker can be used by defining a compressive stress wave causing a compressive strain as [30]:

$$\varepsilon_c = \frac{V_i}{V_s}, \tag{2.3}$$

where V_i is the velocity of impact and V_s is the speed of sound in the material. For epoxy composite laminates, considering failure strain of 0.5-1%, a transition to the stress wave dominated response is at approximately 10 to 20 m/s.

Increasing the impact velocity increases the peak force and the internal stresses in the laminate. During LVI, FRP laminates absorb the impact energy mainly in the form of strain energy and by means of matrix cracking, matrix deformation, delamination and moderate degree of fibre fracture, discarding the effects of energy loss through the boundaries and supports. Damage arising as the result of LVI usually progresses as depicted in Figure 2.13.

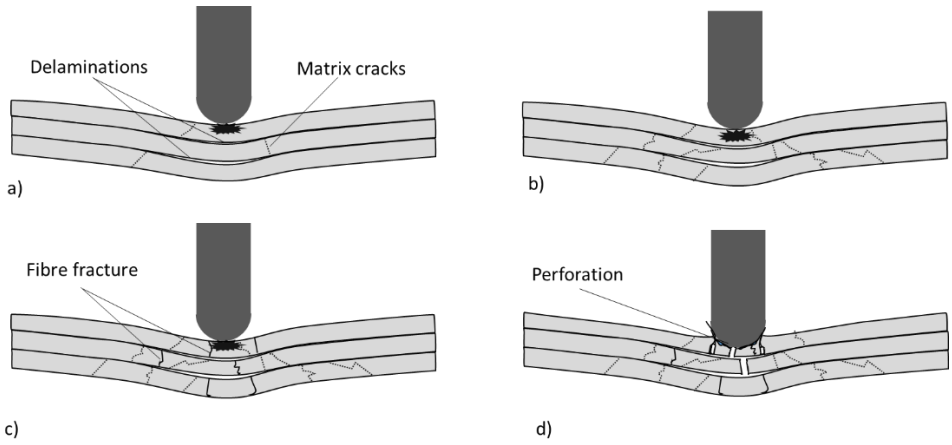

Figure 2.13: damage progression in a composite laminate during LVI.

Following an initial contact of the impactor with the composite plate, a damage confined to the impact area of contact occurs and is characterised by the matrix and fibre failure. Subsequently, the laminate deforms globally by bending which results in the top surface being in compression and the back/bottom surface being in tension. Matrix damage usually manifests first as matrix cracking and the onset of the fibre-matrix debonding and delamination. These cracks typically propagate in planes parallel to the fibre direction in the angle-ply laminates. The internal crack pattern is different for thin and thick composites as can be seen in Figure 2.14. Thin and flexible laminates tend to develop cracks perpendicular to the plate that originate at the back surface due to high concentration of tensile bending/membrane stresses. The ensuing cracks tend to propagate upwards initiating delaminations at the ply interfaces that resembles a “reverse-pine” tree pattern.

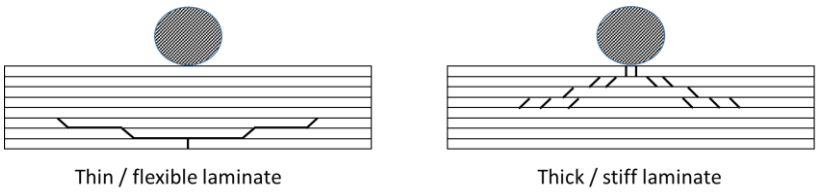

Figure 2.14: “reverse pine tree” and “pine tree” internal through-thickness crack pattern is characteristic in thin and thick laminates during LVI respectively; adopted from [30].

Contrary to the long thin specimens, short and thick laminates are stiffer which results in higher contact forces which in turn induce transverse shear cracks and damage propagates into the inner plies. The resulting delaminations increase the overall flexibility of the structure with the intralaminar cracks forming close to the delaminations which leads to a “pine-tree” like pattern. The damage propagation ceases in case the impact energy is insufficient to activate further crack opening mechanisms.

In general, higher areas of delamination occur between the layers of different fibre orientation due to the increased bending stiffness mismatch and consequently an increase in the transverse shear

stresses which typically appear to be maximum in the mid-layer of the laminate under low velocity impact [34]. In other words, the mismatch (difference) of the mechanical properties such as the Poisson's ratio ν_{12} between the plies is highly correlated with the extent of the delamination in the presence of bending stresses. Shear coupling coefficient m_1, which is also termed a coefficient of mutual influence, represents the amount of shearing in the x-y plane caused by the normal stress in the x-y plane and is defined as [30]:

$$m_1 = -\frac{\gamma_{12}}{\varepsilon_1} \ . \qquad \textbf{(2.4)}$$

The higher the $\Delta\nu_{12}$ between the adjacent plies the higher the interlaminar stresses. Furthermore, the effect of the Poisson's ratio mismatch depends on the overall stacking sequence of the laminate. The size of the delamination in a composite layup also depends on the difference in elastic constants of the layers, its thickness and the overall deflection of the laminate. Increasing the values of these factors will increase the delaminated area. As discussed earlier, this damage mode is an important energy absorption mechanism that can increase the toughness of a composite material.

Sometimes, it may be advantageous to determine the value of the impact force that causes the onset of delamination as it typically takes a certain threshold impact force level for damage to take place. Davies et al. [36] proposed a model based on *Hertzian contact*[6] for the critical force threshold required to cause delamination:

$$P_c^2 = \frac{8\pi^2 E_{11} t^3}{9(1-{\nu_{12}}^2)} G_{IIc} \ , \qquad \textbf{(2.5)}$$

where t is the laminate thickness, E_{11} is the elastic modulus, and G_{IIc} is the critical energy release rate for mode II fracture. In the above equation, a quasi-isotropic laminate is considered isotropic with a single delamination in the middle of a circular simply supported plate. Although considerably simplistic, this model implies that the critical force threshold is proportional to $t^{3/2}$.

The elastic energy absorbed during delamination failure under the transverse impact can be calculated using an empirical relationship [29]:

$$E = \frac{2{\tau_{IL}}^2 w L^3}{9 E_f t} , \qquad \textbf{(2.6)}$$

where τ is the interlaminar shear strength (ILSS), w is the width, L is the unsupported length hand E_f is the flexural modulus. According to Equation (2.6, the elastic strain energy is inversely

[6] *Hertzian contact law* defines a relationship between contact force and the associated displacement. Several assumptions are made in the derivation such as that the bodies in contact are perfect isotropic spheres. Further details can be found in [37]S. Timoshenko, J. Goodier, and H. N. Abramson, "Theory of elasticity," *Journal of Applied Mechanics,* vol. 37, p. 888, 1970.

proportional to the laminate thickness and the flexural modulus which indicates that thicker and stiffer composites dissipate less energy through an elastic deformation.

During low energy LVI, the corresponding delamination area typically grows linearly with increasing incident impact energy. At a certain higher energy level, this relationship is no longer linear and the main energy dissipating mechanisms are fibre fracture and perforation. Fibre failure generally takes places later than matrix related damage modes in the fracture process chronology, apart from the damage occurring locally in the vicinity of the striker surface. Fibre failure is considered as a precursor to the subsequent catastrophic failure by a significant perforation/penetration of the impactor into the material. The energy required for the fibre failure to occur at the tension face of the laminate can be stated as [38]:

$$E = \frac{\sigma^2 wL}{18E_f}, \tag{2.7}$$

where σ denotes a flexural strength and all other terms have already been defined in Equation (2.6. Perforation is considered a macroscopic failure mode occurring with a substantial extent of fibre failure which enables the impactor to penetrate the material. The energy absorbed by perforation during LVI involving a cylindrical impactor and a square target plate may be approximately estimated as [38]:

$$E = \pi\gamma^2 td\,, \tag{2.8}$$

where γ is the fracture energy, d is the diameter of the striker and t is the thickness of the plate.

It is important to note that LVI testing is very sensitive to the test setup and the geometry of the target plate. In fact, all factors outlined in Figure 2.3 may affect the dynamic response of the specimen. Early LVI testing of composite materials was conducted using a variety of methods such as *Charpy pendulum* [39] and *Izod test* to name a few. Relatively recently, a standard low velocity testing procedure specific to laminated composite materials was established, namely ASTM D7136/D7136M [40], and constitutes a drop-weight impact test where a striker of a certain mass and hemispherical shape is allowed to fall from a pre-set height hitting the test specimen supported in a horizontal plane. The setup allows testing more complex geometries than in Charpy and Izod tests. Figure 2.15 schematically demonstrates a typical instrumented falling weight setup used in LVI testing.

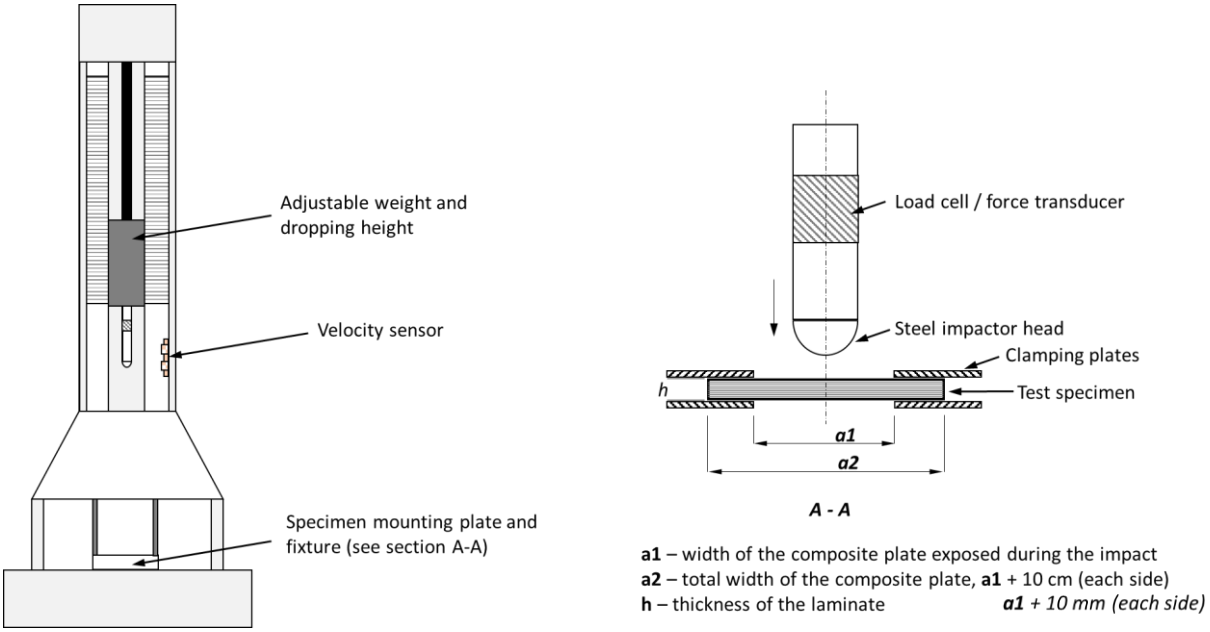

Figure 2.15: schematic view of a LVI weight-drop tower testing setup.

Treating the impactor as a free falling body, the impact energy can be calculated using potential energy:

$$PE = mgh\,, \tag{2.9}$$

where *m* is the mass of the impactor, *h* is the height from which the weight is dropped and *g* is the acceleration due to gravity. The kinetic energy of the striker prior to impact is:

$$KE = \frac{1}{2}mv^2\,, \tag{2.10}$$

Equating Eqs. (2.9) and (2.10), the velocity of the impactor prior to impact can be defined as:

$$v = \sqrt{2gh}\,, \tag{2.11}$$

The energy absorbed during the impact can be evaluated as follows:

$$E_a = E_0 - E_f = \frac{1}{2}m\left(v_0^2 - v_f^2\right), \tag{2.12}$$

where E_0 and E_f are the initial and final energies respectively with corresponding impact velocities immediately before (v_0) and immediately after (v_f) the impact. A typical time-response of the striker in terms of contact energy and contact force is show in Figure 2.16.

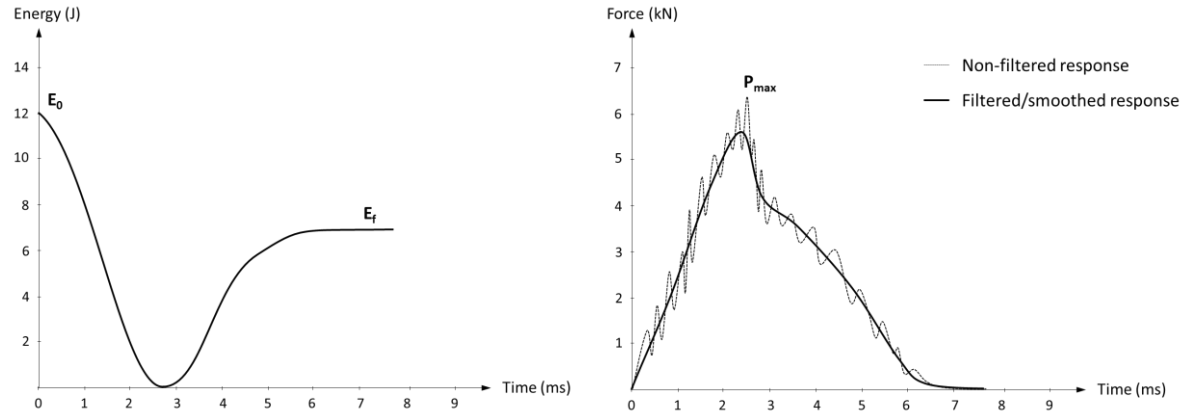

(a) (b)

Figure 2.16: a characteristic energy (a) and force (b) time response of a composite laminate during a typical LVI; adopted from [30].

As presented in Figure 2.16(b) above, the force response recorded by the load cell is characterised by the oscillatory behaviour as the resonance frequencies are excited following the impact. However, as the contact force increases from the initial contact, at some point, the incipient damage takes place as delamination or extensive matrix/fibre failure in the composite, which manifests as an abrupt reduction in the recorded force. This can occur before or after the maximum force (P_{max}) is reached and may contribute to higher oscillations. Therefore, smoothing the response data by using a numerical filtering algorithm can assist in interpreting the force-time curves especially when comparing the responses between various samples. However, an unfiltered response is used in determining the maximum impact force (P_{max}).

2.2.2.2 Intermediate and High Rate Impact

Examples of Intermediate Velocity Impact (IVI) are impacts arising from foreign object debris on roads and runways, secondary blast debris, hurricane debris and hail. The velocity range characteristic to IVI events is 10-50 m/s. High Velocity Impact (HVI) or ballistic impact can typically transpire as a result of impact from rifle fire, hail occurring in-flight and fragments during warhead explosions. The structural response during such events is dominated by the propagation of the stress wave through the thickness of the target material leading to a highly localised damage as the structure does not have enough time to respond globally. Damage in composite materials resulting from HVI is generally characterised by perforation with a delaminated area surrounding the ruptured area. The boundary conditions are of little importance and are usually not considered in HVI analysis as the impact elapses and the majority of the damage occurs before the stress wave can reach the boundaries. Damage mechanisms during HVI are highly dependent on projectile geometry and its corresponding velocity, the properties of the constituents and the level of adhesion between them. *Ballistic impact* is usually referred to impact

cases when a projectile completely penetrates a target material. While contact force may be of interest during LVI, quantities such as *ballistic limit*[7] and residual velocity are considered in ballistic impact. In ballistic applications, such as armour for personnel and vehicle protection, weaker matrix may be desired as delamination is readily activated allowing the fibres to extend until failure, which has a net effect of enhancing the energy absorption capacity. At intermediate and high velocity impacts, the strain rate considerations become important as the material properties start to depart from their quasi-static values. However, somewhat conflicting information exists in published literature regarding the effect the strain rate has on elastic and strength properties of FRPs [29, 41]. Daniel and LaBedz [42] measured compressive properties of 8-ply graphite/epoxy composite at strain rates up to 500 s^{-1} and reported that elastic modulus and strength was much higher in transverse direction with almost no difference in longitudinal one, as compared to quasi-static values; a decrease of 33% in the dynamic ultimate compressive strains was measured in the same testing. Hall and Guden [43] studied the dynamic response of graphite/epoxy laminates at the strain rates of up to 2000 s^{-1} indicating 60% increase in transverse strength but no significant change in elastic modulus and the failure strains in comparison to the quasi-static values. Some authors reported CFRPs as virtually strain rate insensitive [44], whereas Cazeneuve and Maile [45] reported 30% increase in transverse strength and 50% increase in longitudinal strength at the strain rate of 600 s^{-1} for carbon/epoxy composites. In general, with rising strain rate, FRP materials tend to respond by elevated elastic modulus and maximum stress with lower corresponding strains at failure. Therefore, it is evidently important that a given material should be characterised at the strain rate typical for the intended application.

Hyper velocity impact is considered when the projectile velocity is on the order of 2,500 m/s or higher which is comparable to the impact velocities during a potential scenario of space debris hitting a spacecraft in Low Earth Orbit (LEO). During hyper velocity events, the material behaves in a fluid like manner and this impact and velocity regime is well outside the scope of this work.

[7] *Ballistic limit* is defined as the initial velocity of the projectile that will cause complete penetration with probability of 50%.

2.3 Structural Theories for Analysis of Composite Plates

By their structure, composite laminates have the planar dimensions several orders of magnitude larger than the thickness which allows to treat them as plates. In this chapter, several commonly used plate theories are introduced, namely classical laminated plate theory (CLPT) and first shear deformation theory (FSDT) which are collectively referred to as equivalent single-layer (ESL) models [46]. These theories are derived from 3D elasticity reducing the problem to a 2D case which in turn requires making certain assumptions about the kinematics and the stress state distribution through the thickness of the laminate. For completeness, a brief introduction to 3D elasticity and continuum mechanics is presented first, which is also of importance in introducing the wave propagating phenomena discussed in Chapter 3.3.

2.3.1 3D Elasticity and Continuum Mechanics

A deformation in a body according to classical solid mechanics can be represented using a *Green-Lagrange strain*, $\mathbf{E}$. In terms of the displacement gradient, it can be written in a tensorial notation as [46]

$$\mathbf{E} = \frac{1}{2}[\nabla\mathbf{u} + (\nabla\mathbf{u})^T + \nabla\mathbf{u}\cdot(\nabla\mathbf{u})^T], \tag{2.13}$$

and in the rectangular Cartesian component form as [46]

$$E_{ij} = \frac{1}{2}\left(\frac{\partial u_j}{\partial X_k} + \frac{\partial u_k}{\partial X_j} + \frac{\partial u_m}{\partial X_j}\frac{\partial u_m}{\partial X_k}\right), \tag{2.14}$$

where ∇ is a gradient operator with respect to material coordinates, X; summation over the range of 1 to 3 is assumed on the repeated indices. In the case of small displacement gradients, $|\nabla\mathbf{u}| \ll 1$, the Green Lagrange strain tensor reducers to the infinitesimal strain tensor, $\mathbf{E} \approx \varepsilon$ [46]

$$\varepsilon = \frac{\mathbf{1}}{\mathbf{2}}[\nabla\mathbf{u} + (\nabla\mathbf{u})^T], \qquad \varepsilon_{ij} = \frac{1}{2}\left(\frac{\partial u_i}{\partial x_j} + \frac{\partial u_j}{\partial x_i}\right). \tag{2.15}$$

Eq. (2.13)-(2.15) are denoted strain-displacement relationships. A stress state of the body can be defined recalling Eq. (6.1) of Appendix A which represents a constitutive equation (stress-strain relation) also referred to as a material model. Subsequently, an equation of motion of a deformable body can be stated in a vector form and Cartesian component form as [46]

$$\nabla\cdot\sigma + \mathbf{f} = \rho\frac{\partial^2\mathbf{u}}{\partial t^2}, \qquad or \qquad \frac{\partial\sigma_{ij}}{\partial x_j} + f_i = \rho\frac{\partial^2 u_i}{\partial t^2}, \tag{2.16}$$

where $\mathbf{f}$ is a vector of the body forces per unit volume. Removing the right hand side (i.e. setting the time derivative term to zero), the usual equations of equilibrium are formed.

2.3.2 Equivalent Single-Layer (ESL) Plate Theories (2D)

According to the three-dimensional elasticity theory, each composite layer is represented by a 3D solid. Most composite plates are typically thin, and therefore, experience a *plane state of stress* assuming that transverse stress components ($\sigma_{33}, \sigma_{13}, \sigma_{23}$) are small in-plane (*xy* - plane) of the lamina compared to $\sigma_{11}, \sigma_{22}, \sigma_{12}$

$$\begin{Bmatrix}\sigma_{11}\\ \sigma_{22}\\ \sigma_{12}\end{Bmatrix} = \begin{bmatrix}\frac{E_{11}}{1-\nu_{12}\nu_{21}} & \frac{\nu_{12}E_{22}}{1-\nu_{12}\nu_{21}} & 0\\ \frac{\nu_{12}E_{22}}{1-\nu_{12}\nu_{21}} & \frac{E_{22}}{1-\nu_{12}\nu_{21}} & 0\\ 0 & 0 & G_{12}\end{bmatrix}\begin{Bmatrix}\varepsilon_{11}\\ \varepsilon_{22}\\ \gamma_{xy}\end{Bmatrix}, \quad \textbf{(2.17)}$$

where $\gamma_{xy} = 2\varepsilon_{12}$ and all other terms have their usual meaning defined in Appendix A.

Plane stress-reduced constitutive relation is one of the assumptions that allows to reduce the problem from 3D to 2D case. More generally, a heterogeneous laminate consisting of multiple layers is considered to act as one homogenised or equivalent layer assuming the displacement (or stress) field as a linear combination of unknown functions defined through the thickness coordinate (*z*).

Figure 2.17: coordinate system and layer numbering for a laminated plate.

2.3.2.1 The Classical Laminated Plate Theory (CLPT)

Due to its relative simplicity, CLPT is by far the most frequently used ESL analysis approach in the field of composite materials and is based on a number of assumptions about the nature of the constituents as well as the kinematic behaviour of the laminate. The matrix and the fibres are assumed to be homogeneous, equally spaced and perfectly aligned to form lamina (layers or plies) which are perfectly bonded together into a laminate (composite plate) restricted to behave as an orthotropic (three planes of material symmetry) elastic material. Several other restrictions are imposed such as uniform thickness of layers, only small strains and displacements are permissible, the transverse shear stresses are zero on top and bottom surfaces of the laminate. Furthermore, it is assumed that the Kirchhoff

hypothesis holds in the CLPT which states that transverse normals[8] are inextensible and remain straight and perpendicular to the mid-surface before and after deformation.

CLPT is essentially an extension of the classical (Kirchhoff) plate theory to laminated composite plates and assumes the following displacement field [46]

$$\begin{aligned} u(x,y,z,t) &= u_0(x,y,t) - z\frac{\partial w_0}{\partial x} \\ v(x,y,z,t) &= v_0(x,y,t) - z\frac{\partial w_0}{\partial y} \\ w(x,y,z,t) &= w_0(x,y,t) \end{aligned} \quad \textbf{(2.18)}$$

where (u_0, v_0, w_0) are the displacements along the $(x, y, z,)$ coordinate directions and $\frac{\partial w}{\partial z}$ is assumed to be zero. Collectively, these assumptions allow reducing the 3D problem to the analysis of the midplane (z=0). Further assuming small strain theory with ($\varepsilon_{xy} = \varepsilon_{yz} = \varepsilon_{zz} = 0$), the strains associated with the displacement field in Eq. (2.14) can be defined as follows [46]

$$\begin{Bmatrix} \varepsilon_{xx} \\ \varepsilon_{yy} \\ \gamma_{xy} \end{Bmatrix} = \begin{Bmatrix} \varepsilon_{xx}^{(0)} \\ \varepsilon_{yy}^{(0)} \\ \gamma_{xy}^{(0)} \end{Bmatrix} + z\begin{Bmatrix} \varepsilon_{xx}^{(1)} \\ \varepsilon_{yy}^{(1)} \\ \gamma_{xy}^{(1)} \end{Bmatrix} = \begin{Bmatrix} \frac{\partial u_0}{\partial x} + \frac{1}{2}\left(\frac{\partial w_0}{\partial x}\right)^2 \\ \frac{\partial v_0}{\partial y} + \frac{1}{2}\left(\frac{\partial w_0}{\partial y}\right)^2 \\ \frac{\partial u_0}{\partial x} + \frac{\partial v_0}{\partial y} + \frac{\partial w_0}{\partial x}\frac{\partial w_0}{\partial y} \end{Bmatrix} + z\begin{Bmatrix} -\frac{\partial^2 w_0}{\partial x^2} \\ -\frac{\partial^2 w_0}{\partial y^2} \\ -\frac{\partial^2 w_0}{\partial x \partial y} \end{Bmatrix}, \quad \textbf{(2.19)}$$

where $(\varepsilon_{xx}^{(0)}, \varepsilon_{yy}^{(0)}, \gamma_{xy}^{(0)})$ are called the *membrane strains*, and $(\varepsilon_{xx}^{(1)}, \varepsilon_{yy}^{(1)}, \gamma_{xy}^{(1)})$ represent the flexural (bending) strains which are known as the *curvatures*. Subsequently, the stress-strain relationship for the *k*th orthotropic layer in the laminate coordinates can be written based on the planes tress assumption [46]

$$\begin{Bmatrix} \sigma_{xx} \\ \sigma_{yy} \\ \sigma_{xy} \end{Bmatrix}^{(k)} = \begin{bmatrix} \bar{Q}_{11} & \bar{Q}_{12} & \bar{Q}_{16} \\ \bar{Q}_{12} & \bar{Q}_{22} & \bar{Q}_{21} \\ \bar{Q}_{16} & \bar{Q}_{26} & \bar{Q}_{66} \end{bmatrix}^{(k)} \begin{Bmatrix} \varepsilon_{xx} \\ \varepsilon_{yy} \\ \gamma_{xy} \end{Bmatrix}, \quad \textbf{(2.20)}$$

where $\bar{Q}_{ij}$ are the plane stress reduced stiffnesses with an overbar implying that the quantities are in the laminate coordinate system. In CLPT, the laminate constitutive equations are usually written in terms of *stress resultants* [46]

$$\begin{Bmatrix} \{N\} \\ \{M\} \end{Bmatrix} = \begin{bmatrix} [A] & [B] \\ [B] & [D] \end{bmatrix} \begin{Bmatrix} \{\varepsilon^0\} \\ \{\varepsilon^1\} \end{Bmatrix}, \quad \textbf{(2.21)}$$

where $\{\varepsilon^0\}$ and $\{\varepsilon^1\}$ are the vectors containing the membrane and bending strains; $\{N\}$ is a vector of *force resultants* and $\{M\}$ is a vector of *moment resultants* which unlike stresses are only function of *x* and *y* making tracking stresses in plates more convenient [46]

[8] Transverse normals are straight lines perpendicular to the mid-surface.

$$\begin{Bmatrix} N_{xx} \\ N_{yy} \\ N_{xy} \end{Bmatrix} = \int_{-\frac{h}{2}}^{\frac{h}{2}} \begin{Bmatrix} \sigma_{xx} \\ \sigma_{yy} \\ \sigma_{xy} \end{Bmatrix} dz, \qquad \begin{Bmatrix} M_{xx} \\ M_{yy} \\ M_{xy} \end{Bmatrix} = \int_{-\frac{h}{2}}^{\frac{h}{2}} \begin{Bmatrix} \sigma_{xx} \\ \sigma_{yy} \\ \sigma_{xy} \end{Bmatrix} z\, dz, \tag{2.22}$$

while $[A]$ is an extensional stiffness matrix, $[D]$ is a bending stiffness matrix, and $[B]$ is a bending-extensional coupling stiffness matrix. These stiffness matrices can be calculated for integrating the stiffness coefficients through the thickness of the laminate [46]

$$(A_{ij}, B_{ij}, D_{ij}) = \sum_{k=1}^{N} \int_{-\frac{h}{2}}^{\frac{h}{2}} \bar{Q}_{ij}(1, z, z^2) dz, \tag{2.23}$$

where *N* is the number of layers in the laminate. In general, the laminate stiffness can be a function of (*x,y*) position, although, homogenous plates (constant A_{ij}, B_{ij}, D_{ij}) are usually considered in analytical studies. Eq. (2.21) can be expressed in terms of displacement and substituted into Eq. (2.16) to form the equations of motion for composite plates based on CLPT. These equations can be solved analytically and/or numerically for the generalised strains and stresses. However, the exact solutions can only be obtained for a class of laminates called *specially orthotropic* such as $[0]_n$, $[90]_n$ and $[(0/90)_n]_s$ [47]. The analysis of such plates is greatly simplified because the bending and extensional deformation is decoupled ($B_{ij} = 0$) and $D_{16} = D_{26} = 0$. Considering the static bending of a specially orthotropic plate in the absence of the in-plane and thermal forces, the governing equation becomes [46]

$$D_{11} \frac{\partial^4 w_0}{\partial x^4} + 2(D_{12} + D_{66}) \frac{\partial^4 w_0}{\partial x^2 \partial y^2} + D_{22} \frac{\partial^4 w_0}{\partial y^4} = q \tag{2.24}$$

where D_{ij} are the terms of the flexural stiffness matrix, w_0 is the out-of-plane displacement and q is the applied load. For rectangular plates, depending on the boundary conditions, a number of solution methods can be applied such as *Navier*, *Lévy* and *Rits* methods [46].

2.3.2.2 Shear Deformation Theories

It is important to note that although the transverse stress components ($\sigma_{33}, \sigma_{13}, \sigma_{23}$) are small in thin composite plates, they are often the stresses that induce composite failure as FRP plates are weak in the transverse direction given that the strength of the fibres is optimum in the X-Y plane. Therefore, the second theory in the hierarchy of ESL models is called *first order shear deformation theory* (FSDT) with the corresponding displacement field stated as follows [46]

$$\begin{aligned} u(x,y,z,t) &= u_0(x,y,t) + z\varphi_x(x,y,t) \\ v(x,y,z,t) &= v_0(x,y,t) + z\varphi_y(x,y,t) \\ w(x,y,z,t) &= w_0(x,y,t) \end{aligned} \quad \textbf{(2.25)}$$

where φ_x and φ_y denote the rotations about the y and x axes, respectively.

FSDT essentially relaxes the Kirchhoff condition that the normals must remain normal before and after the deformation. This leads to a requirement for non-zero transverse shear strains which are assumed to be constant through the thickness of the laminate in the framework of FSDT. It follows that the transverse stresses are also constant through the thickness. However, it is well known that the shear stresses vary quadratically in the case of homogenous beams. This discrepancy requires the use of shear correction factors which are generally difficult to compute as they tend to depend on lamination sequence, geometry, loading and boundary conditions.

Higher order theories use higher order polynomials to expand the displacement components through the thickness of the laminate and typically include additional unknowns which are difficult to compute and define in physical terms. Due to the limitations and assumptions of the ESL theories, they are usually not applicable in situations involving geometric, material discontinuities and concentrated loads. In such cases, 3D theories are more appropriate. While further discussion of this topic is outside the scope of this thesis, a number of plate theories and a good treatment of the underlying mathematics is covered by Reddy [46].

2.4 Composite Failure Criteria

The aforementioned 3D elasticity and ESL models are often used in conjunction with composite failure criteria in order to predict the onset of damage, damage progression and ultimate failure of composite laminates. However, it is important to note that while many theories and failure criteria have been proposed, accurate prediction of failure in laminated angle-ply composite materials is currently an active field of research. Indeed, international studies [48-50] have demonstrated differences by the factor of two and more obtained using the leading composite failure criteria, even for simple test specimens such as flat and cylindrical plates under uniform loading and simple boundary conditions. Moreover, there is no unified consensus on what in fact constitutes "failure" in terms of composite laminates. This difficulty is illustrated using idealised but representative stress-strain curve for a quasi-isotropic CFRP plate uniaxially loaded in tension as shown in Figure 2.18.

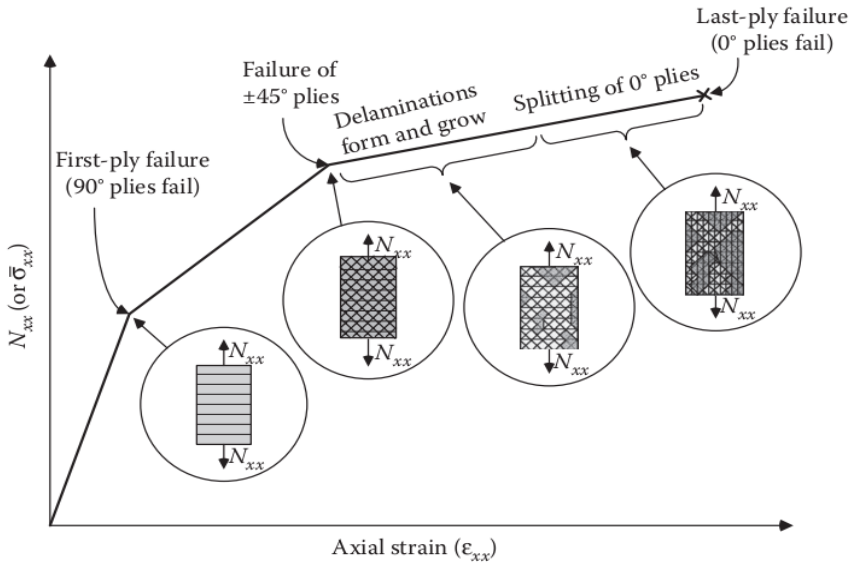

Figure 2.18: idealised stress-strain plot for a $[0/45/90/-45]_s$ laminate outlining the internal damage evolution; reproduced from [47].

Evident from Figure 2.18, the first plies that yield or crack are typically the 90˚ ones (assuming loading in 0˚ direction). The effective stress associated with this point is usually termed *first-ply failure stress*. A range of stress or strain based failure criteria (e.g. *maximum stress*, *maximum strain*, *Tsai-Hill*, *Tsai-Wu*, *Hashin*, *Puck* etc.) can be used to predict the first-ply failure [47]. In these failure criteria, a combination of stress or strain components estimated from 3D or ESL models are considered in order to check if any of the plies in the laminate reached a maximum value (typically defined as unity) associated with the specific failure criterion. In the *first-ply failure analysis*, the composite laminate is considered failed when the first ply reaches the maximum allowable value. In the *last-ply failure analysis*, a *ply-discounting* approach is used. It entails estimating the loading conditions required for the first ply to fail which is followed by the reduction of the stiffness matrix coefficients of the laminate

and thus removing the contribution of the failed ply to the overall strength/stiffness of the laminate in the subsequent analyses. The process is repeated until the failure of the last ply is predicted. Generally, the catastrophic laminate failure is characterised by the extensive fibre failure in 0˚ plies with the effective stress associated with this point termed *last-ply failure stress*[47].

Therefore, the definition of composite failure may depend on a number of factors such as intended service life, the loading cycles, the rate of applied loading and ultimately the consequences of the structural failure. Furthermore, structural analysis of complex real world composite structures increasingly involves numerical modelling by means of *finite element method* (FEM) which is addressed next.

2.5 The Finite Element Method (FEM)

As noted in Section 2.3, the exact analytical solutions can only be developed for simple layered composite structures such as specially orthotropic plates. The FEM is a class of numerical methods which allows one to obtain an approximate solution to structural response (static and dynamic) of isotropic, orthotropic and generally anisotropic components of virtually any geometry, layup and loading conditions. In this approach, the solution is obtained as an approximation to the true (exact) solution of the governing equations describing the physical problem. However, it is important to understand that the governing equations are themselves approximate as it is practically impossible to describe the geometry, boundary conditions, loading and material behaviour in exact manner. Nevertheless, FEM has proven to be a powerful tool in simulating real world events from earthquakes to automotive crush tests and is utilised by all major engineering industries on the daily basis. Furthermore, many studies involving FEM of composite materials have been reported in the past decade [51-53].

2.5.1 Fundamentals

The fundamental purpose of the FEM is to take a complex physical problem (represented by ordinary and partial differential equations) and transform it into a collection of smaller problems that can be solved numerically. In more mathematical terms, a structure is analysed by subdividing it into a *mesh* comprised of finite sized elements (finite elements (FE)) of simple geometrical shapes. The process of such subdividing is referred to as *meshing*. A variation of displacement within each FE is assumed to be determined by simple polynomial shape functions and nodal displacements, which are in turn used to develop the relationships for strains and stresses in order to assemble a global momentum (or

equilibrium for static problems) equation in a matrix form. This allows the implementation of the method into computer programs referred to as finite element analysis (FEA) solvers (e.g. LS-DYNA®, ANYSYS®, ABAQUS®, PAM-CRASH®, MSC NASTRAN®, COMSOL® etc.). After applying the appropriate boundary and loading conditions, the nodal displacements can be found allowing to calculate the strains and stress for each FE.

The form of the momentum equation shown in Eq. (2.16) is known as the *strong form* as it implies a strict continuity condition with no singularities or jumps present in the 3D continuum that it describes. However, it cannot be discretised directly using the FEM. For this purpose, variational principles such as a *principle of virtual displacement* (PVD) or *minimum potential energy* are employed. In dynamic FEA, the deformed body, can be described at each point by six independent equations (3 for translation and 3 for rotation). PVD is a single equation capable of enshrining these six equations. It is obtained by pre-multiplying the terms of the strong form with a test function called a *variation* (δ) which allows to derive the weak form that can be implemented as a set of discrete equations in the FEA code. Considering a current domain Ω with a boundary Γ of a body, a weak form of the momentum equation can be stated using the PVD as

$$\int_{\Omega} \delta \mathrm{u}\, \boldsymbol{\sigma}\, d\Omega + \int_{\Omega} \delta \dot{\mathrm{u}}\, \rho \ddot{\mathbf{u}}\, d\Omega - \int_{\Omega} \delta \dot{\mathrm{u}}\, \mathbf{b}\, d\Omega - \int_{\Gamma} \delta \dot{\mathrm{u}}\, \mathbf{t}_{\mathrm{x}}\, d\Gamma = 0, \tag{2.26}$$

where $\delta \mathrm{u}$ is a virtual displacement, $\delta \dot{\mathrm{u}}$ is a virtual velocity, $\boldsymbol{\sigma}$ is a stress tensor, ρ is density**,** $\mathbf{b}$ is vector of body forces and $\mathbf{t}_{\mathrm{x}}$ represents surface tractions (subscript x is used to avoid confusion with time variable). First term signifies the contribution of internal forces, whereas the second, third and fourth terms stand for contributions of inertial forces, body forces and surface tractions respectively. Eq. (2.26) is a governing equation and is discretised in space and time.

The governing equation can be written in a discreet form as follows

$$\mathbf{M}\ddot{\mathbf{u}} = \mathbf{F}^{ext} - \mathbf{F}^{int}, \tag{2.27}$$

where $\ddot{\mathbf{u}}$ is the second time derivative of the global displacement vector, $\mathbf{F}^{int}$ is the global internal forces vector obtained by scattering each element vector into the global element array

$$\mathbf{F}^{\mathrm{int}} = \sum_{e=1}^{n_{el}} \mathbf{L}_e^T \left[\int_{\Omega_e} \mathbf{B}^T \boldsymbol{\sigma} d\Omega \right], \tag{2.28}$$

where Ω_e and Γ_e are the domain and boundary of each element respectively, n_{el} is the total number elements, $\mathbf{B}$ is the matrix of spatial derivatives of shape functions. $\mathbf{F}^{ext}$ is the global external forces vector given by

$$\mathbf{F}^{ext} = \sum_{e=1}^{n_{el}} \mathbf{L}_e^T \left[\int_{\Omega_e} \mathbf{N}^T \rho \mathbf{b} d\Omega + \int_{\Gamma_e} \mathbf{N}^T \bar{\mathbf{t}}_e d\Gamma \right], \tag{2.29}$$

where $\bar{\mathbf{t}}_e$ is a vector of traction forces acting on the standard finite element (not cohesive) and the over-bar is used to highlight that the quantity is a prescribed one; $\mathbf{b}$ is a vector of body forces and ρ is density.

Finally, the lumped mass matrix is assembled as follows

$$\mathbf{M} = \sum_{e=1}^{n_{el}} \mathbf{L}_e^T \left[\int_{\Omega_e} \rho \mathbf{N}^T \mathbf{N} d\Omega \right] \mathbf{L}_e . \tag{2.30}$$

Eq. (2.27) represents a system of nonlinear second order differential equations which are solved using explicit finite element code using direct time integration technique. Explicit time integration scheme of LS-DYNA® was used as it is well suited for simulating wave propagation that lasts on the order of milliseconds. The global displacements at time $t + \Delta t$ using the central difference method is given by

$$\mathbf{u}_{t+\Delta t} = \Delta t^2 \mathbf{M}^{-1} \left(\mathbf{F}_t^{ext} - \mathbf{F}_t^{int} \right) - \mathbf{u}_{t-\Delta t} + 2\mathbf{u}_t, \tag{2.31}$$

where Δt is time increment or time step. Explicit time integration is computationally inexpensive for small durations and is conditionally stable – CFL (after Courant, Friedrichs and Lewy) stability criterion must be satisfied

$$\begin{aligned} \Delta t &< \Delta t_{critical}, \\ \Delta t_{critical} &\leq \frac{2}{\omega_{max}}, \end{aligned} \tag{2.32}$$

where ω_{max} is the highest natural frequency of the system, which for the assembled finite element model is bounded by the maximum frequency of the unassembled and unsupported elements. Physically, this means that Δt must be small enough that the information does not propagate across more than one element per time step. Determining the maximum natural frequency of each finite element in the model is a very computationally demanding task as it would require performing a *modal analysis* on each element; in this case, the solver would extract the maximum natural frequency for each finite element in the model and the absolute maximum frequency value in the model would be used according to Eq. (2.32) in order to evaluate a critical time step for the problem. Moreover, this procedure would have to be repeated at every time step as the finite elements undergo deformation. This demonstrates the computationally demanding nature of this approach of determining the critical time step for the analysis. An alternative and much more efficient technique, which is utilised by LS-DYNA®, is addressed next.

For a problem of *n* degrees of freedom, there are at most *n* solutions referred to as *mode shapes* of the structure which can be resonantly excited by applying an external excitation at frequencies called *natural frequencies* of the structure. In order to find these frequencies and the corresponding mode shapes, a linear equation of equilibrium (usually without damping) is defined as

$$\mathbf{M\ddot{u}} + \mathbf{Ku} = \mathbf{0}, \tag{2.33}$$

where $\mathbf{M}$ is a square lumped mass matrix, $\mathbf{\ddot{u}}$ is a column vector of nodal accelerations, $\mathbf{K}$ is the stiffness matrix and $\mathbf{u}$ is the column vector of nodal displacements. Assuming that all particles execute simple harmonic motion and are in phase with each other a displacement and the corresponding acceleration arrays can be stated as

$$\mathbf{u} = \mathbf{U}\sin\omega t, \quad \mathbf{\ddot{u}} = -\omega^2\mathbf{U}\sin\omega t, \tag{2.34}$$

where $\mathbf{U}$ is and array of amplitude values for each degree of freedom and ω is the angular frequency. Combining Eq. (2.33) and Eq. (2.34)

$$(\mathbf{K} - \omega^2\mathbf{M})\mathbf{U} = 0. \tag{2.35}$$

From purely mathematical perspective, Eq. (2.33) presents a linear (as $\mathbf{K}$ and $\mathbf{M}$ do not depend on ω) eigenvalue problem which can be solved using a number of algorithms (e.g. *Lanczos algorithm* [54]) in order to compute the *eigenvalues* and the corresponding *eigenvectors* which represent the natural frequencies and the mode shapes of the structure.

Although, performing the outlined modal analysis is well within the capabilities of LS-DYNA®, it is not called upon during the general dynamic analysis. Instead, the LS-DYNA® solver calculates the critical time step considering a propagation of *longitudinal waves* in solids. Generally, in solid medium, two types of waves can propagate: longitudinal and *shear waves* (more on this in Chapter 4.2.3). However, the fastest travelling wave is the longitudinal one, and therefore, leads to a more conservative estimation of the required time step. The formula for the longitudinal wave velocity in 3D solid medium is

$$C_L = \sqrt{\frac{E(1-\nu)}{(1+\nu)(1-2\nu)\rho}}, \tag{2.36}$$

where *E* is Young's modulus, *ν* is the Poisson's ratio, and *ρ* is the mass density of the material. The time step corresponding to a solid 8-node hexahedron element is calculated as follows

$$\Delta t_e = \frac{L_e}{C_L}, \tag{2.37}$$

where L_e is the characteristic element dimension. The critical time step, which is the time step used for the simulation, is finally estimated by looping over all elements in the FE domain [55]

$$\Delta t_c = \mathrm{TSSFAC} \times \min\left\{\Delta t_1, \Delta t_2, \Delta t_3 \ldots, \Delta t_N\right\}, \quad \textbf{(2.38)}$$

where *N* is the total number of elements in the model and TSSFAC is a parameter usually taken as a value in the range 0.5-0.9 which allows to further aid the numerical stability.

In explicit FE, the equilibrium is achieved at each time step solving for the acceleration, velocity and the displacement. The total response time of the system is divided into smaller time intervals termed time steps. The momentum equation is solved by determining the unknown variables at time $t + \Delta t$ based on the values of these variables at time t using the outlined central difference method.

In the implicit FE, the equilibrium is achieved at each time step using an iterative procedure. The implicit time integration in LS-DYNA® employs Newmark formula for displacement and velocity integration. The solution at the new time step depends on the velocity and the acceleration at the next step which implies that iterative procedure is required. For this purpose, LS-DYNA® solver utilises the Newton-Raphson method [55].

Implicit method is unconditionally stable and can be efficiently used for static problems. It is also relatively inexpensive for simulating long events (seconds to hours) but requires large amount of computer memory and can experience convergence problems in models involving strong nonlinearities.

Explicit method is computationally very fast and robust even for strong nonlinear problems. However, it is conditionally stable and expensive to run for long durations. Explicit FE is well suited for impact and wave propagation simulations considered in this thesis as the corresponding physical events are highly nonlinear and last milliseconds in duration.

2.5.2 Composite Modelling Capabilities of LS-DYNA®

One of the advantages of LS-DYNA® over other FEA solvers is its extensive material library (over 260 material models) with over a dozen composite material models. The choice of the composite constitutive model is critical for adequate analysis and generally depends on the following factors:

1. *Composition* – the overall modelling approach depends on the physical structure of the material - e.g. concrete (steel/stone/steel), short/long FRPs, sandwich/laminates, and fabric/woven/UD layers.

2. *Anisotropy* – the composite laminates considered in this thesis are assumed to be orthotropic, and therefore, material directions (axes) must be specified for each finite element which enables the FEA solver to track the material orientation throughout the simulation. This is done via an AOPT option available within the software. More generally, layered materials consisting of isotropic layers or fully anisotropic ones can also be modelled and will require the use of the appropriate material models.
3. *Failure criteria and damage progression* – damage mechanics including intralaminar and interlaminar failure drive the damage response of the material. The initiation of damage is modelled via the failure criteria approach and often a simple one can suffice. The subsequent stiffness degradation can be modelled as soft/ductile or brittle failure. Some materials require more elaborate modelling as, for example, brittle failure can be difficult to predict due to many different failure modes manifesting concurrently and at various length scales (micro-meso-macro); the complexity and multi-mode nature of composite failure is demonstrated by micrographs of physical composite damage and schematic representation of discrete failure modes shown in Figure 2.19.

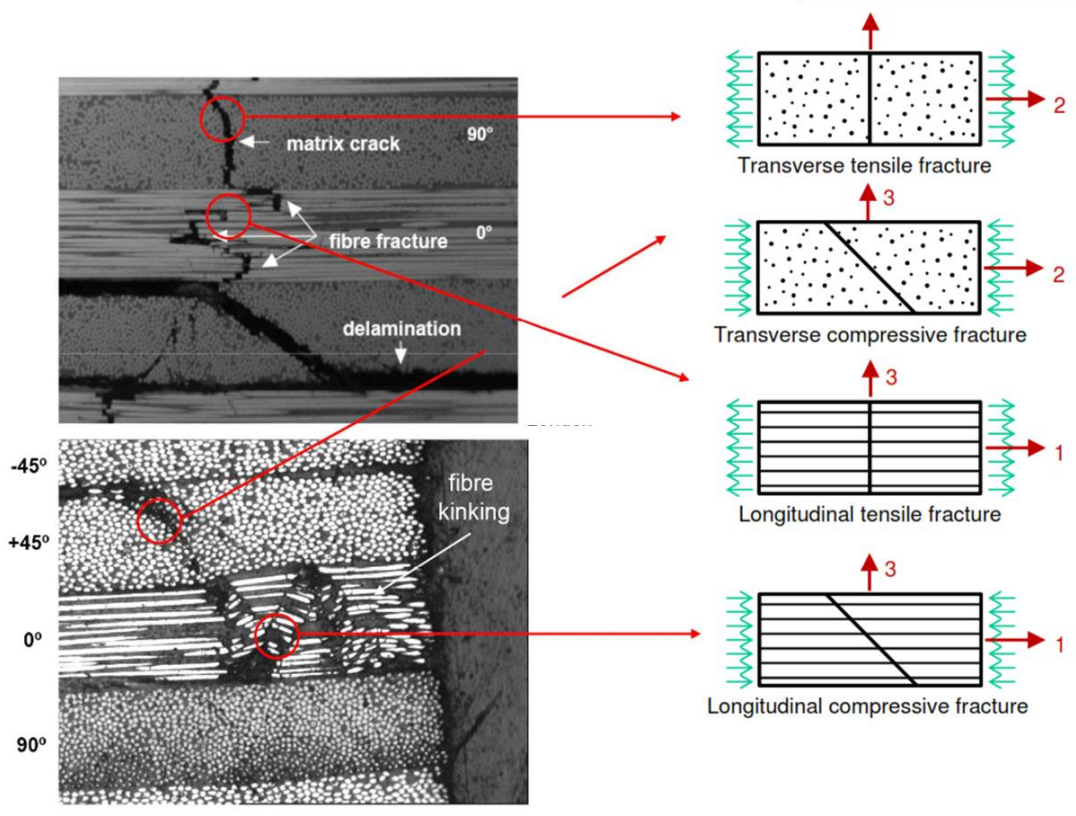

Figure 2.19: failure mechanics of composites; reproduced from [56].

4. *Strain rate* – if the rate of strain is expected to have a significant effect on the structural response, then a material model with strain rate sensitivity should be used.

5. *Material characterisation* – the use of any material model always requires knowing or determination of physical material characteristics. Whilst simple models may accept a few parameters such as elastic moduli and strength, more sophisticated models may require extensive physical Material characterisation testing.
6. *Computational time/power available*
7. *Local/global analysis* – global analysis typically implies modelling and simulating assemblies and sub-assemblies of a product or structure which can be many meters in length and width. In such cases, *layered shell elements* are usually employed as they are much less computationally demanding than *solid (brick)* elements. Shell elements have no physical/geometrical thickness and are represented as 2D elements in 3D space. A number of shell element formulations and associated material models are available in LS-DYNA® but they tend to behave in overly stiff manner unless laminated shell theory is invoked using LAMSHT parameter, which activates the FSDT approach with an algorithm that calculates a shear correction factor for each shell in order to correct the assumption of uniform transverse shear strain through the thickness of the element. In local analysis, 3D elements also known as solids or bricks are a reasonable choice as they do not use assumed transvers shear stress field which is especially important when considering delamination. Generally, the choice between the use of shells and solids depends on the material thickness relative to its length or width, loading conditions, amount of deformation and the degree of accuracy required. Figure 2.20 schematically shows the shell and solids finite elements along with their essential attributes.

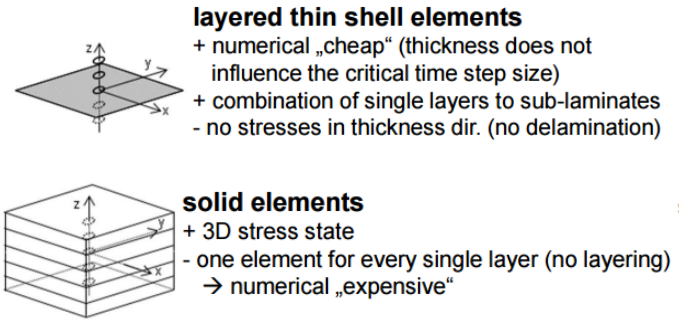

Figure 2.20: shell and solid finite elements for modelling laminated composites; reproduced from [56].

In addition to standard shells and solids, LS-DYNA® also offers layered *thick shell* elements which consider a 3D state of stress but assumed state of strain and allow multiple ply definitions through the thickness. The idea of this finite element type is to bridge the gap between standard shell and solid elements in terms of computational time and accuracy, however, thick shell formulation has known accuracy and numerical issues when subjected to bending, and therefore, it was not used in this study [55, 57].

To put the aforementioned points into context of composite modelling capabilities of LS-DYNA®, some of more prominent constitutive models for composite structures available within the FEA code are presented in Table 2-1. The description of the models is based on several sources that can be consulted for further reference [15, 55, 58, 59].

*MAT_002	Elastic, no failure; shells and solids
*MAT_022	Plane stress, Chang-Chang failure criteria, "sudden" failure (stiffness is set to zero) as soon as failure criteria are met; shells and solids
*MAT_054/55	Plane stress, 54: Chang-Chang failure criteria, 55: Tsai-Wu failure criteria, stresses are kept constant until failure strains are reached followed by setting stiffness to zero; shells only
*MAT_058	Plane stress, modified Hashin failure criteria, smooth stress-strain relation, continuum damage modelling approach with exponential softening, non-linear shear behaviour; shells only
*MAT_116/117/118	Elastic, no failure, full anisotropy allowed (21 coefficients), resultant formulation; shells only
*MAT_158	Modified Hashin failure criteria, continuum damage modelling approach with exponential softening; shells only
*MAT_162	Linear elastic orthotropic until failure, Hashin failure criteria, continuum damage modelling approach with exponential softening, rate sensitive, requires an extra license; solids only
*MAT_261	Linear elastic orthotropic until failure, Pinho failure criteria (3D stress state), 1D plasticity formulation for in-plane shear, continuum damage model with linear softening evolution based on fracture toughness; shells and solids
*MAT_262	Linear elastic orthotropic until failure, Camanho failure criteria (plane stress), 1D plasticity formulation for in-plane shear, continuum damage model with bilinear softening evolution based on fracture toughness; shells and solids

Table 2-1: some of frequently used composite constitutive models of LS-DYNA®.

Figure 2.21 shows a comparison between various material models using one element test with a single shell layer.

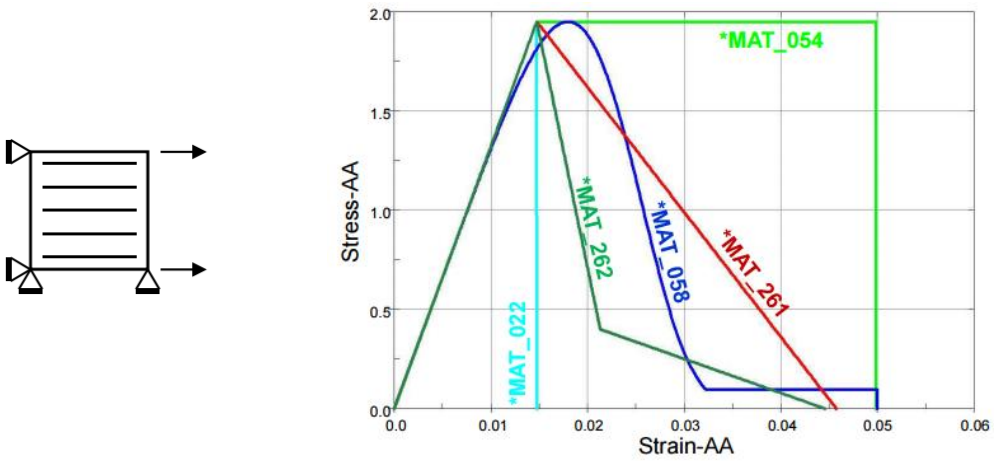

Figure 2.21: 1-element test with a single shell layer for various material models; reproduced from [56].

Similarly, stress-strain relations obtained from one solid element tests using composite material model MAT162 with various values of the softening parameter (m) are shown in Figure 2.22.

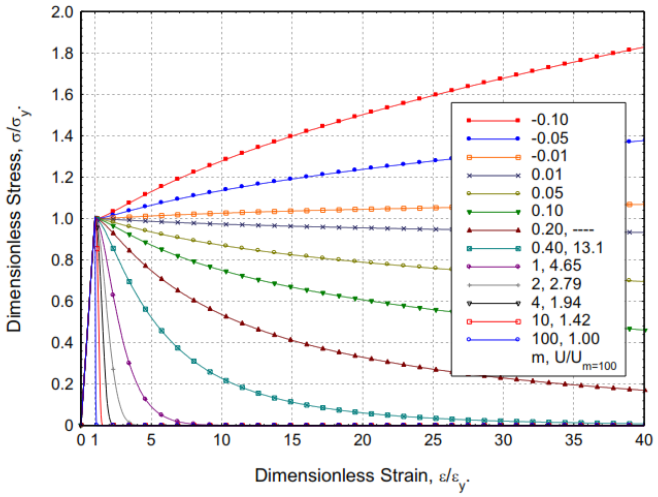

Figure 2.22: nonlinear stress-strain response of progressive composite constitutive model MAT162 obtained using single element test for various values of post-yield damage softening parameter *m*; reproduced from [60].

Composite material model MAT162 which is developed by Materials Sciences Corporation, is part of LS-DYNA® material library and deserves a special attention as it is arguably the most advanced composite damage model for impact analysis currently available. It employs an orthotropic elastic behaviour until damage onset which occurs according to progressive Hashin [61] failure criteria. It has been extensively validated [53, 62] and was shown [63] to be effective at predicting the initiation of fibre failure, matrix damage and delamination under various conditions such as opening, closing and sliding of failure surfaces. For example, Xiao *et al.* [63] reported a comparison between experimental and numerical (MAT162) results of a calibrated model was well within 5% in terms of stiffness, contact force and displacement covering a range of impact energies from LVI to HVI events.

In MAT162, composite damage progression following the failure initiation is characterised by softening behaviour based on the continuum damage mechanics (CDM) approach devised by Matzenmiller [64]. The model is capable of simulating UD as well as woven fabric composite lamina, while the UD option was selected for this study. For completeness, the fibre and matrix failure criteria based on 3D stresses/strains are presented in Eq. (2.39)-(2.44), for further reference, please see MAT162 User Manual [60]:

Tension-shear fibre mode
$$\mathbf{f_1} = \left(\frac{\mathbf{E_a}\langle\boldsymbol{\varepsilon_a}\rangle}{\mathbf{S_{aT}}}\right)^2 + \left(\frac{\mathbf{G_{ab}^2}\boldsymbol{\varepsilon_{ab}^2}+\mathbf{G_{ca}^2}\boldsymbol{\varepsilon_{ca}^2}}{\mathbf{S_{FS}^2}}\right) - \mathbf{1} = \mathbf{0}, \quad \textbf{(2.39)}$$

Compression fibre mode
$$\mathbf{f_2} = \left(\frac{\mathbf{E_a}\langle\boldsymbol{\varepsilon_a^{/}}\rangle}{\mathbf{S_{aC}}}\right)^2 - \mathbf{1} = \mathbf{0}, \rightarrow \ \boldsymbol{\varepsilon_a^{/}} = -\boldsymbol{\varepsilon_a} - \frac{\langle-\mathbf{E_c}\boldsymbol{\varepsilon_c}-\mathbf{E_b}\boldsymbol{\varepsilon_b}\rangle}{\mathbf{2E_a}}, \quad \textbf{(2.40)}$$

Fibre crush mode
$$\mathbf{f_3} = \left(\frac{\mathbf{E_c}\langle-\boldsymbol{\varepsilon_c}\rangle}{\mathbf{S_{FC}}}\right)^2 - \mathbf{1} = \mathbf{0}, \quad \textbf{(2.41)}$$

Transverse compressive matrix mode
$$\mathbf{f_4} = \left(\frac{\mathbf{E_b}\langle-\boldsymbol{\varepsilon_b}\rangle}{\mathbf{S_{bC}}}\right)^2 - \mathbf{1} = \mathbf{0}, \quad \textbf{(2.42)}$$

Perpendicular matrix mode
$$\mathbf{f_5} = \left(\frac{\mathbf{E_b}\langle\boldsymbol{\varepsilon_b}\rangle}{\mathbf{S_{bT}}}\right)^2 + \left(\frac{\mathbf{G_{bc}}\boldsymbol{\varepsilon_{bc}}}{\mathbf{S_{bc0}}+\mathbf{S_{SRB}}}\right)^2 + \left(\frac{\mathbf{G_{ab}}\boldsymbol{\varepsilon_{ab}}}{\mathbf{S_{bc0}}+\mathbf{S_{SRB}}}\right)^2 - \mathbf{1} = \mathbf{0}, \quad \textbf{(2.43)}$$

Parallel matrix mode (delamination)
$$\mathbf{f_6} = \mathbf{S^2}\left\{\left(\frac{\mathbf{E_c}\langle\boldsymbol{\varepsilon_c}\rangle}{\mathbf{S_{cT}}}\right)^2 + \left(\frac{\mathbf{G_{bc}}\boldsymbol{\varepsilon_{bc}}}{\mathbf{S_{bc0}}+\mathbf{S_{SRC}}}\right)^2 + \left(\frac{\mathbf{G_{ca}}\boldsymbol{\varepsilon_{ca}}}{\mathbf{S_{ca0}}+\mathbf{S_{SRC}}}\right)^2\right\} - \mathbf{1} = \mathbf{0}, \quad \textbf{(2.44)}$$

where subscripts *a*, *b*, and *c* are fibre, in-plane transverse and out-of-plane directions respectively; *E* is Young's modulus, S_{aT} is strength with subscripts indicating the direction and failure mode (i.e. tension/compression) it relates to; positive values of failure mode functions f correspond to the damage thresholds with initial value of unity before damage onset. Following the damage initiation, the damage variables are updated according to the exponential function

$$\varpi = 1 - e^{\frac{1}{m}\left(1-\left(\frac{\varepsilon}{\varepsilon_y}\right)^m\right)} \quad \textbf{(2.45)}$$

where ϖ is a damage variable associated with a particular elastic property, ε_y is the yield strain and m is a material softening parameter governing the stress-strain response of the damaged lamina. High values of m (~100) lead to a brittle behaviour and very low values of m (~0.01) allow modelling a near perfectly plastic response – see Figure 2.22. Following the initiation of damage, the terms of the stiffness matrix are updated according to

$$E = (1 - \varpi)E_0, \quad \textbf{(2.46)}$$

where E_0 is an initial elastic moduli corresponding to the undamaged response of the material. The stress state can therefore be updated as

$$\sigma = E\varepsilon = E_0\varepsilon e^{\frac{1}{m}\left(1-\left(\frac{\varepsilon}{\varepsilon_y}\right)^m\right)}. \quad \textbf{(2.47)}$$

By employing the aforementioned methodology, it is possible to simulate an intrinsically complex nature of coupling between various failure modes and visualise the damage at the post-processing

stage of the FEA analysis. It is important to note that even after any of the failure criteria are met, an element may still retain some residual capacity to carry loads and resist deformation in some directions. However, after accumulating significant amount of damage (as local element stiffness approaches zero, $E \rightarrow 0$) , an element may be required to be deleted (i.e. eroded) from the subsequent simulation as such elements no longer inhibit any residual capacity to carry loads. Therefore, in addition to the previously established failure criteria, MAT162 provides three mechanisms that enable finite element erosion or deletion from the analysis:

1. Fibre tensile failure is initiated and the axial tensile strain is greater than E_LIMIT
2. Compressive relative volume (ratio of current volume to initial volume) in a failed element is smaller than ECRSH
3. Expansive relative volume in a failed element is greater than EEXPN

An element is deleted in case any of these conditions are met.

It is important to note that the methodology and material models presented in this thesis are transferable to other explicit/implicit FEA software (e.g. ANSYS®, ABAQUS®, RADIOSS® etc.). Some equivalent constitutive models already exist within other codes, while some may require user defined implementation. Andresson and Liedberg [58] provide a description and comparison of composite simulation capabilities of LS-DYNA® along with four other leading structural analysis FEA codes.

2.6 Fracture and Damage Modelling

As pointed out in the previous Section, modelling of fracture and failure of composite materials is complicated by the fact that it takes place on various length scales as illustrated in Figure 2.23.

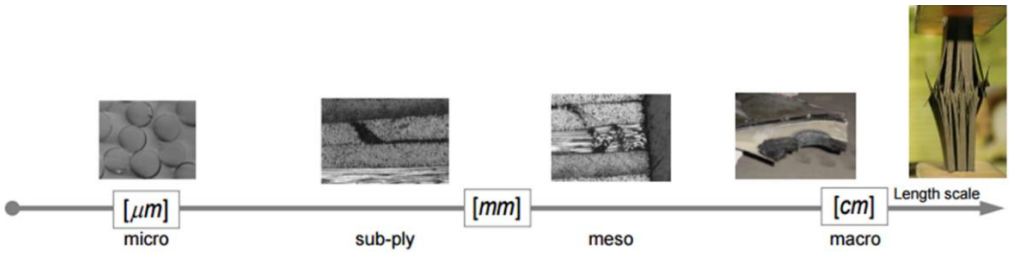

Figure 2.23: length scales in composite damage analysis; reproduced from [65].

Perhaps most accurate approach would be to mesh the entire structure using 3D continuum solid element at microscale. However, even for small and simple geometries (e.g. flat plate 100 mm x 100 mm) this would result in unacceptably large mesh sizes (millions of finite elements) and computational times (weeks). Indeed, in typical crashworthiness and impact analyses performed in aerospace [66, 67] and automotive [65] industry at the time of writing this thesis, the characteristic structural finite elements are typically 1-2 orders of magnitude bigger than shown in micrographs of Figure 2.19. Therefore, a *smeared* approach is unavoidable and implies homogenising the micro/sub-ply behaviour of laminates as into finite elements at meso and macro scales using layered shells and solid elements. Applying the appropriate failure criteria and damage modelling techniques, complex failure modes can be simulated as schematically shown in Figure 2.24.

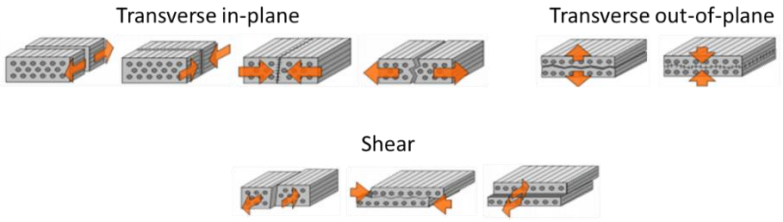

Figure 2.24: composite failure modes; reproduced from [65].

For completeness, the following Sections introduce some of the most prominent composite damage modelling techniques in the context of FEA including well established and more novel approaches. The Extended Finite Element Method (XFEM) and Multiresolution Continuum Theory (MCT) methods are briefly mentioned. The former refers to a technique used for representing weak and strong discontinuities in the FEM, while the latter entails high fidelity modelling of the material response considering its composition and constituent behaviour at various superimposed levels (micro-meso-macro). Although these novel techniques have not been used in this work, they are of relevance in the sense that they can provide a possible direction for future modelling of damage propagation in isotropic and anisotropic materials.

2.6.1 Continuum Damage Mechanics (CDM)

In the CDM approach, which was already mentioned in the preceding Sections, the aim is to predict the effects of damage and defects at the microscale level by making certain assumptions about the nature of damage and its effect on the macroscale properties (e.g. elastic modulus) of the structure. The method is based on the principle of stress-strain energy equivalence. Considering a damaged material subjected to a certain strain and stress state, can be represented by an equivalent damage-free material subjected to the same strain value but experiencing a different effective state of stress. Eq. (2.47) mathematically explains this concept. Since CDM was first suggested by Kachanov [68, 69], many authors have contributed this techniques and numerous constitutive models have been developed and implemented in various FEA codes [70-72]. Williams and Vaziri [73] implemented a Matzenmiller [64] CDM based model and simulated a number of non-penetrating impact evens on CFRP (T800/H3900-2) composite plates using a range of incident energy levels and compared the numerically obtained data to the experimental results. Significant improvements in terms of overall damage prediction, force and energy histories were reported in comparison to other LS-DYNA® models available at the time. Subsequently, important aspects associated with CDM and generally composite damage modelling were raised and include strain rate and mesh size influence on the damage growth, which were addressed in more recently developed models such as MAT162 and MAT261/262 [74, 75].

Crack growth, fibre breakage and interface debonding in composites can be modelled on the basis of CDM. One of the main advantages of this method is that damage variables can be relatively easily defined and the implementation is rather straightforward. However, the CDM approach is most effective when the problem size is sufficiently larger than a defect size [76]. Furthermore, extensive material characterisation is usually required in order to validate and calibrate the parameters used in the constitutive model. Liu [77] and Forghani *et al.* [72] extensively surveyed the methodologies used for damage constitutive modelling of composite laminates using CDM as well as its finite element implementation for the progressive damage analysis.

2.6.2 Cohesive Zone Models (CZM)

Cohesive zone modelling (CZM) is currently the most frequently used approach in simulating interlaminar/delamination damage characterised by ply separation due to bonding failure between plies caused by excessive shear and normal stresses in a composite laminate. The crack plane in CZM is predefined between the adjacent plies, although, in reality, the crack may often split a ply near the fibres and jump across the plies as shown in Figure 2.25.

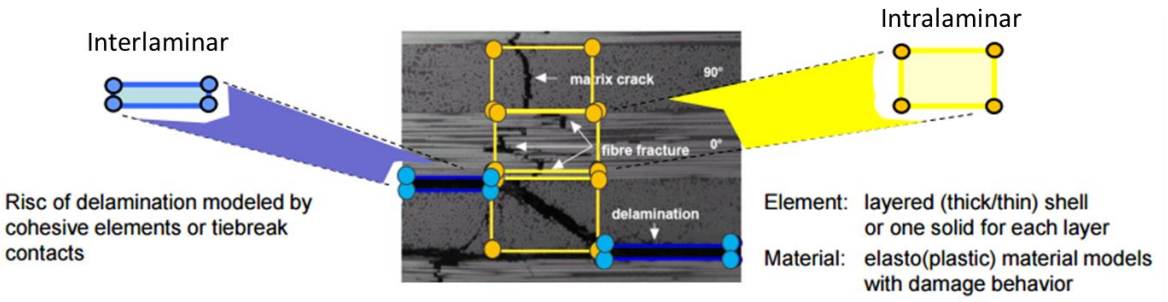

Figure 2.25: interlaminar and intralaminar damage modelling in FEA; reproduced from [78].

Most CZM methods and all of the ones available in LS-DYNA® utilise traction-separation laws based on fracture mechanics considering mode I, mode II and sometimes mode III [79]. LS-DYNA® offers two discrete delamination modelling techniques: (i) tiebreak contact and (ii) cohesive zone materials and element formulations. The latter involves explicitly placing solid elements, also called interface elements in the context of CZM, at the interface between the plies, while the former treats the connection ("tie") between the plies at the level of contact algorithm. Tiebreak algorithms are more appropriate when the inertial effects of the bonding layer are not important (e.g. bonding layer is very thin). A schematic of ply separation by tension loading in normal direction using a cohesive zone constitutive model is shown in Figure 2.26.

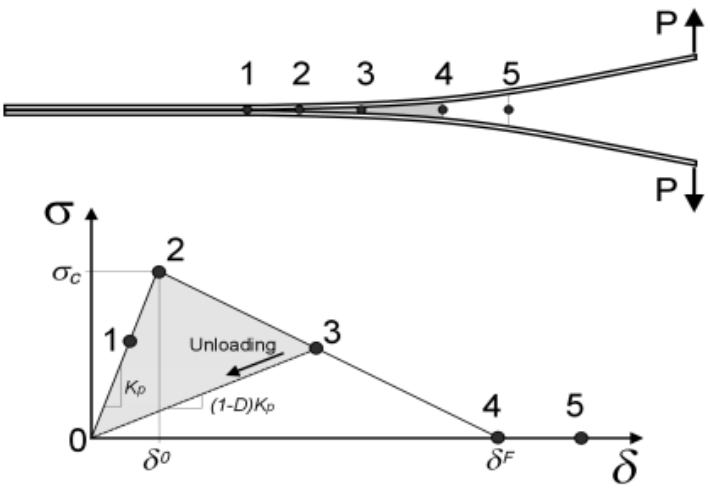

Figure 2.26: bilinear cohesive constitutive model (traction-separation relation for mode I in tension); reproduced from [78].

Both cohesive zone element and tiebreak contact approaches require the user input of *fracture energy* and several other parameters for each failure mode. Indeed, the fracture energy (units of energy/area), also referred to as the *fracture toughness* and the *energy release rate, G*, is the most important variable and corresponds to the energy dissipated during the separation of the plies; it is represented by the overall area under the stress-separation relation in Figure 2.26. The slope at point 1 along with the peak traction σ_c and the separation at failure δ^F must also be specified. The behaviour between points 0 and 2 is considered perfectly elastic. Beyond point 2 but before point 4 is reached, the interface material is considered damaged with the shaded area representing the nonrecoverable energy dissipated due to incurred partial damage. Once δ^F is reached, the cohesive elements or the tied contacts are removed locally to the finite elements connecting the two plies that reached the maximum allowable separation distance. From that point onwards, the interaction between those finite elements is treated via the usual surface-to-surface contact algorithm, meaning that their surfaces cannot interpenetrate.

Although the interface elements are widely used in industry for modelling delamination, this approach has some drawbacks and can lead to spurious traction oscillations due to sudden damage growth following the onset of damage at point 2 and sudden failure at point 4 causing erroneous crack patterns [80]. While some techniques have been proposed to mitigate this issue, it takes an experienced user to adequately calibrate the model [66].

2.6.3 Virtual Crack Closer Technique (VCCT)

As explained in the preceding Section, CZM requires a user input of fracture toughness or strain energy release rates. These values can be obtained experimentally by means of DCB testing [14, 81], which is schematically represented in Figure 2.26 (top). One of the typically used formulas for the calculation of the strain energy release rate for mode I fracture from DCB testing can be defined as follows [81]

$$G_{IC} = \frac{4L^2(3a^2 + h^2)}{Eb^2h^3}, \quad \textbf{(2.48)}$$

where *L* is the force required to initiate the crack propagation, *E* is tensile modulus of the adherend, *b* is specimen width, *h* is the thickness of the adherend and *a* is the crack length.

VCCT is a numerical (FEA) approach of calculating the fracture toughness values specific to the materials used in the simulations. Subsequently, these values can be used in CZM or other fracture modelling methodologies. In a typical VCCT procedure, a FE mesh of a closed or open crack is created and the simulation of crack opening/closing is performed recording the history of the normal and shear stresses and displacements at the crack tip, which in turn allows to calculate the required fracture toughness. A good treatment of the mathematics involved in the technique and its implementation is provided by Krueger [15].

2.6.4 Extended Finite Element Method (XFEM)

XFEM is employed for modelling discontinuities such as fracture/cracks/delamination (i.e. strong discontinuities) and weak discontinuities characterised as kinks in the displacement field resulting in strain jumps [82]. The standard FEM requires the FE mesh to conform to the crack geometry (see Figure 2.27(a)) and typically involves remeshing of the crack front which is a very computationally demanding process. Elements erosion algorithms are also typically used to simulate fracture evolution, where the elements are assigned zero stiffness and are deleted from the analysis upon meeting a certain failure criteria – see Figure 2.27(b). CZM is another example of modelling facture using FEM and requires knowing the fracture planes a priori.

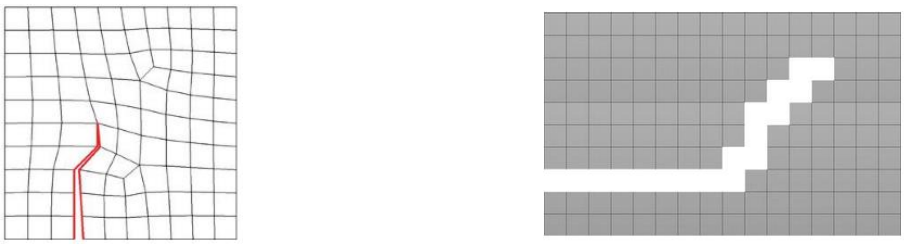

(a) (b)

Figure 2.27: (a) crack conforms to the mesh; (b) element deletion (erosion).

XFEM aims to tackle the problems associated with the crack-conforming meshing, element erosion and CZM methods by exploiting the fact that the FE shape functions summed over a given domain add up to one. This property is called a *partition of unity* and can be stated as [82]

$$\sum_{\forall I} N_I(\mathbf{X}) = 1, \qquad \forall X \in \Omega, \tag{2.49}$$

where I are nodal degrees of freedom, N_I are shape functions and $\mathbf{X}$ is the Lagrangian (material) coordinates. More generally, the standard FE approximations can be defined as [82]

$$\mathbf{u}(\mathbf{X}) = \sum_{\forall I} N_I(\mathbf{X})\mathbf{u}_I \,, \tag{2.50}$$

where $\mathbf{u}(\mathbf{X})$ are the displacements at a material point $\mathbf{X}$, while $\mathbf{u}_I$ are the displacements at the nodal degrees of freedom. Eq. (2.50) simply means that the displacements anywhere in the FE domain can be calculated by a product of the interpolating functions and the known nodal displacements. In the XFEM, this statement is split into standard FE and *enriched* components as follows [82]

$$\mathbf{u}(\mathbf{X}) = \underbrace{\sum_{\forall I} N_I(\mathbf{X})\mathbf{u}_I}_{\text{Standard FE}} + \underbrace{\sum_{\forall I} \varphi_I(\mathbf{X})\Psi(\mathbf{X})\mathbf{q}_I}_{\text{Enrichment}}, \tag{2.51}$$

where $\varphi_I(\mathbf{X})$ are the approximation functions for the enrichment which can be different or the same as the standard FE ones (i.e. $N_I(\mathbf{X})$), $\Psi(\mathbf{X})$ is a function representing a discontinuity and $\mathbf{q}_I$ are the unknown nodal parameters adjusting the enrichment such that it attains the best approximation of the solution. This approach allows to use nonconforming mesh to represent a discontinuity such as a crack by locally (subset of the nodes) enriching the FE domain – see Figure 2.28(b).

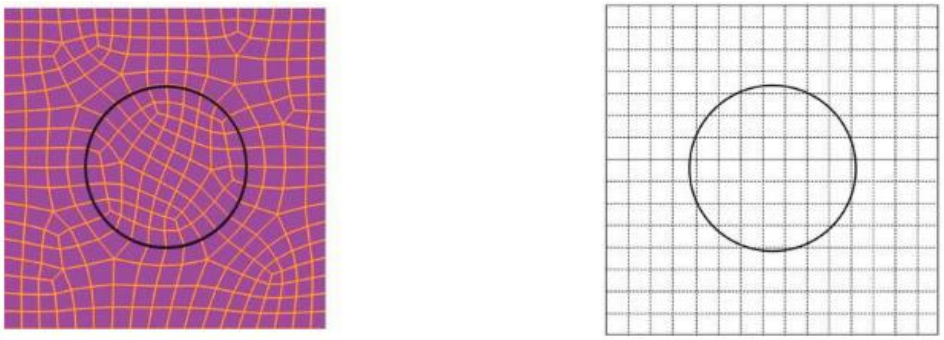

(a) (b)

Figure 2.28: (a) crack-conforming mesh which is required by the classical FEM and (b) nonconforming mesh which is permissible by the XFEM.

Although XFEM offers some clear advantages in terms of representing discontinuities in the FE domain without resort to remeshing, this approach is rarely used in practice and is the subject of ongoing

research. Some of the issues associate with XFEM include numerical problems in explicit and dynamic FE implementation, branching and interaction of cracks is problematic, only one crack may exist in one elements, sharp turning of the crack impedes convergence, crack initiation criteria are not trivial etc [83] . Further discussion of the method is outside the scope of this thesis. A good introduction to the technique along with the underlying mathematics and references for further reading is provided by Belytschko *et al.* [82].

2.6.5 Multiresolution Continuum Theory (MCT)

The response of materials at engineering or macroscale is to a large extent driven by the microstructure [84]. In case of metals, the microstructures span various length scales and include grains, atomic lattice and crustal structure [85]. This emphasises the multilevel nature of engineering materials – see Figure 2.29.

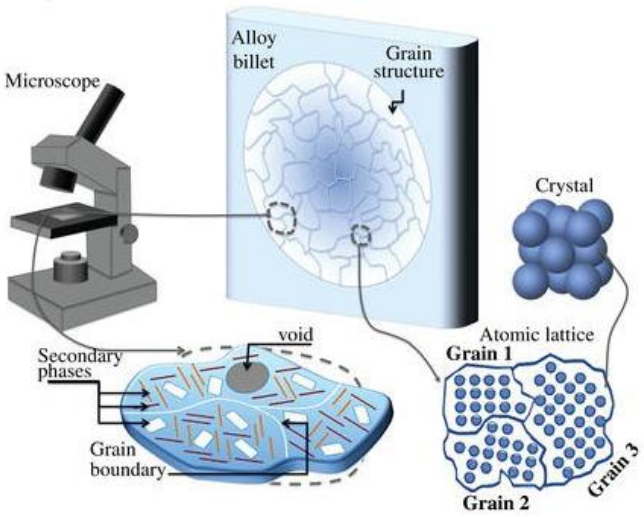

Figure 2.29: multilevel structure of metals; reproduced from [82].

The microstructure can be tailored by process control such as the addition of alloying elements and increasing the working temperature in order to achieve the required performance in terms of strength, toughness, cost etc. However, the process of creating and testing new materials is somewhat inhibited by the expensive and time-consuming experimentation. Thus, there is a requirement for mechanical theories and methods that can supply material scientists with predictions of the material properties from the information of their microstructure while minimising the experimentation effort. MCT is an example of such methods, Conceptually, MCT relates the material structure to its properties with high fidelity in such a manner that can be modelled by means of FEM; at the basis of this approach lies a multilevel view of the material microstructures and its embedded features at the micro level which can contribute in a separate or coupled manner to the evolving mechanical behaviour of the

material at the engineering (macro) scale [86]. Hence, different material properties and deformation states are assumed at each of these structural levels. Indeed, the response of a material point at a micro level to a local load can generally be very different to the macro-response, which tends to be an aggregate of microstructural responses averaged over a representative volume [82]. Therefore, MCT allows incorporating separate material laws for each level of microstructure at a material point of the specimen at the macro level. A good introduction to the technique along with the underlying mathematics and references for further reading is provided by Belytschko *et al.* [82].

2.7 Conclusion

In this Chapter, the mechanics associated with the laminated composites materials have been introduced including experimental techniques (e.g. LVI) and analytical methods such as CLPT and FSDT. It was shown that exact analytical solutions exist only for a small group of laminates such as specially orthotropic ones, and therefore, in many problems involving laminated structures, a solution can only be obtained with numerical methods such as a FEM. It was shown that the approximate solution can be obtained for an arbitrary laminate and boundary/loading conditions using a FEM. Using the failure criteria approach along with damage modelling techniques (e.g. CDM), dynamic response of composite laminates can be simulated using various FEA software such as LS-DYNA®. Furthermore, the capabilities of LS-DYNA® for modelling composite failure were discussed. Lastly, several advanced FE methods, namely XFEM and MCT, were briefly mentioned.

The review provided in this Chapter guided the process of selecting appropriate software tools and techniques for the numerical modelling of helicoidal laminates provided in Chapter 4. Furthermore, the introduced failure mechanics and damage propagation in composite materials is important for understanding the structural response and damage tolerance capabilities of these bio-inspired structures. Moreover, these concepts are of primary relevance to the second objective of this thesis which aimed at developing novel NDT techniques for damage detection in metallic and composite structures. In addition, the numerical studies presented in Chapter 5 make full use of the FEM/FEA methodology covered in Section 2.5 of the present Chapter for simulating various nonlinear elastic wave phenomena in the context of NDT and SHM techniques. The succeeding Chapter addresses a range of NDT/NDE methods in detail with emphasis on nonlinear ultrasonics due to its high sensitivity to sensing and evaluating early signs of material degradation.

3 NDE Methods based on Nonlinear Elastic Wave Interactions in Damaged Media

3.1 Introduction

Over the past decades a multitude of NDE and SHM methods have been developed aimed at enabling effective damage detection and evaluation. In particular, the NDT methods that are based on several linear phenomena associated with the ultrasonic wave propagation have been extensively researched and applied for many years. Linear methods, which are addressed in Section 3.2, work adequately well on components with high impedance contrast induced by the presence of voids and air gaps in areas of structural damage. However, the application of these methods is limited in structures that contain micro-damages as the acoustic impedance mismatch at the defect interface is not significant enough for the incipient wave to reflect and scatter to the detectable extent. This limitation can be overcome by the new class of NDT techniques and SHM systems that rely on the assessment of nonlinear elastic behaviour of materials which have demonstrated a much higher sensitivity in detecting early signs of material degradation long before the changes of the linear acoustic properties become prominent [87-89]. However, before delving into the field of nonlinear methods, this chapter introduces a range of currently used linear NDT/NDE techniques with emphasis on the ultrasonic testing followed by the fundamentals of wave propagation theory and guided waves.

3.2 Linear NDT Techniques

3.2.1 Visual and Optical Testing

There are many types of visually prominent composite damage types such as dents, scorches, stains, or abrades. Hence, a visual observation is by far the most regularly used and is a primary inspection method, especially during in-service inspections. The corresponding procedures range from simply looking at the surface of the component in search of the signs of visible defects to using specialised camera systems and borescopes to examine the parts which are not readily accessible. In some relatively translucent composites (e.g. glass-epoxy), internal damage such as delaminations may be visually detected using strong black light. However, most advanced composites are opaque, and therefore, the presence and the extent of internal damage cannot be detected visually. The application of more sophisticated NDT methods is necessary.

One of the most frequently used optical NDT techniques is called *laser shearography* or *speckle interferometry* and relies on detecting the out-of-plane displacement caused by applied loading using

a coherent laser light. A sample can be loaded by a range of excitation methods such as thermal, acoustic or mechanical loading which in turn results in a proportional strain on the surface of the material. By illuminating the surface with a laser beam and using an appropriate imaging system, a *speckle pattern* can be recorded. By comparing a speckle pattern of the deformed and the original states, a *shearographic fringe pattern* can be produced displaying the amount of relative deformation before and after the application of stress. In the presence of subsurface defects such as delaminations, voids and porosity, a disturbed fringe pattern can be observed allowing the operator to detect the location of the flaw with some indication of its size. Several review papers exist on this method and assess the applicability of shearography in comparison to other NDT techniques [90, 91]. In general, speckle interferometry can allow rapid and non-contact testing of large scale components. However, the main disadvantage is that it is only capable of detection of surface and subsurface defects with unreliable estimation of the internal damage extent.

3.2.2 Audible Sonic Testing

This technique, which is also known as sonic or coin tapping, implies the use of frequencies in the audible range, typically 10-20 Hz. It involves tapping on a surface of the specimen with a solid disc or lightweight hammer device and listening to the produced sound. This can be a surprisingly effective technique in the hands of an experienced person. By tapping at a sufficient rate on the well-bonded structure, a sharp/ringing sound is typically produced, whereas a dull sound may be indicative of a noncompliant area. However, it may be possible for the pitch changes to appear due to the internal components or the geometry inherent to the structure by design and not due to the presence of a defect. The tap testing can sometimes be effective in detecting delaminations or disbonds on the skin-stiffener bond lines, honeycomb sandwich panels with thin face sheets, and generally in relatively thin (4-5 plies) laminates or surface layers of thick laminates.

3.2.3 Ultrasonic Testing

Ultrasonic testing or ultrasonic *tomography*[9] is successfully and routinely used in detecting and evaluating internal damage (e.g. delaminations, porosity, voids etc.) not otherwise discernible by visual or tap techniques. In ultrasonic testing, sound waves are transmitted into the material of interest in order to detect the presence of flaws or identify the changes in the material properties. While ultrasound is formally defined as sound waves travelling at frequencies above the audible range (i.e. above 20 kHz), typical linear ultrasonic NDT utilises frequencies in the rage of 5 MHz to 20 MHz, which will be shown to be driven by a requirement on the smallest detectable damage size.

Pulse echo is one of the most commonly used ultrasonic NDT techniques and entails placing a *transducer* on a single side of a specimen and sending an acoustic pulse into the material. Consequently, the *sound wave* is reflected from the internal structure of the specimen (e.g. defects or wall boundaries) and the echoes are returned to the transducer, which can be used as both a transmitter and a receiver. The corresponding changes in the amplitude and the transit time of the wave, which is termed the *time of flight* (TOF), can be interpreted in order to indicate the presence of flaws in the material. There are a number of transducer types, however, *piezoelectric* transducers are among the most regularly used ones and are usually excited by the application of high voltage, whereby an electrical pulse applied to the piezoelectric element is converted into the mechanical waves and vice-versa – a mechanical strain in the piezoelectric material (e.g. *Quartz*, *Lead Zirconate Titanate* etc.) causes voltage generation across it. Figure 3.1 graphically shows a pulse echo test setup with a laminated composite specimen with damage present in the material.

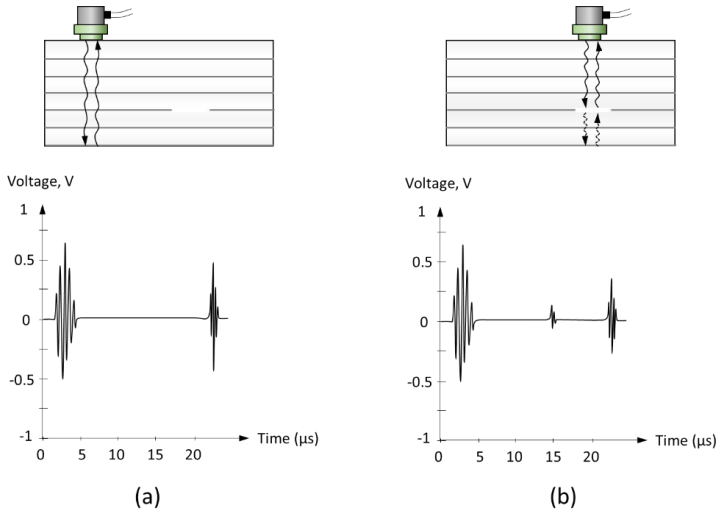

Figure 3.1: a schematic of a test specimen under an ultrasonic pulse echo testing with a piezoelectric transducer located above (a) an undamaged region and (b) a cracked region.

[9] *Tomography* is imaging by taking sections of an object by means of a penetrating wave.

In the undamaged zone (see Figure 3.1(a)), an ultrasonic pulse is reflected from the back of the specimen and is detected by the transducer. In the presence of the damage (e.g. cracks, delaminations), extra reflection are existent in the received signal - Figure 3.1(b). The time trace provides the information about the depth/thickness of the material and of the corresponding defects if any are present. A more detailed view of the test setup and the instrumentation is displayed in Figure 3.2.

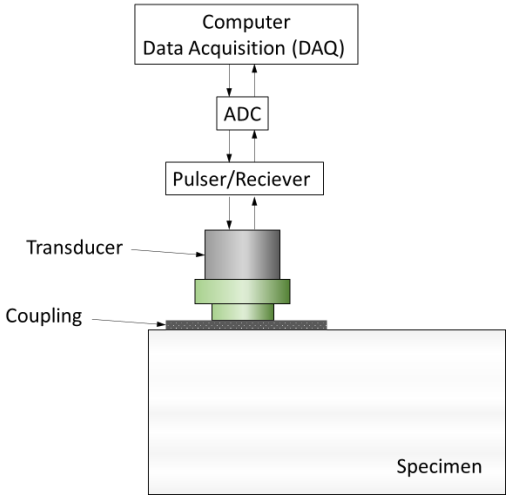

Figure 3.2: typical instrumentation setup in the pulse echo testing.

The experiments and the gathered data are typically managed by a computer system connected to an electrical pulser/receiver device which generates a wave form at the required voltage and applies it to a transducer element. The transducer converts the mechanical waves into an electrical signal, which is subsequently amplified, filtered and digitised prior to passing to the computer for the analysis. A coupling medium (e.g. water) is often used between the transducer and the specimen surface in order to facilitate and optimise the transmission of the ultrasound waves to and from the material. Longitudinal waves travel at a higher velocity than transverse waves, and that is why they are also termed as primary and secondary waves respectively – a more comprehensive explanation of wave propagation theory is provided in Chapter 3.3. Considering a longitudinal wave propagating in an isotropic homogeneous solid medium, the corresponding velocity of the wave can be defined as

$$c_L = \sqrt{\frac{K + \frac{4}{3}G}{\rho}} = f\lambda\,, \qquad \textbf{(3.1)}$$

where K and G are the bulk and shear moduli of elasticity respectively; ρ is density of the material, f is the frequency and λ is the wavelength.

Evidently, the wave propagation velocity c_L, depends on the stiffness and density of the media which together with frequency determines the wavelength, which in turn determines the size of the defects that can be detected

$$w > \frac{\lambda}{2}. \quad \textbf{(3.2)}$$

If the defect size (w) is smaller than half the wavelength of the signal, then the wave propagates without reflecting from the defect boundaries. As the sound speed is fixed by the material properties, a user may need to increase the frequency in order to achieve a required wavelength. However, *attenuation* may need to be taken into account in case a signal is expected to travel a considerable distance. As the sound propagates through a medium, its intensity or pressure decreases with distance due to spreading of the wave, scattering[10] and absorption[11]. Attenuation is the combination of these effects and is defined as an exponential decay rate of the amplitude of the wave as it propagates through a material

$$I = I_0 e^{-\alpha d}, \quad \textbf{(3.3)}$$

where I_0 is the intensity[12] (W/m^2) of the propagating wave at a certain location in the material and I is the intensity of the attenuated wave at a distance d away from that location; α is the *attenuation coefficient* which is generally proportional to the square of the sound frequency, and therefore, higher frequency waves attenuate faster than lower frequency ones. The attenuation coefficient depends on the material properties, experimental setup and the type of wave that is being transmitted and it can only be reliably determined by the experimental measurements.

The time it takes for the signal to return to the transmitter can be simply stated as follows

$$t = \frac{2d}{c_L}, \quad \textbf{(3.4)}$$

where, t is the time window between the transmitted and the received part of the signal; d is the thickness of the specimen or the distance to the flaw in the material. As the wave front reaches the flaw boundary and propagates further, some acoustic energy is transmitted into the flaw, while the remaining energy is reflected from the boundary as shown in Figure 3.3, where Material 1 is the bulk material of the specimen and Material 2 is the medium of the defect (e.g. air).

[10] In the present context, *scattering* is the deviation of the sound waves by paths other than its original direction of travel.
[11] In the present context, *absorption* refers to the conversion of the energy of sound into other energy forms.
[12] In the present context, *Intensity* is a measure of how much energy is passing through an area of material per unit time.

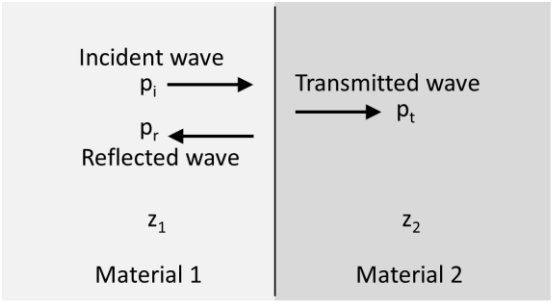

Figure 3.3: transmitted and reflected waves at the boundary of two materials.

Ratio of the reflected acoustic power to the incident power is termed a *reflection coefficient*, *R*; a *transmission coefficient* is defined as the remaining portion of the acoustic power $T = 1 - R$. These coefficients can be determined by specifying an *acoustic impedance* of the material, which is a ratio of pressure to material displacement amplitudes

$$z = \frac{p}{u} = \rho c_L \,, \tag{3.5}$$

where z is the acoustic impedance, p is the pressure amplitude and u is the displacement amplitude. Furthermore, z is a material parameter dependent on the density and the sound speed in the material. A reflection coefficient at the boundary of two dissimilar materials can be defined as

$$R = \left(\frac{\frac{z_2}{z_1} - 1}{\frac{z_2}{z_1} + 1} \right)^2 , \tag{3.6}$$

The corresponding transmission coefficient is

$$T = \frac{4\frac{z_2}{z_1}}{(\frac{z_2}{z_1} + 1)^2} . \tag{3.7}$$

Evidently, the greater the difference in acoustic impedance of the two materials, the greater the reflection coefficient is. Moreover, the pressure amplitude is proportional to the square root of acoustic power, and therefore, the following relationships can be stated

$$p_r = \sqrt{R} p_i \,, \qquad p_t = \sqrt{T} p_i \,, \tag{3.8}$$

where subscripts have their apparent meaning as shown in Figure 3.3.

Acoustic impedance is measured in *MRayl* ($10^6 \mathrm{kgm^{-2}s^{-1}}$). A typical value for air is 0.0004 MRayl, while it is 1.5 MRayl for water and 3.6 MRayl for CFRP. A reflection coefficient grows rapidly with increasing air gap width and that is why an ultrasonic scan over a sample containing air-filled cracks/delaminations normally results in strong reflections. Furthermore, this explains the use of coupling substance (water or ultrasonic jell) between the transducer and the test piece as this allows

the ultrasonic waves to penetrate into the test material with little impedance. This is an example of impedance matching. Moreover, specimens are often immersed in water tanks during the testing process.

Ultrasonic scanning can generally be of three types denoted *A*, *B* and *C*. A-scan is a single point measurement providing information through the thickness of the sample in the form of a signal amplitude versus time. Small width cracks usually produce a signature characteristic to the plot in Figure 3.1(b), whereas a delamination tends to produce a strong single reflection as virtually no energy is transmitted beyond it. B-scan (see Figure 3.4(a)) can be performed by translating a probe/transducer along a straight line acquiring multiple A-scan data points in the process and plotting them as greyscale/colour maps of amplitude values through the thickness versus length of the scan. Similarly, C-scan (see Figure 3.4(b)) can be constructed by translating the transducer in two dimensions acquiring A-scan data at a sufficiently high rate. Subsequently, the maximum amplitude or TOF data at each point can be plotted in two or three spatial dimensions.

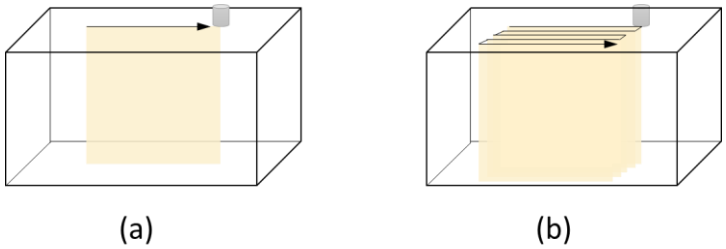

Figure 3.4: schematic of a transducer movement in typical (a) B-scan and (b) C-scan.

Figure 3.5 shows actual experimental results of C-scan performed on a square CFRP plate subjected to a LVI test. Arrows indicate the locations of the corresponding A-scans and B-scans that were used to plot a C-scan with colour indicating the depth of the reflections. In the undamaged region, only the front and back wall reflections are visible, whereas a 'pine-tree' pattern of reflections caused by delaminations is present in the damaged zone.

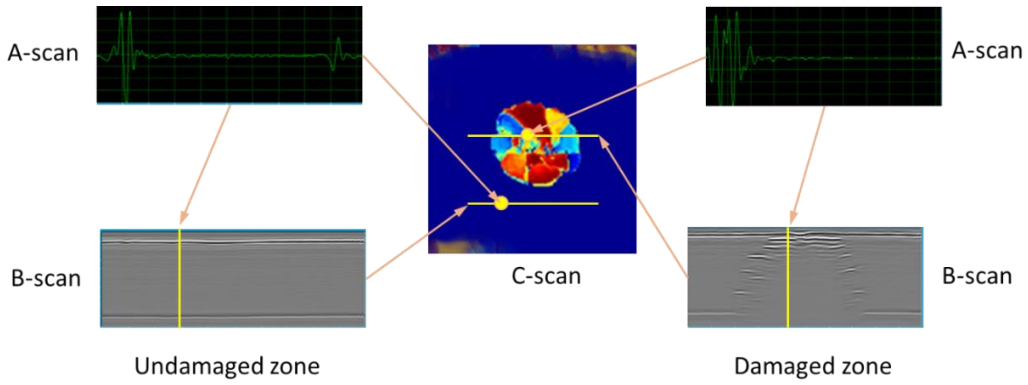

Figure 3.5: a typical C-scan and the corresponding A and B-scans of a composite (CFRP) plate subjected to a LVI event.

As mentioned earlier, a conventional ultrasonic NDT instrument consists of a single active probe element such as a piezoelectric transducer that both generates and receives high frequency sound waves. In some applications, more than one transducer may be placed on a sample in order to introduce more energy into the system and/or speed up the scanning process by covering a larger area. For instance, by placing two transducers on top and bottom side of the area to be inspected, a *through transmission* ultrasonic (TTU) testing also referred to as pitch-catch testing can be performed. As the signal is transmitted from one transducer element and is received by another, any loss of signal strength can be indicative of a defective area.

Multiple transducers can be grouped together to act as a single unit using multi-channel instrumentation. This technique is called p*hased array* testing and is currently considered a state-of-the-art in ultrasonic inspection. It operates in accordance with the same principles as pulse echo ultrasound but with an array of transducer elements (typically 64 or 128), compactly stacked next to each other in a line or in a 2D pattern. The fundamental feature of a phased array instrument is the facility to program the pulsing and receiving delay time for each of the elements in the array. Sending the excitation pules at different times to different elements allows to control the characteristics of the resulting ultrasonic beam. A schematic of the phased array setup is presented in Figure 3.6.

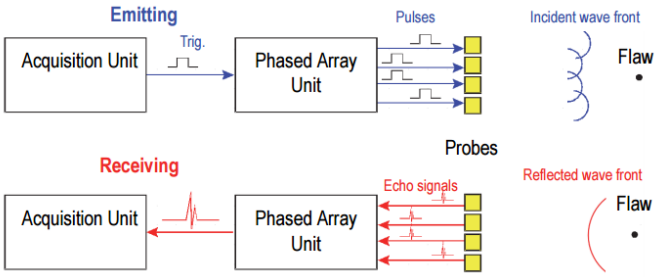

Figure 3.6: emitting/receiving in a phased array system; reproduced from [92].

By pulsing all elements simultaneously, a series of arc waves is produced resulting in a wave front/envelope that is parallel to the transducer plane which has similar effect to firing a single transducer element of the equivalent size – see Figure 3.7(a). If the various elements are fired in a sequential manner by introducing a precise time delay between the pulses from the different elements, the resulting wave front propagates at an angle to the linear transducer array as shown in Figure 3.7(b). These excitation patterns are referred to as *delay laws* or *focal laws* which enable to shape, steer or focus the beam of emitted ultrasound.

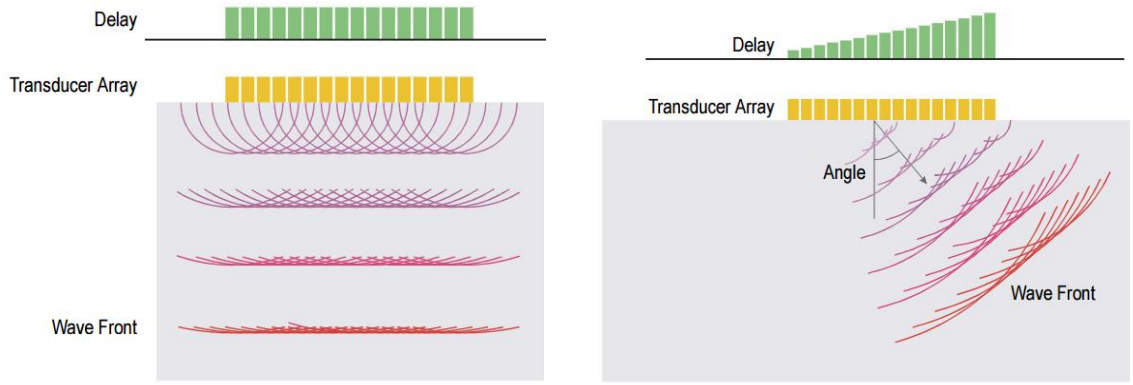

(a) (b)

Figure 3.7: ultrasonic wave fronts of a linear transducer array - (a) parallel transmission, (b) angle control of the beam; reproduced from [92].

This seemingly complex setup allows to capture more data, increase zone coverage and potentially obtain further insights into the defect size and characteristics which may not be readily obtainable with conventional single pulse echo ultrasonic system. However, phased array inspection is very computationally demanding and requires sophisticated hardware and software tools in order to accommodate effective data acquisition along with its interpretation and analysis. An example of a phased array transducer and the corresponding B-scan is shown in Figure 3.8.

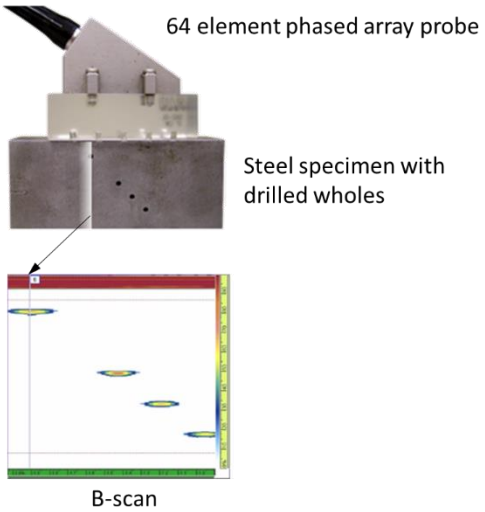

Figure 3.8: a typical B-scan produced by a phased array probe; reproduced from [93].

3.2.4 Radiography

Radiographic testing (RT) involves using short wave electromagnetic radiation, such as gamma or X-rays, which are able to penetrate various materials, in order to detect and evaluate hidden features in a test piece. Gamma radiation is generated by radioactive atoms, while X-rays are typically produced using X-ray generation processes such as *Bremsstrahlung* and *K-shell* emission radiation. Both X- and gamma- rays are characterised by frequency, energy and wavelength as shown on the electromagnetic spectrum in Figure 3.9. They possess properties of particles and waves travelling at speed of light in *packets* of energy referred to as *photons*.

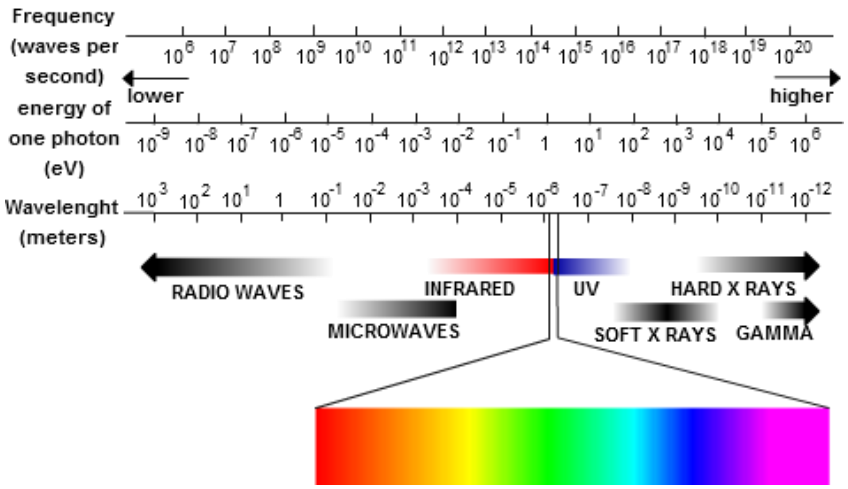

Figure 3.9: the electromagnetic spectrum; reproduced from [94].

The shorter the wave length, the more energy the photons have enabling them to pass through matter. As the radiation is directed into the specimen, the photons are scattered and absorbed as they propagate through the material. X-rays and gamma rays can also be *diffracted* (bent) at the interfaces of two different materials. In a conventional RT setup, a film or some other detector type is placed behind the test piece which absorbs the incident X-radiation and results in a shadowgraph revealing the internal features of the component. Figure 3.10 demonstrates a typical RT setup.

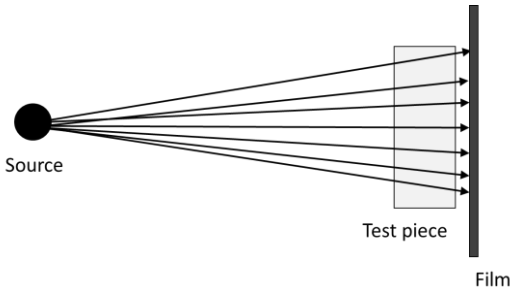

Figure 3.10: a schematic of a RT setup.

Lighter/darker areas on the detector depend on the material thickness, the density changes and the attenuation coefficient. The dark areas observed on the radiograph represent the internal voids

present in the material. Attenuation of X-rays passing through matter generally follows the exponential law defined by Equation (3.3 with the attenuation (absorption) coefficient increasing with the increasing atomic number of a material, and decreasing with the increasing X-ray energy. High attenuation reduces penetration, whereas low attenuation leads to little variation in intensity. Consequently, this affects the level of shadowgraph image contrast and the level of discernible internal details. However, a desirable result can be obtained by varying the *film gradient*[13] and/or by adjusting the *exposure*. Exposure can be defined as

$$E = It\,, \tag{3.9}$$

where I is the intensity (W/m^2) and t is time. Longer exposure time leads to darker image. CFRP has a relatively low attenuation coefficient and therefore requires low energy X-rays (<50 keV). As an example, Figure 3.11 depicts the actual results of X-ray RT performed on a woven CFRP plate subjected to LVI testing.

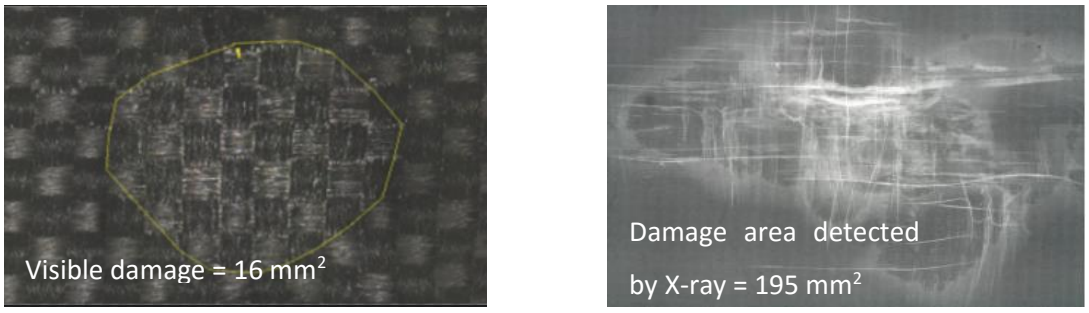

(a) (b)

Figure 3.11: a BVID of a woven composite (CFRP) plate as detected (a) visually and by (b) RT.

While the above image is the result of a single X-ray RT scan, the radiographic scanning is widely performed using computer *tomography* (CT) scanning, whereby many X-ray slices (scans) are taken as the test piece is rotated. This allows imaging from many directions avoiding the problem of defect orientation. Resulting 2D slices can be stacked and processed using specialised computer software in order to construct a 3D image or a CAD model.

To sum up, X-ray RT produces a 2D image due to absorption along path from the source to the image point. A scanning system can be portable allowing rapid (few seconds per scan) inspection of large areas (~1m). CT scan produces an image where each point represents an absorption of that point in the object. It typically takes minutes to produce a single 2D image depending on the required resolution. However, 3D image or CAD model of an object can also be produced. CT scan systems are usually fixed location equipment with the size of a test specimen limited to less than ~1 m.

[13] *Film gradient* is a measure of sensitivity of a given film to X-rays.

3.2.5 Thermography

Thermographic NDT relies on *infrared radiation* (IR), which is emitted by heated objects, to detect subsurface defects that may be observed as temperature gradients on the surface of the test piece using IR camera. Infrared range of electromagnetic spectrum in the wavelength bands of 2-5.6 mm and 8-14 mm are conventionally used due to their low atmosphere absorption. IR or thermal imaging can generally be of passive or active types. In passive approach, the test object is at constant temperature which is typically higher than ambient. In active approach, a test piece is thermally stimulated by a heat source and the corresponding transient response in temperature is captured by an IR camera. A typical instrumentation setup for performing thermographic testing is shown in Figure 3.12.

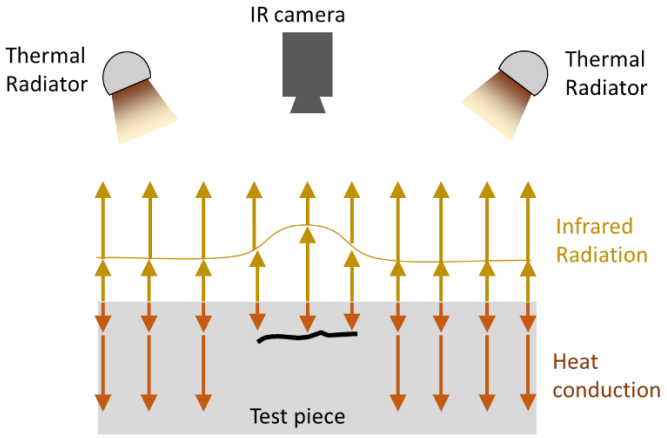

Figure 3.12: equipment setup for IR thermal imaging.

Pulsed thermography is one of the conventionally used NDT techniques which involves using a xenon flash for a short pulse (milliseconds) or halogen lamp as a transient (seconds) heat source. An IR camera connected to a PC records the dynamic response (time dependant) of the surface temperature of the test piece. Surface areas closest to a thermal discontinuity (e.g. delaminations) locally exhibit transient surface temperature increase as the flow of heat into the bulk of the material is inhibited [95]. In other words, internal defects act as insulation layers causing the front surface of the sample above the regions containing a flaw to heat up at a faster rate and cool down at a slower rate than in the areas free of internal discontinuities. This effect is generally due to thermal conductivity mismatch at the interfaces of different materials. A dynamic temperature response of a semi-finite defect free sample to an instantaneous application of heat pulse can be analytically defined as [96]

$$T(t) - T(0) = \frac{Q}{k\rho c_p \sqrt{\pi t}}, \qquad \textbf{(3.10)}$$

where Q is the input energy per unit area (Jm^{-2}), k denotes the thermal conductivity ($Wm^{-1}K^{-1}$), ρ is density (g/cm^3) and c_p is the specific heat ($Jkg^{-1}K^{-1}$) of a material.

As a common *post-processing* technique, a natural logarithm of both sides of the Equation (3.10 is plotted using the experimentally obtained data for each pixel for all images in a sequence as recorded by the IR camera. This typically reveals a characteristic linear profile for defect free zones, while a significant deviation from the linearity is observed in the vicinity of the subsurface discontinuities. The time window for the onset of this nonlinear behaviour to occur is a function of the depth to the defect.

Thermal propagation generally depends on a property known as *thermal diffusivity* (m^2/s) which is also referred to as *thermal inertia*

$$\alpha = \frac{k}{\rho c_p}. \qquad \textbf{(3.11)}$$

Materials with low thermal diffusivity, such as composites, have a long thermal propagation time, limiting the effectiveness of flash thermography to the detection of subsurface damage up to ~3 mm through the thickness; transient pulses of applied heat, which can last from seconds to hours, can increase the depth of detectable defects up to approximately 6 mm [97]. By means of a *lock-in* technique, defects at the depth of up to a double of transient thermography can potentially be detected. Lock-in thermography involves applying a dynamic stimulation to a surface to be inspected. This can be performed using a variety of sources such as halogen lamps, ultrasound transducers or a mechanical loading. The loading is usually applied as a sinusoidal or square wave function of a low frequency (0.01 Hz – 1 Hz) depending on the material properties and the thermal inertia. The corresponding temperature generation is recorded with an IR camera and post-processed using a *fast Fourier-transform* (FFT) on the temporal evolution of the temperature signal for each pixel. Subsequently, the corresponding phase and amplitude information are plotted. The areas containing defects are expected to reveal themselves as phase lag or phase lead in the response spectrum. A typical IR camera has a temperature sensitivity of 15µK for cooled to 80 µK for uncooled configuration. Lock-in thermography can expand this sensitivity by a factor of 100 to 1000. Another advantage is that phase information is insensitive to external environmental factors such as sunlight, reflections and *emissivity differences*. A flow chart in Figure 3.13 summarises the major thermographic techniques.

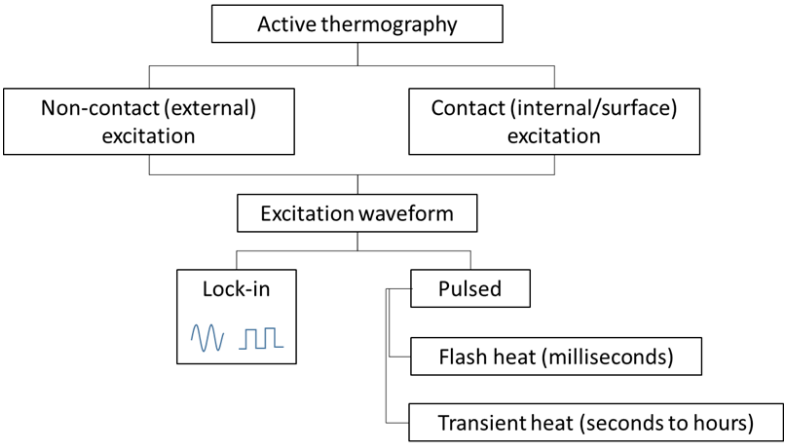

Figure 3.13: classification of IR thermography techniques.

To conclude, flash thermography is an attractive and indeed a frequently used technique as it allows short measuring time and can effectively resolve shallow defects. Thermographic techniques have been estimated to be up to 30 times quicker than underwater ultrasonic C-scan methods illustrating the ability to rapidly inspect large areas of composite materials [98]. Thermal NDT/NDE relies on the generation of thermal waves in the specimen which allow the transient thermal images of the sample to be captured [98]. The theory of heat conduction including differential equations governing the propagation of thermal waves has been extensively discussed by Almond and Patel [99].

When a large surface area needs to be inspected, transient technique can be readily applied leading to a lower thermal load on the inspected component using affordable halogen lamps as heat sources. In cases involving thick structures, lock-in thermography is a superior technique which can significantly expand the effective sensitivity of the IR camera and resolve internal material flaws such as deep cracks. However, the considerations limiting the utilisation of thermographic NDT include part thickness and environmental effects. Furthermore, the effectiveness of these methods can be further impeded in situations where the delaminated surfaces are in contact with each other or with little separation between them which as the result would not restrict the heat flow into the bulk of the material.

3.2.6 Thermosonics

Thermosonic techniques (also known as *sonic thermography*, *ultrasonically stimulated thermography*, *vibro-thermography*, and *sonic IR* [100-102]) can generally be grouped under thermographic NDT methods. However, thermosonic testing has been recently emerging as a separate class of NDT/NDE techniques and has also been demonstrated to be more efficient in detecting composite damage than previously mentioned thermographic techniques [103-105]. In its classical form, it involves generating large amplitude vibrations in a sample under inspection in order to activate frictional heating at crack surfaces and monitoring the resulting surface temperature patterns with an IR camera. The excitation is typically produced by pressing an *ultrasonic horn*[14] against the surface of the test piece and using the excitation frequencies in the range of 15 to 40 kHz (acousto-ultrasonic range). The horn acts as an ultrasonic hummer that clatters against the part surface promoting a complex nonlinear vibration process characterised by the generation of *sub-* and *super- harmonics* in the frequency spectrum of the component under testing. Some authors referred to this phenomena as a condition of '*acoustic chaos*' that can stimulate the crack heating [106]. On one hand, this technique has been shown to be capable of detecting a crack of 1 mm length in gas turbine component [107], and in the detection of impact damage areas on the order of 3 cm^2 in laminated composites [108]. On the other hand, one of the main intrinsic drawbacks of this approach is poor reproducibility due to the inherent nonlinearity of the excitation process [104]. In other words, repeating the same testing procedure on the same test piece does not usually yield the same results in terms of damage detection. It follows that an appropriate selection of the excitation level is crucial in performing a successful thermosonic testing. For a given test sample and type of damage, a threshold excitation energy exists that would generate sufficient frictional heating at a defect which can in turn be detected with a thermal camera. Morbidini and Cawley [103] suggested that a temperature rise at a crack is directly related to the power dissipated at the crack during the vibration process

$$P = 2\pi\eta_{crack} f V, \qquad \textbf{(3.12)}$$

where P is dissipated power at the crack, η_{crack} is the crack loss factor, f is the frequency of a mode of vibration and V is the strain energy associated with the mode. Taking into account that the strain energy is proportional to the square of the vibration amplitude, relationships for the so-called '*the energy index'* and the '*the heating index*' in terms of the measured vibration amplitude and the amplitudes of the individual frequency components were proposed [109]. It was shown that by exceeding a certain threshold level of these indices, IR imaging of a specific crack size and location

[14] *Ultrasonic horn* which is also known as ultrasonic welding horn or acoustic horn is a cylindrical metallic rod or bar of varying cross-sectional area that is used to augment the displacement oscillation amplitude induced by an ultrasonic transducer. The requirement for the use of the ultrasonic horns arises due to the fact that ultrasonic transducers by themselves produce relatively small amplitudes.

may be achieved [104]. However, in general, these threshold values are highly dependent on the component geometry, material properties and the sought defect type. Moreover, exceeding a certain energy level, the ultrasonic horn may start to induce micro or macro damage into the structure, defeating the point of testing.

3.2.7 Acoustic Emission Testing

Subjecting a solid medium to mechanical or thermal loading results in the redistribution of stress in the material which leads to short bursts of elastic waves termed *acoustic emissions* (AE). Unlike other NDT methods, where the energy is introduced into the system, the energy released by the flaw itself is the phenomenon of interest in AE testing. Fundamentally, acoustic emission can occur due to the presence of discontinuities in the material, slip and dislocation motion at lattice planes on the atomic level and due to the manifestation of internal flaws such as initiation and growth of cracks/delaminations on microscopic level [110]. As in the case of ultrasonic testing, the resulting stress waves can be captured by specialised transducers in order to evaluate the size of internal damage and possibly its location. One of the advantages is that a network of strategically placed sensors actively or passively 'listening' for the AE can be used as an 'in situ' SHM system. However, in most cases, AE testing can merely qualitatively indicate the overall risk of component failure, while other NDT methods are required in order to localize the defect and evaluate its extent.

3.2.8 Dye Penetrant Testing

This testing method is also called *liquid penetrant testing* and involves coating a test specimen with a solution of visible or fluorescent dye. Subsequently, excess solution is removed and a developer is applied in order to draw the dye out of the cracks which become readily visible under UV light in case a fluorescent substance is used. It is a low-cost inspection method that can be used to reveal the surface breaking defects such as welding defects, surface porosity, leaks and fatigue cracks.

3.2.9 Electromagnetic Testing

As the name suggests, this NDT method relies on the electrical current or the magnetic field to detect fractures and other types of damage in the conductive materials. Introduction of *eddy current* into a FRP material creates detectable perturbations/discontinuities of magnetic field in areas of fibre fracture [111]. One of the main disadvantages of this technique is the limitation on the penetration depth which is usually confined to within 5 mm.

3.3 Wave Propagation Theory

As mentioned in the previous Section, ultrasonic NDT/NDE methods rely on the propagation and reflection of elastic waves within the material. These waves can be induced by placing an energised piezoelectric probe/transducer on the material surface. The ultrasonic testing aims at determining the wave-field disturbances caused by presence of flaws and local damage by determining: amplitude, phase, path length, time of flight (TOF) (transit time of the wave), etc. In an infinite, unbound solid medium, elastic waves propagate as bulk waves of two types: *dilatational* (also known as *pressure wave*, *compressional wave*, *P-wave*, *primary wave* or *longitudinal wave*) and *distortional* (also known as *S-wave*, *secondary wave* or *shear wave, transverse wave*). P-waves travel longitudinally by compression and rarefaction in the direction of the wave propagation, whereas the material particle motion is transverse (perpendicular) to the propagation direction in S-waves. However, in case of a bounded medium, the wave reflects at the boundaries of the wave-guides leading to more complicated wave patterns such as seen in *L. Rayleigh* [112], *Shear Horizontal (SH)*, *Lamb* [113]. These types of waves are referred to as guided waves. Studied for more than a century [112-114], they are of high importance in many acousto-ultrasonic SHM and NDT methods as most man-made structures are thin-walled (aircraft components, storage tanks, pipes etc.) and feature solid boundaries which enable guided waves to propagate. In the following chapters, these waves and their significance are briefly addressed, whereas a good treatment of underlying mathematics is provided in numerous texts, for example by Giurgiutiu [115].

3.3.1 The Wave Equation in Elastodynamics

In order to introduce the guided waves, it is first essential to understand the propagation of elastic waves in the unbounded solid medium. In the absence of body forces, the equation of motion in *classical linear elasticity* can be stated as a combination of force equilibrium equation Eq. (2.16), the linear Hooks law Eq. (6.1) and the strain-displacement relationship Eq. (2.15) [116]

$$\rho \frac{\partial^2 u_i}{\partial t^2} = \frac{1}{2} C_{ijkl} \frac{\partial}{\partial x_j} \left(\frac{\partial u_l}{\partial x_k} + \frac{\partial u_k}{\partial x_l} \right) \tag{3.13}$$

The stress field can be decoupled into the longitudinal (*hydrostatic*) and transverse (*deviatoric*) components

$$\sigma_{ij} = \lambda \epsilon_{kk} \delta_{ij} + 2\mu \epsilon_{ij} = \lambda \frac{\partial u_k}{\partial x_k} \delta_{ij} + \mu \left(\frac{\partial u_i}{\partial x_j} + \frac{\partial u_j}{\partial x_i} \right) \tag{3.14}$$

where $\lambda = \frac{\nu E}{(1+\nu)(1-2\nu)}$ and $\mu = \frac{E}{2(1+\nu)}$ are known as *Lame constants*, E is the Young's modulus, ν is Poisson's ratio and $\delta = 1$ if $i = j$, $\delta = 0, i \neq j$ is the Kronecker delta. The linear wave equation can be obtained by differentiating Eq. (3.14) and substituting it into Eq. (2.16) neglecting the body force term

$$\rho \frac{\partial^2 u_i}{\partial t^2} = \frac{\partial}{\partial x_i} \left(\lambda \frac{\partial u_k}{\partial x_k} \right) + \mu \frac{\partial^2 u_i}{\partial x_k^2} + \frac{\partial}{\partial x_i} \left(\mu \frac{\partial u_k}{\partial x_k} \right) = (\lambda + \mu) \frac{\partial^2 u_k}{\partial x_i \partial x_k} + \mu \frac{\partial^2 u_i}{\partial x_k^2} \tag{3.15}$$

Eq. (3.35) can be written in an invariant form known as the *Navier's equation* which can be stated in terms of the longitudinal c_l wave speed (already defined in Eq. (2.36) and Eq. (3.1)) and transverse (shear) c_t wave speed

$$\rho \frac{\partial^2 \mathbf{u}(\mathbf{r}, t)}{\partial t^2} = \rho c_l^2 \nabla [\nabla \cdot \mathbf{u}(\mathbf{r}, t)] + \rho c_t^2 [\nabla^2 \mathbf{u}(\mathbf{r}, t) - \nabla \cdot \mathbf{u}(\mathbf{r}, t)] \tag{3.16}$$

where $\mathbf{r} = x\hat{\imath} + y\hat{\jmath} + z\hat{n}$ and $\nabla^2 = \left(\frac{\partial^2}{\partial x^2} \hat{\imath} + \frac{\partial^2}{\partial y^2} \hat{\jmath} + \frac{\partial^2}{\partial z^2} \hat{n} \right)$ is the Laplacian operator and

$$c_l = \sqrt{\frac{\lambda + 2\mu}{\rho}} \tag{3.17}$$

$$c_t = \sqrt{\frac{\mu}{\rho}} \tag{3.18}$$

Therefore, the solution to Navier's equation comprises a combination of the longitudinal and shear waves.

3.3.2 Guided Waves

When the medium is constrained by the presence of free surfaces (guides), a class of waves called guided waves can propagate by reflecting from the boundaries. Therefore, these waves are confined to thin-wall structures and can travel large distances with little attenuation or energy loss which makes them of special importance in SHM and NDT applications. In solids containing a free surface, *surface acoustic waves* (SAW) known as Rayleigh waves [112] can exist which travel close to the surface with little propagation through the depth of the material. In plates, ultrasonic guided waves propagate as shear horizontal (SH) [115] and Lamb waves [113]. The qualitative difference between them lies mainly in the plane of *polarisation*. Considering a plate and coordinate system convention shown in Figure 3.14, SH waves are *horizontally polarised* (parallel to the plate surface) which means that the wave particle motion is constrained to z-x plane, whereas Lamb waves are *vertically polarised* (i.e. particle motion in x-y plane). SAW, SH and Lamb waves travel in x-direction following the axis convening of Figure 3.14. The latter ones arise in plates due to multiple reflections from the boundaries and constructive/destructive interference of a combination of P-waves and vertically polarised S-waves. As the result, Lamb waves consist of standing wave patterns in the y-direction, while appearing as travelling waves in the x-direction. These patterns can be of two basic types: (i) *symmetric Lamb wave modes* (S_0, S_1, S_2, …) and (ii) *antisymmetric lamb wave modes* (A_0, A_1, A_2, …). All lamb wave modes are highly dispersive which means that the velocity of wave propagation depends on the frequency. Indeed, the higher the number of the frequency-thickness product *fd*, the higher the number of modes that can simultaneously exist. As the $fd \rightarrow \infty$, the basic modes (S_0, A_0) regress into Rayleigh waves confined to the surface.

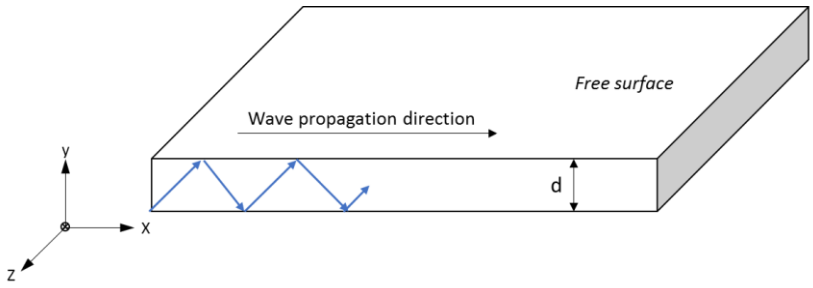

Figure 3.14: axis notation typically used for guided waves.

Figure 3.15 shows velocity-frequency relationships (dispersion curves) for various wave types in an aluminium plate of 1 mm thickness.

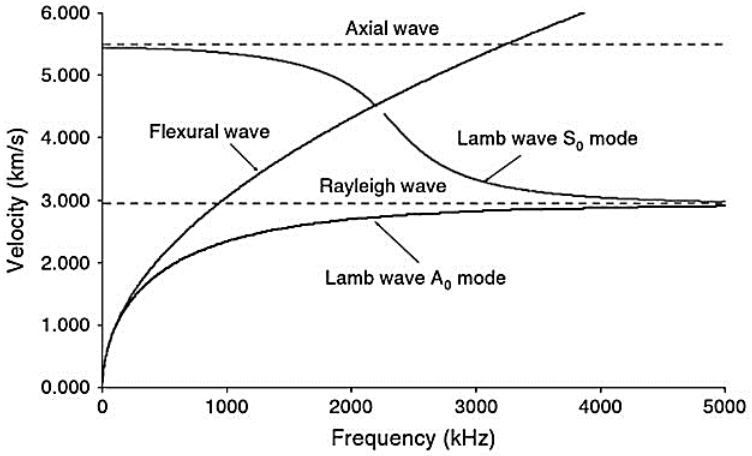

Figure 3.15: dispersion curves for axial, flexural, Rayleigh and Lamb (S_0, A_0) waves; reproduced from [115].

In order to obtain characteristic Lamb wave equations, a solution is typically sought assuming a harmonic motion ($e^{-i\omega t}$), z-invariance ($\frac{\partial}{\partial z} = 0$) and rewriting the Navier's equation (Eq. (3.13)) using *Helmholtz decomposition* involving scalar potentials Φ and H_z [117]

$$c_l^2 \nabla^2 \Phi = \ddot{\Phi} \tag{3.19}$$

$$c_t^2 \nabla^2 H_z = \ddot{H}_z \tag{3.20}$$

An extensive treatment of the derivation of Lamb wave equations is provided by Victorov [117]. After considerable mathematical manipulations, one can arrive at dispersion equations also known as Rayleigh-Lamb frequency relations for symmetric modes

$$\frac{\tan\left(\frac{pd}{2}\right)}{\tan\left(\frac{qd}{2}\right)} = -\frac{(k^2 - q^2)^2}{4k^2 pq}, \tag{3.21}$$

And antisymmetric modes

$$\frac{\tan\left(\frac{pd}{2}\right)}{\tan\left(\frac{qd}{2}\right)} = -\frac{4k^2 pq}{(k^2 - q^2)^2}, \tag{3.22}$$

where $p = \sqrt{k_l^2 - k^2}$, $q = \sqrt{k_t^2 - k^2}$, $k = \omega / c_{ph}$ is a wave number defined as a ratio of angular frequency ω and *phase velocity* c_{ph}. Indeed, in dispersive wave propagation, individual waves in the packet travel at different velocity to the wave packet itself. Therefore, there is a phase velocity (c_{ph}) corresponding to the velocity of the individual waves in the packet, and a *group velocity* (c_g) corresponding to the propagation of the wave packet. In case of dispersive waves, the energy of the wave propagates at the group velocity which can be defined as follows [115]

$$c_g = \frac{\partial \omega}{\partial k} = c_{ph} + k \frac{\partial c_{ph}}{\partial k} \tag{3.23}$$

The solution of Eq. (3.21) and Eq. (3.22) leads to the wave speed dispersion curves which are typically plotted as phase or group velocity against *fd*, $f = \omega/2\pi$.

Determination of the dispersion curves in terms of phase and group velocity is essential for the successful application of Lamb waves in NDE. It was shown [118] that these waves can be used for disbond detection in adhesive joints of a Boeing 737 aircraft by careful velocity-frequency tuning which allowed the wave to propagate ("leak") from one side of the bond to another; by measuring the signal strength, it was possible to discern between the sufficiently bonded and partially debonded joints. More recently, Chona *et al.* [119] reported that A_0 mode is sensitive to damage associated with disbonds and delaminations in layered composite structures. Although, multi-mode character, sensitivity to various defect types and propagation over long distances provides a clear potential for the use of Lamb waves in NDT/NDE applications, a routine use of these waves is scarce. Sending a Lamb wave through a complex aircraft component, such as a stiffener panel, will cause many effects such as phase shift, amplitude change and mode-conversion which can be erroneously interpreted as damage and therefore extensive and rigorous base line testing is required. Moreover, in addition to the aforementioned waves, other wave types are also defined in literature, such as Love waves [114], which generally propagate in semi-finite medium with varying density through the thickness. Moreover, guided waves exist in many thin-wall structures such as rods, shells and tubes. Indeed, Love [114] showed that at high frequencies, multimodal and dispersive longitudinal, flexural and torsional waves can propagate in isotropic cylinders, while Meitzler [120] showed that these modes can couple into a complex wave propagation pattern under certain condition. Therefore, in order to study an intrinsically complex phenomenon of wave propagation and scattering in finite and semi-finite media especially in presence of structural defects, numerical and semi-analytical methods are often employed.

In general, there are two methods used for studying acousto-vibrational response of structures: (i) response or wave propagation method and (ii) the modal analysis. As the names suggest, the former one aims at analysing the reflection, transmission and scattering of the propagating wave, whereas the latter method is concerned with evaluating the standing wave properties of a system. Both techniques rely on representing the system in a matrix form. A number of methods have been suggested for studying wave propagation in layered anisotropic structures, namely transfer matrix [121] and global matrix [122]. In these methods, the displacement and stress fields are expressed as a superposition of bulk waves with the displacement field expressed for each layer as a function of material properties and wave number. Enforcing the appropriate boundary conditions and the continuity of stress at the top and bottom surfaces of each layer leads to a nonlinear transcendental eigenvalue problem which requires iterative root searching algorithms unless 3D proximate plate

theories are employed. McKeon [123] studied the scattering of Lamb waves from the through holes using an in-plane Mindlin plate theory [124] (also known as FSDT discussed in Chapter 2.3.2.2). More recently, Tang and Henneke [125] used FSDT to derive the phase velocities of A_0 and S_0 modes in laminated composite plates, although the approximate method was not adequate for obtaining higher frequency modes, where the plate thickness is comparable to the wavelengths.

An extensive use of the FEM was reported for studying wave propagation phenomenon including Lamb waves in plates [126-129]. Other FE-based numerical schemes, such as boundary element method (BEM), [130] and spectral finite element method (SFEM) [131], can also be employed to study elastic wave propagation. The former one encompasses the spatial discretisation of merely the boundaries of the physical domain which enables numerically efficient modelling of wave reflection and scattering, whereas SFEM uses high order polynomials to interpolate the displacement field of finite elements and thus enables higher accuracy than standard FEM. In addition, according to several authors [132], SFEM is more computationally efficient than standard FEM in simulating wave propagation phenomenon. However, no commercial SFEM codes currently exist, and therefore, the efficiency of the method is somewhat offset by the implementation of the in-house written codes in light of the availability of highly optimised and extensively validated commercial explicit FEA solvers such as LS-DYNA® and ABAQUS®. Willberg *et al.* [133] compared the numerical efficiency and performance of various order FE schemes, such as SFEM and standard FEM among others, for simulating Lamb wave propagation in solid medium, reporting a negligible discrepancy in results when using a commercial explicit FEA code with adequately meshed computational domain. This further reinforces the use of the LS-DYNA® solver in present work.

3.4 Nonlinear Elasticity Theory and Applications

The multimodal, coupled and dispersive behaviour of guided waves complicates their use in SHM and NDT applications. In the experimental and numerical work presented in this thesis, no attempt is made to utilise a particular guided wave and its mode. Instead, the focus is on the nonlinear acousto-ultrasonic detection methods which allow a high degree of flexibility in terms of excitation frequency selection and do not necessarily require to generate a particular wave mode. The scope for the nonlinear ultrasonic methods was briefly introduced in Chapter 1.1.2. In this chapter, a number of nonlinear elastic wave phenomena and their NDT/NDE applications is presented.

3.4.1.1 Classical Nonlinear Elasticity

As mentioned in Chapter 1.1.2, the theory and applications of nonlinear elasticity are generally concerned with the generation of frequencies in the response spectrum that are not necessarily the fundamental driving/exciting frequencies. At the basis of the nonlinear NDT/NDE methods is the hypothesis that at a sufficient finite amplitude of excitation, the wave propagating through a region containing a defect, will cause the medium to respond in a nonlinear fashion. In a classical view of nonlinear ultrasonics, the nonlinearities arise due to local velocity variations which in turn cause the waveform to deform and transition from a harmonic wave into a saw-tooth type one as it propagates through a nonlinear medium [134]. As the result, a wave of an amplitude A_1 and frequency f_1 propagating through the defects, such as fatigue crack, will contain multiples (harmonics) of the driving frequency (f_1), namely $2f_1$, $3f_1$, etc. with the corresponding amplitudes A_2, A_3, etc.; harmonic frequencies above the f_1 are termed higher harmonics or super-/ultra- harmonics, while the ones below f_1 are denoted subharmonics. Subsequently, the extent of the defect can be evaluated by measuring the level of these nonlinearities. Figure 3.16 schematically demonstrates the process of higher harmonics generation.

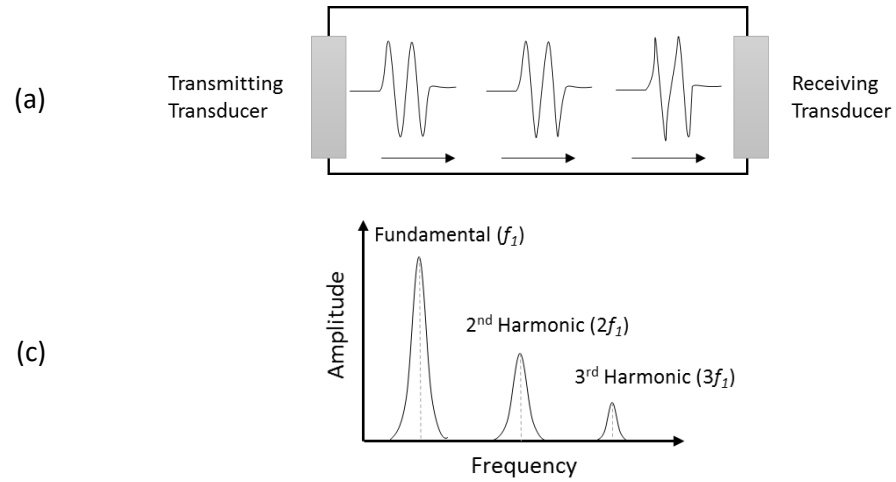

Figure 3.16: (a) distortion of the harmonic signal as it travels through a nonlinear medium; (b) as the waveform is distorted, even and odd multiples of the fundamental frequency appear in the frequency spectrum; adopted from [135].

From a mathematical perspective, the generation of the 2nd harmonic ($2f_1$) can be explained by considering a system that acts to square an input signal. Therefore, for an input of $(\sin \omega t)$ the system will produce $(\sin \omega t)^2$ which can be written using a trigonometric identity as $0.5(1 + \cos 2\omega t)$, which in turn contains a frequency which is a double of the input one. Similar analogy can be applied to represent the 3rd and higher order nonlinearities. In fact, L. Rayleigh [136] pointed out that inclusion of nonlinear terms in the wave equation leads to a solution containing waves with new frequencies which are multiples of the initial acoustic wave frequency. Subsequently, a number of authors have contributed to the field of nonlinear elasticity through theoretical [137, 138] and experimental [139-141] studies. Indeed, in both damaged and intact states, traditional materials such as aluminium and CFRP exhibit classical nonlinear (also termed *anharmonic*) effects (e.g. higher harmonics) arising from the atomic level elasticity which can be described by the nonlinear elasticity theory of Landau [142]. Higher harmonics generation can be generally represented expressing a Hook's law using a nonlinear modulus of elasticity (C_C) expanded in 1D power law as follows [143, 144]

$$\sigma = C_C \varepsilon, \quad C_C = C_0\left(1 + \beta\varepsilon + \delta\varepsilon^2 + \cdots\right), \tag{3.24}$$

where C_0 denotes a linear elastic modulus, while β and δ are termed as classical 2nd order (quadratic) and 3rd order (cubic) nonlinear parameters/coefficients (constants) respectively.

Considering a wave equation in 1D (e.g. longitudinal waves in thin circular rods)

$$\frac{\partial \sigma}{\partial x} = \rho \frac{\partial^2 u}{\partial t^2}, \tag{3.25}$$

and combining Eq. (3.24) with Eq. (3.25), a 1D wave equation with a nonlinear material behaviour can be defined as follows

$$\frac{\partial^2 u}{\partial t^2} = c_l{}^2 \frac{\partial^2 u}{\partial x^2}\left[1 + \beta \frac{\partial u}{\partial x} + \frac{\gamma}{2}\left(\frac{\partial u}{\partial x}\right)^2\right], \tag{3.26}$$

where $c_l^2 = C_0/\rho$ is the longitudinal wave speed in 1D and $\varepsilon = du/dx$ is the strain. Eq. (3.26) can be solved using a perturbation method which assumes a solution as a combination of linear and nonlinear terms assuming the nonlinear terms are much smaller than then the linear one

$$u = u^{(1)} + u^{(2)} + u^{(3)}, \tag{3.27}$$

where $u^{(1)} = A_1 \cos(kx - \omega t)$ represents a solution of a linear case with a wave amplitude A_1 and wave number $k = \omega/c_l$; $u^{(2)}$ and $u^{(3)}$ are the 2nd and 3rd order nonlinear terms which are found by subsequent substitution of the linear solution into Eq. (3.26). As the result, it is possible to obtain an approximate solution as follows [135]

$$u = u^{(1)} + u^{(2)} = A_1 \cos(kx - \omega t) - A_2 \sin 2(kx - \omega t), \tag{3.28}$$

which in the present case considers merely $u^{(1)}$ and $u^{(2)}$, however, the same approach can be followed to obtain a solution considering the 3rd order nonlinearity, although, the 2nd order term has a larger contribution than further higher order ones. Subsequently, the nonlinear parameter (β) can be evaluated taking into account the amplitudes of the fundamental and the 2nd harmonic responses as follows [145]

$$\beta = \frac{8}{k^2 x}\frac{A_2}{A_1^2}, \tag{3.29}$$

where x is defined as the propagation distance and other terms have already been defined. It should be noted that the quadratic nonlinearity produces both even and odd harmonics, while the cubic one leads to the odd harmonics only. This is graphically shown in

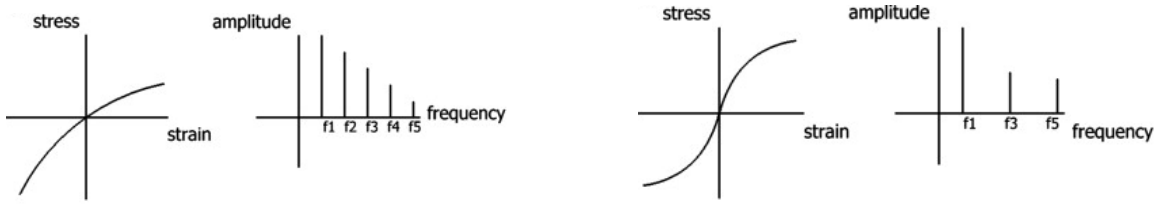

(a) (b)

Figure 3.17: stress-strain relations and the corresponding frequency spectra for materials exhibiting (a) 2nd order and (b) 3rd order nonlinearities subjected to single frequency excitation; adopted from [146].

As mentioned earlier, ordinary materials exhibit the aforementioned classical nonlinear elasticity effects even in the damage-free state as the strain-stress behaviour in most materials is not perfectly

linear. However, in the damaged state, the nonlinear effects are typically orders of magnitude higher [147] than the inherent nonlinearities. These damage-related effects can be evaluated using a class of methods knowns as nonlinear elastic wave spectroscopy (NEWS) [88, 89, 141, 148] by explicitly interrogating the nonlinear elastic response of materials. Cantrell [149] and Frouin [147] showed that the nonlinear parameter β increased with increasing number of fatigue cycles in an aluminium fatigue sample subjected to a single tone ultrasonic excitation, while a number of authors also applied NEWS techniques to other damage mechanisms such as material hardening [150], thermal aging and corrosion [151, 152]. The greater sensitivity of the nonlinear parameter to the defects/damage present in a material as compared to the increase in the fundamental amplitude is illustrated in Figure 3.18 and in Figure 3.19.

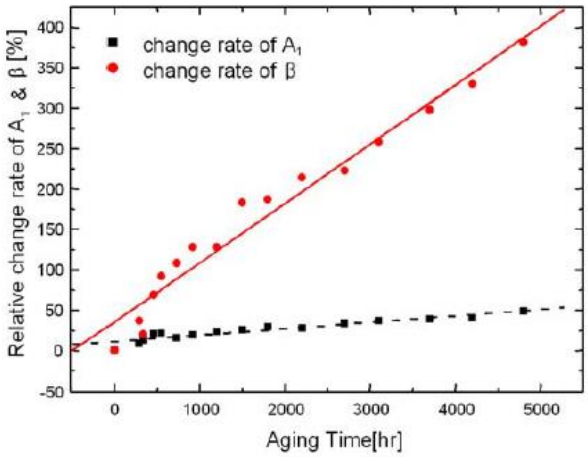

Figure 3.18: % relative rate of change of the fundamental amplitude (A_1) and the nonlinear parameter (β) for an aging material; reproduced from [151].

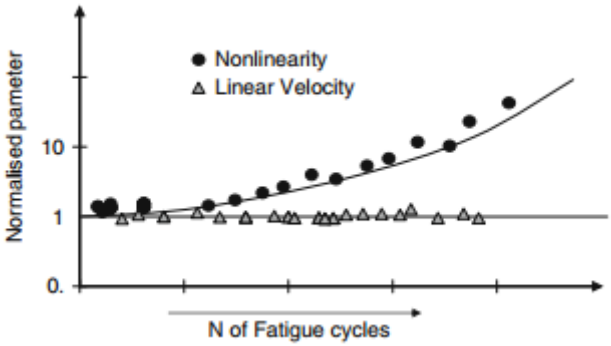

Figure 3.19: evolution of the linear and nonlinear effects in a metallic fatigued sample [153].

In general, the classical nonlinear elastic wave phenomena are characterised by higher harmonics generation in the frequency spectrum response of a material under harmonic loading assuming small strains and the nonlinear stress-strain relation. In case of significantly large strains in a material, harmonics generation can be explained by the presence of geometrical (kinematic) nonlinearities fundamentally arising from the nonlinear strain-displacement relations (Eq. (2.13)-(2.14)) [146];

however, these effects are usually insignificant in solid materials due to relatively low strain levels used in ultrasonic NDT/NDE applications [154]. The nonlinear material response can also be triggered by other physical phenomena such as a dynamic interaction of closed or partially closed surfaces of a crack [155] leading to a number of *nonclassical* nonlinear effects such as *subharmonic generation* [156], *slow dynamics* [146], *resonance frequency shift* [157] and *hysteresis* [158]. These effects are generally considered nonclassical as they cannot be directly explained by the theory of classical nonlinear elasticity addressed in this chapter.

3.4.1.2 Clapping/Rubbing Contacts and Contact Acoustic Nonlinearity

In the previous Section, the nonlinear structural response of a damaged solid material was connected with the high elastic nonlinearity of a local region in the material containing microscale inclusions such as cracks. The existence of non-bonded contact interfaces that are in close proximity to each other is a characteristic feature of such discontinuities, which can be formed by the compressive stresses in the medium. As the surfaces of these defect fragments remain in contact (closed), the impedance mismatch is typically too low for the linear acoustic NDT techniques to be effective, especially if the crack size is comparable or smaller than the wavelength of the probing elastic wave [155]. In presence of the intense acoustic field caused by the structural vibration or the incipient acoustic wave, a range of nonlinear elastic effects may arise at the crack interface which are often collectively referred to as contact acoustic nonlinearity (CAN) [134, 155, 159, 160]. The fundamental mechanisms of CAN are known as *clapping* and *rubbing*, where the former refers to the opening and closing of the contact interface, while the latter one signifies the in-plane motion or the relative sliding of the crack faces. In addition, the crack surfaces can move relative to each other in what is called a *tearing mode*. These modes are generally analogous to the ones of classical fracture mechanics (see Figure 2.4 of Chapter 2.1) and for completeness are summarised in Figure 3.20. Clapping mechanism is sometimes referred to as *kissing* particularly in adhesive joints, where the partial or complete disbond between the adherent surfaces is called a *kissing bond* [146, 161]. Indeed, CAN was also used by Berndt *et al.* [162] in the context of assessing the capability of NDT methods for evaluating the strength and structural integrity of adhesively bonded joints, whereas Hirsekorn [163] provided a theoretical description of the nonlinear acoustic energy transfer in adhesive joints. More recently, Brotherhood *et al.* [164] studied the detectability of dry contact kissing bonds in adhesive joints by means of ultrasonic longitudinal and shear waves evaluating the amplitude change of the fundamental frequency as well as nonlinear β parameter and found that at low contact pressure, the nonlinear parameter provided an indication of the disbond presence, while at larger contact pressure, the linear technique was more effective. A numerical model based on 1D wave propagation in an adherent-adhesive-adherent

structure was presented by Yan *et al.* [165] who reported that the nonlinear parameter was strongly dependent on adhesive thickness-to-wavelength ratio and the geometry of the adhesive layer.

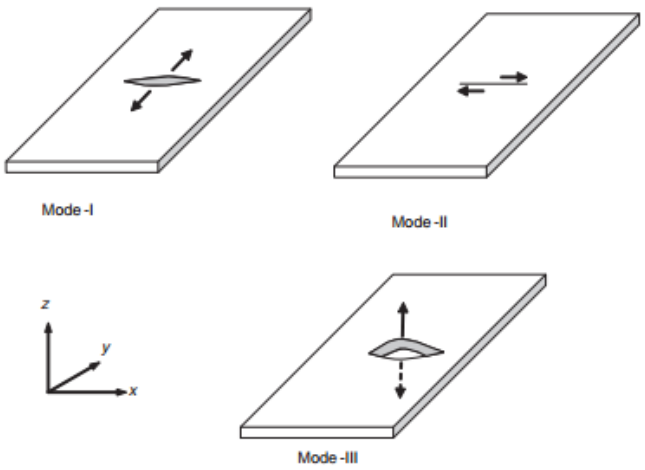

Figure 3.20: classical modes of crack deformation in plates; adopted from [166].

A number of authors [164, 167, 168] have experimentally and theoretically shown that defects characteristic to CAN may be detected and evaluated using alternative acousto-ultrasonic techniques known as nonlinear elastic wave spectroscopy (NEWS) methods [87, 169] that directly interrogate the acoustic nonlinearities arising from discontinuities in the form of parametric instabilities, subharmonic generation and local defect resonance to name a few. Nazarov [170] used a rough crack surface contact model of Greenwood [171] considering nonlinear parameters for a single crack to predict the nonlinear behaviour of cracked solids. More recently, Kim *et al.* [172] and Biwa *et al.* [173] calculated the interface stiffness parameters assuming on a simple power-law relationship between the contact pressure and the corresponding displacement, and subsequently used it to predict the nonlinearities in the transmitted and reflected elastic waves. At present, there is a lack of methodologies for relating the macroscopic acoustic response from the asperities at the crack interface to the surface parameters considering realistic/physical processes at the interface caused by the elastic wave-crack interaction.

The interface between the fractured or debonded surfaces can exhibit some degree of altered residual normal and shear stiffness in compression and/or tension due to the presence of contaminants and/or surface roughness, and therefore, the crack interface may manifest rather complex behaviour during the application of elastic stimulus. However, the behaviour of the defect interface is often approximated using *a bilinear* stiffness considering perfectly flat surfaces [174]. Considering a 1D spring-damper model, the nonlinear stiffness can be represented by assigning two stiffness coefficients based on the strain or displacement values [175]

$$m\ddot{u} + c\dot{u} + k(u)u = f(t), \tag{3.30}$$

$$k(u) = \begin{cases} k_c & \text{if} \quad u < u_1 \\ k_t & \text{if} \quad u > u_2 \end{cases}, \tag{3.31}$$

where u is the displacement at the crack, u_1 and u_2 are the threshold values triggering the opening/closing of the crack, k_c and k_t are the stiffness coefficients in compression and tension. The outlined nonlinear model represents a *breathing crack* (clapping mechanism) which is also known as a *bi-modular* relationship [161] and "*mechanical-diode*" effect – see Figure 3.21.

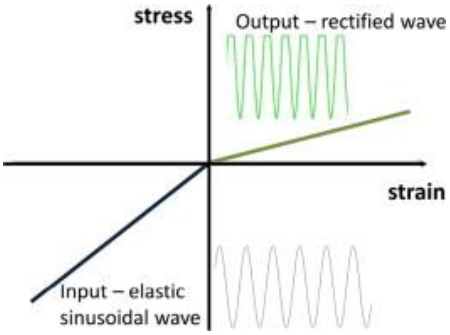

Figure 3.21: bilinear stiffness, "*mechanical-diode*" effect; reproduced from [146].

Indeed, Solodov *et al.* [161] used such a bi-modular stress-strain relation in formulation of 1D anharmonic (nonlinear) oscillator; the asymmetric stiffness combined with the 2nd and 3rd order nonlinear terms led to the generation not merely higher harmonics but also parametric (amplitude dependent) resonance and subharmonic generation which were also experimentally confirmed. Moreover, several studies [176, 177] have shown that the subharmonic generation in CAN phenomena exhibit a threshold behaviour which means that a certain amplitude of excitation must be exceeded in order for the subharmonic frequencies to arise in the response spectrum. Therefore, the asymmetric stiffness alone is not sufficient in order to model the aforementioned effect. Ohara *et al.* [178] and Jhang [135] hypothesised that a subharmonic generation condition exists at a certain level of displacement amplitude, where the output crack surface cannot follow the motion of the input side of the crack due to the inertial effect at the interface. Experimentally and via analytical model based on the 1D nonlinear oscillator, Ohara [178] showed the production of subharmonics in line with the threshold behaviour using a fatigued aluminium sample containing a transverse crack.

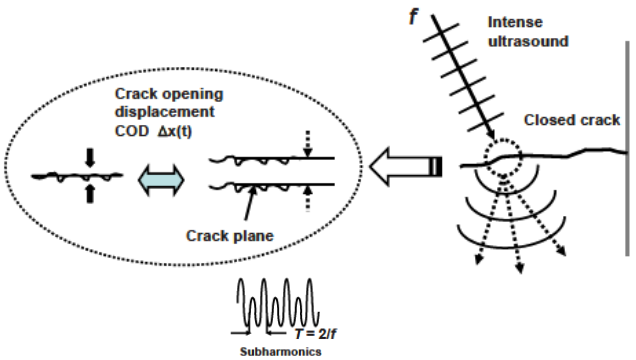

Figure 3.22: subharmonic generation model in closed cracks; reproduced from [178].

Indeed, NEWS techniques for defect detection and imaging based on the subharmonic sensing are advantageous as the resulting spectrum is virtually unhindered by the intrinsic presence of the classical nonlinear effects and instrumentation harmonics [159, 179, 180]. However, certain conditions in terms of the excitation configuration must be met for the subharmonic frequencies to manifest in such a way that allows qualitative and/or quantitative evaluation of the defects at the macroscopic (structural) level. Johnson *et al.* [156] devised a single degreed of freedom crack model based on the dual stiffness (bilinear stiffness) oscillator which indicated that production of subharmonics appreciably increased close to twice the natural frequency of vibration. Wang *et al.* [179] numerically and experimentally confirmed this behaviour using a metallic structure with a fatigue crack by applying the excitation frequency twice the value of the natural mode of the structure; the one dimensional numerical crack model was based on a linear oscillator with a hysteretic crack-related force formulation originally proposed by Delrue and Van Den Abeele [181]. An analytical basis for the generation of the subharmonic frequencies in one dimensional space was provided by Solodov *et al.* [180], while a two dimensional numerical finite difference model was proposed by Yamanaka *et al.* [182], whose crack model incorporated adhesion and atomic related stresses.

In addition to the subharmonic generation modelling, bilinear stiffness of the crack interface was also applied to the *wave mixing* phenomena generally termed *nonlinear acoustic modulation* or *vibro-acoustic modulation* with the corresponding NDE techniques often abbreviated as NEWM (*nonlinear elastic wave modulation*) [177, 183]. It typically involves transmitting a strong low frequency (LF) wave modulating a weaker high frequency (HF) one, i.e. $f_1 \ll f_2$ and $A_1 \gg A_2$. It is hypothesised that in this manner the mixed (combined) elastic wave is able to propagate across the crack with the stronger wave dynamically perturbing the crack surfaces, while the weaker wave passes through the crack without causing any substantial motion of crack faces. The resulting opening/closing of the defect interface tends to cause the distortion of both waves triggering a rather complex nonlinear interaction in this wave-modulation mechanism which is schematically illustrated in Figure 3.23. As can be seen in the figure, the technique leads to a production of combination frequencies and sidebands in the response spectrum. Straka *et al.* [184] used this methodology to evaluate the amplitudes of various spectral components in the intermodulated response in an attempt to relate them to the fatigue life of a metallic sample. He utilised a LF wave at 20-40 Hz and HF wave at 4.7 MHz and reported that the amplitudes of the intermodulated products ($f_2 \pm f_1$ and $f_2 \pm 2f_1$)) were significantly higher after 15,000 fatigue cycles, and also recognised a strong dependence of the intermodulation response on the selection of the LF and HF wave frequencies and their respective amplitudes. Although, the NEWM methods can be used in certain setups as an indication of the overall structural health of a component, they offer little capability of damage localisation especially in cases involving multiple and distributed

defects. Moreover, at present, there seem to be no clear strategy for the selection of the HF/LF excitation frequencies.

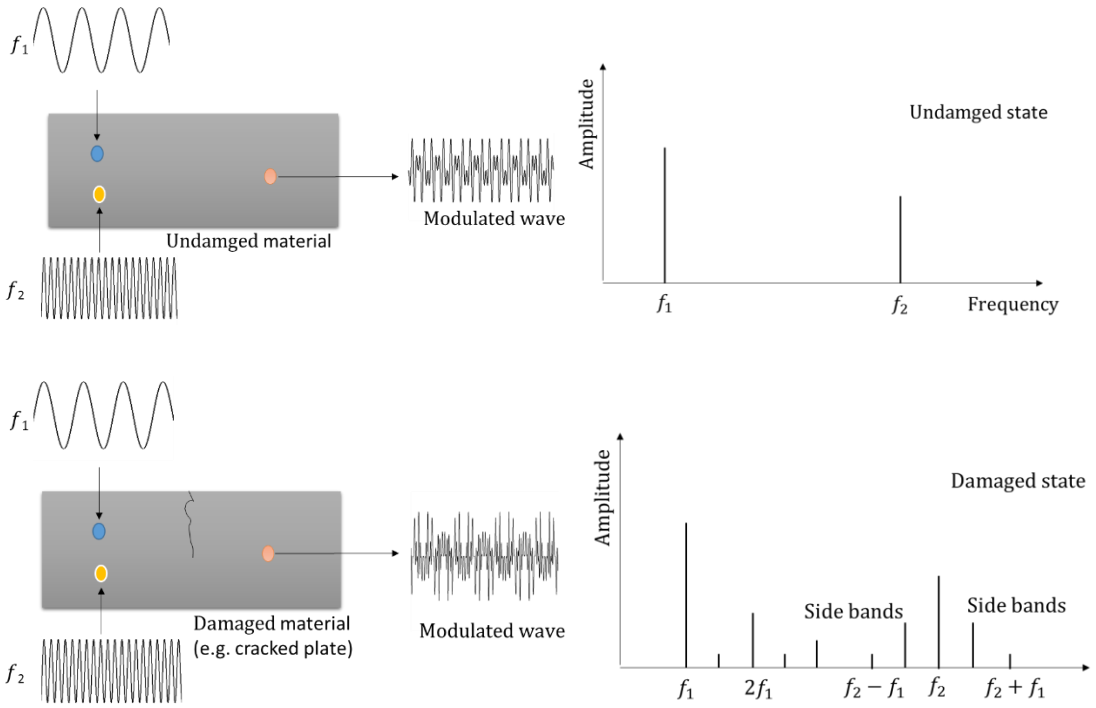

Figure 3.23: schematic representation of the nonlinear acoustic modulation.

Courtney *et al.* [183] used the bi-frequency excitation in conjunction with a crack represented by the bi-stiffness model and obtained several but not all frequency combinations that were experimentally observed. While simple bi-modular functions can be used as a numerically efficient tool in evaluating certain characteristics of the dynamic response of cracked/damaged structures, the physical contact interface of cracks typically contains rough surfaces with deformable (elastically and/or plastically) asperities which is not accounted for in such models. To address these complexities, contact mechanics models are often considered with the simplest one known as the already mentioned (see Chapter 2.2.2.1) *Hertzian contact* based on the *Hertz theory* [37] assuming a contact between two elastic spheres. It relates the indentation depth (*h*) to the loading (*F*) as $h \propto F^{2/3}$ and was used to explain the physical nature of the dynamic nonlinear behaviour in geomaterials by Ostrovsky and Johnson [185]. Indeed, the Hertz theory has been used by a number of authors as a starting point in developing more elaborate contact models involving rough surfaces [154, 186].

Intrinsic to the aforementioned methods is the clapping phenomenon which is one of the mechanisms linked to the hysteretic behaviour observed in cracked materials [187]. Indeed, the presence of cracks in the medium leads to a number of effects such as *hysteresis* and *nonlinear dissipation* which are addressed next.

3.4.1.3 Resonant Frequency Shift

In addition to the generation of harmonics and other nonlinear effects, a nonlinear elastic response of a system can be characterised by its resonant frequency behaving as a function of the drive amplitude. Landau [188] analytically demonstrated that even such a simplified system as a 1D anharmonic oscillator (nonlinear spring-damper) exhibits what is called a *parametric resonance*, which means that the vibration eigenmodes (natural frequencies) are dependent on the amplitude of the driving function. This is not just a hypothetical phenomenon. In fact, a class of techniques called *nonlinear resonant ultrasound* spectroscopy (NRUS) [189, 190] relies on this underlying principle. NRUS typically involves carrying out a set of frequency response measurements by exciting a structure using a frequency sweep function over a certain interval containing known resonance frequencies. The procedure is repeated while sequentially increasing the level of the applied excitation. In the undamaged state, no amplitude-frequency should be evident, whereas the damaged (nonlinear) medium tends to manifest clear relative frequency shift with varying amplitude. To demonstrate this, Figure 3.24(a) shows multiple amplitude-frequency plots for an undamaged resonant PVC (polyvinylchloride) bar, while Figure 3.24(b) presents the results obtained using damaged and undamaged samples made from structural concrete.

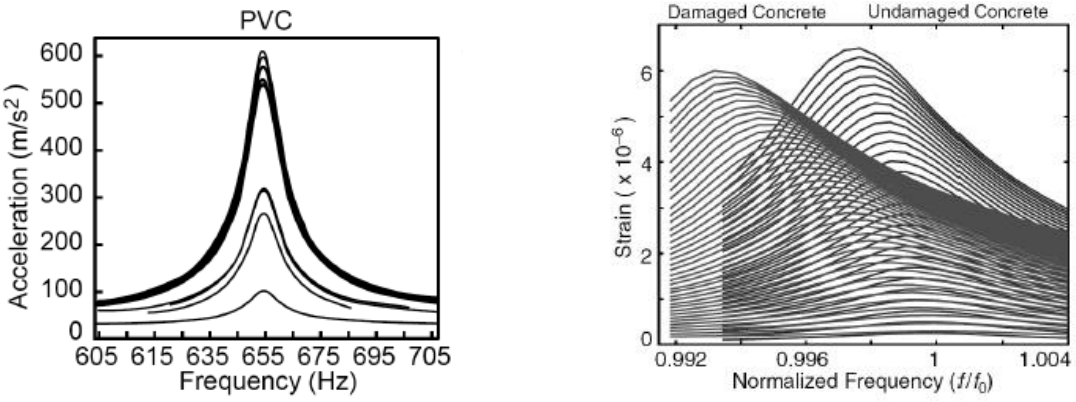

(a) (b)

Figure 3.24: (a) resonance response (acceleration) of PVC beam at a range of drive amplitudes – reproduced from [185]; (b) resonance response (strain) of undamaged and damaged concrete samples normalised to the natural frequency – reproduced from [190].

Johnson [190] defined a *hysteretic* parameter α (typically ranging from 10 to 10^4) by recording the frequency change according to the strain amplitude [190]

$$\frac{f_0 - f_i}{f_0} = \alpha \Delta e_x \qquad \textbf{(3.32)}$$

where f_0 denotes a natural frequency of the intact medium, f_i is the new (shifted) frequency corresponding to each driving amplitude and Δe_x is the mean amplitude of the measured strain.

Downward resonant frequency shift with rising amplitude displayed in Figure 3.24(b) is a behaviour which is typical to the materials exhibiting classical material elasticity as shown by Landau [188] studying the response of the anharmonic resonator with a quadratic and cubic nonlinearities. Therefore, while the resonance frequency shift is largely considered a nonclassical effect [185], it can, in fact, be explained by the classical elasticity theory.

3.4.1.4 Slow Dynamics

Another nonlinear elastic effect which is considered nonclassical is called *slow dynamics* which refers to a slow (seconds to hours) return of the material parameters to the original values following a cyclic excitation of the material [146, 185]. As in the aforementioned phenomena, slow dynamics is associated with the cracked and generally damaged solid materials. The structure is typically excited for several minutes with a relatively large strain ($\sim 10^{-4}$-10^{-5}) in order to induce softening (reduction in elastic modulus) followed by the low strain ($\sim 10^{-7}$) amplitude excitation while monitoring the peak amplitude of a chosen resonant frequency [191]. The experimental setup identical to the NRUS methods can be used in order to evaluate the recovery time which can be used as a parameter specific to the material and its relative structural health [185].

3.4.1.5 Hysteresis, Thermo-Elasticity and Nonlinear Dissipation

Hysteretic nonlinearity, which is characterised by a strongly nonlinear hysteretic stress-strain relation (i.e. loading and unloading curves are different), occurs in heterogeneous materials containing inclusions such as cracks, grain contacts and dislocations at micro and mesoscopic (one to hundreds of μm) level [134]. Figure 3.25 demonstrates this phenomenon considering an example of a uniaxial quasi-static compression test performed on a sandstone specimen. Figure 3.25 (b)-(c) shows that as the stress reaches the maximum point (B) and returns towards zero, the stress-strain path is different in loading and unloading describing a *hysteresis loop*. Furthermore, as can be seen from Figure 3.25 (b), the loading protocol involved local decrease of stress level, which resulted in the smaller inner hysteresis loops, while the main loop was maintained as the strain “kept memory” of the previously attained maximum value – see Figure 3.25 (c).This is a typical indicator of the nonlinear hysteretic behaviour of a material and is referred to as *discrete memory* [144].

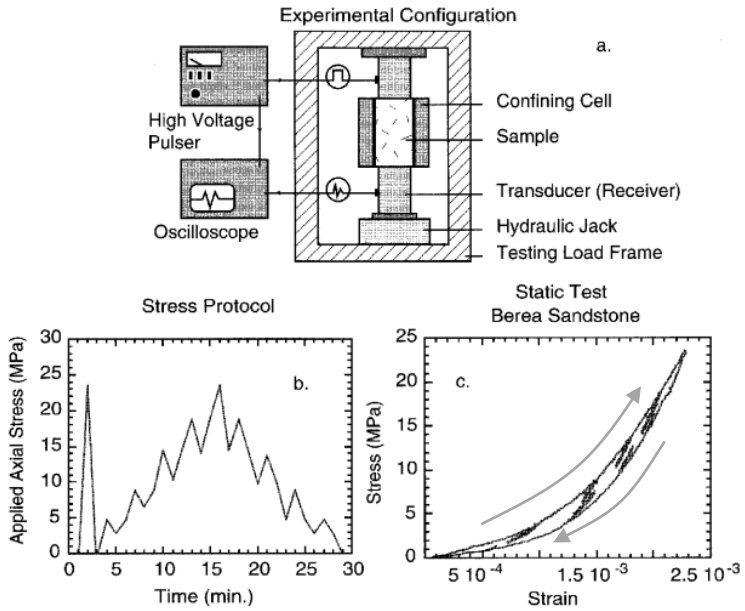

Figure 3.25: (a) test setup for a uniaxial quasi-static compression test performed on a sandstone specimen, (b) loading cycle, (c) stress-strain plot; reproduced from [185].

In general, the hysteretic behaviour of materials strongly depends on the rate, frequency and amplitude of loading [146]. Gist [192] showed that the hysteresis and discrete memory in rocks originate in the bond system, where a collection of "hard" *viscoelastic* grains are assembled in the system of locked bonds and rough contact bonds – see Figure 3.26.

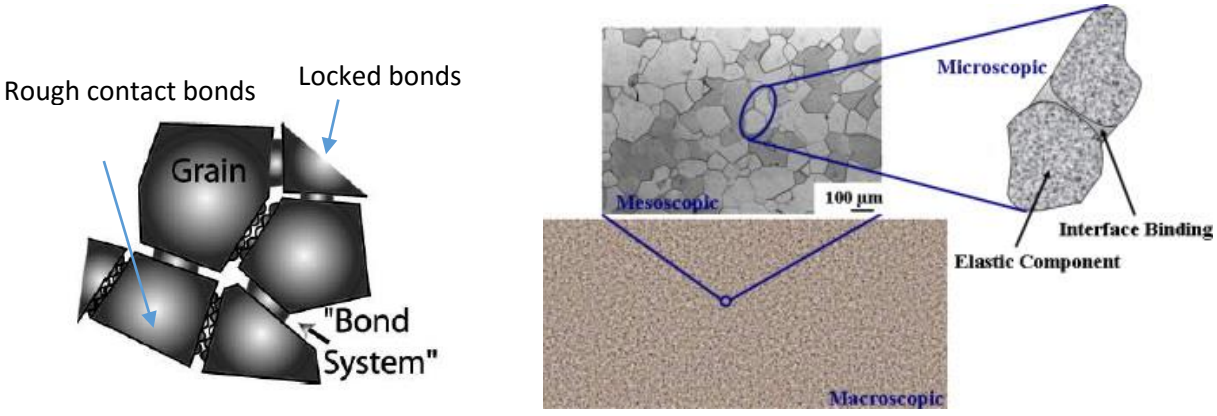

(a) (b)

Figure 3.26: (a) mesoscopic grain and bond system model typical for rocks – reproduced from [144]; (b) multiscale model of a titanium alloy – reproduced from [89].

Similar analogy can be drawn for metals which represent an aggregate system of interconnected crystalline lattice units which exhibit the aforementioned phenomena due to the presence of inclusions, dislocations and cracks at mesoscopic level [193]. Moreover, in layered FRP composite materials, there are inherently large number of cracks, inclusions and asperities at the micro/meso level, and therefore, they also tend to exhibit strong hysteresis [89]. To account for the presence of a large number of distributed hysteretic cells (e.g. grains, crystalline structures etc.), a mathematical

model called *Preisach-Mayergoyz (PM) space* [194] was developed that treats a material as a statistically distributed collection of *hysteretic mesoscopic elastic units* (HMEU). Guyer *et al.* [195] used the basis of the PM space model with a modified version of the classical nonlinear elasticity model (Eq. (3.33)) that includes strain rate term accounting for the hysteretic behaviour [195]

$$K_C = K_0\left(1 + \beta\varepsilon + \delta\varepsilon^2 + \alpha\left[\Delta\varepsilon + \varepsilon(t)sign(\dot{\varepsilon})\right]\right), \quad \textbf{(3.33)}$$

where $\Delta\varepsilon$ is the strain amplitude in the previous cycle, $\dot{\varepsilon}$ is strain rate and other terms have already been defined in Section 3.4.1.1. Zumpano and Meo [89] applied the PM space model along with a constitutive relationship stated in Eq. (3.33) for the numerical validation of a NEWS-based technique for detection and localisation of nonlinear (e.g. damaged regions) in a laminated composite plate by evaluating the amplitude and TOF of the 3rd harmonic generated at the damage location. Indeed, the hysteretic PM space model was shown to lead to the production of strong harmonics of third order ($3f_0$) [146, 189]. The flexibility of the PM space model to associate it with physical mechanisms is advantageous. However, it cannot be readily applied for a single crack as it intrinsically assumes a high number of distributed defects (e.g. micro-cracks). Furthermore, hysteresis models cannot generally explain the nonlinear phenomenon of slow dynamics [146] (see Section 3.4.1.4).

Generally, hysteresis is a known signature of viscoelastic materials which exhibit time-dependent strain relationship. A viscoelastic material that recovers fully after the application of the transient load is often termed anelastic. These effects generally arise due to bond stretching in crystalline solids by the action of internal *deviatoric*[15] *stresses* leading to dislocation motion, which in turn responds with a phase lag between the applied oscillatory stresses (e.g. caused by the ultrasonic stimulation) and the resulting strain [196].

Viscoelasticity and hysteresis is always accompanied by energy dissipation which is typically associated with heat. Indeed, the discussed clapping/rubbing phenomena triggered by the ultrasonic excitation in damaged materials can lead to frictional heating at the crack interface. There is a vast amount of literature that covers frictional heating and contact temperatures [197-202] which can be potentially used to determine the heat generated by damage due to nonlinear ultrasound effects. Klepka *et al.* [166] used the concept of vibro-acoustic wave modulation to study the energy dissipation in a cracked aluminium plate considering three crack modes discussed in the previous Section. Their work indicated a link between several modes and heat generation along with a *nonclassical attenuat*ion of the HF wave with increasing amplitude. The latter effect is addressed later in this Section.

[15] Deviatoric stress acts to change the shape of the media but preserve its volume, while the hydrostatic stress has the opposite effect.

Homma *et al.* [203] suggested an equation for estimating the frictional work (W_f) associated with the ultrasonic excitation as [203]

$$W_f = \mu_k F_N s = \mu_k F_N \int_0^{\tau} |v'(t)| dt \quad \propto \quad \mu_k F_N V' \tau \,, \tag{3.34}$$

where μ_k is the coefficient of kinetic friction assuming dry and clean surfaces, F_N the normal force that presses the defect faces together, s is the total path taken by the cracked faces during time τ and v' is the relative velocity of the crack faces with $v'(t) = V'\sin(\omega t), \omega = 2\pi f.$ Eq. (3.34) is based on the well-known Coulomb's law of friction which assumes that the frictional force mutually exerted by each surface is in independent of the sliding velocity. In practice, both the normal force and the coefficient of frictional can be dependent on the eigenmodes of vibration, the level of adhesion, surface roughness, relative deformation and contamination of the cracked surfaces. Furthermore, according to the study of tribology [204], the consequence of the work of frictional forces especially in the regions of elevated temperature can be wear [203], which can in turn lead to stiffness degradation and generally altered system response.

Friction is merely one possible mechanism of heat generation and energy dissipation. A number of thermosonic NDT methods [205, 206] rely on the conversion of mechanical energy at the damage location into heat through *thermo-elastic effects* induced by the piezoelectric transducers or welding horns. According to the classical thermoelastic relationship, linear homogeneous elastic bodies under adiabatic conditions experience a temperature change induced by the accompanying stress change [207]

$$\Delta T = \frac{T}{\rho C_p} \sum_i \frac{\partial \sigma_i}{\partial T} \, \Delta \varepsilon_i; \quad with \; i = 1, \dots, 6, \tag{3.35}$$

where T is the absolute temperature, C_p is the specific heat at constant strain, ρ is the mass density, σ_i and ε_i are the stress and strain components, respectively, referred to a system of Cartesian coordinate axes. The concept of thermoelasticity is central to a class of linear stress measurement and NDT/NDE techniques called *thermoelastic stress analysis* (TSA). Emery and Dulieu-Barton [206] applied this concept to study strain distribution in the vicinity of delamination in laminated GFRP composite coupons and showed that the method could be used to provide an indication of fatigue damage accumulated by the composite components.

To conclude this Section, it is worth mentioning another interesting nonclassical nonlinear phenomenon called *Luxemburg-Gorky (LG) effect* [208] leading to a type of cross-modulation between LF and HF waves very similar in its response spectrum to the effect seen in NEWM experiments (see

Figure 3.23). First reported and theoretically studied by Ginzburg [208], this effect was originally observed in two European cities as a transfer of a modulated radio wave (LF) from a powerful radio station to another carrier wave (HF), which was understood to be caused by the variations of absorption in ionosphere plasma induced by the stronger wave which in turn resulted in pronounced amplitude modulation of the weaker wave. In this process, the HF wave is damped by a LF wave. Zaitsev *et al.* [209] hypothesised that an acoustic equivalent of LG effect can exist in cracked solid media which is induced by a kind of thermo-elastic *nonlinear dissipation* local to crack interface that is not associated with clapping/rubbing, hysteresis and friction; they have ruled out the contribution of these effects through carefully controlled experiments. One of the main aspects of the experimentation procedure was that it was carried our using very small strain amplitudes ($\sim 10^{-7}$-10^{-9}) which were not sufficient enough to cause crack opening/closing as the displacements at the crack interface did not exceed atomic size [209]. Similar evidence and explanation of nonlinear dissipation paralleled with LG effect was also reported by other authors [166, 210]. Aymerich and Staszewski [210] applied the concept of the acoustically-induced LG effect in an attempt to use the spectrum components of the cross-modulated signal for impact damage detection in composite materials. The work showed that the amplitude of the sidebands of the HF wave (probing wave) increased with increasing delamination area and could be potentially used as an indication of damage extent. However, the method suffered from the influence of nonlinearities intrinsic to the system (e.g. boundary conditions, clamping locations, transducer positions etc.).

3.4.1.6 LDR

In addition to the already mentioned classical and nonclassical nonlinear elastic wave phenomena, a class of nonclassical effects called *local defect resonance* (LDR) was experimentally observed and investigated [157, 211]. In essence, the LDR is based on the premise that inclusion of a defect in a material results in a local rigidity decrease of a certain mass associated with the defect area which in turn should lead to the manifestation of a specific frequency, characteristic of the defect [157]. Unlike the resonance of the whole specimen, an efficient generation of harmonics and wave mixing can be achieved even at moderate input signal levels by exciting a specimen at the LDR frequency associated with the defect [157]. A successful application of this technique requires a definitive identification (analytically, numerically or experimentally) of the defect resonance frequency, which can be analytically estimated for certain artificial defect types such as flat bottom holes (FBH) [212]. More specifically, the LDR corresponds to an interaction of acousto-ultrasonic waves with the damage/defect at a frequency matching the defect resonance, which in turn tends to result in a considerable amplification of local vibration amplitude in the damage region. Several recent studies showed the application of the phenomenon of linear and nonlinear LDR in non-contact NDE techniques for the detection of artificial defects in metals and composite materials using digital shearography [213], and in detection of impact-induced delamination in CFRP and GFRP composite materials using the LDV imaging [157]. Furthermore, as explained in Section 3.4.1.3, the amplitude-dependent dynamic resonance frequency shift occurring locally to the defect area can be used as an indication of the severity of the damage [157]. In terms of LDR, this effect occurs locally to the defect, which contrasts the NRUS methods [189] in the sense that NRUS works on the principle that the resonance frequency of the whole structure shifts as the strength of the nonlinearity increases in a damaged material. However, the locality of LDR is an advantage as well as a detriment. Although, the concept of LDR showed promising results in some non-contact NDE applications [214], where the detector in the form of digital camera or LDV focused exclusively on the damage area, the use of LDR in contact applications (e.g. using piezoelectric transducers) is still limited. This implies that the LDR-enhanced nonlinear damage response can be sensed merely at the defect location. In real world structures, where the damage location and its characteristics are unknown, the determination of the LDR frequencies is problematic.

3.5 Conclusion

In this chapter, the linear NDT/NDE techniques were introduced first. The linear ultrasound-based NDT is currently the major method used across many industries as it enables relatively short inspection times while providing a direct relation of the measured physical quantities (e.g. impedance, reflections etc.) to the size and location of a damage/defect present in a structure. However, this approach has proved rather ineffective in discerning the low level defects (e.g. closed cracks, disbonds etc.) characterised by low acoustic impedance sources. A class of NDT/NDE techniques called NEWS has shown a great potential at overcoming this limitation. As explained in the preceding Sections, the presence of microscopic, mesoscopic and macroscopic damage in a material results in some type of nonlinear relationship between the applied dynamic stimulus and the subsequent response of the structure. Subharmonics, higher harmonics and vibro-acoustic intermodulation can be used as signatures of the nonlinear damage-related behaviour potentially enabling effective damage detection. Incipient elastic waves and structural vibration cause these effects to arise at the crack interface. Several crack-wave interaction modelling techniques were addressed as the numerical simulations of the associated nonlinear effects can provide further understanding of the phenomena and increase the reliability of NEWS methods. The bilinear stiffness models were shown to be capable of representing a single crack while qualitatively explaining some of the nonlinear effects such as harmonic generation and frequency mixing. However, they do not directly account for the physical structure of the crack, poorly explain the phenomenon of slow dynamics and generally do not consider the hysteretic behaviour of materials. Hysteresis-based models proved effective at explaining the generation of 3rd harmonic, frequency mixing and natural frequency shift; PM space approach can be used to qualitatively represent multiple distributed micro-cracks in a structure but has shortcomings similar to the ones stated for the bilinear stiffness models in terms of slow dynamics and physical crack structure. On the contrary, the rough surface contact models have a potential to cover a range of physical phenomena taking into account the real shape of the crack but generally result in extremely complex modelling.

Another nonlinear effect, termed nonclassical dissipation, was mentioned which may explain the nonlinear phenomena such as slow dynamics, modulation of waves at small strains and the acoustic LG effect. However, the mathematical modelling of this effect is very challenging. Although, some evidence of an acoustic equivalent of the LG effect exists in published literature, the physical explanation of this phenomenon and indeed the nonclassical dissipation in the field of acoustics/NDT is not clear. Whilst the elastic wave-crack interaction and possible acousto-vibrational responses have been extensively studied and reported over the past decades, an in-depth physical understanding of the generation of these effects is incomplete and requires further scientific research and analysis.

Having discussed damage mechanics and damage detection techniques, several nonstandard composite layups will be considered from the perspective of damage resistance by means of LVI testing and FEA, and therefore, the concepts introduced in Chapter 2 will be used throughout in the succeeding Chapter. Moreover, the concepts presented in both preceding chapters will also be shown to be relevant in the context of NDT/NDE work presented in Chapter 5.

4 Dynamic Response and Damage Tolerance of Bio-Inspired FRP Laminates

4.1 Introduction

In structural sense, natural materials are incredibly efficient, satisfying a wide range of often competing requirements such as strength and toughness, while utilising as little amount of material as possible. Practically, all natural materials are composites comprised of rather limited selection of constituents such as collagen, keratin and fibroin proteins [215]. Characteristic dimensions of these bio-structures range from nanoscale to macroscale and they typically consist of hard and soft segments organized in complex hierarchical architectures and therefore have proven challenging to replicate synthetically [216].

It took hundreds of millions of years of convergent evolution for nature to create multifunctional dermal armour present in fish (e.g. Arapaima gigas and Coelacanth), reptiles (e.g. crocodilian and squamata), and mammals (e.g. armadillo and pangolin) [217]. It usually consists of hierarchical structures with collagen fibres linking rigid steoderms (scales) for enhanced flexibility while marinating strength properties [218]. These structures serve a range of purposes such as body protection, thermal regulation, coloration for supressing intra-species recognition and decreasing hydrodynamic drag in fish, thereby making these materials multifunctional by nature [219]. The shapes and forms of these natural protection units vary but they all exhibit several common characteristics of relatively low density / light weight, high strength, capacity for energy absorption and conformance to the body shape in order to facilitate rapid motion and agility. For example, scales of fish are typically comprised of a combination of a rigid protective external layer and a flexible internal one providing mobility and effective load distribution [217].

Evidently, it is important to study these creatures with naturally occurring armour as it can lead to fabrication of synthetic structures mimicking the advanced mechanical architectures of their natural counterparts. One particularly interesting feature of naturally strong materials, which is a subject of this study, is a helicoidal arrangement present in several strong and damage-resisting creatures. Bouligand [220] studied the existence of twisted morphologies in various Crustaceans by observing the bow / arc-shaped fibrous patterns using electron and light microscopy. In close examination of these transverse cross-sections, Bouligand concluded that these periodic patterns are in fact formed by stacked laminae of aligned fibres with each layer rotated by a small angle relative to the previous one producing a twisted (helicoidal) arrangement.

A number of biological systems reveal a twisted laminated structure, however, one of the most remarkable ones incorporating such a configuration is mantis shrimp or stomatopods which is an ancient member of an order of crustaceans, Stomatopoda - Figure 4.1 shows the mantis shrimp highlighting its biological hammer.

Figure 4.1: an Odontodactylus scyllarus which is also known as peacock mantis shrimp; reproduced from [59].

Dactyl clubs of the stomatopods are adapted for withstanding many thousands of high velocity (over 20 m/s) impacts on sea shells and other prey on which they feed [221]. The micro and macro mechanical characteristic of dactyl clubs reveal a range of impact-resisting characteristics not seen in other damage-tolerant bio-composites such as shells [27, 222]. Hammer-like clubs of mantis shrimp have a virtually constant and well defined point of impact which has been biologically optimized for damage resistance [27]. They are formed of multiphase composite incorporating oriented crystalline hydroxyapatite and amorphous calcium phosphate arranged into a highly expanded helicoidal organization containing fibrillar chitinous organic matrix; a structural combination of these elements acts as an effective line of defence preventing a catastrophic failure during repetitive high-energy loading events typically exceeding 200 N [222]. The club is comprised of a hard impact region (about 1 mm thick) exhibiting higher Young's modulus, higher strength, and a periodic (helicoidal) region (2-3 mm thick) of much lower and oscillating modulus of elasticity, where chitin fibres are stacked forming a twisted configuration, whereby each layer has fibres oriented parallel to each other and every layer is rotated to a certain pitch angle relative to the layer underneath resulting in a Bouligand structure [222]. Figure 4.2 illustrates the main features of the dactyl clubs including its two-phase architecture and the oscillating elastic modulus.

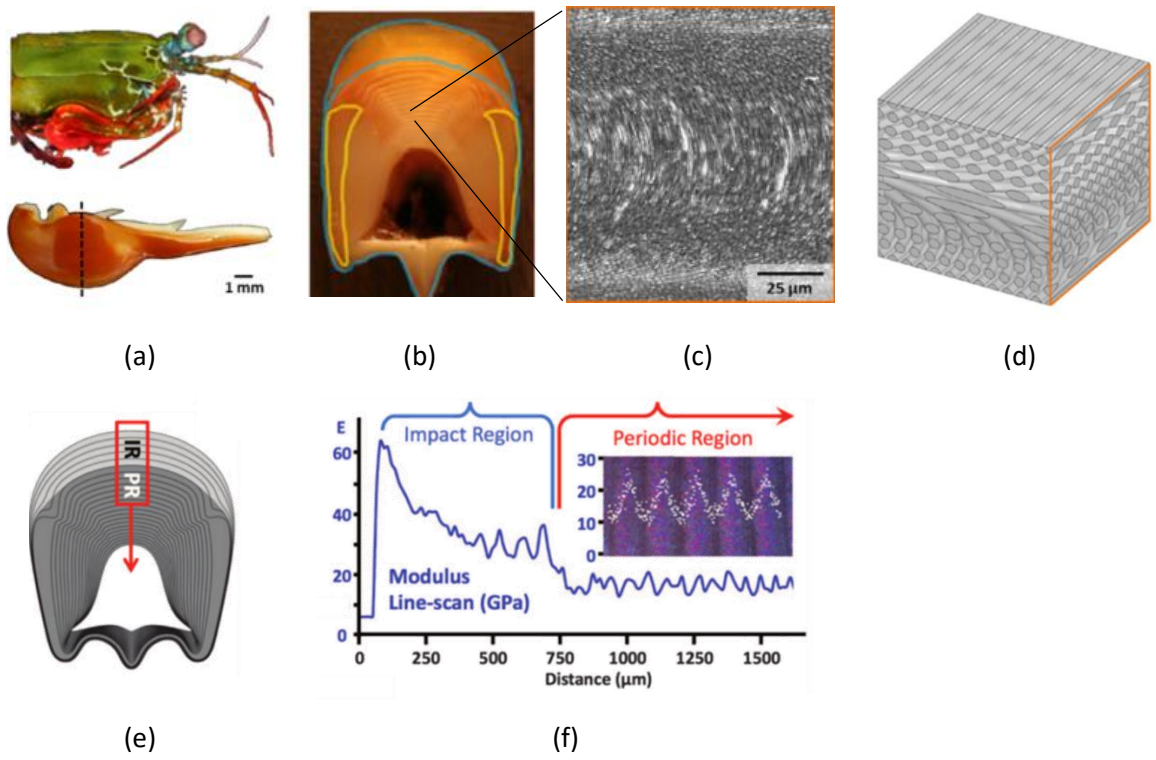

Figure 4.2: (a) an image of Odontodactylus scyllarus and its dactyl club, (b) and (e) a photograph and a schematic of a cross-section taken through the dactyl club revealing its two-phase organisation, (c) a SEM image of a section through a single period of the periodic zone depicting a characteristic nested arc pattern, (d) a 3D schematic visualisation of the Bouligand structure clarifying the origin of the nested arc pattern, (f) elastic modulus scan of the impact region (IR) and the periodic region (PR); (a), (b), (c) and (d) – reproduced from [223]; (e) and (f) – reproduced from [222].

A two phase organization is not exclusive to stomatopods. One of the largest freshwater fish, Arapaima gigas has scales with characteristic dimension of 50–100 mm and are composed of an external highly mineralized layer with ridges and an internal layer of collagen fibres in orientations describing a helicoid or Bouligand architecture [218]. This structure is also found in one of the oldest and rarest surviving orders of fish, coelacanths [224]. Weaver *et al.* [222] explained that this hard-soft two phase organisation is effective in arresting the crack-propagation during impact - a crack approaching the impact surface encounters an elastic modulus mismatch which can either be deflected at the interface or propagated through the stiffer region [222].

There are many more examples of helicoidal structures present in nature such as the osteons in mammalian bones [225], certain plant cell walls, various insect cuticles [226] and DNA structure. Motivated by these examples, several authors have studied the applicability of these twisted laminae arrangements to conventional design of laminates using plates manufactured from various fibre-reinforced composite pre-pregs [223, 227-229]. In all the studies, unidirectional composite plates consisting of aligned fibre layers/plies mimicking those observed in the crustacean exoskeleton were fabricated and examined under a range of loading conditions. A helicoidal lamination sequence/layup is readily achieved by stacking of unidirectional layers with a gradual change in ply orientation from

layer to layer. Changes in ply orientation are known to influence the toughness and strength of composite materials by altering damage mechanisms and propagation [230]. Motivated by Bouligand structure observed in beetle exoskeleton, Chen *et al.* [226] reported that fracture toughness of glass fibre-reinforced composites is significantly higher for helicoidal layup compared to that of a unidirectional control under static loading conditions. Apichattrabrut and Ravi-Chandar [227] performed tension, bending and high-velocity impact (HVI) tests along with simplified finite element analysis (FEA) in an attempt to characterize an arbitrary helicoidal layup versus unidirectional and cross-ply laminates using carbon/epoxy pre-pregs. Helicoidal architecture showed improved debonding resistance and higher energy absorption facilitating penetration resistance in comparison to control cross-ply layups. Most recently, Ngern *et al.* [229] reported on damage resistance of helicoidal compared to cross-ply composites comprised of carbon/epoxy under ballistic impact loading. The results for the helicoidal configuration yielded higher ballistic limit for smaller inter-ply angle with larger delamination area providing a mechanism for energy absorption during impact loading. Inspired by the twisted architecture of the periodic phase observed in dactyl clubs of stomatopods, Grunenfelder *et al.* [223] explored several helicoidal layups differencing in inter-ply angle against a quasi-isotropic laminate by means of experimentation as well as nonlinear explicit FEA. Through LVI and CAI testing, helicoidal composites retained higher residual strength compared to quasi-isotropic control samples [223]. However, they utilised layered shell elements with Hashin failure criteria, and therefore, the delamination could not be captured.

Past studies focused on comparing helicoidal layups against unidirectional, cross-ply and quasi-isotropic ones considering FRP composite plates under static and dynamic loading. This study is an effort to expand that knowledge by examining the structural behaviour of twisted composite configurations arranged in plates of various width-to-thickness ratios. The hypothesis here is that the helicoidal composites should show more enhanced performance with the increasing width-to-thickness ratio as they would have relatively larger area to dissipate the energy in the in-plane directions. First, the possibility of using FE shell elements for simulating LVI on helicoidal composites is considered. This is followed by a more advanced FEA approach involving material model MAT162. Cross-ply and quasi-isotropic layups were used as controls because both of these configurations are considered a standard in the aerospace industry especially in applications requiring damage-tolerance capabilities. Dynamic loading via LVI events with impact energies of 40 J and 80 J as well as CAI testing were used for the investigation. Experimental campaign reported herein was primarily carried out in order to validate a progressive FEA approach used for further analysis involving LS-DYNA® and MAT162.

4.2 Preliminary Numerical Simulations Using Finite Element Shells

As explained in Chapter 2, various experimental and numerical methods can be used in order to examine a dynamic structural behaviour of FRP laminates. However, before commencing an experimental study, FEA can be employed as a flexible and robust numerical approach to simulating the structural response. Thus, the methodology reported by Heimbs *et al.* [51] was followed in this work in order to carry out several LVI simulations using LS-DYNA®. Their numerical test involved impacting the clamped quasi-isotropic ($[-45°/0°/+45°/90°]_{3s}$) CFRP panel comprised of UD prepreg layers with a steel impactor at an energy level (30-40 J) sufficient to cause internal damage but not catastrophic failure (i.e. perforation). The simulations showed good correlation with the experiments in terms of contact force, energy and the damage prediction. However, the results were reported to be highly dependent on many simulation parameters such as the ones associated with the contact algorithm treatment. Nevertheless, as Heimbs *et al.* [51] validated their FEA model and reported all the required simulation settings, their approach was replicated and used in the present study as a baseline for evaluating a helicoidal layup.

Subsequently, a helicoidal layup $[180/165/150/135/120/105/90/75/60/45/30/15]_s$ with a rotation angle of 15˚ was compared against the baseline in terms of incurred damage extent. The choice of the pitch angle was driven by the requirement for the mid-plane symmetry and constraint on the number of plies (i.e. 24) which were characteristic features of the baseline model reported by Heimbs *et al.* [51]. Figure 4.3 depicts a schematic of the numerical LVI test setup.

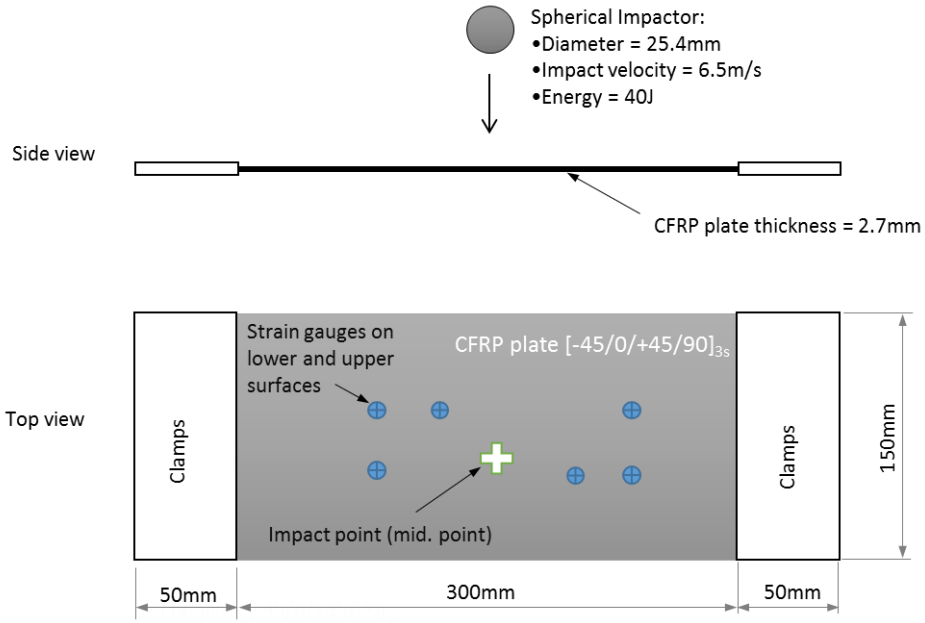

Figure 4.3: LVI test setup; adopted from Heimbs *et al.* [51]

4.2.1 Numerical Modelling

The FE model was developed using LS-PrePost software which is an advanced pre- and post-processor supplied free with LS-DYNA®. The resulting model comprised the discretised (meshed) CFRP plate and the impactor using quadrilateral FE shells which is a reasonable approach taking into account that the thickness of the plate was significantly smaller than its length and width. This is consistent with the underlying assumptions of FSDT which these FE elements are based on. The FE mesh with an element side of 3 mm was chosen for the CFRP plate model, while 1 mm mesh size was used for the Impactor based on the published data [51]. Figure 4.4 shows the meshed FE model.

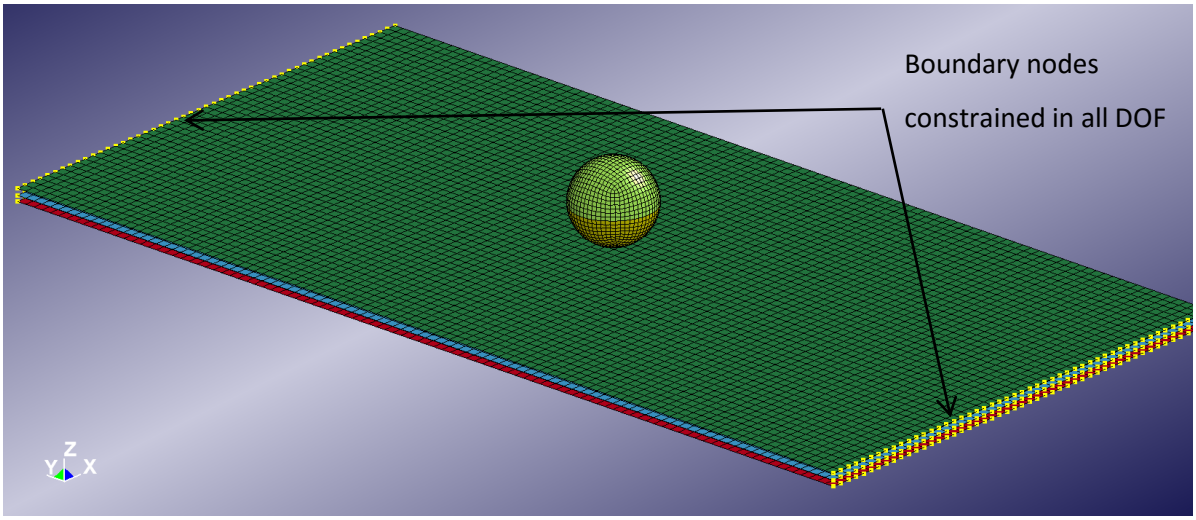

Figure 4.4: computational mesh used for the LS-DYNA® simulations

The Impactor was modelled as a sphere meshed using standard shell elements; the properties of standard structural steel (ρ = 7.83 g/cm^3, E = 207 GPa, ν = 0.33) were assigned to the model using elastic isotropic material model available in LS-DYNA®.

The plies were modelled using 2D layered shell elements which is computationally less expensive than using 3D solid (brick) elements. Composite plate was modelled using element formulation 2 (ELFORM=2) which is underintegrated Belytschko-Tsay shell element type; hourglass control set to 4 (IHQ=4). These parameters were chosen based on the reported [51] recommendations for achieving optimal numerical stability for this type of simulation. In each layered shell element, sub-layers (i.e. plies) can be defined. A constitutive relation is evaluated at each integration point representing each ply of the shell element. Hence, all plies were defined as individual integration points with their respective orientation angles and thicknesses using PART_COMPOSITE card available within LS-PrePost. It is also important to note that only 3 layers of FE shells with 8 integration points per layer were modelled in order to maintain numerical stability and reduce the computation time when using the chosen element formulation and the material model - Figure 4.5 schematically shows this concept.

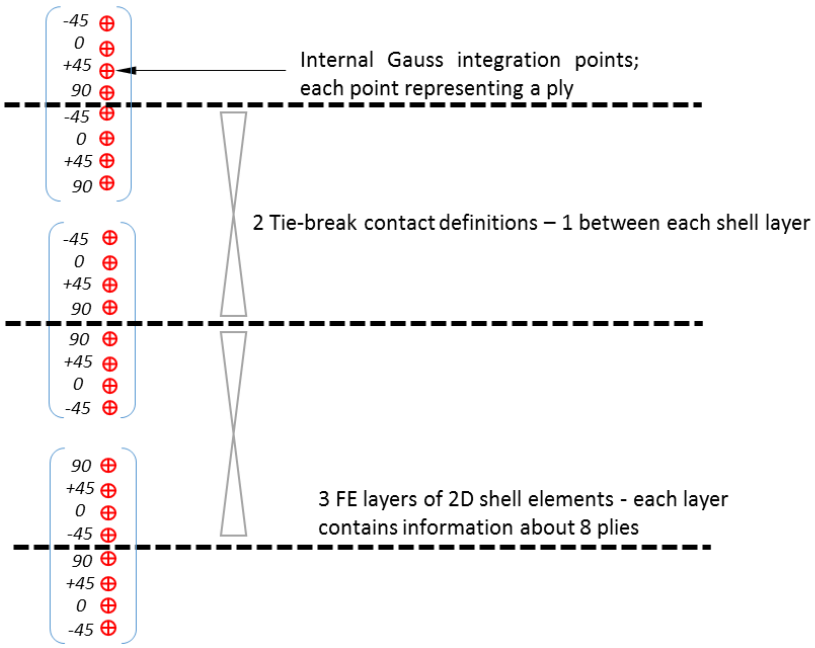

Figure 4.5: schematic representation of FE shell element layers and integration points used for the analysis.

Following the methodology of Heimbs *et al.* [51], MAT54 (MAT_ENHANCED_COMPOSITE_DAMAGE) was used in this study, chosen as the constitutive material model for simulating the structural behaviour of the CFRP plate.

MAT54 is an orthotropic elastic material model with implemented Chang-Chang [231] damage criteria corresponding to the four failure modes

Tensile fibre mode (fibre rupture) $\sigma_{11} \geq 0$:

$$f_1^2 = (\frac{\sigma_{11}}{XT})^2 - 1 \begin{cases} \geq 0 \; failed \\ < 0 \; elastic \end{cases};$$

Compressive fibre mode (fibre buckling) $\sigma_{11} < 0$:

$$f_2^2 = (\frac{\sigma_{11}}{XC})^2 - 1 \begin{cases} \geq 0 \; failed \\ < 0 \; elastic \end{cases}; \quad \textbf{(4.1)}$$

Tensile matrix mode (matrix cracking under transverse tension and shearing)

$$f_3^2 = (\frac{\sigma_{22}}{YT})^2 + (\frac{\tau}{SC})^2 - 1 \begin{cases} \geq 0 \; failed \\ < 0 \; elastic \end{cases}; \quad \textbf{(4.2)}$$

Compressive matrix mode (matrix cracking under transverse compression + shearing):

$$f_4^2 = (\frac{\sigma_{22}}{2SC})^2 + \frac{\sigma_{22}}{YC}\left[\frac{YC^2}{4SC^2} - 1\right] + (\frac{\tau}{SC})^2 - 1 \begin{cases} \geq 0 \; failed \\ < 0 \; elastic \end{cases}. \quad \textbf{(4.3)}$$

The failure criteria stated in Eq. (4.6)-(4.3) are based on the local stress field of the finite elements, while sometimes it is also desirable to limit the strains and this option is available in MAT54 by specifying the values of DFAILT, DFAILC, DFAILM, DFAILS; the critical strain parameters used for the simulations are given in Table 4-1.

DFAILT	0.017	*Maximum strain for fibre tension*
DFAILC	0.0135	*Maximum strain for fibre compression*
DFAILM	0.1	*Maximum strain for matrix (tension and compression)*
DFAILS	0.03	*Maximum shear strain*

Table 4-1: description and values of the failure strains used for composite material model MAT54 [51].

In case any of the four Chang-Chang criteria are met, stresses are kept at constant level until the failure strains are exceeded, at which point a ply at the integration point of the corresponding element is assigned zero stiffness, and can no longer carry any loads. Material properties used for the definition of MAT54 are presented in Table 4-2. LS-DYNA® User Guide [79] can be referred for further details of the constitutive model MAT54.

ρ (g/cm^3)	E_{11} (GPa)	E_{22} (GPa)	G_{12} (GPa)	ν_{12}	XT (MPa)	XC (MPa)	YT (MPa)	YC (MPa)	SC (MPa)	G_{IC} (J/m^2)	G_{IIC} (J/m^2)
1.6	153	10.3	5.2	0.3	2540	1500	82	236	90	225	640

Table 4-2: CFRP material properties specified for the composite material model MAT54 [51].

In the above table, ρ, E_{11}, E_{22}, G_{12} and ν_{12} have their usual meanings, whereas XT, XC, YT, YC and SC refer to maximum tension (XT, YT), compression (XC, YC) and shear (SC) in-plane stresses; G_{IC} and G_{IIC} are the energy release rates in mode I and mode II respectively.

As discussed in Chapter 2.1, delamination is an important composite damage phenomenon and can act as an energy absorption mechanism. LS-DYNA® is capable of simulating delamination by means of both cohesive zone represented by 3D 8-node solid elements connecting the opposite surfaces as well as using tie-break contact algorithms. The former method leads to a substantially higher computational effort due to the physical presence of cohesive elements in the FE mesh. Hence, a tie-break contact card was used in LS-DYNA® to simulate crack propagation and debonding of layers during low velocity impact test. This algorithm is based on the cohesive zone model of delamination devised by Borg [232] (OPTION=8) in which the opposing layers of shell elements are virtually "tied" together without the need for placing the discrete elements between them. The tie-break contact card requires a user input of normal failure stress (NFLS), shear failure stress (SFLS) and critical crack opening length (CCRIT) which can be obtained from DOB testing. The energy release rates due to normal and shear interface failures are approximated by

$$G_{IC} = \frac{1}{2} \times NFLS \times CCRIT, \quad (4.4)$$

$$G_{IIC} = \frac{1}{2} \times SFLS \times CCRIT. \quad (4.5)$$

Once normal and shear failure stresses are reached, damage is a linear function of the two points initially in contact; the contact is then released as soon as CCRIT parameter is met and the contact between surfaces is treated using standard non-penetrating surface-to-surface penalty stiffness contact algorithm of LS-DYNA®.

4.2.2 Results and Discussion

The extent of delamination was visualised at the final simulation step for each plate by plotting the *contact gap* parameter of INFOR database which records the occurrence of separation between the tied elements. The outcome is shown in Figure 4.6.

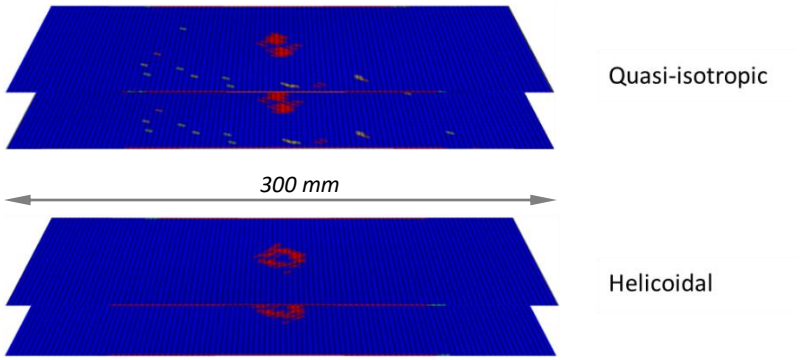

Figure 4.6: the extent of the delamination between the shell layers as predicted using tie-break contact of LS-DYNA®.

Evidently, the quasi-isotropic laminate exhibited a delamination resembling a peanut shape which is typical for such layups [30]. On the contrary, the helicoidal plate experienced the delaminations which are more circular and spread out in nature than the quasi-isotropic ones. The difference in the overall area of separation between the layups was relatively insignificant which was approximately 5% lower in a helicoidal one. It is important to note, however, that physical representation of the delamination phenomenon was limited in this study due to the fact that only 3 shell layers were modelled and therefore only two tie-break contacts were defined. Furthermore, Heimbs *et al.* [51] reported that defining more shell layers (e.g. 5 and more) with increasing number of tie-break contact between them resulted in numerical instabilities which ultimately limits the extent to which the delamination can be modelled in the overall approach involving shell elements.

In addition to tie-break, four damage modes were considered by means of MAT54 and the results for each mode were visualised during the post-processing. It was found that both configurations failed only in mode 3 which is a tensile/shearing matrix failure – see Eq. (4.2). This is expected as this failure mode relies on the maximum shear (SC) and transverse tensile (YT) strengths which are the lowest strength values as presented in Table 4-2. The results of transverse matrix damage are shown in Figure 4.7.

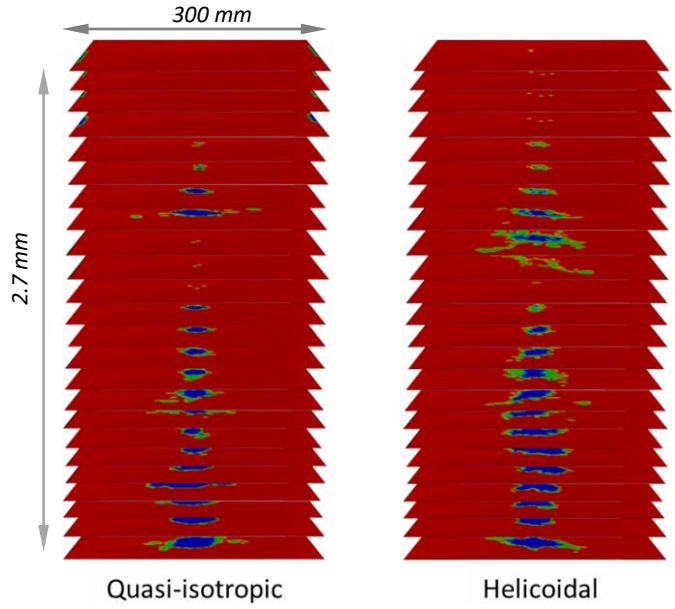

Figure 4.7: the extent of transverse matrix failure plotted at each integration point as predicted by the MAT54 material model of LS-DYNA®.

As it can be seen from Figure 4.7, the overall damage distribution is similar in both configurations characterised by the transition from being minimum in the top layers (compression) and maximum in the bottom ones (tension), although, the total damage area was approximately 5% higher in the helicoidal one.

4.2.3 Conclusion

A significant cause of the delamination in composites is believed to be due to high intralaminar stresses which are particularly high in layups comprised of layers with abrupt changes in fibre direction. The extent of the delamination was slightly lower in the helicoidal composite configuration, which displayed higher tensile matrix failure distribution compared to the quasi-isotropic case. Although the presented modelling approach can be used to study the effects of layup configurations on the global mechanical response of the laminated composite materials, it has several disadvantages such as:

- Finite element shells are based on CLPT and FSDT which make simplistic assumptions about the transverse shear stress field, and therefore, provide a limited capability in capturing inter-laminar shear stresses which are of high importance in laminated composite materials
- Only a limited number of tie-break contacts can be employed for a single plate simultaneously
- The 2-D stress field of the material models using finite element shells is not sufficient for capturing the complex and coupled nature of composite failure modes

Consequently, a more elaborate modelling approach is required in order to further study the dynamic response and damage tolerance capabilities of the helicoidal composites. Therefore, the subsequent Section provides a more comprehensive approach that involves a numerical modelling of LVI as well as CAI tests.

4.3 LVI and CAI Simulations on Helicoidal Composites

Considering the shortcomings of the FE shell elements in modelling LVI tests, solid elements along with the constitutive material model MAT162 were utilised in order to further study the damage resistance and energy absorption capabilities of the helicoidal layups. Two control and three helicoidal laminates were considered. The following Section explains the important aspects of layup selection.

4.3.1 Layup Consideration

The choice of lamination sequence is crucial in defining a helicoidal laminate and effectively depends on the chosen angle difference between the adjacent plies referred to as pitch or rotation angle. Previous research efforts used pitch angles of 8˚ (48 plies [223], 24 plies [228]), 10˚ (40 plies [227]) , 16˚ (48 plies [223], 24 plies [228]) and 26˚ (48 plies [223], 24 plies [228]). In the present work, in order to investigate how the different pitch angles affect the impact resistance of the laminate, two different angles were considered, namely 6˚ in layup LS3 and 12˚ in layups LS4 and LS5 – see Figure 4.8 and Table 4-3. It is important to underline that the choice of a specific pitch angle can affect the overall symmetry and balance of the laminate that has a fixed total number of layers. This in turn affects the loading and deformation behaviour. For example, taking 32 plies and setting the pitch angle to 3 ˚ for the helicoidal arrangement, the plies in the stack would rotate from 0˚ to merely 93˚ resulting in an unsymmetrical and unbalanced layup which in turn would lead to certain generally undesired effects which are addressed later on in this Section.

In order to achieve symmetry and/or balance of the helicoidal laminate, some researchers [227] added several additional mid-plane layers in the laminate sequence. In general, the larger the total number of layers the more flexibility a designer has in terms of the choice of the pitch angle and ultimately the lamination scheme. Guided by the previously published research, cost considerations and the manufacturing constraints, the total number of layers (plies) used in this study was fixed at 32 for each plate leading to a nominal plate thickness of 4 mm.

Figure 4.8 graphically displays the layup arrangements used in this work.

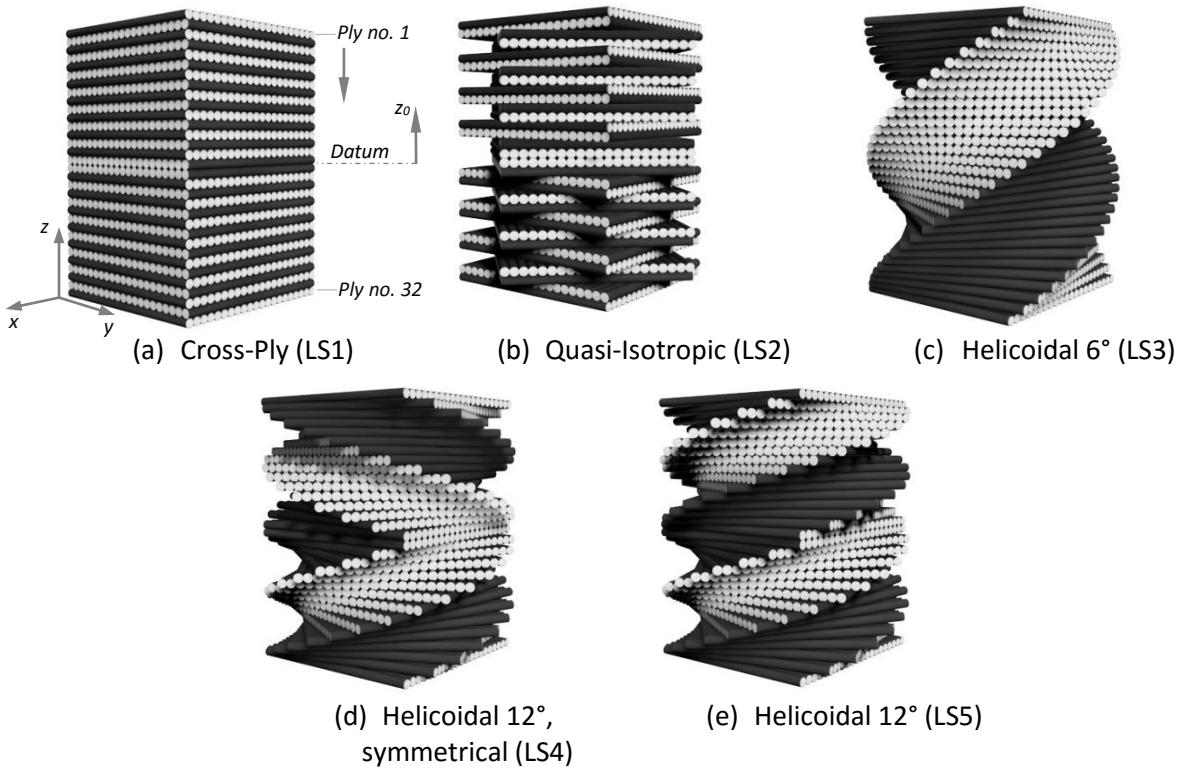

(a) Cross-Ply (LS1) (b) Quasi-Isotropic (LS2) (c) Helicoidal 6° (LS3)

(d) Helicoidal 12°, symmetrical (LS4) (e) Helicoidal 12° (LS5)

Figure 4.8: computer generated visualisation of the lamination schemes used in the present study.

Table 4-3 presents the specifications of the chosen layup configurations.

No.	No. of layers	Stacking Sequence	Type	Description	Flatness After Curing
LS1	32	[0/90]8s	Cross-Ply	Symmetrical, balanced	Flat
LS2	32	[+45/-45/0/90]4s	Quasi-Isotropic	Symmetrical, balanced	Flat
LS3	32	[0/6/12/18/…/180]	Helicoidal (6°)	Non-Symmetrical, balanced	Induced twist
LS4	32	[0/12/24/36/…/180]s	Helicoidal (12°)	Symmetrical, balanced	Flat
LS5	32	[0/12/24/36/…/360]	Helicoidal (12°)	Non-Symmetrical, balanced	Induced twist

Table 4-3: specifications of the lamination sequences used in this study.

The non-symmetry of the stacking sequence combined with the directionally dependent coefficients of thermal expansion driven by the orthotropic nature of the composite plates leads to the physical twisting of the laminate, while the net effect of the non-balance is to induce curvature. Curvature and twisting in laminated composite components are usually undesired and can physically occur during a

typical curing process in an autoclave under elevated thermal conditions. This can be further examined by performing an analysis using classical laminated plate theory (CLPT) with nominal elastic properties of the CFRP prepreg material given Table 4-4.

E_{11} (GPa)	E_{22} (GPa)	G_{12} (GPa)	ν_{xy}
160.5	12.5	4.6	0.303

Table 4-4: mechanical properties of the CFRP used for CLPT analysis.

Matrices of extensional stiffness *A* ($\mathrm{GPa \cdot mm}$), bending-extensional coupling stiffness *B* ($\mathrm{GPa \cdot mm^2}$) and bending stiffness *D* ($\mathrm{GPa \cdot mm^3}$) of the cross-ply (LS1) laminate are:

$$A = \begin{bmatrix} 348.5 & 15.3 & 0 \\ 15.3 & 348.5 & 0 \\ 0 & 0 & 18.4 \end{bmatrix},\ B = 0\ ,\ D = \begin{bmatrix} 501.9 & 20.4 & 0 \\ 20.4 & 427.4 & 0 \\ 0 & 0 & 24.5 \end{bmatrix}; \quad \textbf{(4.6)}$$

the quasi-isotropic (LS2) laminate:

$$A = \begin{bmatrix} 274.4 & 89.4 & 0 \\ 89.4 & 274.4 & 0 \\ 0 & 0 & 92.5 \end{bmatrix},\ B = 0,\ D = \begin{bmatrix} 363.6 & 137.7 & 10.5 \\ 137.7 & 331.0 & 10.5 \\ 10.5 & 10.5 & 141.9 \end{bmatrix}; \quad \textbf{(4.7)}$$

the helicoidal (LS3) laminate:

$$A = \begin{bmatrix} 279.0 & 84.7 & 0 \\ 84.7 & 279.0 & 0 \\ 0 & 0 & 87.9 \end{bmatrix},\ B = \begin{bmatrix} 0 & 0 & -109.1 \\ 0 & 0 & -68.2 \\ -109.1 & -68.2 & 0 \end{bmatrix},\ D = \begin{bmatrix} 635.2 & 97.9 & 0 \\ 97.9 & 139.0 & 0 \\ 0 & 0 & 102.1 \end{bmatrix}; \quad \textbf{(4.8)}$$

the helicoidal (LS4) laminate

$$A = \begin{bmatrix} 297.7 & 84.7 & 0 \\ 84.7 & 260.4 & 0 \\ 0 & 0 & 87.9 \end{bmatrix},\ B = 0,\ D = \begin{bmatrix} 463.4 & 107.2 & 101.7 \\ 107.2 & 292.3 & 62.7 \\ 101.7 & 62.7 & 111.4 \end{bmatrix}; \quad \textbf{(4.9)}$$

the helicoidal (LS5) laminate:

$$A = \begin{bmatrix} 297.7 & 84.7 & 0 \\ 84.7 & 260.4 & 0 \\ 0 & 0 & 87.9 \end{bmatrix},\ B = \begin{bmatrix} 0 & 0 & -50.8 \\ 0 & 0 & -31.3 \\ -50.8 & -31.3 & 0 \end{bmatrix},\ D = \begin{bmatrix} 463.4 & 107.2 & 0 \\ 107.2 & 292.3 & 0 \\ 0 & 0 & 111.4 \end{bmatrix}. \quad \textbf{(4.10)}$$

For a general kth layer of a laminate, the thermo-elastic stress-strain relationship can be calculated as [46]

$$\{\sigma\}^{(k)} = [\boldsymbol{C}]^{(k)}\left(\{\varepsilon\}^{(k)} - \{\alpha_T\}^{(k)}\Delta T\right), \quad \textbf{(4.11)}$$

where σ and ε are stress and strain vectors in the laminate coordinate system respectively, $\boldsymbol{C}$ is the stiffness matrix, α_T is a vector of thermal expansion coefficients and ΔT is a given temperature gradient. Applying the CLPT and Eq. (4.11) with a thermal gradient of 180°C representative of a typical curing cycle, the residual thermal stresses for each ply can be estimated as shown for the quasi-isotropic (LS2) and helicoidal (LS3) laminates in Figure 4.9 and in Figure 4.10 respectively.

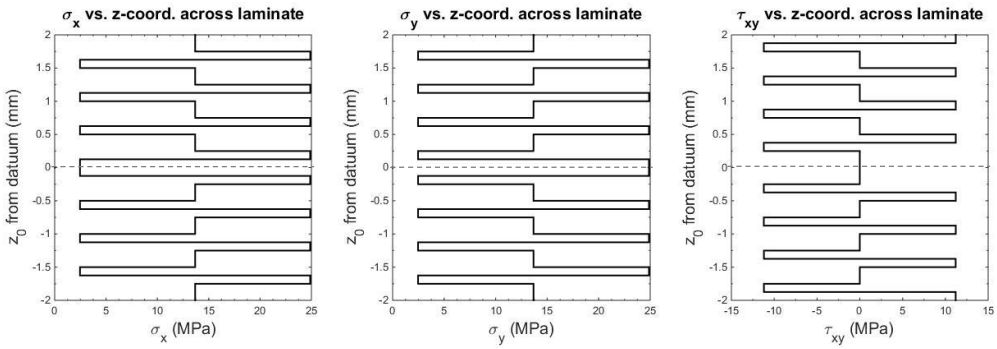

Figure 4.9: stress distributions in quasi-isotropic (LS2) laminate subjected to thermal gradient as predicted by CLPT.

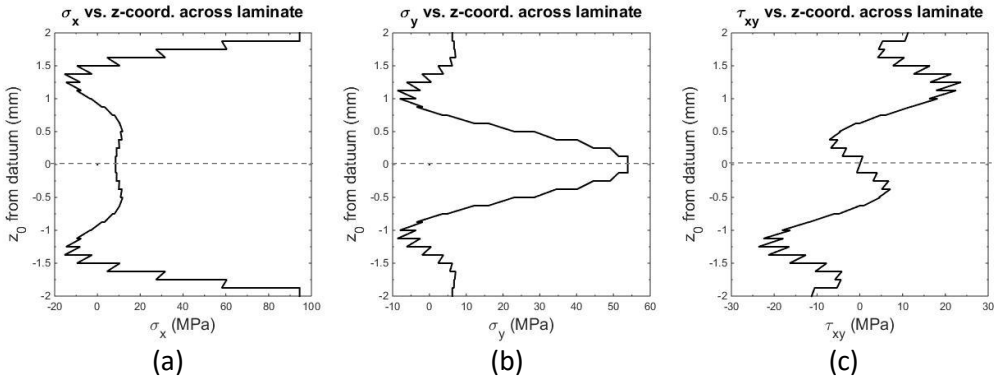

Figure 4.10: stress distributions in helicoidal (LS3) laminate subjected to thermal gradient as predicted by CLPT.

It can be clearly seen that both layups are balanced as normal principal stresses are symmetric about the mid-plane (datum) of the laminate which is further confirmed by the fact that the in-plane shear stiffness components A_{16} and A_{26} of the extensional stiffness matrix are zero for all laminates. On the contrary, the through-thickness distribution of the in-plane shear stress τ_{xy} of the helicoidal layup LS3 is non-symmetric about the datum plane - Figure 4.10. This in turn leads to the thermally induced twist of the laminate. Consequently, in order to avoid possible twist-induced shape inconsistencies of the plates, only the symmetric and balanced layups are considered in the experimental work which aimed at validating the numerical model. However, in the subsequent numerical analysis, the effect of the non-symmetry on the dynamic response is studied considering a pitch angle of 12˚ in symmetric laminate LS4, which has the ply orientations mirror-imaged about its structural mid-plane, and LS5 which features the same pitch angle but the laminate is asymmetric. In fact, both LS3 and LS5 are characterised by the coupling between the in-plane and flexural behaviour (B matrix ≠ 0), whereas all laminates in this study are balanced and therefore do not exhibit coupling between the in-plane axial and shear deformations (since A_{16} and A_{26} = 0).

In order to evaluate how the increasing planar dimensions affect the response of helicoidal composites against the controls, three plate sizes, namely 100 mm x 100 mm, 200 mm x 200 and 300 mm x 300

mm were used. A square shape of the samples was chosen in order to avoid any variability in results that can be associated with the aspect ratio, which is not an unusual choice of dimensions [233, 234].

4.3.2 Experimental Setup

The primary purpose of the experimental work was to validate the numerical model so that further simulations could be performed without their experimental counterparts with a certain confidence level. Due to the fact the non-symmetrical layups LS3 and LS5 produce undesired twist during manufacturing, they were not considered during the physical testing in order to avoid inconsistencies induced by the possible variability of the shape across various samples. Only two plate dimensions with lamination schemes LS1, LS2 and LS3 were evaluated during the validation process. Four sets of identical test samples were manufactured and tested for each configuration (i.e. plate size, impact energy and layup) in order to assess the repeatability of results.

4.3.2.1 Sample Manufacturing

A standard manual layup and vacuum bagging procedure was followed for manufacturing of the samples. The basic layer employed for the fabrication of the laminates in the work was a unidirectional carbon fibre epoxy prepreg T800/M21 (Hexcel®) which is a typical aerospace industry grade CFRP material owing to its high stiffness and strength properties. All prepreg plies were cut to specific angles prior to laying up procedure. The temperature and pressure cycle used in the autoclave for curing the specimens was according to the manufacturer's material data sheet. After curing, the composite samples were machined to square dimensions of 120 mm x 120 mm and 220 mm x 220 mm using a water-fed diamond saw. A clearance of 20 mm was added to the plates in order to enable appropriate clamping during the subsequent testing, where the exposed part of the plates measured 100 mm x 100 mm and 200 mm x 200 mm.

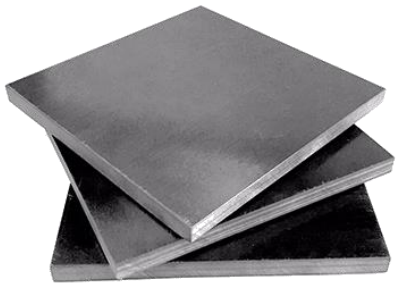

Figure 4.11: manufactured 100 mm x 100 mm CFRP plates.

4.3.2.2 LVI Test

Dynamic LVI tests were performed using a drop weight impact testing system equipped with a hemispherical tip following a drop-weight tower testing procedure ASTM D7136/D7136M [40], which was described in some detail in Section 2.2.2.1. The impactor mass (12.864 kg) and geometry (hemispherical tip, 10.25 mm radius) were held constant throughout the experimental program, whereas the impact energy was varied by setting the drop height appropriately. The height was determined based on the distance between the tip of the impactor head and the upper surface of the base plate. During impact specimens were held using two steel-plate fixtures, as shown in Figure 4.12. The clamping plates were fixed in place with four screws allowing the test piece to be constrained. Each set of samples was subjected to two impact energies, 40 J and 80 J.

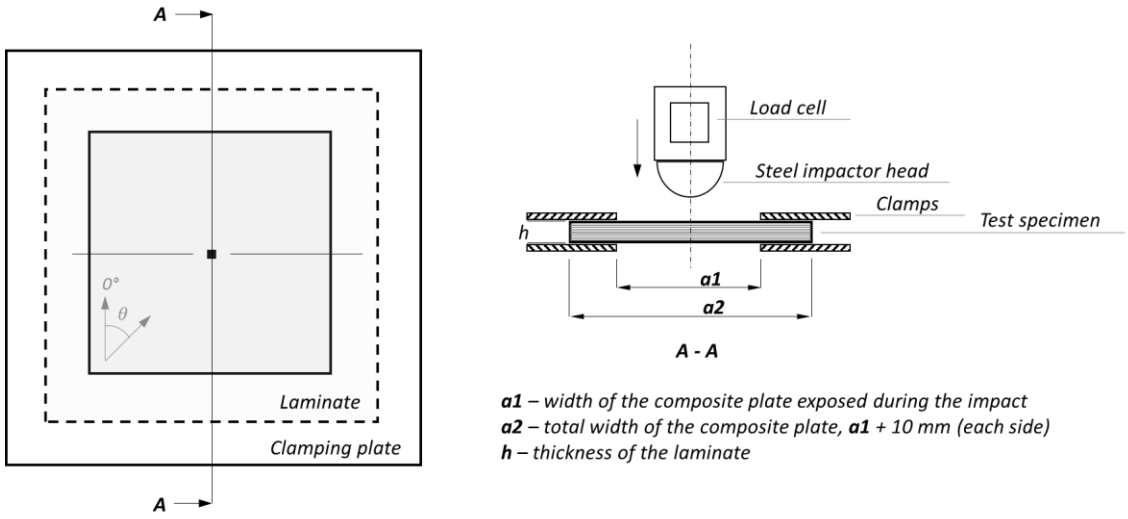

Figure 4.12: a schematic of the LVI testing setup.

During the LVI testing, the velocity of the impactor and the force exerted on it were recorded. The kinetic energy (KE) was calculated based on the velocity of the impactor, whereas the force was registered by the load cell. Using the force-time curve and assuming prefect contact between the test piece and the impactor, the displacement and the KE associated with the impactor were determined by successive integration

$$x(t) = x_0 + \left[\int_0^t v_0 - \int_0^t \frac{F(t) - mg}{m} dt\right] dt, \quad \textbf{(4.12)}$$

$$E(t) = E_0 - \frac{1}{2} m(v_0 + \int_0^t \frac{F(t) - mg}{m} dt)^2, \quad \textbf{(4.13)}$$

where x_0 is initial (at time of first contact) displacement (assumed zero), v_0 is the initial velocity (prior to impact), E_0 is the initial KE (i.e. 40 J and 80 J), $F(t)$ is the impact force and m is the mass of the impactor.

4.3.2.3 CAI Test

To evaluate the residual strength of each composite laminate following the impact tests, the samples were subjected to a quasi-static compression after impact (CAI) testing by following a standard procedure ASTM D7137/D7137M [28]. Indeed, this test method is typically performed in aerospace industry to assess the ability of samples to support a load after the onset of damage. The CAI tests were conducted using a universal testing machine Instron 5585. In order to test the impacted specimens without altering their geometry, two square fixtures were used, of 100 mm x 100 mm and 200 mm x 200 mm respectively, to perform the CAI test. Figure 4.13 schematically shows the testing setup.

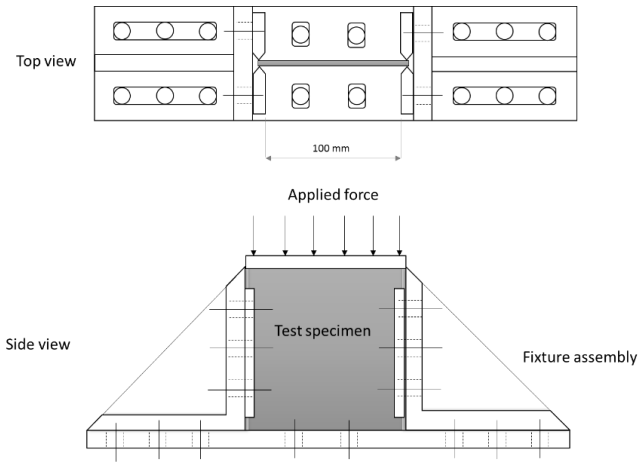

Figure 4.13: a schematic view of the CAI fixture assembly.

The fixtures stabilised the specimens at the edges without constraining the transverse deformation due to Poisson's effect. Appropriate measures were taken to ensure the flatness and parallelism when positioning and aligning the samples in the testing rig. Four strain gages along the front and back faces of the specimens were used during all tests. The recorded strain gauge data was used to determine if the specimen has been positioned in the correct way. In case the load is not applied correctly to the specimen, a bending of the sample can be detected by the strain gage data. Four samples for each configuration were end-loaded and compressed to failure. As an essential requirement for the test results to be acceptable, the compressive failure had to be confined to the impact area. In case when the samples buckled above/below the impact zone or buckled globally, the results were discarded.

During CAI testing, the force, displacement and strain were recorded. Compressive residual strength can be evaluated from the peak force (F_{CAI}) achieved during the compression of the samples divided by its cross sectional area ($a \times h$), as stated in the standard test method [28]

$$\sigma_{\mathrm{CAI}} = \frac{\mathrm{F_{CAI}}}{a \times h}. \qquad \textbf{(4.14)}$$

4.3.3 Numerical Modelling

4.3.3.1 FEA Model

In order to simulate a complex structural dynamic response of the composite laminates during impact events, a full 3D explicit finite element method was employed using FEA software LS-DYNA®. A FE mesh of the computation model reproducing the experimental setup is shown in Figure 4.14. The impactor was modelled as a hemispherical elastic body with mass of 12.864 kg and a radius of 10.25 mm which is representative of the physical arrangement used in the experiments. An assumption of elastic body which does not exhibit any plastic deformation is appropriate as in the real experiments the impact velocity was low (approx. 2.5 - 3.5 m/s) and the impactor was made of high strength steel alloy which resulted in insignificant deformation of the impactor relative to the CFRP plate. An initial velocity was applied to the nodes of the impactor to achieve the required impact energy – 40 J and 80 J were considered in this study.

The composite plate model was meshed using 3D solid (brick) constant stress elements with 2 elements through-the-thickness of each ply in order to capture a through-thickness stress distribution which is crucial for prediction of various failure modes including delamination. Average thickness of each ply was 0.125 mm corresponding to the total thickness of 4 mm determined from physical measurements. Constant laminate thickness with three plate sizes were considered in this analysis – 100 mm x 100 mm, 200 mm x 200 mm, 1200 mm x 200 mm. A unidirectional progressive composite damage material model MAT162 of Materials Sciences Corporation [60] was assigned to each ply individually in the FE model. The use of this particular model has been successfully validated for a vast variety of low and high velocity impact events especially involving thick composites [235] structures. It considers a full 3D stress state of finite elements as opposed to the assumed through the thickness stress field used by shell element formulations. This makes MAT162 applicable for thick and moderately thick plates such as the ones used in the present analysis. Furthermore, this material model features stress-based delamination failure criterion which allows to predict interlaminar damage without recourse to computationally expensive cohesive elements or tie-break contacts.

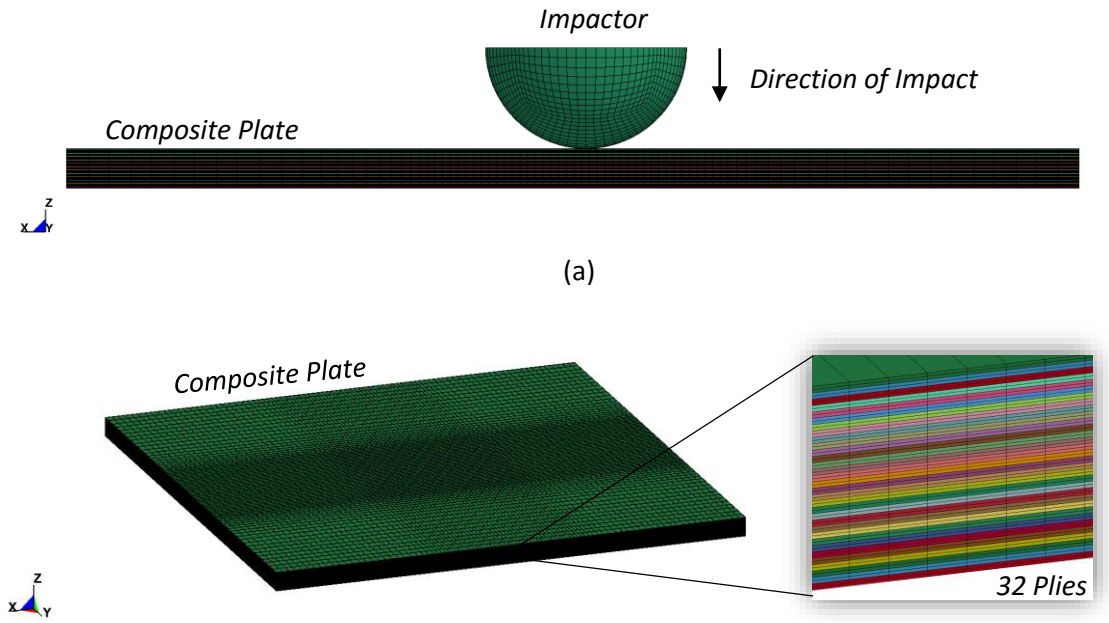

Figure 4.14: a finite element mesh used in LVI simulations with (a) a side view of the impactor and the composite target plate and (b) an isometric view of the laminate detailing the through-thickness ply definition.

The computational nodes on the top and bottom edges of the FE model of the composite plate were constrained in all translational degrees of freedom; such boundary conditions were set in order to mimic the effect of the clamps used in the impactor rig for fixing the laminates in pace. All nodes relating to the impactor were constrained in X and Y direction restricting the motion to be only perpendicular to the plate. A penalty based automatic surface-to-surface contact definition was used to simulate the interaction between the impactor and the plies.

An appropriate choice of a composite material model is critical for adequate FEA simulations incorporating complex composite failure mechanisms. Therefore, further details on the chosen constitutive model are provided in the next Section.

4.3.3.2 Progressive Composite Damage Modelling

As discussed previously, a number of techniques have been devised and used to model composite damage in general [51, 52] and specifically in the context of helicoidal/twisted laminates [223, 227]. In this study, MAT162 of LS-DYNA® was employed due to its proven capabilities in modelling impact on laminated composite materials. The utilised material properties* are presented in Table 4-5 and were determined using a combination of physical coupon testing and numerical sensitivity analyses along with the extensive calibration procedures.

MID	**RO (kg/m³)**	**EA (GPa)**	**EB (GPa)**	**EC (GPa)**	**PRAB**	**PRCA**	**PRCB**
162	1560	162	11.8	8.9	0.449	0.0535	0.449
GAP (GPa)	**GBC (GPa)**	**GCA (GPa)**					
4.9	4.6	2.6					
SAT (MPa)	**SAC (MPa)**	**SBT (MPa)**	**SBC (MPa)**	**SCT (MPa)**	**SFC (MPa)**	**SFS (MPa)**	**SAB (MPa)**
2089	1669	420	355	67	950	350	88
SBC (MPa)	**SCA (MPa)**	**SFFC**	**PHIC**	**E_LIMIT**	**S_DELM**		
55	76	0.3	10	0.015	1.27		
OMGMX	**ECRSH**	**EEXPN**	**CRATE1**	**AM1**			
0.99	0.25	1.28	0	1.8			
AM2	**AM3**	**AM4**	**CRATE2**	**CRATE3**	**CRATE4**		
1.8	0.45	0.25	0	0	0		

Table 4-5: MAT162 material model properties used in the numerical analysis for modelling CFRP plates.

* RO – density; EA, EB, EC – modulus of elasticity (E_{11}, E_{22}, E_{33}); PRBA, PRCA, PRCB – Poisson's ratio (υ_{21}, υ_{31}, υ_{32}); GAB, GBC, GCA – shear modulus (G_{12}, G_{23}, G_{31}); SAT, SAC, SBT, SBC, SCT – normal and transverse strengths under tension and compression (X_1^T, X_1^C, X_2^T, X_2^C, X_3^T); SFC, SFS - punch crush strength & punch shear strength (X_3^{PCS}, S_{13-23}^{PSS}); SAB, SBC, SCA – shear strengths (S_{12}, S_{23}, S_{31}). SFFC – residual compression strength factor, PHIC – coulombs friction angle in degrees, E_LIMT – axial strain for fibre failure, S_DELM delamination scale factor, OMGMX – limit damage parameter, ECRSH – limit compressive volume for element erosion, EEXPN – limit expansive volume for element erosion, CERATE1-CERATE4 – strain rate parameters, AM1-AM4 – damage softening parameters.

Firstly, the basic mechanical properties were evaluated through coupon testing and the FEA model was validated for a number of impact energies using standard layups. In addition, some parameters such as ECRSH, EEXPN, E_LIMIT and the damage softening parameters were identified via numerical calibration as they cannot be measured directly from the experiments.

Subsequently, the volume of all eroded (deleted) elements was calculated at the post-processing stage and used as an indicator of the extent of the catastrophic damage incurred by the laminates.

4.3.4 FEA Model Validation

4.3.4.1 LVI Testing

The experimental results were used to validate the devised numerical model. As explained earlier, only lamination schemes LS1, LS2 and LS4 with plate widths of 100 mm and 200 mm were considered. The general response in terms of history of kinetic energy (KE) and force vs. out-of-plane displacement for 100 mm x 100 mm plates is reported in Figure 4.15 and Figure 4.16.

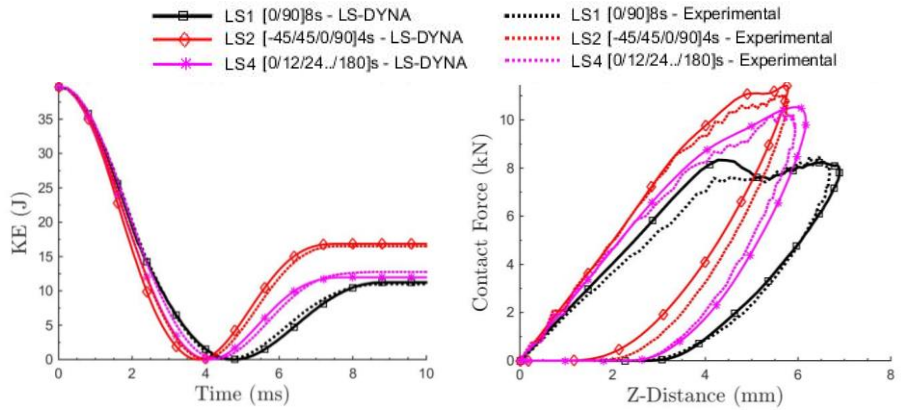

(a) (b)

Figure 4.15: comparison between the numerical (LS-DYNA®) and experimental results for 100 mm x 100 mm plates subjected to LVI events at 40 J.

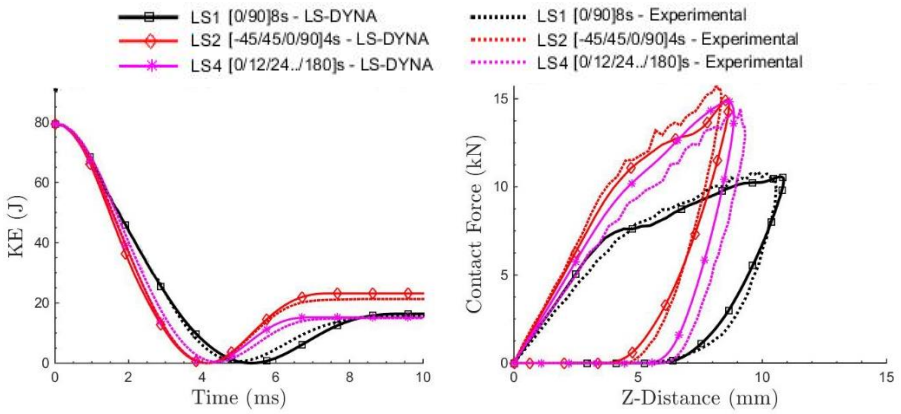

(a) (b)

Figure 4.16: comparison between the numerical (LS-DYNA®) and experimental results for 100 mm x 100 mm plates subjected to LVI events at 80 J.

The response data shows that there was generally a very good correlation between the computational and experimental results. For clarity, the curves in Figure 4.15 and Figure 4.16 were smoothed using standard moving average filter, while the actual recorded values were used for comparing various

parameters such as absorbed KE (Figure 4.17) and maximum force (Figure 4.18). The absorbed energy was estimated as the difference between the initial and the final KE recorded during each test.

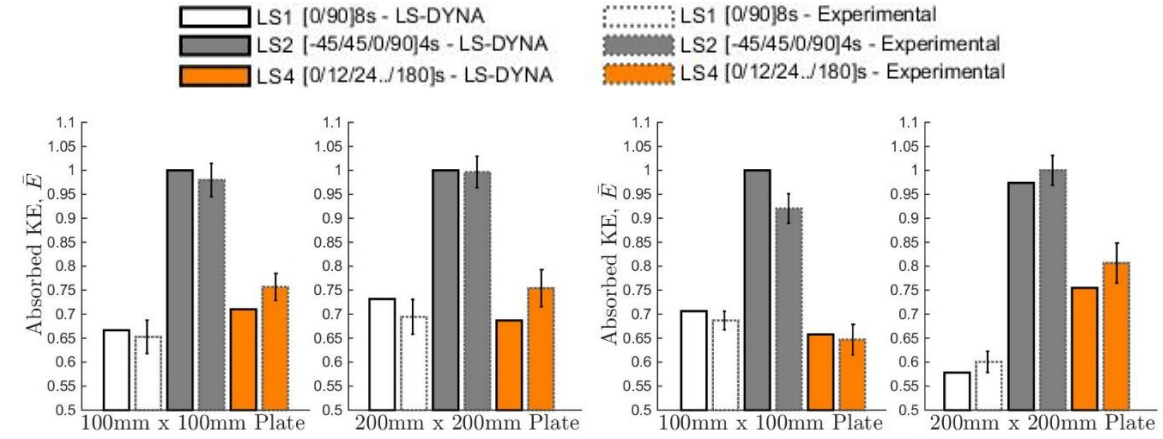

(a) 40J Impact (b) 80J Impact

Figure 4.17: comparison between the numerical (LS-DYNA®) and experimental LVI results of the absorbed kinetic energy (normalised to the maximum value for each test configuration); error bars represent the standard deviation.

For most configurations, the experimental and numerical results correlated to within 10-15% which can be considered as a good correlation considering other results published in literature [51, 228, 236].

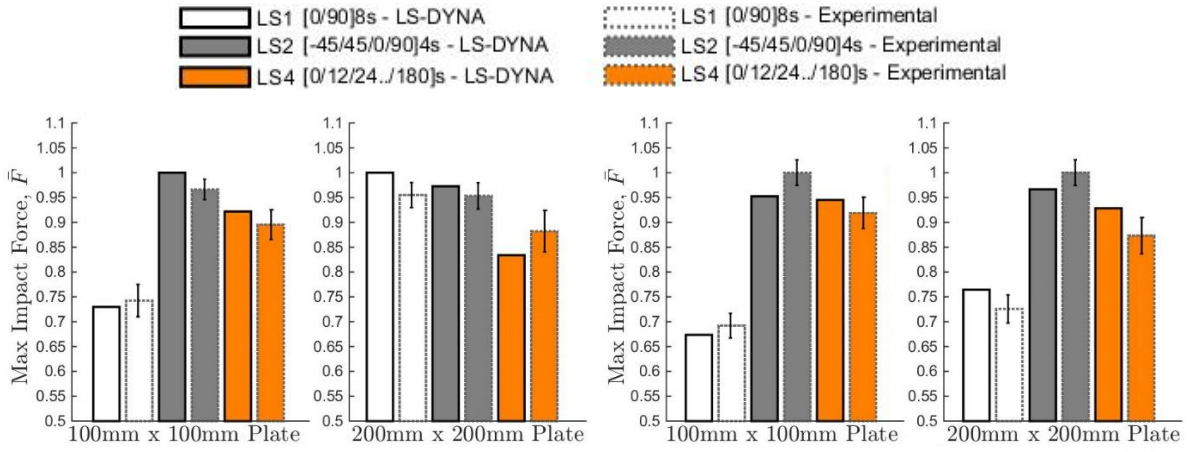

(a) 40J Impact (b) 80J Impact

Figure 4.18: comparison between the numerical (LS-DYNA®) and experimental LVI results of the recorded peak force (normalised to the maximum value for each test configuration); error bars represent the standard deviation.

4.3.4.2 BVID Damage Assessment

The composite material model MAT162 calculates the internal material damage by means of various damage criteria (Eq. (2.39)-(2.44)). However, most of these failure modes cannot be directly evaluated experimentally apart from the delamination which can be experimentally measured using a range of nondestructive testing (NDT) methods such as ultrasonic C-scan and computer tomography (CT) scanning. Moreover, delamination is by far the prevailing damage mode in laminated composite materials. Therefore, Figure 4.19 visually highlights the extent of the delamination as obtained experimentally via C-scan, and via LS-DYNA® simulations by plotting the area of finite elements that reached the damage threshold associated with the delamination.

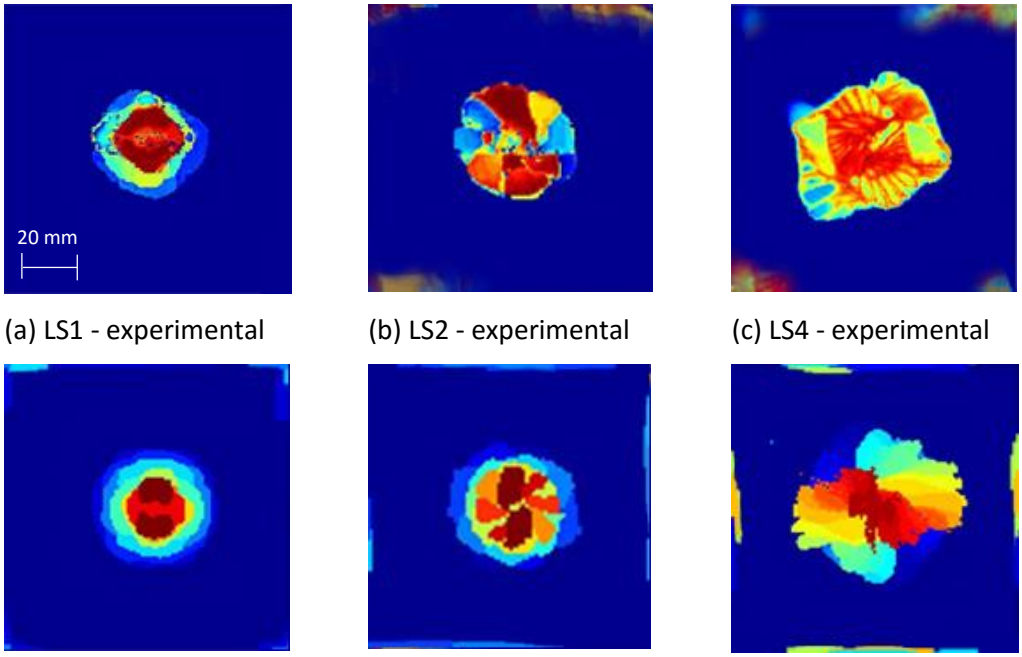

(a) LS1 - experimental (b) LS2 - experimental (c) LS4 - experimental

(d) LS1 - FEA (e) LS2 - FEA (f) LS4 - FEA

Figure 4.19: contours of the delamination extent for the impacted (40 J) 100 mm x 100 mm plates obtained using (a)-(c) ultrasonic C-scan method (TOF + Amplitude) and (d)-(f) delamination damage mode predicted by the material model MAT162; colour shading is representative of the depth of the defect.

Evident from Figure 4.19, the delaminated area was the lowest in the cross-ply (LS1) laminates and the largest in the case of the helicoidal one (LS4). Generally, the achieved results correlated well with the experimental ones in terms of the overall area of delaminations and the shape of the delaminations.

A through-the-thickness distribution of the numerically obtained delamination contours along with the comparison to the experimentally obtained CT scans of the damaged regions is shown in Figure 4.20. The dark red colour regions represent the elements that reached the delamination damage threshold, while other colours indicate the elements that are close to but have not yet failed in this failure mode. The through-the-thickness damage distribution is clearly the highest in the cross-ply (LS1) layup according to the CT scan data, whereas it is mainly arranged in-plane in the helicoidal one.

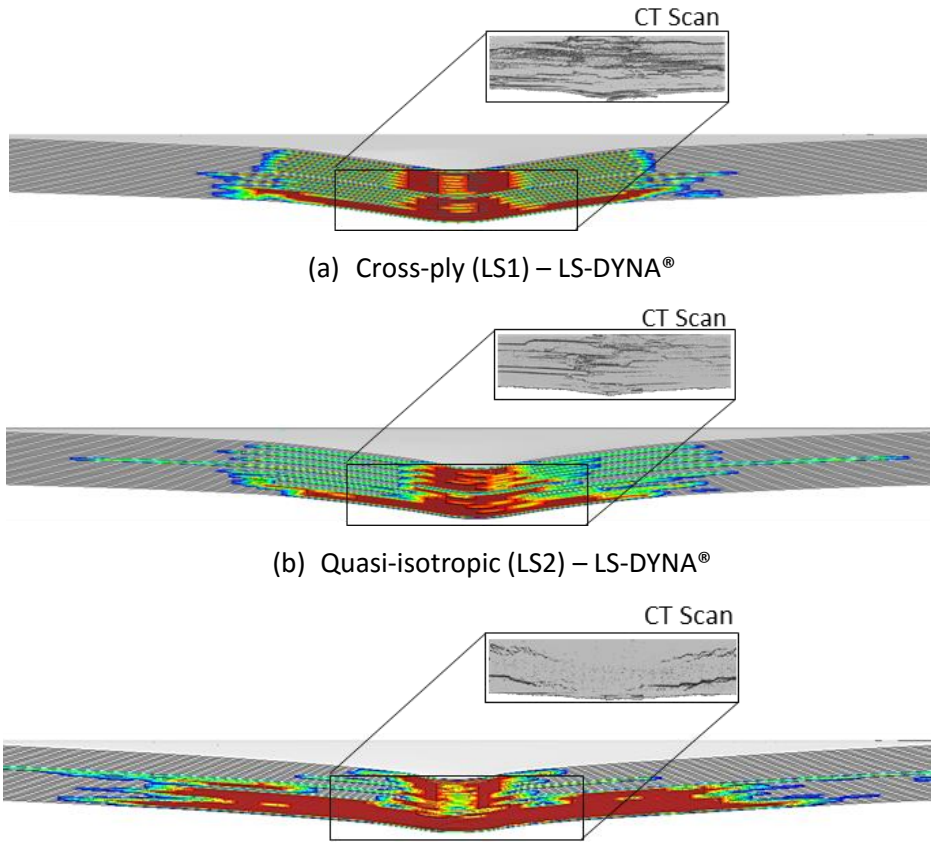

(a) Cross-ply (LS1) – LS-DYNA®

(b) Quasi-isotropic (LS2) – LS-DYNA®

(c) Helicoidal (LS3) – LS-DYNA®

Figure 4.20: contours of delamination of 100 mm x 100 mm plate under 40J LVI event – comparison of numerical (LS-DYNA®) to experimental (CT-scan) results.

Quantitatively, a single value of delaminated area was obtained for each configuration by considering the overall extent of the delamination damage incurred by the plates in the experimental and simulated LVI test. The corresponding results are shown in Figure 4.21 which indicates that the experimental and numerical results correlated well considering other results published in literature [51, 228].

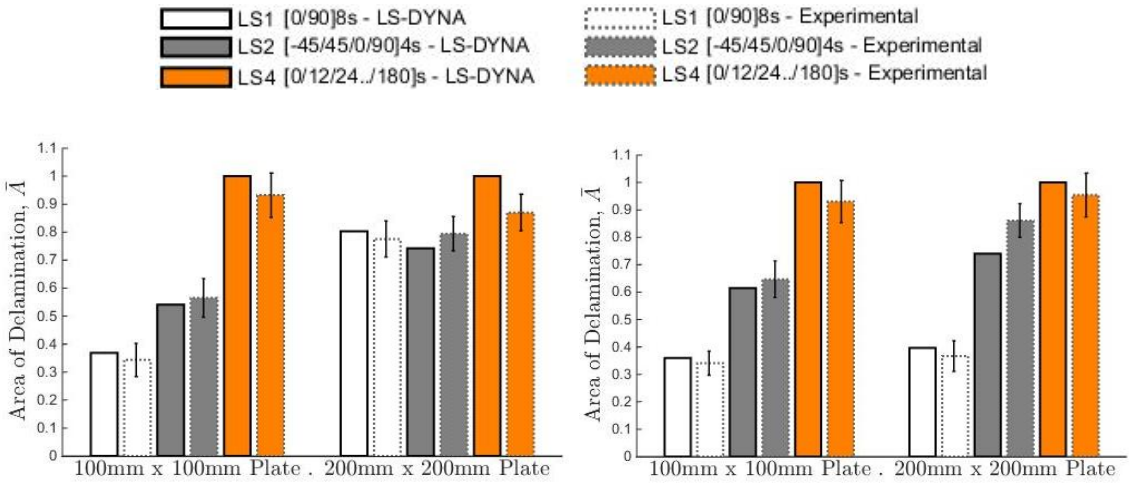

(a) 40J Impact Energy (b) 80J Impact Energy

Figure 4.21: comparison between the numerical (LS-DYNA®) and experimental LVI results of the delamination area (normalised to the maximum value for each test configuration); error bars represent the standard deviation.

The damage on the back face (opposite to the impact face) was also observed and is shown in Figure 4.22. The cracks at the face are most pronounced for LS1 layup and least obvious in LS4. A virtual counterpart indicating this damage type was evident numerically as a number of finite elements were automatically eroded (deleted) from the simulation due to excessive failure and deformation driven by the internal algorithm of the material model MAT162.

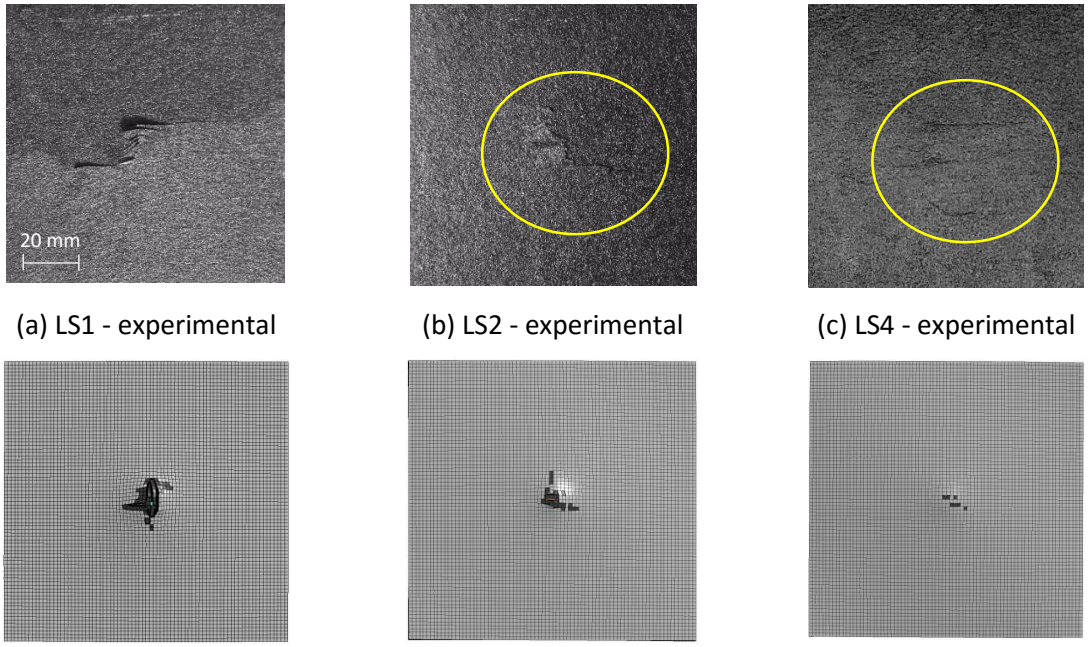

(a) LS1 - experimental (b) LS2 - experimental (c) LS4 - experimental

(d) LS1 - FEA (e) LS2 - FEA (f) LS4 - FEA

Figure 4.22: back face damage incurred by 100 mm x 100 mm plates in (a)-(c) LVI experiments; (d)-(f) LS-DYNA® simulations.

4.3.4.3 CAI Testing

Once the impact has been simulated using LS-DYNA®, the resulting model with incurred damage at the final numerical step was used for the subsequent CAI simulations. The setup used in the FEA model mimicked the experimental one and is shown in Figure 4.23. All nodes at the bottom face of the plate were constrained in all degrees of freedom, while a portion of the impact and back face of the plate were constrain in out-of-plane direction only to approximating the effect of the side guides used in the experimental setup.

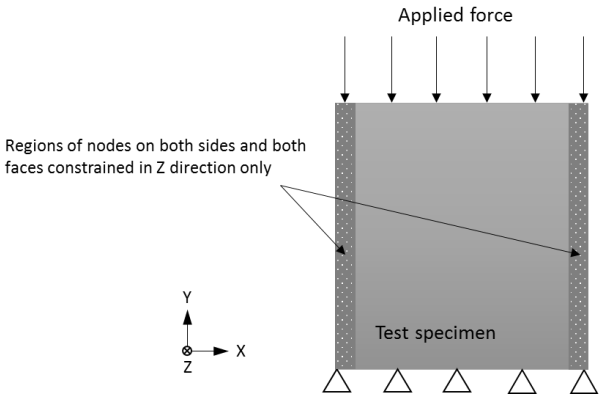

Figure 4.23: schematic view of the CAI setup used in the FEA simulations.

It is important to note that the results only for 100 mm x 100 mm plates are presented in Figure 4.24. This is due to the fact that during both numerical and experimental procedure, the larger plate sizes failed by global buckling which according to the testing procedure, invalidates the results.

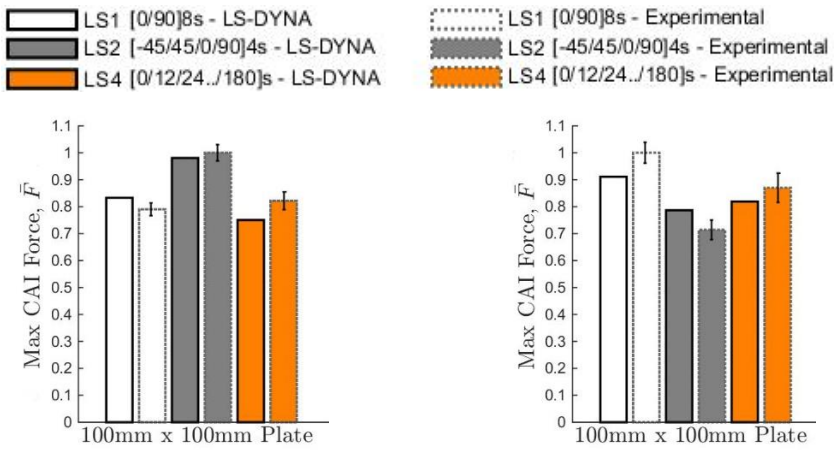

(a) 40J Impact Energy (b) 80J Impact Energy

Figure 4.24: comparison between the numerical (LS-DYNA®) and experimental LVI results of the maximum recorded CAI force (normalised to the maximum value for each test configuration); error bars represent the standard deviation.

Evidently from Figure 4.24, a good correlation (to within 5-10%) between the experimental and numerical results was achieved in terms of CAI strength. Quantitative results and analysis are provided in the following Section.

4.3.5 FEA Results and Discussion

Following the validation procedure, the behaviour of the helicoidal samples was further evaluated by subjecting them to LVI events via numerical simulations using LS-DYNA®. The responses of the different laminates were analysed considering two impact energies (40 J and 80 J), while the energy dissipation mechanisms were also investigated by testing different samples characterised by increasing the planar dimensions, namely 100 mm x 100 mm, 200 mm x 200 mm to 300 mm x 300 mm. The results and discussion is structured in the following manner: first, the results of kinetic energy (KE), contact force and out-of-plane displacement are presented; next, the energy absorption of the various layups is analysed fixing the plate size at 100 mm x 100 mm; this is followed by the discussion of the absorbed energy and the volume of eroded element comparison considering three plate sizes at 40 J only; finally, the predicted delamination extent is presented and compared for the three plate sizes considering all layups under both 40 J and 80 J impact energies.

4.3.5.1 LVI Simulations

Figure 4.25, Figure 4.26 and Figure 4.27 show the results of the KE (a) evolution with time and the contact force vs. out-of-plane displacement (b) considering all five layups with various dimensions impacted at 40 J.

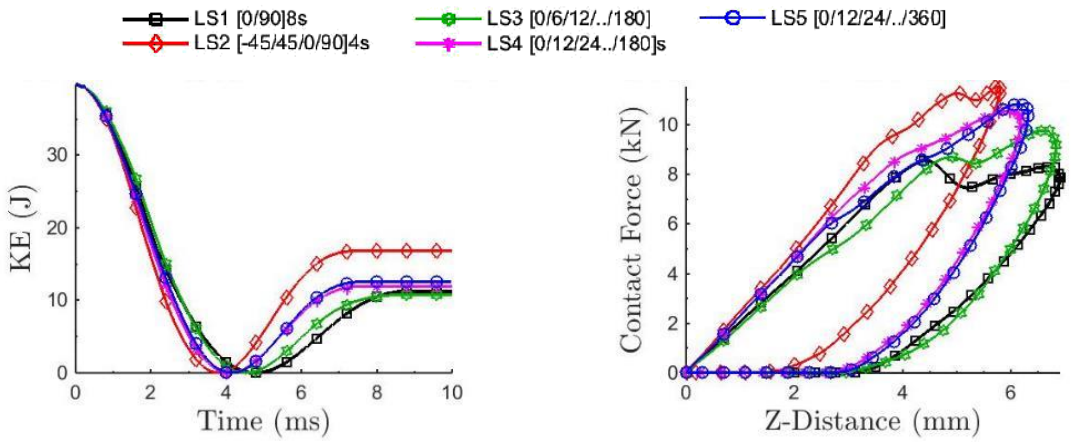

(a) (b)

Figure 4.25: numerical results of the dynamic response of 100 mm x 100 mm CFRP plates at 40 J impact energy during LVI simulations.

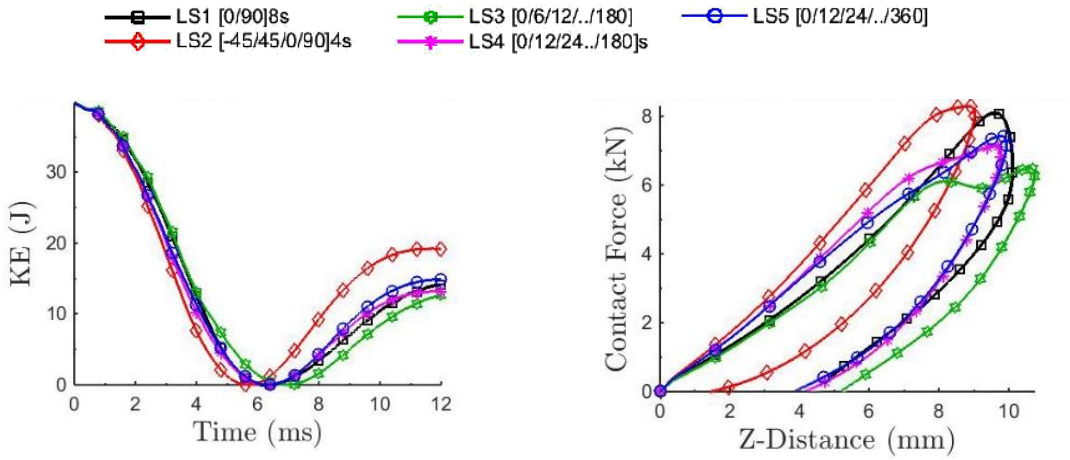

(a) (b)

Figure 4.26: numerical results of the dynamic response of 200 mm x 200 mm CFRP plates at 40 J impact energy during LVI simulations.

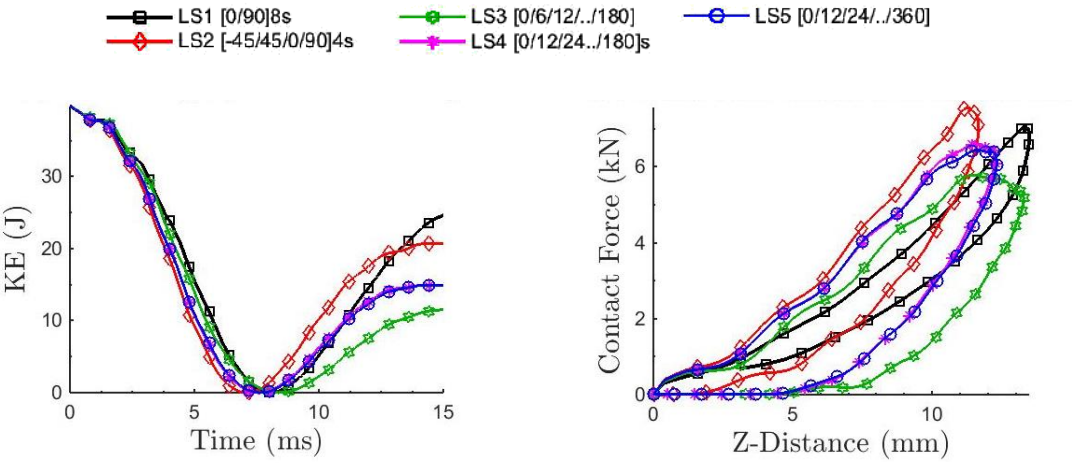

(a) (b)

Figure 4.27: numerical results of the dynamic response of 300 mm x 300 mm CFRP plates at 40 J impact energy during LVI simulations.

As expected, as the planar size of the laminates increased, the maximum contact force and the absorbed energy decreased. Similar trend could be observed in case of 80 J impact.

Considering only 100 mm x 100 mm plates, the results of energy absorption vs. impact energy (Figure 4.28(a)) and eroded element volume vs. impact energy (Figure 4.28(b)) are presented in respectively.

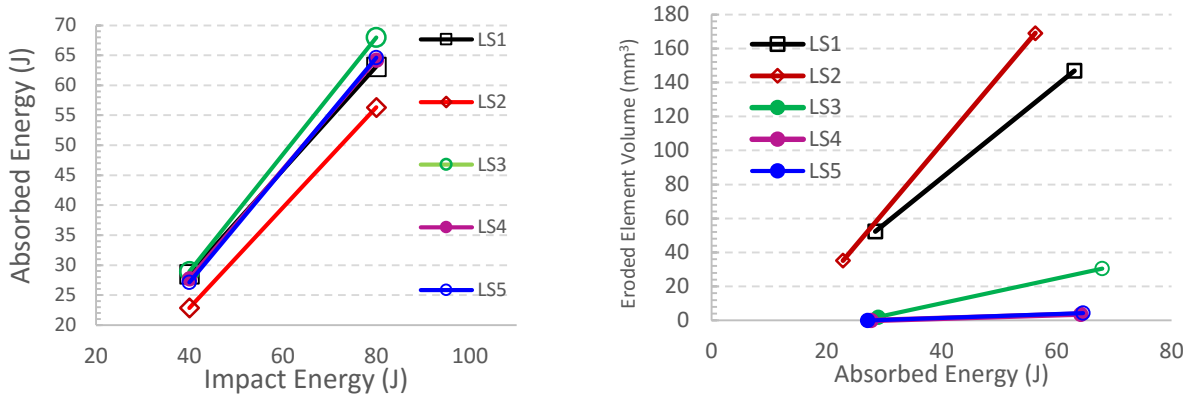

(a) (b)

Figure 4.28: energy absorption comparison for various lamination sequences of 100 mm x 100 mm CFRP plates.

As it is possible to see in Figure 4.28(a), for the 40 J impact, all the helicoidal arrangements (LS3, LS4 and LS5) overcome the quasi-isotropic layup (LS2), showing an enhancement in the energy absorption by more than 26.6%. The highest energy absorption value belongs to the helicoidal arrangement LS3 (6° pitch angle), while increasing the pitch angle up to 12 degrees leads to a decrement in the value of absorbed energy by almost 5% (from 28.96 J to 27.75 J), which is consistent with the data present in literature. However, in this case, the difference between the asymmetric (LS5) and symmetric layup (LS4) is almost negligible (~2%).

The different behaviour of the laminates can be explained by analysing the mismatch between two consecutive layers in the different arrangements. Bending modulus is a key characteristic in the interlaminar strength of a laminate especially for mode-II (in-plane shear) rather than mode I. Indeed, considering two unidirectional layers placed at 0°, the high bending modulus of the resulting laminate will make the opening of a delamination in the interphase able to dissipate a large amount of energy. Since the mismatch between the two following laminae decreases moving between cross-ply (LS1, 90°), quasi-isotropic (LS2 45°), helical (LS4 and LS5, 12°) and helical (LS3, 6°), the resulting bending modulus of the laminate will increase leading to an improvement of the energy absorption for the helicoidal laminates [237].

The cross-ply lamination sequence (LS1) displayed interesting behaviour as it performed second best after LS3 in terms of energy absorption, absorbing only 0.47 J (~2.5%) less than the best helicoidal sample with 6° pitch angle (LS3). This seems to be in contrast with previous results obtained in literature that show an increase in the impact resistance for lower pitch angles [227, 238, 239] in

comparison with traditional cross-ply laminates. This behaviour can be explained by taking into account the internal damage distribution for the different laminates as represented in Figure 4.20 and Figure 4.28(b). As it is possible to see, both cross-ply (LS1) and quasi-isotropic (LS2) layups show a higher through-the-thickness damage distribution and indeed higher volume of eroded elements, while all the helicoidal samples appear completely undamaged after the impact. Indeed, due to the small angle between two subsequent layers, the helicoidal sequence is able to absorb the impact by distributing its energy all over the sample elastically with minimal internal damage, while traditional laminates dissipate impact energy predominantly via the creation of new surfaces (delaminations and internal cracks). This mechanism absorbs enough energy to bring the total energy absorption of the cross-ply laminate up to the value comparable with the helicoidal samples. It is important to underline that although the levels of absorbed energy are similar for both the cross-ply and the helicoidal samples, the former one results in more critically damaged samples indicated by the volume of eroded elements.

The beneficial effect of the helicoidal arrangement is clearer when the same lamination sequences are impacted at higher energy levels (80 J) as represented in Figure 4.28(b). As it is possible to see from the curves, in this case the helicoidal arrangement in LS3, LS4 and LS5 allows a better distribution of the energy during the impact event, resulting in an increased value of the absorbed energy in comparison with the LS1 and LS2. Analysing the eroded element volumes for these laminates, it is possible to note that for 80 J, the discrepancy between traditional and helical layup is more pronounced: the traditional layup sequences still require the opening of new surfaces to absorb the impact energy, however, this mechanism was not sufficient to reach the absorbed energy displayed by the helicoidal arrangements. Further considering the helical arrangements, it is possible to notice that the pitch angle plays a key role in the enhancement of the interlaminar toughness. Moving from 12° (LS4 and LS5) to 6° (LS3) it is possible to observe an enhancement in the energy absorption of 5%. It is important to notice that in the case of the latter one (LS3), a small amount of internal damage is recorded also for the helicoidal arrangement, although, it is considerably lower than what observed for the traditional layouts (-81%).

When a sample is subjected to a low velocity impact, the contact between the penetrator and the sample is long enough for the entire structure to respond to the impact, therefore the dynamic structural response is strongly affected by the dimensions of the specimen. Based on this premise, the effect of the sample dimensions was investigated by testing samples at 40 J with different dimensions, 100 mm x 100 mm, 200 mm x 200 mm and 300 mm x 300 mm.

The performance of all the lamination sequences considering various plate sizes in presented in Figure 4.29.

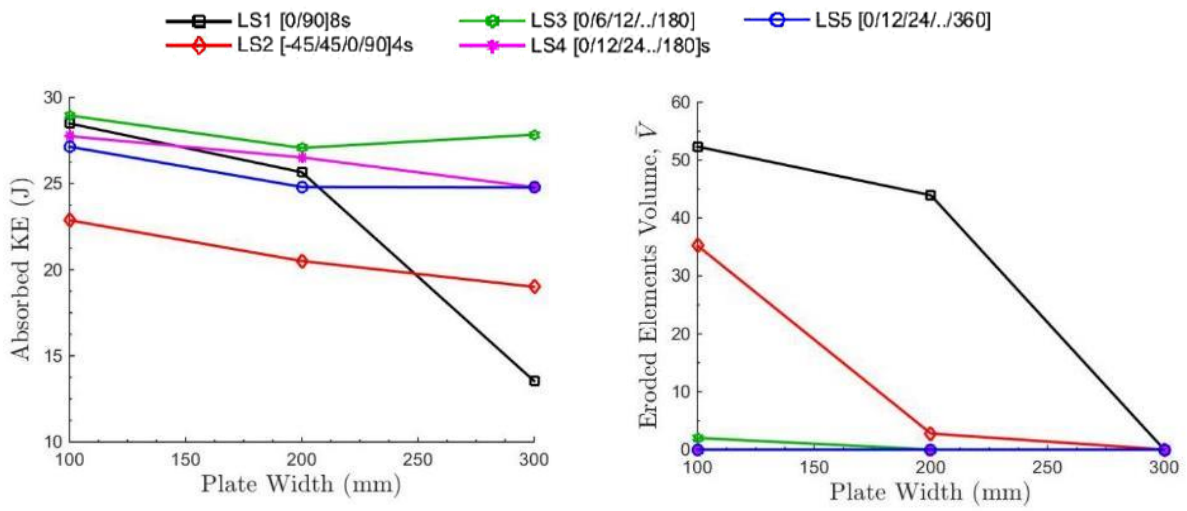

(a) (b)

Figure 4.29: absorbed energy and volume of eroded elements for various CFRP plate sizes subjected to impact energy of 40 J.

Evident from Figure 4.29, when a larger plate size is used, the results show a general decrease of the energy absorption for all the samples as a larger structural area is available for the elastic response of the entire specimen. Analysing the results further, the energy absorption corresponding to the cross-ply and quasi-isotropic laminate (LS1) drops down losing more than 50% (from 28.49 J to 13.53 J) and almost 20% (from 22.87 to 19.00J) respectively, the helicoidal arrangements lose merely an average of 8%. The large drop in the value of absorbed energy for the cross-ply layup sequence can be explained by analysing how the increase in the sample dimensions influence the volume of eroded elements for the different laminates. Examining Figure 4.29(b), it appears clear that the cross-ply laminate is the layup that is most affected by the dimensional change since the volume of eroded elements drops down from 52.33 to 0 mm^3. As we observed previously, because of the large mismatch between two subsequent layers the only way the cross-ply arrangement has to dissipate energy is by opening new surfaces, hence creating intra and inter layer damages. Since the increase of the dimensions of the sample allows the entire surface to respond to the external excitation elastically, this mechanism (the formation of new surfaces) is suppressed and the energy dissipated by the entire laminate during the contact time is dramatically reduced. On the other side, since the helicoidal arrangement provides a good elastic dissipation of energy without the need of large fracture areas, the change in the dimensions of the samples affects only marginally the behaviours of LS3, LS4 and LS5. Further considering the helicoidal arrangements, there is an inverse proportion between the pitch angle of the helical layup and impact resistance when larger dimensions are used: for both 200 mm x 200 mm and 300 mm x 300 mm samples, the sample with 6° (LS3) pitch displays higher values of

absorbed energy in comparison with the one with 12° (LS5), showing an increase of 9% and 12% respectively. Moreover, it is important to note that the symmetry of the lamination sequence affects the energy absorption mechanism when different dimensions are used. Indeed, it appears that the asymmetric lamination of LS3 and LS5 leads to a non-linear variation in the absorbed energy with the sample's dimensions, showing first a decrease in the passage between 100 mm x 100 mm and 200 x 200 mm of 6.5% and then an increase of 3% when the dimensions are further increased up to 300 mm x 300 mm. For comparison, the symmetric layup sequence of LS2 and LS3 leads to a more traditional linear behaviour.

In addition to the volume of eroded elements, the composite material model MAT162 calculates the extent of delamination among other damage modes. Figure 4.30 presents the results of overall delamination for increasing plate widths for simulated LVI events under the impact energies of 40 J and 80 J; this was calculated by summing the area of finite elements for all layers that reached the damage threshold associated with the delamination failure mode.

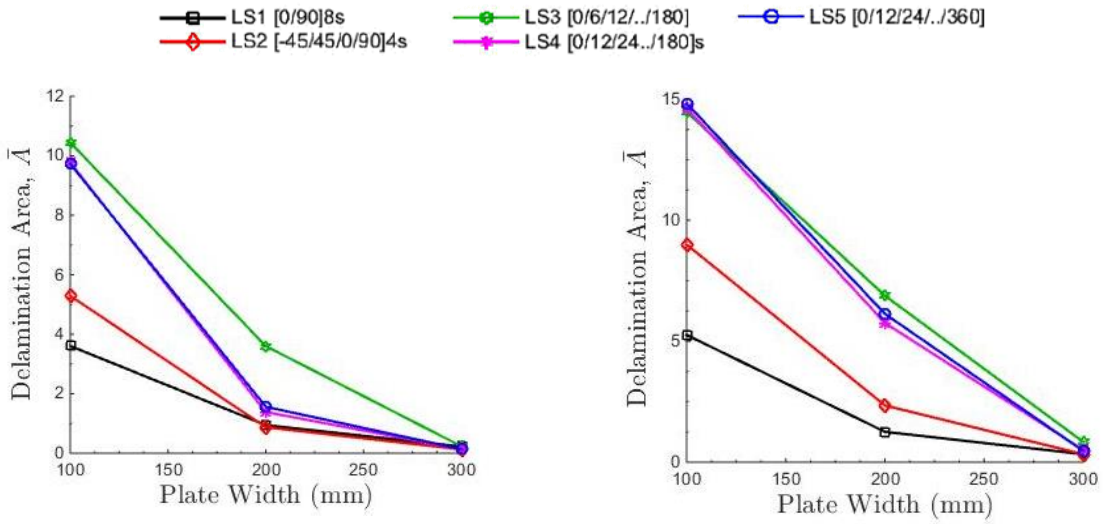

(a) 40 J (b) 80 J

Figure 4.30: total delamination area (normalised according to the plate area) vs. plate width under LVI impact energy of (a) 40 J and (b) 80 J.

As can be seen from Figure 4.30, the delamination areas decreased with increasing plate width which allowed the structure to distribute the impact energy across a larger area enabling higher degree of elastic deformation. Notably, the cross-ply (LS1) laminates displayed the least amount of delamination as most of the energy was absorbed through open fracture indicated by the high number of eroded elements which is ultimately symptomatic of catastrophic failure. Although, the area of delamination for helicoidal laminates was consistently estimated as higher than for cross-ply and quasi-isotropic ones, helical configurations especially LS4 and LS5 showed a significant improvement as the plate size was increased. For instance, at 40 J the overall delamination area calculated for LS4 and LS5 was

almost twice the one obtained for quasi-isotropic (LS2) laminates with plate size of 100 mm x 100 mm with, while the difference subsequently reduced to about 65% using 200 mm x 200 mm plates. Similar but less pronounced trend was observed at 80 J considering a transition from 100 mm x 100 mm to 200 mm x 200 mm plates as at higher energy the impact response becomes more localised to the area of incipient striker contact and the structure has less time to respond globally. However, as the plate size increased from 200 mm x 200 mm to 300 mm x 300 mm under impact energy of 80 J, the helicoidal laminates improved to a larger extent than the quasi-isotropic one, although, the overall delaminated area was still higher. Evidently, the helicoidal layups are absorbing energy more efficiently (i.e. with less damage) as the plate size increases. It is also important to note that while there was a good correlation between the experimentally obtained (C-scan) delamination areas and the numerically estimated one, the CT-scan showed a higher distribution of damage through-the-thickness of the cross-ply and quasi-isotropic plates than in the case of helicoidal ones.

Moreover, it is possible to plot the contours of finite elements that failed in longitudinal fibre mode as predicted by the material model MAT162 – see Figure 4.31 overleaf. It is also important to note that no NDT technique currently exists that can evaluate the internal damage in such a way that enables to reliably discern between the longitudinal fibre damage (in tension/compression) and other failure modes, whereas this becomes possible by employing a FEA modelling approach using LS-DYNA® with material mode MAT162.

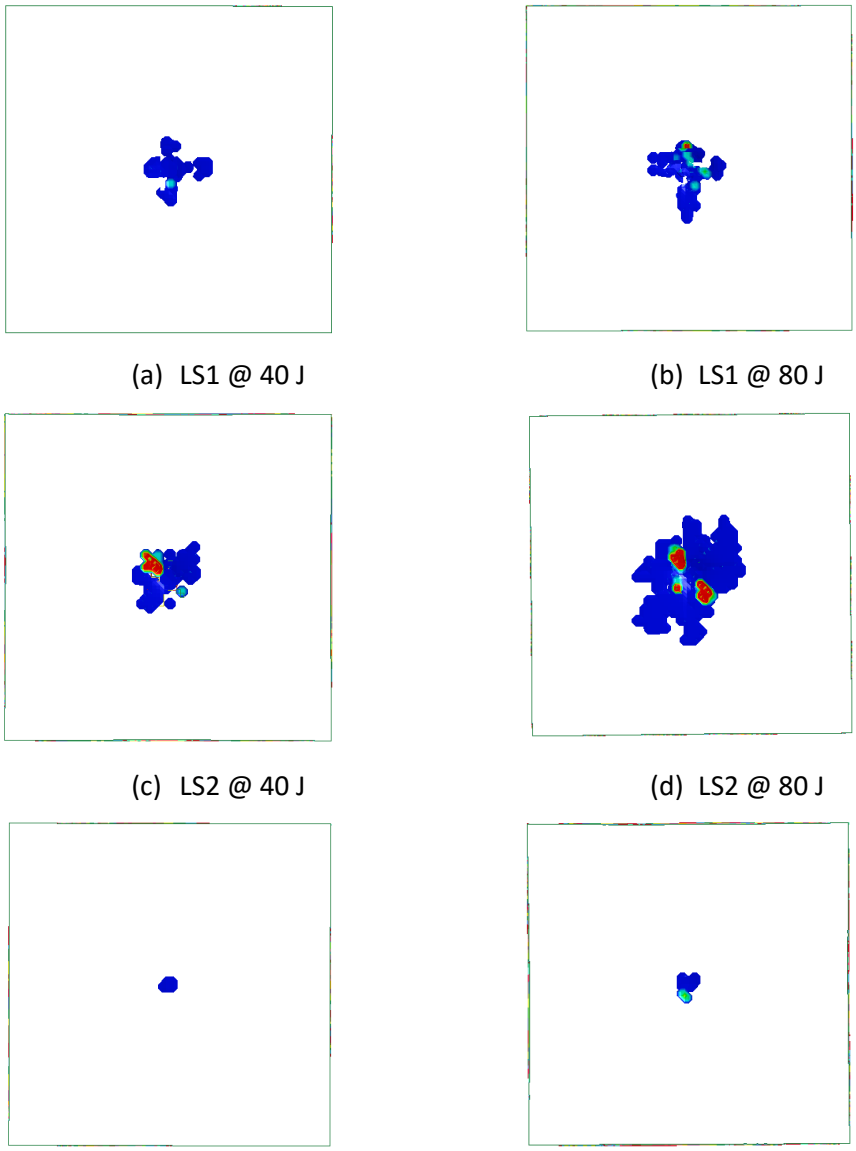

(a) LS1 @ 40 J (b) LS1 @ 80 J

(c) LS2 @ 40 J (d) LS2 @ 80 J

(e) LS4 @ 40 J (f) LS4 @ 80 J

Figure 4.31: contours of iso-surfaces of the finite elements (after LVI but prior to CAI testing) that failed in longitudinal fibre mode as predicted by MAT162 – 100 mm x 100 mm plates; colour indicates the severity of the incurred damage.

The significance of the extent of fibre failure is particularly relevant in the case of CAI testing which is further addressed in the following Section.

4.3.5.2 CAI Simulations

Following the analysis of impact damage induced during simulated LVI events, simulations of compression after impact (CAI) were performed. The samples were end-loaded and compressed to failure. All tests have been carried out in order to avoid global buckling of the impacted specimens. CAI strength is one of the most critical properties from a design/structural point of view. The CAI simulations give the ability of the sample to carry load following the onset of damage. Indeed, the test is sometimes used as an index of the toughness of the sample. Compressive residual strength was evaluated from the peak force (F_{CAI}) attained during the compression of the samples divided by its cross sectional area ($a \times h$), as specified in the standard procedure [28]. The details of the residual strength are presented in Figure 4.32 with the percentage change, using the quasi-isotropic (LS2) CAI strength as a reference (control) sample.

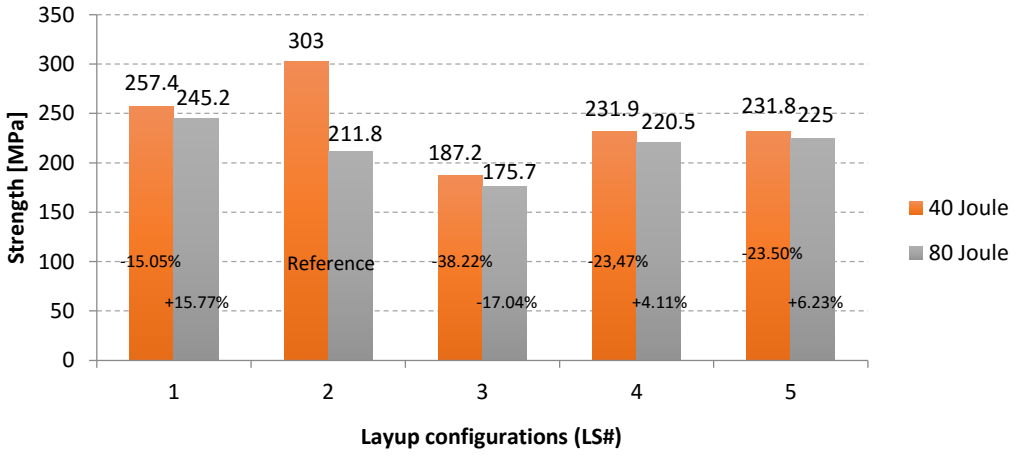

Figure 4.32: CAI strength obtained from the LS-DYNA® simulations using post-impacted 100 mm x 100 mm plates.

At both 40 J and 80 J, the configuration LS3 (6˚) with the smallest angle used for the helicoidal layup shows the lowest CAI strength. Instead, the helicoidal layups LS4 (12˚) and LS5 (12˚) show a small increase (~4% and ~6% percent respectively) in residual strength with respect to the quasi-isotropic configuration. Furthermore, considering the layups with their corresponding rotational angle, the obtained CAI strength trends are consistent with the ones published by Grunenfelder *et al.* [223], although, they used a different composite material and impact energy.

In order to understand the reasons behind the difference in results at 40 J and 80 J, it is important to consider the longitudinal fibre damage mode as during the CAI testing the load is resisted primarily by the fibres. At impact energy of 40 J, the cross-ply (LS1) and quasi-isotropic layups (LS2) outperformed the helicoidal ones as at this impact energy level, the fibre-related stiffness degradation experienced by LS1 and LS2 was not sufficient to reduce the CAI strength below the values recorded for the

helicoidal laminates. In fact, considering a very small impact energy or indeed in a damage-free state, lamination sequences LS1 and LS2 are expected to withstand higher loads before failure than helicoidal ones as LS1 and LS2 contain more layers with fibres oriented in the direction of applied loading. However, at higher energy, more fibre damage is incurred by the quasi-isotropic (LS2) laminate as the helicoidal ones are more effective at distributing the damage in-plane resulting in less fibre fracture prior to CAI testing. This in not just a hypothetical explanation. This was confirmed by plotting the contours of finite elements that failed in longitudinal fibre mode prior to CAI testing as predicted by the material model MAT162 – see Figure 4.31. Furthermore, in the case of the cross-ply (LS1) composite plate, the fibre damage is more localised to the incipient impact location and therefore it experienced the least reduction in CAI strength at the higher impact energy.

4.3.6 Conclusion

In this work, the impact resistance of CFRP laminates with plies arranged in various bio-inspired helicoidal layups was evaluated. Full 3D FEA simulations of the LVI and CAI testing were performed using LS-DYNA® with an advanced composite constitutive model MAT162. In comparison to the cross-ply and quasi-isotropic controls, the helicoidal laminates exhibited a lower degree of internal damage through the thickness of the plates which was confirmed experimentally by the CT scans and numerically by plotting the volume of eroded elements and the contours of finite elements failed in longitudinal fibre mode. However, higher delaminations extent was recorded for the helicoidal layups compared to the controls which is consistent with the published research. Three plate sizes were considered and it was found that the helicoidal laminates tend to dissipate the impact energy more efficiently by spreading it in-plane and with less damage as the plate size is increased, assuming all other parameters are kept the same. This was especially true for the smaller impact energy given that as the velocity and the impact energy is increased, the dynamic response of the specimens becomes more localised. Interestingly, some nonlinear relation between the absorbed energy and the plate size was recorded for the bio-inspired lamination sequences. CAI testing revealed that at a higher energy, the residual strength of these laminates was higher than for the aerospace standard quasi-isotropic one. Although, only the smallest plate size was used for the CAI testing due to the onset of global buckling for the larger plate sizes.

Furthermore, the linear ultrasonic C-scan method proved effective at revealing the overall delimitation extent, whereas the CT scan provided further information about through the thickness damage distribution. However, CT scanning is expensive, time consuming and cannot be practically applied on the scale required in the aerospace industry (e.g. during regular inspection intervals). Therefore, the following chapters will focus on efficient nondestructive testing methods that are especially sensitive to damage that cannot be readily detected by the linear techniques. This in turn can contribute to the damage tolerance philosophy, whereby the defects can be detected at the early stages, and therefore, increase the overall safety of the air travel.

5 Nonlinear Elastic Wave Interactions in Damaged Media

Due to the shortcomings of the linear ultrasonic techniques, this work focused on the nonlinear class of NDE methods as they can provide a much increased sensitivity to the presence of micro damage in a structure. A number of experimental techniques and theoretical descriptions of classical and nonclassical acoustic effects was presented in the previous chapter. However, computational techniques capable of simulating these nonlinear phenomena are scarce and the limited number of them that are published in literature are usually implemented as part of the in-house written codes making it difficult for other researchers to verify or extend their efforts. In order to make the developed techniques more accessible, a commercially available FEA code LS-DYNA® is used throughout this work. First, a numerical model is devised for the purpose of simulating typical low level defects in conventional materials (e.g. aluminium and composites) that induce anharmonic effects characterised by the classical nonlinear elasticity [88, 89, 141, 148]. This is followed by an application of the approach to a complex composite structure (i.e. stiffener panel) containing multiple BVIDs. There is also an increased drive from industry to develop inspection techniques aimed at bonded joints as used in adhesively bonded composites and metallic structures. Therefore, a numerical and experimental technique that relies on several nonclassical nonlinear elastic wave phenomena that overcome the limitations of the classical techniques is developed and applied for detection of disbonds in an adhesive isotropic single lap joint. Finally, a nonlinear phased array system is developed and several nonlinear C-scan methods are evaluated which conclude this Chapter.

5.1 Modelling and Validation of Nonlinear Elastic Wave-Crack Interactions in Fatigued Structures

5.1.1 Introduction

A more in-depth understanding of nonlinear dynamic behaviour of solids can be attained by the development of the corresponding numerical models. Therefore, the aim of this work was to devise a material model that would enable simulating higher harmonic generation in cracked or generally damaged regions of the material under a harmonic excitation. Several FEM methodologies that could be used to simulate a nonlinear acousto-ultrasonic response in solids incorporating a crack were explored [240, 241]. In this study, LS-DYNA® was used due to its computational efficiency and capabilities in simulating highly nonlinear dynamic phenomena.

Experimental work was carried out using aluminium "dogbone" sample evaluating its nonlinear behaviour caused by the propagation of the crack at a number of intervals during its fatigue life. Many studies [135, 242] have shown that the generation of higher harmonics can be directly related to the manifestation and propagation of damage. Furthermore, it was demonstrated that the nonlinearity parameter β increases as the crack propagates further during the fatigue life of a component [243]. As explained in the previous chapter, the generation of harmonics in the presence of cracks is generally attributed to clapping/rubbing phenomena classed as CAN which are induced by small stresses due to wave propagation through the medium. Hence, as these nonlinear interactions occur locally to the damage zone, the devised constitutive model was applied to a certain 3D region of the overall FE mesh of the model. In present work, this region of nonlinear response elements led to the generation of the 2nd harmonic when the sample was excited using a single frequency. Experimentally, the magnitude of the nonlinear response was estimated using a well-known β which takes into account the amplitude of the fundamental and the 2nd harmonic as shown in Eq. (3.1). This parameter was also used in the constitutive model to enable the 2nd harmonic ($2f_0$) generation in the nonlinear response elements and determine its amplitude.

5.1.2 Experimental Setup

Experimental campaign was comprised of fatigue and ultrasonic testing. The former one aimed at inducing a crack in the specimen by sinusoidal tensile loading using an Instron 1332 machine with a *stress ratio*[16] of 0.027 and amplitude of 18.5kN. A number of tests have been carried out on identical samples in order to attain the appropriate cyclic fatigue conditions for consistent crack propagation. The specimens failed consistently just above 40,000 cycles. The corresponding fatigue testing setup specification is shown in Table 5-1, while a photograph of a crack at 40,000 cycles is presented in Figure 5.1.

Fatigue Life	0%/25%/32%/40%/87%/90%
Number of Cycles	0/10,000/13,000/16,000/35,000/40,000
Stress Ratio ($\sigma_{min}/\sigma_{max}$)	0.027
Amplitude	18.5 kN

Table 5-1: fatigue testing setup.

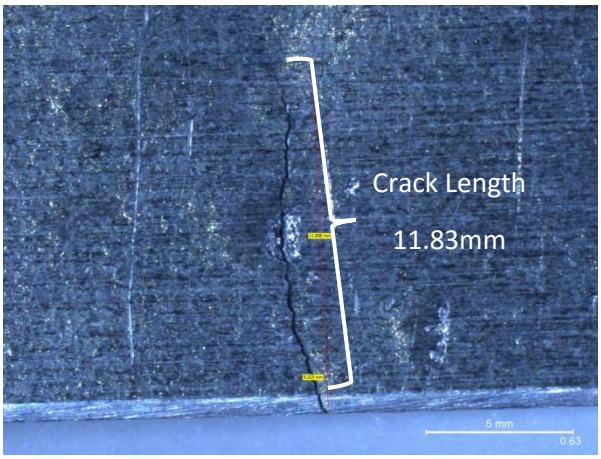

Figure 5.1: crack propagation at 40,000cycles.

The second part of the experimental setup aimed at evaluating the 2nd harmonic generation associated with the crack size growth at each stage over the fatigue life of the test piece and the magnitude of associated β parameter. A classical "dogbone" coupon sample manufactured from Aluminum 6061 was used for fatigue testing. The design of the coupon ensured a high stress concentration in the initial crack region and promoted a controlled crack propagation. The instrumentation setup incorporated broadband piezoelectric sensors adhesively bonded to the sample and is shown in Figure 5.2.

[16] In cyclic fatigue testing, a stress ratio is a ratio of minimum to maximum stress in one loading cycle.

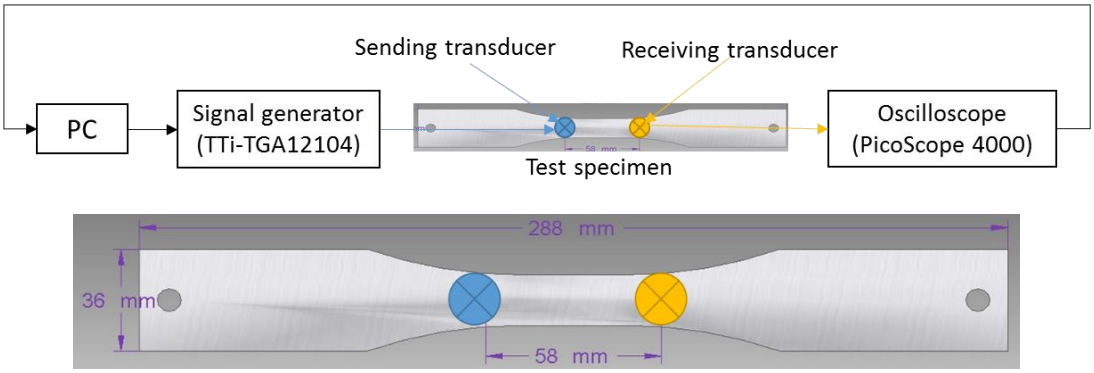

Figure 5.2: the ultrasonic experimental setup.

A frequency sweep in the range from 50 kHZ to 200 kHz was carried out. The frequency that resulted in the highest amplitude while containing a minimum level of 2nd harmonic amplitude in the frequency response of the undamaged (fatigue-free) sample was chosen as the excitation frequency. It is also important to note that a voltage level of the input signal was limited to 7 V_{pp} (peak-to-peak) as at this value the 2nd harmonic amplitude originating from the equipment setup was at the level of noise floor of the received spectrum. However, higher voltage input resulted in the appearance of higher harmonics in the response spectrum even in the undamaged state of material. As the result, the excitation frequency was evaluated and set at 100.24 kHz and is further referred to as f_0. Subsequently, at various intervals throughout its fatigue life the specimen was subjected to ultrasonic testing by sending a harmonic (sinusoidal) wave at this frequency using the outlined setup in order to evaluate the nonlinear behaviour of the propagating crack. The acquired time domain signal was transformed into the frequency domain by means of a well-known technique called fast Fourier transform (FFT) using MATLAB software which allowed to determine the amplitudes of the individual frequency components (i.e. fundamental and the 2nd harmonic) in the spectrum.

5.1.3 Numerical Modelling

5.1.3.1 Constitutive Model

As explained in Section 3.4.1.1 of the previous chapter, higher harmonics generation associated with the material damage and defects such as fatigue cracks can be explained and indeed modelled using classical nonlinear theory by 1D series expansion of the constitutive relationship Eq. (3.24). For most solid materials, the first nonlinear parameter β is sufficient to represent the nonlinear elastic behaviour in its classical form and can be measured using the amplitude of the 2nd harmonic considering a single tone input [244]. Furthermore, the material constants such as linear elastic modulus and β itself can be assumed constant in the up-scaling from the microscopic to the mesoscopic level (i.e. characteristic dimension of 1-10 mm). However, as Eq. (3.24) is a scalar model, it cannot be readily applied to study nonlinear wave propagation phenomena of anisotropic structures in 3D space. In order to overcome this limitation, a methodology proposed by Ciampa et al. [245] was adopted in this study which employed the stress-strain formulation in Kelvin notation, thereby extending the standard Voigt constitutive relation to a tensorial equivalent form for the 3D Cartesian space. Therefore, the Voigt stress-strain relationship for a homogeneous orthotropic elastic medium in Kelvin notation can be trivially stated as

$$\tilde{\boldsymbol{\sigma}} = \tilde{\mathbf{C}}\tilde{\boldsymbol{\varepsilon}} \tag{5.1}$$

where the components of the stress and strain vectors in 6D space are

$$\begin{aligned} \tilde{\boldsymbol{\sigma}} &= \left(\sigma_{11}, \sigma_{22}, \sigma_{33}, \sqrt{2}\sigma_{12}, \sqrt{2}\sigma_{13}, \sqrt{2}\sigma_{23}\right)^T \\ \tilde{\boldsymbol{\varepsilon}} &= \left(\varepsilon_{11}, \varepsilon_{22}, \varepsilon_{33}, \sqrt{2}\varepsilon_{12}, \sqrt{2}\varepsilon_{13}, \sqrt{2}\varepsilon_{23}\right)^T \end{aligned}, \tag{5.2}$$

and $\tilde{\mathbf{C}}$ is the new 6 x 6 stiffness matrix defined by

$$\tilde{\mathbf{C}} = \mathbf{TCT} \text{ with } \mathbf{T} = \begin{bmatrix} \mathbf{I} & 0 \\ 0 & \sqrt{2}\mathbf{I} \end{bmatrix}, \tag{5.3}$$

where **C** is the stiffness matrix in Voigt notation, whereas the symmetric matrix $\tilde{\mathbf{C}}$ represents the components of a second-rank tensor in the 6D space [246]. According to Ciampa and Meo [247], this approach allows to form an orthogonal basis for the stress and strain tensors of the second rank by determining the eigenmoduli Λ and the associated eigentensors $\tilde{\boldsymbol{\varepsilon}}$. Hence, these stress and strain tensors can be decomposed with respect to this basis in the 6D space. In other words, it is required to find the eigenvalues Λ known as *Kelvin moduli* that satisfy the following equation

$$\left(\tilde{\mathbf{C}} - \Lambda\mathbf{I}\right)\tilde{\boldsymbol{\varepsilon}} = 0\,. \tag{5.4}$$

There are six positive eigenelastic constants Λ_i ($i=1,\ldots,6$) since a symmetric and positive definite transformation $\widetilde{\mathbf{C}}$ is assumed. The six component of $\widetilde{\boldsymbol{\varepsilon}}$ in Eq. (5.21) are denoted by the vector $\widetilde{\boldsymbol{\varepsilon}}^{(i)}$ in the 6D space. The so-called stress eigentensors $\widetilde{\boldsymbol{\sigma}}^{(i)}$ are obtained by multiplying $\widetilde{\boldsymbol{\varepsilon}}^{(i)}$ with the eigenvalues Λ_i. Hence, the normalized strain eigentensors, denoted by $\widetilde{\mathbf{N}}$, can be used to construct a Cartesian basis in the 6D space

$$\widetilde{\boldsymbol{\varepsilon}} = \widetilde{\mathbf{N}}\left|\widetilde{\boldsymbol{\varepsilon}}\right|; \quad \left|\widetilde{\boldsymbol{\varepsilon}}\right|^2 = \widetilde{\boldsymbol{\varepsilon}} \cdot \widetilde{\boldsymbol{\varepsilon}}; \quad \widetilde{\mathbf{N}} \cdot \widetilde{\mathbf{N}} = 1. \tag{5.5}$$

Subsequently, the stress eigentensors can be stated in terms of the normalized strain eigentensors using Eq. (5.1), (5.4) and (5.5)

$$\widetilde{\boldsymbol{\sigma}}^{(i)} = \Lambda_i \widetilde{\boldsymbol{\varepsilon}}^{(i)}. \tag{5.6}$$

In 6D space, $\widetilde{\boldsymbol{\sigma}}$, $\widetilde{\boldsymbol{\varepsilon}}$ and $\widetilde{\mathbf{C}}$ have the following form

$$\begin{aligned} \widetilde{\boldsymbol{\sigma}} &= \sum_{i=1}^{6} \Lambda_i \widetilde{\boldsymbol{\varepsilon}}^{(i)} = \sum_{i=1}^{6} \Lambda_i \left|\widetilde{\boldsymbol{\varepsilon}}^{(i)}\right| \widetilde{\mathbf{N}}^{(i)} \\ \widetilde{\boldsymbol{\varepsilon}} &= \sum_{i=1}^{6} \widetilde{\boldsymbol{\varepsilon}}^{(i)} = \sum_{i=1}^{6} \left|\widetilde{\boldsymbol{\varepsilon}}^{(i)}\right| \widetilde{\mathbf{N}}^{(i)} \end{aligned}, \tag{5.7}$$

and

$$\widetilde{\mathbf{C}} = \sum_{i=1}^{6} \Lambda_i \widetilde{\mathbf{N}}^{(i)} \otimes \widetilde{\mathbf{N}}^{(i)}. \tag{5.8}$$

where $\otimes$ signifies a tensor or dyadic product. The eigenstrain vector $\widetilde{\varepsilon}_i$ is obtained by projection of the strain state given in Eq. (5.2) along the eigenvectors defined using Eq. (5.7). Subsequently, the total elastic modulus representing the nonlinear material behaviour specified in Eq. (3.24) becomes

$$\widetilde{C}_{TOT,i} = \Lambda_i \left(1 + \beta \widetilde{\varepsilon}_i + \delta \widetilde{\varepsilon}_i^{\,2} + \cdots\right). \tag{5.9}$$

Once $\widetilde{C}_{TOT,i}$ ($i=1,\ldots,6$) is known, the 6 x 6 nonlinear stiffness matrix $\mathbf{C}^{TOT}$ can be obtained by the transformation from Kelvin to Voigt formulation for the implementation in the material model of the explicit FE numerical scheme at each time step.

5.1.3.2 Material Model Implementation

The mathematical procedure outlined in the preceding Section was implemented into a commercial explicit FEA code LS-DYNA® by means of user-defined material model (UMAT) as an orthotropic nonlinear elastic material. The UMAT interface involves using FORTRAN programming language in order to define a constitutive relationship which is evaluated by the LS-DYNA® at every simulation step and for every finite element. Put simply, the input to the UMAT are the calculated strain increments and a set of parameters specified by the user, while the output comprises a set of stress components that can be identified as $\sigma^{(e)}$ in Eq. (2.28) which is computed for each finite element in a loop. This in turn allows to assemble a global internal force vector which is used for the force and energy balance required for the subsequent simulation step to be computed. Figure 5.3 demonstrates a high level call sequence of FORTRAN subroutines that are executed by the LS-DYNA® in order to access a UMAT for solid 8-node elements.

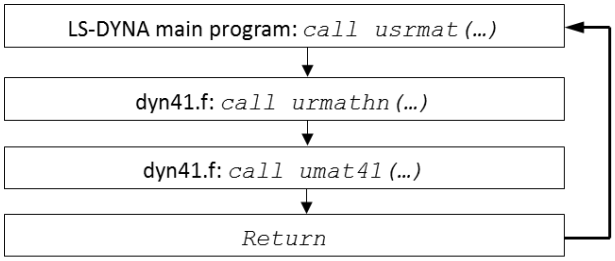

Figure 5.3: call sequence of UMAT subroutines within the LS-DYNA®.

Once the program enters *umat41* function within *dyn41.f* subroutine, it executes a number of calls that perform the calculations that allow the scalar classical nonlinear model (Eq. (3.24)) to be used in a 3D computational domain according to the procedure explained in the previous Section. Figure 5.4 provides a flow chart of the numerical steps that are performed within *umat41*.

1	*Initialization (i.e. input parameters, stiffness matrix calculations)*	
2	*Calculate eigenvalues & eigenvectors of the stiffness matrix*	`call orth1`
3	*Transform the strains & stresses from Voigt to Kelvin notation*	`call epskor`
4	*Compute 6 new elastic moduli using classical nonlinear theory*	`call smodcl`
5	*Transform the stiffness matrix back to Voigt notation*	`call smodvg`
6	*Update the stresses*	
7	*Return to the main program*	

Figure 5.4: the sequence of calculations performed by the devised constitutive model.

The developed UMAT was set as a material model for the finite elements. Collectively, the portion of the global finite element mesh with the assigned UMAT is designated here as nonlinear response elements.

5.1.3.3 FEA Model Setup

In order to represent a discontinuity such a crack in a material, one could attempt to accurately define the crack geometry. However, this would lead to a significant geometrical and computational complexity as it would require extremely fine mesh with elaborate contact algorithms specified at the crack interface. Moreover, this approach could lead to distortion of the elements within the model [248]. Alternatively, in the present methodology, the numerical crack zone of the specimen was defined using finite elements with nonlinear constitutive relationship implemented as UMAT described in the preceding Section. The geometry of the specimen and the corresponding finite element mesh are shown in Figure 5.5 and Figure 5.6 respectively.

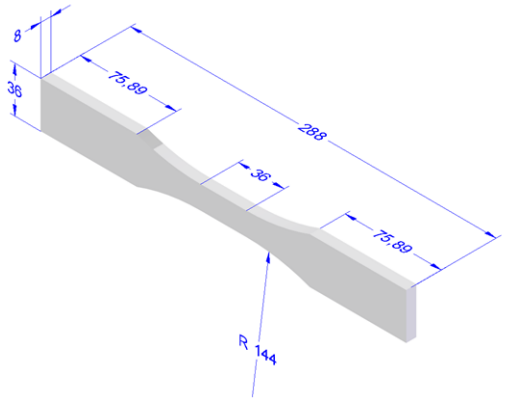

Figure 5.5: specification of the "dogbone" specimen; all dimensions in mm.

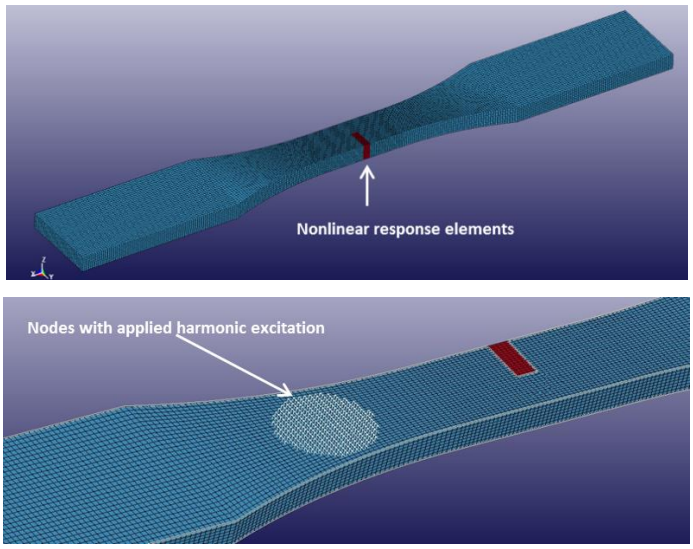

Figure 5.6: FE mesh of the "dogbone" specimen; same size/dimensions as in Figure 5.5, crack length 12 mm.

The mesh density was driven by the requirement for the critical time step. As explained in Section 2.5.1, LS-DYNA® calculates the critical time step size based on the characteristic dimension of the smallest finite element present in the model so that the information does not propagate across more than one element per time step. In wave propagation analysis using FEM, the choice of mesh density plays a critical role with some authors suggesting using a minimum of 20 elements per wavelength. For a harmonic excitation frequency of 100.24 kHz chosen in this study, a high spatial and temporal resolution of the waveform was achieved by taking 100 points per wave cycle which corresponds to a sampling frequency of 10 MHz. Hence, the resulting critical time step was 1e-7 s which in turn yielded the largest element size as 0.6 mm considering the propagation of longitudinal wave in a solid medium as discussed in Chapter 2.5.1. Some further mesh refinement was applied to the area with higher stress concentration in the vicinity of the nonlinear response elements.

Material properties of aluminium are shown in Table 5-2.

	Young's modulus (GPa)	**Mass density (g/cm^3)**	**Poisson's ratio**
Aluminium (T6061)	71	2.70	0.33

Table 5-2: material properties of the specimen used in the numerical analysis.

An isotropic elastic material was used as a material model representing the aluminium specimen, while the nonlinear response elements were modelled using the user defined material model *umat41*. Although, *umat41* was implemented as an orthotropic material model in order to enable modelling of composite materials in the future studies, an isotropy was imposed in this case by assigning the same material properties to longitudinal, in-plane and out-of-plane transverse directions.

The harmonic force was applied in an out-of-plane direction on the nodes representative of the transducer coverage area by means of *LOAD_NODE_SET

$$F(t) = Q_0 \sin(2\pi f_0 t)\,. \qquad \textbf{(5.10)}$$

where Q_0 is the amplitude (100 N) and f_0 is the excitation frequency of 100.24 kHz. The history of the nodal velocities was recorded at the location of the receiving transducer.

No boundary conditions were applied in the FEA setup which means the model was unconstrained. This most adequately represented the experimental setup, whereby the specimen was placed on an acoustic foam during the ultrasonic testing which did not practically restrict the motion of the specimen.

5.1.4 Results and Discussion

At each fatigue stage outlined in Table 5-1, the β parameter was calculated from the received spectrum during ultrasonic testing. However, only the value of β estimated at the first fatigue interval (10,000 cycles) was used as an input to the constitutive model *umat41* in order to simulate the nonlinear wave propagation and determine the level of the generated second harmonic. Therefore, the nonlinear parameter was kept constant for all subsequent simulations. In order to represent the crack growth in the numerical domain, the number of nonlinear response elements was increased according the observed crack length for every simulation condition mimicking the experimental setup. Hence, six simulations were carried out representing each fatigue stage specified in Table 5-1. Figure 5.7 shows the results in the frequency domain which was obtained by preforming a FFT on the received time domain signal, which was experimentally recorded in Volts using a receiving piezoelectric transducer and numerically by post-processing the velocity history at the receiving nodes. Evidently, the 2nd harmonic frequency content is present in both experimental and computational scenarios.

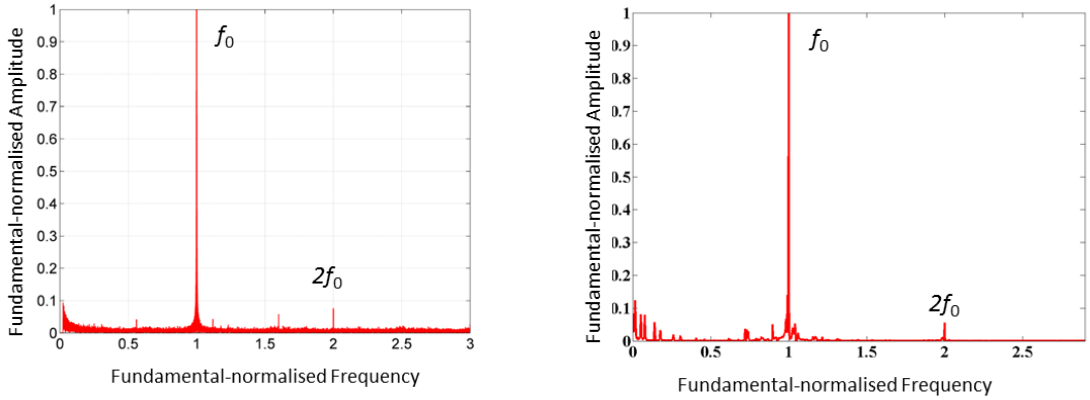

Figure 5.7: (a) experimental and (b) numerical (LS-DYNA®) frequency spectrum response after 10,000 fatigue cycles.

Figure 5.8 presents the overall results in terms of β, normalised to the maximum value obtained at 90% fatigue life of the specimen.

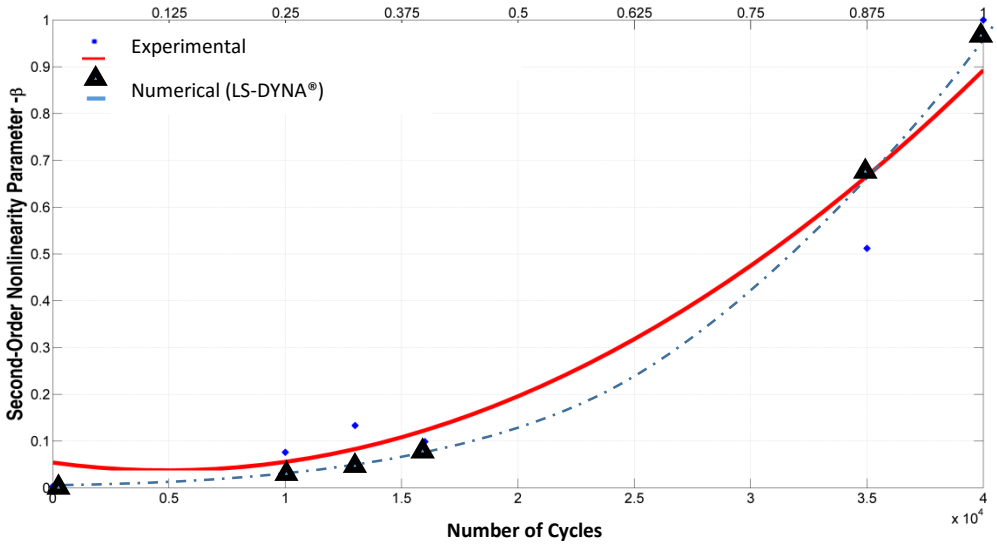

Figure 5.8: normalised 2nd order nonlinear parameter β vs. fatigue life.

The crack length was inspected with a digital microscope at each fatigue interval in order to ensure that the generation of the 2nd harmonic frequency ($2f_0$) and the increasing β corresponded to the crack propagation. Growing value of β signifies an amplitude reduction of f_0 relative to $2f_0$. Experimentally obtained data demonstrates a clear increase of β with increasing fatigue cycles and therefore crack length, which can be expected since the larger crack interface would lead to more prominent "clapping/rubbing" effects generally known as CAN. Furthermore, the devised nonlinear elastic material model based on the 2nd order nonlinearity of the classical nonlinear theory proved capable of simulating the presence of the 2nd harmonic ($2f_0$) in the response spectrum and correlated well with the trend of the experimental data. However, it is important to note that in the present numerical modelling approach, the growth and the propagation area of the crack were known. Moreover, the design of the specimen promoted a controlled crack generation under cyclic loading in the known area of high stress concentration which may not be the case in a real life cycle of a component.

5.1.5 Conclusion

The presented results suggest that it is possible to simulate a complex phenomenon of nonlinear wave propagation in 3D continuum using FEA modelling based on classical nonlinear ultrasound theory. In addition, it may be possible to estimate the frequency response of a cracked structure and its residual fatigue life without the need for base line testing as β can be chosen arbitrarily. By exciting a medium with a specific single harmonic frequency, finite elements with the devised nonlinear material model indicated the generation of the 2nd harmonic frequency in the response spectrum which is consistent with the behaviour of cracked/damaged materials. Indeed, a good correlation was obtained between the experimental and numerical results obtained at various stages of the fatigue life of the sample and therefore the numerical model can provide useful insight about the progression of damage within a component. Although, an isotropic material was used in the present case as the fatigued sample was manufactured from aluminum alloy, the devised nonlinear constitutive model allows for general orthotropy, and therefore, can be employed to represent laminated composite materials. Hence, it can provide the first step in potential FEA methods enabling the incorporation of nonlinear ultrasound effects for assessment of the generation/dispersion of damage-induced nonlinearities in complex structures.

5.2 Thermosonic Evaluation of the 2nd Order Harmonic Generation and Frictional Heating in Fatigued Structures

Having experimentally (by means of piezoelectric transducers) and numerically (LS-DYNA®) considered the 2nd harmonic generation in a fatigued specimen in the previous Section, this Section focuses on thermal imaging and imaging of the 2nd harmonic frequency component in the vicinity of the crack.

5.2.1 Introduction

Combining the nonlinear ultrasound techniques with sonic thermography (thermosonic) has a potential to provide an efficient and consistent (repeatable) NDT/NDE solution. As explained in Chapter 3, thermosonic methods typically use ultrasound in order to excite the regions of the component containing damage such as fatigue cracks. This ultrasonic stimulation causes the defect surfaces to move relative to each other generating heat that can be detected using an IR camera. In addition, the heating can be a result of the thermoelastic effects (see Chapter 3.4.1.3), heat dissipation due to reversible anelastic damping and irreversible plastic deformation [249]. However, as mentioned in Chapter 3.2.6, the main detriment of the thermosonic NDT methods is poor repeatability of testing results, especially involving high-power ultrasound horns producing a complex non-reproducible state of acoustic chaos characterised by the broad range of the excitation frequencies [104, 250]. It was shown that the heat generation in damaged regions can be enhanced by single tone ultrasonic stimulation of the structure at defect-related resonance frequencies referred to as LDR [251]. The principle of LDR was used in present study to aid the frequency selection process in evaluating heat generation at crack interface in a fatigued aluminium coupon. Furthermore, the frequencies were chosen both arbitrarily and by considering the highest 2nd harmonic amplitude in the response spectrum. The laser-Doppler vibrometer (LDV) equipment was used in order to measure the out-of-plane vibration velocity in the vicinity of the crack, while the IR camera provided the information about the heating at the chosen frequencies.

Due to relatively low finite-amplitude excitation resulting in small strains, the present analysis adequately assumed that no wear took place.

Other studies [103] related the power dissipated by the crack during vibration defining a crack loss factor η_{crack} (see Eq. (3.12) of Chapter 3.2.6) and evaluated the thermographic efficiency by the magnitude of the temperature gradient at the crack. It is generally expected that exciting a structure at global and local (LDR) resonant frequencies would result in higher thermal gradients driven by the increase in vibration levels. Indeed, the temperature rise can be predicted by studying the vibration

damping at the crack which can be determined from the local vibrational strain [250]. Therefore, it is important to evaluate the modes of vibration associated with the fatigue crack in order to determine the corresponding heating mechanisms. As explained in Chapter 3.4, nonlinear ultrasonic methods rely on the production of harmonics that arise due to clapping and rubbing phenomena at the crack interface stimulated by the propagating wave or structural vibration. Rubbing is associated with frictional heating, while clapping is related to the transfer of the deformation energy; collectively, three mechanisms can be defined similarly to the crack modes from classical fracture mechanics shown in Figure 2.4 of Chapter 2.1: mode I can be attributed to clapping, mode II to in-plane rubbing and mode III to out-of-plane rubbing. Mode III was of primary interest to this study driven by the higher sensitivity of the LDV equipment to the out-of-plane (normal to the laser beam) surface vibration velocity as compared to the in-plane velocity. Modal analysis by means of FEA using LS-DYNA® was conducted in order to identify the natural frequencies and the corresponding vibration modes that would lead to high displacement in the vicinity of the crack interface which would in turn increase the likelihood of clapping or rubbing. Subsequently, these frequencies were sought in the experimental work using LDV.

5.2.2 Experimental Setup

The physical testing involved harmonically exciting an aluminium coupon in defect free and in fatigued state (with a transverse crack) with a single tone sinusoidal signal. The test piece (Aluminium (6061)) was manufactured and cyclically tension-loaded using an Instron 1332 machine in in accordance with the ASTM standards E399 [252] and E647 [253] in order to generate a prolonged fatigue crack. The aim of the experimental setup was twofold: (i) to measure the vibration velocity amplitude polarised in the out-of-plane direction on the surface of an aluminium specimen using a laser-Doppler vibrometer (LDV) (Polytec PSV-400) and (ii) to measure the infrared intensity (heating) on the surface of the specimen using an IR camera (CEDIP Jade 3 MWIR 3-5 µm). The setup is shown in Figure 5.9.

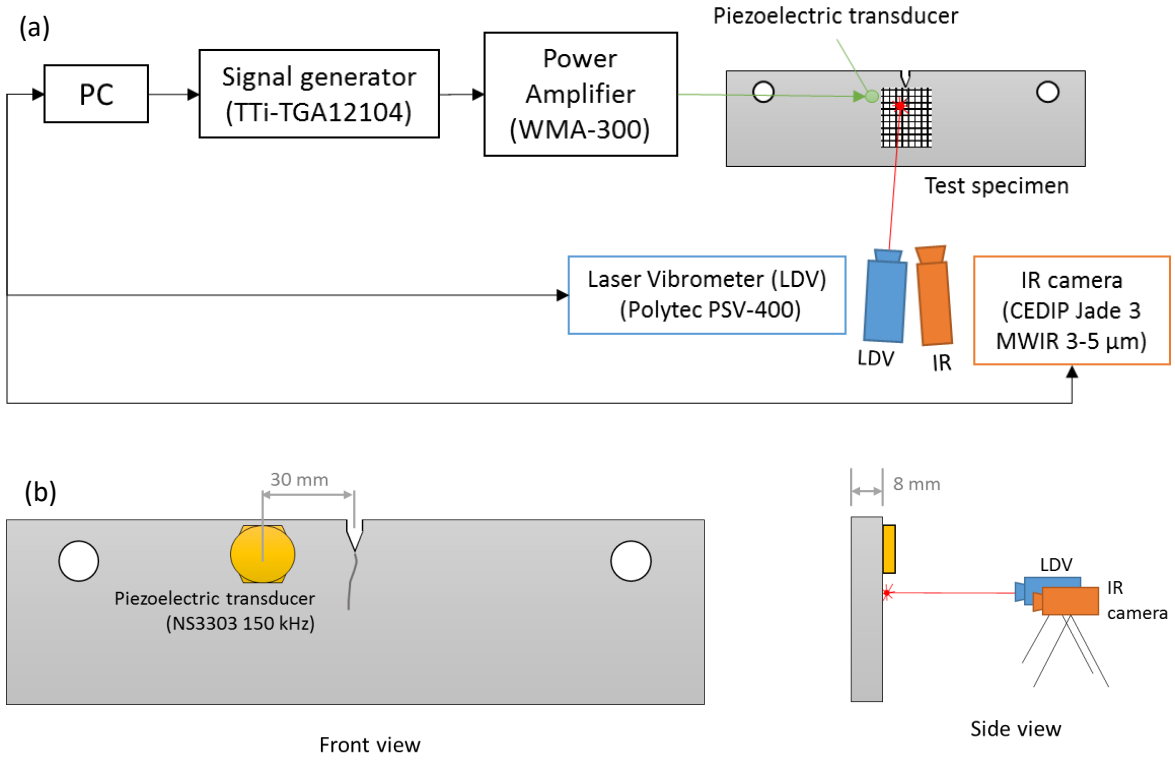

Figure 5.9: instrumentation setup.

As illustrated in Figure 5.9 (a), a waveform generator (TTi-TGA12104) was connected to an amplifier (WMA-300) and piezoelectric transducer (McWade Associates NS3303 150 kHz) in order to provide the excitation ranging from 110 kHz to 120 kHz at 200 V. The frequency range was chosen based on the amplitude level in the response spectrum during the initial frequency sweep. The transducer was fixed with a clamp, while the coupon was lightly clamped with the aid of damping pads at both ends just below the fatigue loading holes. The IR camera used was a mid-wavelength infrared device that uses an electrically cooled indium antimonide detector and has a frame rate of up to 150 Hz, a resolution of 320 x 256 pixels and average NeDT of 30 mK.

The specification of the sample geometry is presented in Figure 5.10.

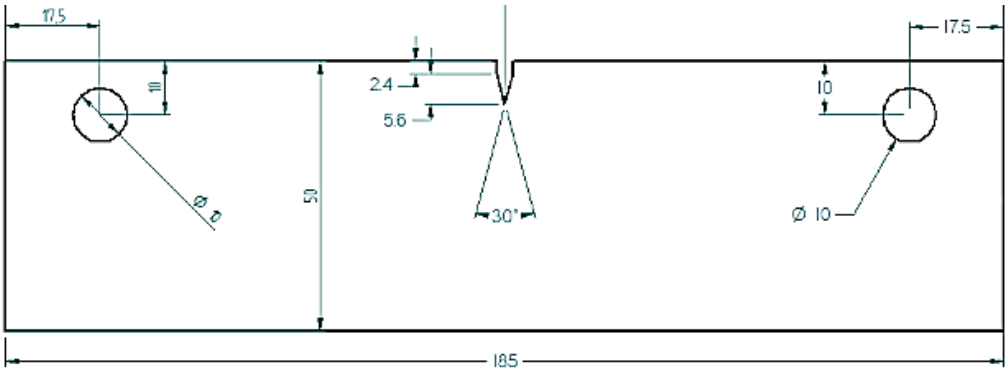

Figure 5.10: specification of the aluminium sample; all dimensions in mm.

The crack lengths as observed using a digital microscope as well as the grid of data points used in LDV experiments is shown in Figure 5.12.

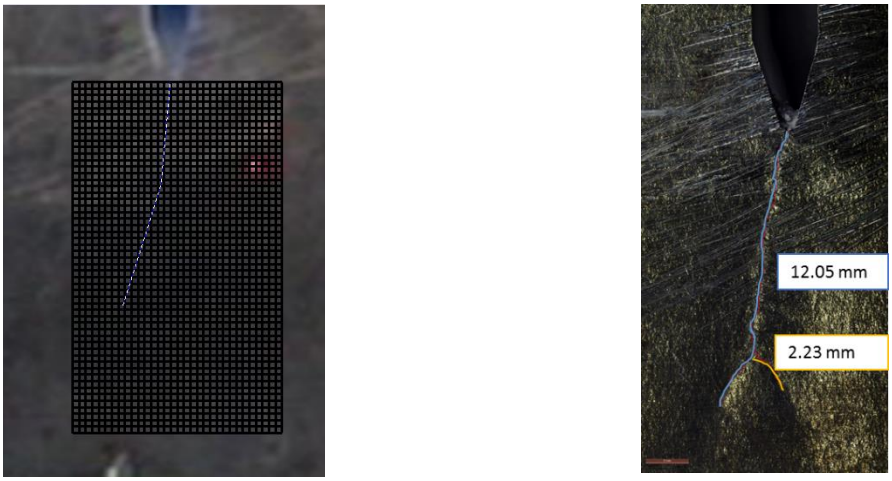

(a) (b)

Figure 5.11: (a) grid of data acquisition points - LDV scan region; (b) fatigue crack microscope inspection (front surface).

Figure 5.12 shows an actual image from the IR camera indicating the heat production at the crack.

Figure 5.12: IR camera image of crack heating at 120 kHz excitation frequency.

5.2.3 Resonant Frequency Analysis

First, a modal analysis was performed numerically on the undamaged (fatigue-free) structure using an implicit solver capability of LS-DYNA® in order to explore the natural modes of vibration of the structure focusing on the expected crack area. This provided an understanding of the potential for activating "clapping"/"rubbing" phenomena. It is well-known that the stiffness of the structure changes in its damaged state, and therefore, various modes of vibration would be affected differently in presence of a crack. Overall, this approach allowed to discern the modes that would be more pronounced in the out-of-plane direction. Figure 5.13 shows one of the numerically determined natural modes. The geometry was meshed using 3D solid elements.

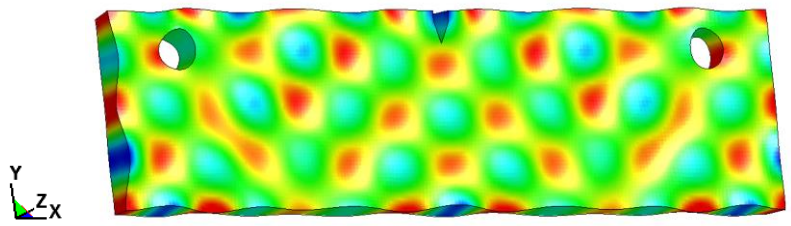

Figure 5.13: a natural mode of vibration determined via numerical modal analysis (LS-DYNA®); contours of out-of-plane displacement at 117,281 Hz for crack-free structure.

The LDV was used to experimentally find the corresponding modes and assess the overall validity of the approach. Figure 5.14 visually shows a good correlation between the experimental and numerical results, which is further confirmed by the quantitative comparison between the attained frequencies listed in Table 5-3.

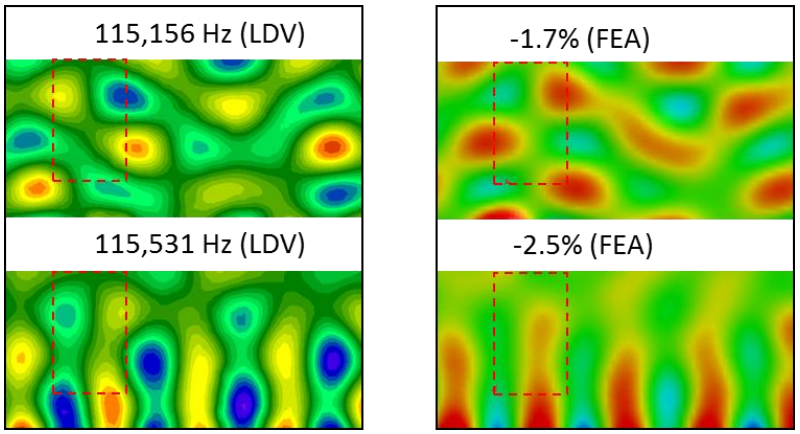

Figure 5.14: comparison between the contours of the out-of-plane velocity (left) obtained by means of LDV experiments and contours of the out-of-plane displacement obtained via modal analysis (LS-DYNA®); crack-free structure.

LDV (Hz)	115,156	115,531	116,531	117,281	118,188	118,500	118,875	119406
FEA (% diff.)	-1.7%	-2.5%	-1.2%	-0.2%	-2.1%	-2.0%	-1.7%	-3.1%

Table 5-3: comparison between the experimentally (LDV) and numerically (LS-DYNA®) obtained natural modes of vibration; crack-free structure.

Subsequently, the aluminium specimen was subjected to fatigue testing resulting in a transverse crack as shown in Figure 5.11. The crack was represented in the computational (FEA) domain by careful modelling of the crack surface and assigning double nodes at the crack interface. Figure 5.15 shows one of the numerically determined natural modes using a meshed model of the specimen containing a fatigue crack. The geometry was meshed using over a million 3D solid elements in order to adequately characterise the topology of the crack.

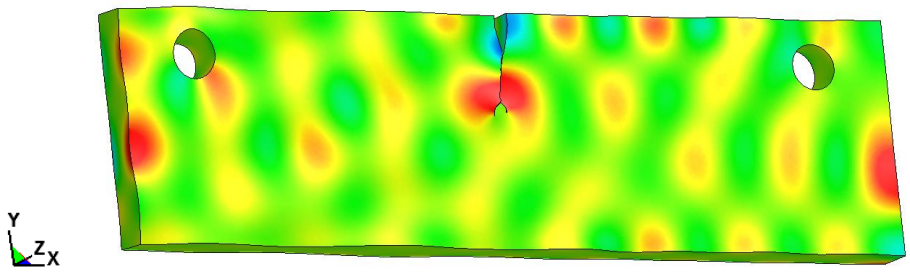

Figure 5.15: a natural mode of vibration determined via numerical modal analysis (LS-DYNA®); contours of out-of-plane displacement at 117,281 Hz for the cracked structure.

Figure 5.16 shows a good correlation between the experimental (LDV) and numerical results, while the quantitative comparison between the attained frequencies is listed in Table 5-3. Only the modes that were characterised by the out-of-plane displacement of the order of magnitude larger than the in-plane were chosen from the results of modal analysis.

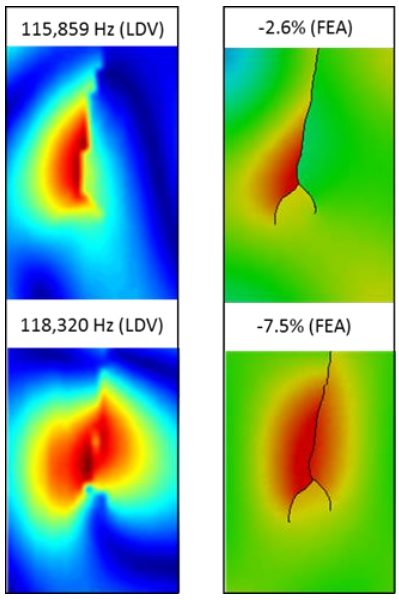

Figure 5.16: comparison between the contours of the out-of-plane velocity (left) obtained by means of LDV experiments and contours of the out-of-plane displacement obtained via modal analysis (LS-DYNA®); cracked structure.

As indicated in Figure 5.16, in the case of 118,320 Hz, both sides of the crack displayed high out-of-plane velocity acting in-phase with each other, while at 115,859 Hz the crack sides were moving in opposite out-of-plane directions. As it will be shown, this behaviour affected the effective heating at

the crack with the latter one resulting in higher temperature gradient as well as enhanced 2nd harmonic generation.

115,078	115,859	116,406	117,345	118,320	118,750	118,820	119,260
-3.6%	-2.6%	-4.0%	-2.1%	-7.5%	-3.3%	-5.7%	-4.1%

Table 5-4: comparison between the experimentally (LDV) and numerically (LS-DYNA®) obtained natural modes of vibration; cracked structure.

Evidently, the discrepancies between the experimentally and numerically obtained natural frequencies were larger when the fatigued sample was considered in a cracked state but were within 7.5%. This was expected as the complex internal structure of the crack was merely approximated in the computational approach. It is also interesting to note that all modes appeared to be to some extent underestimated by the modal FEA for both damaged and undamaged structures.

In order to select a frequency range, a frequency sweep was conducted covering the spectrum up to 200 kHz; the range of 110 kHz to 120 kHz resulted in the highest amplitude of the fundamental (f_0) and the 2nd harmonic ($2f_0$) response. Subsequently, eleven frequencies were chosen based on the level of the fundamental, 2nd harmonic and the outcome of the aforementioned resonant frequency response analysis. Figure 5.17 shows the fundamental and the 2nd harmonic spectrum obtained as an average of the individual spectrums obtained at each data acquisition point in the LDV grid (Figure 5.11(a)).

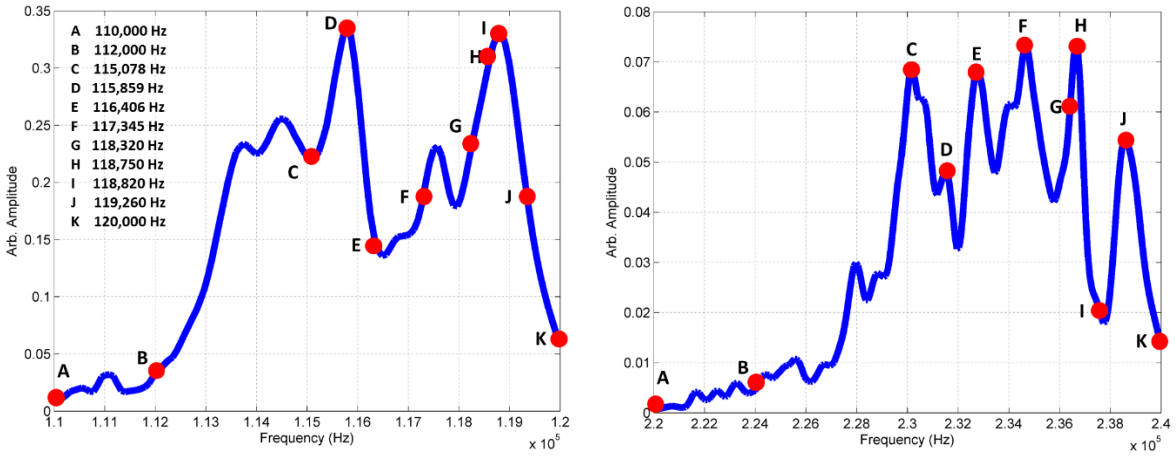

(a) (b)

Figure 5.17: comparison of the average spectrum for (a) the fundamental frequency response and (b) the 2nd harmonic frequency response.

The list of the frequencies selected for further thermosonic testing is presented in Table 5-5. Several frequencies were chose arbitrarily for comparison purpose.

	Frequency (Hz)	Note
A	110,000	Arbitrary Selection
B	112,000	Arbitrary Selection
C	115,078	High 2nd Harmonic Response
D	115,859	High Fundamental Response, High 2nd Harmonic Response
E	116,406	High 2nd Harmonic Response
F	117,345	High 2nd Harmonic Response
G	118,320	High 2nd Harmonic Response
H	118,750	High 2nd Harmonic Response, High Fundamental Response
I	118,820	High Fundamental Response
J	119,260	High 2nd Harmonic Response
K	120,000	Arbitrary Selection

Table 5-5: a list of frequencies selected for further testing.

5.2.4 LDV Testing

A LDV was used to evaluate the out-of-plane amplitudes of f_0 and $2f_0$ for the fatigued coupon. The coupon was continuously excited using an ultrasound transducer at the frequencies chosen (Table 5-5), the time domain signal was captured for the given grid area and a fast fourier transform (FFT) was performed to determine the maximum amplitudes. Figure 5.18 shows f_0 and $2\ f_0$ for the evaluated region superimposed on the cracked region. It is clear to see that for this case f_0 occurs to the left of the crack (the same side as the excitation signal generation), while the 2nd harmonic response occurs on the opposite side. This follows nonlinear ultrasound theory that further harmonic generation occurs at damage interfaces and dislocation positions, shown by: refelction of f_0 to the left of the crack interface, and propagation of further harmonic generation through the crack interface (clapping/rubbing) resulting in displacement occuring on the opposite side.

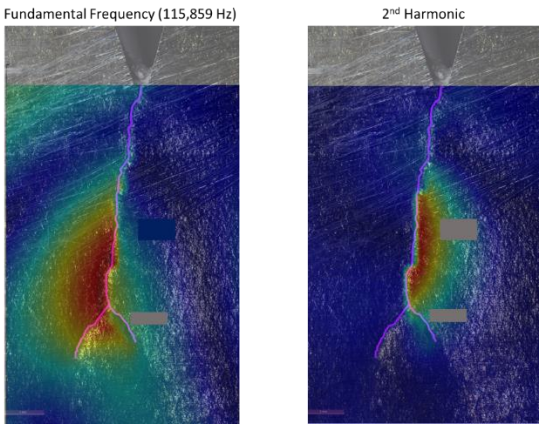

Figure 5.18: fundamental frequency f_0 (left) and the 2nd harmonic $2f_0$ (right) response superimposed over cracked region; excitation frequency of 115,859 Hz.

It is expected that the combined interaction of the f_0 and $2f_0$ at opposite sides of the crack results in greater heating. Reliably evaluating which combination gives rise to the highest heating is the main aim of this investigation. Figure 5.19, Figure 5.20 and Figure 5.21 show the relative fundamental and second harmonic responses for the frequencies tested. For the frequencies that exhibited large second harmonic responses there is a clear separation of f_0 and $2f_0$ on either side of the crack interface.

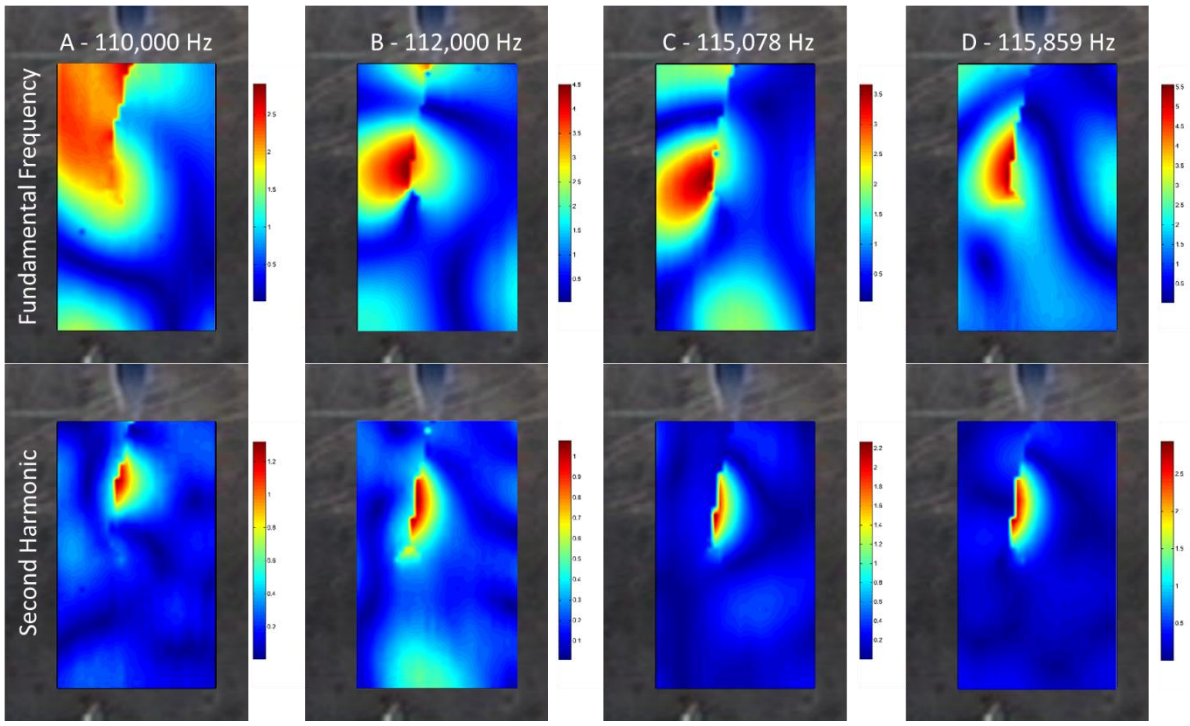

Figure 5.19: fundamental (f_0) and the 2nd harmonic ($2f_0$) relative velocity contour plots at various excitation frequencies (A-D).

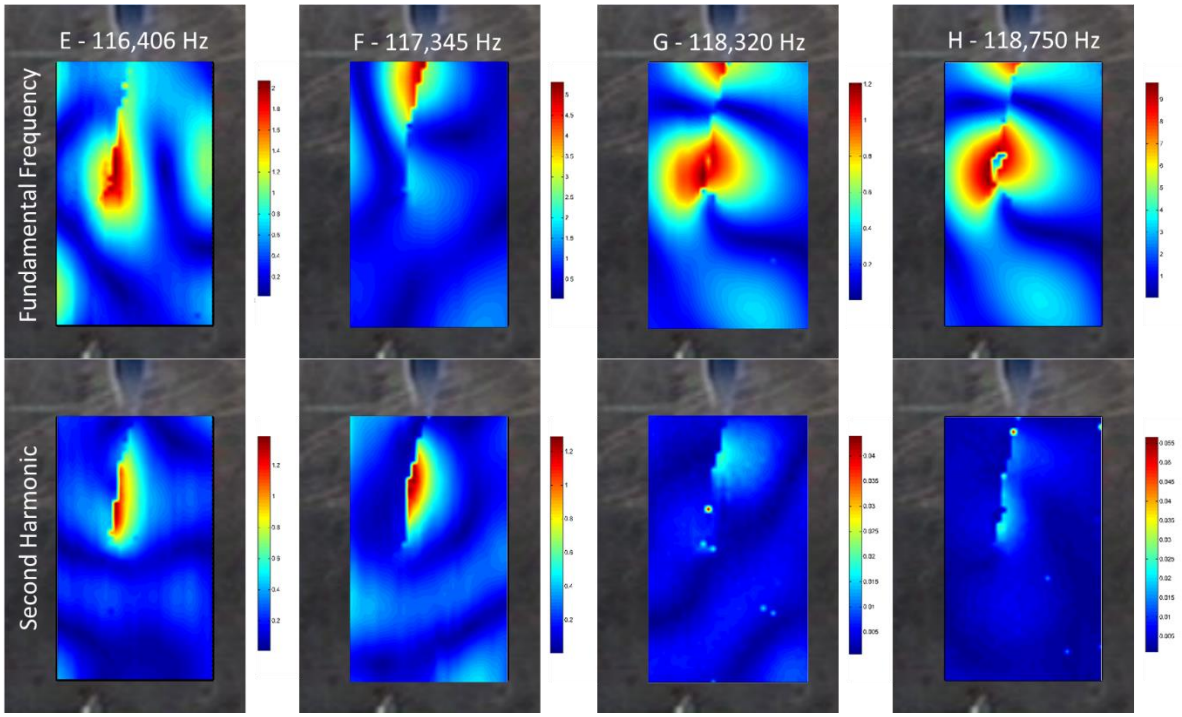

Figure 5.20: fundamental (f_0) and the 2nd harmonic ($2f_0$) relative velocity contour plots at various excitation frequencies (E-H).

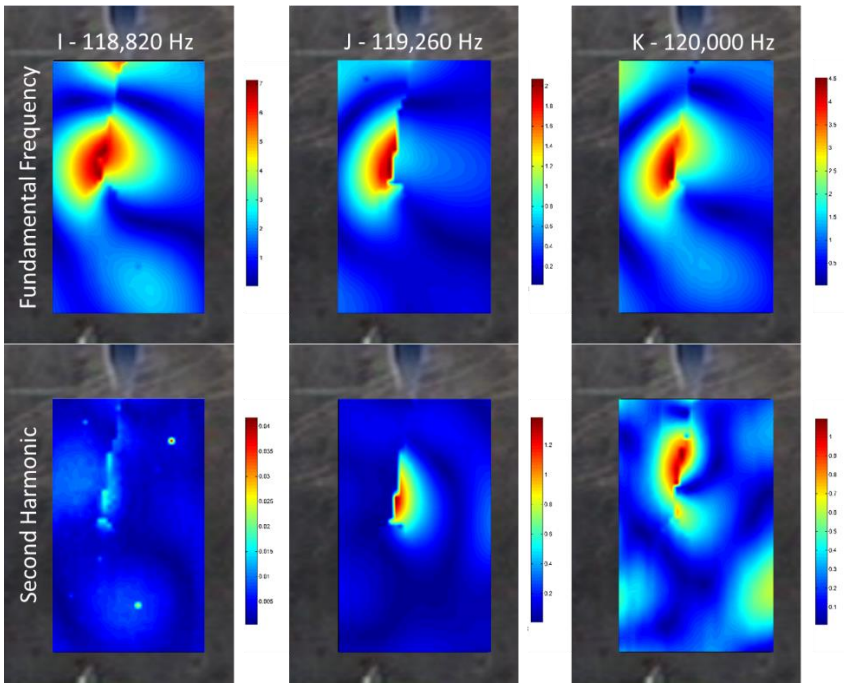

Figure 5.21: fundamental (f_0) and the 2nd harmonic ($2f_0$) relative velocity contour plots at various excitation frequencies (I-K).

By comparing the response of the fundamental and the 2nd harmonic of the damaged coupon to the undamaged modal shape, it is clear that the relative position of the out-of-plane min/max velocity amplitudes directly affects the amplitude and position of f_0 and $2f_0$ responses. In the event that the

min/max locations occur somewhat evenly over the cracked region (rather than on either side - frequencies 115,859 Hz, 117,345 Hz and 119,260 Hz), there is a clear reduction in the production of the second harmonic. Whereas when min/max locations are either side of the cracked region there is a split between f_1 response (which is located on the same side of the excitation frequency) and the production of $2f_1$ which is located on the opposite side of the crack interface (with reference to the excitation signal). Furthermore, the results suggest that when the fundamental and the 2nd harmonic responses are split either side of the crack, a greater out-of-plane rubbing of the crack interface occurs, which should in turn result in a greater generation of frictional heating.

5.2.5 Thermosonic Testing

In order to determine the actual heating at the cracked interface, sonic thermographic testing was conducted using the experimental setup outlined in Section 5.2.2. Various relative temperature profiles were evaluated by capturing temperature changes (using an IR camera, Figure 5.22, Figure 5.23 and Figure 5.24) over time during sonic excitation at various points on the damaged coupon. Figure 5.22 shows the locations of the measured temperatures.

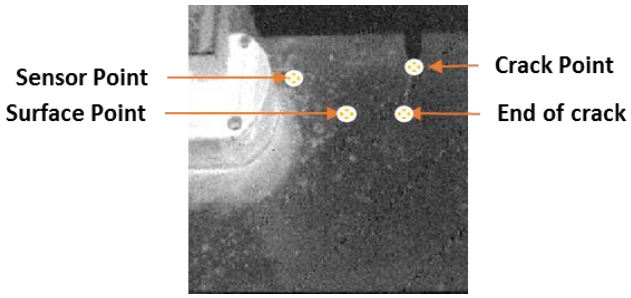

Figure 5.22: IR data acquisition points.

By comparing the thermal gradients between the different excitation frequencies it can be seen that the gradients are greater around the cracked region relative to the surface position (undamaged or non-cracked location) and the crack tip This is in agreement with the fundamental and the 2nd harmonic responses (outlined in Figure 5.19,Figure 5.20 and Figure 5.21) which show that the greatest relative velocity occurs either at the beginning (near the notch) or near the middle of the crack, and therefore heating in these areas should be greater.

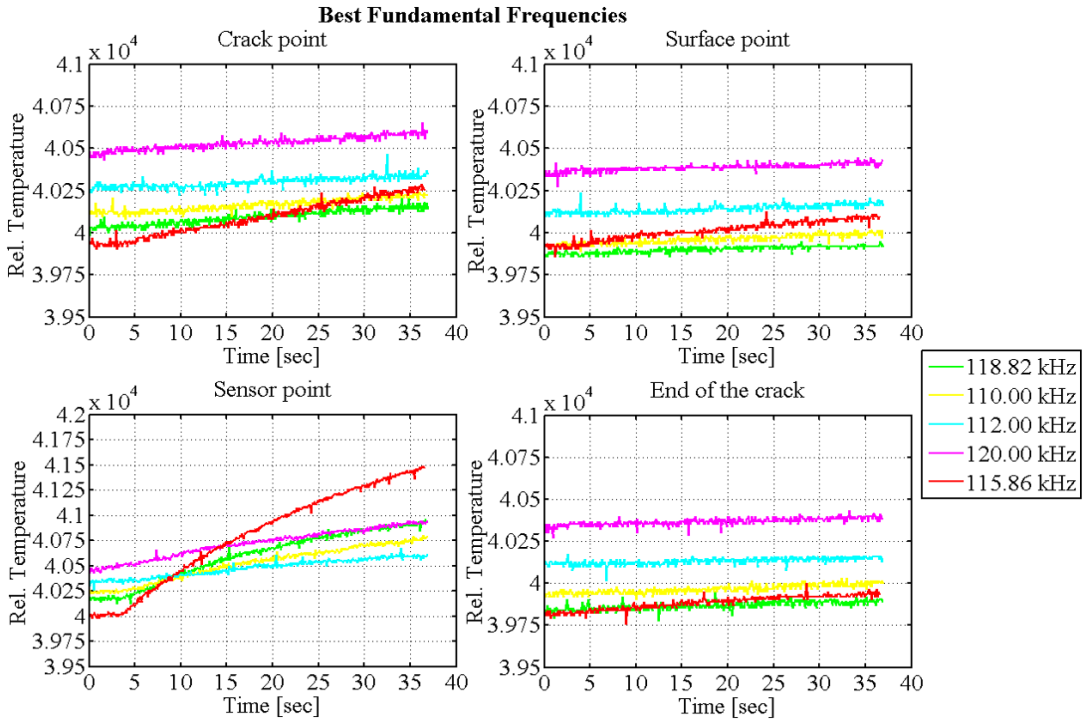

Figure 5.23: best (in terms of amplitude) fundamental (f_0) frequencies relative (arbitrary units) temperature profiles for positions at the crack point, surface point, sensor point and end of the crack.

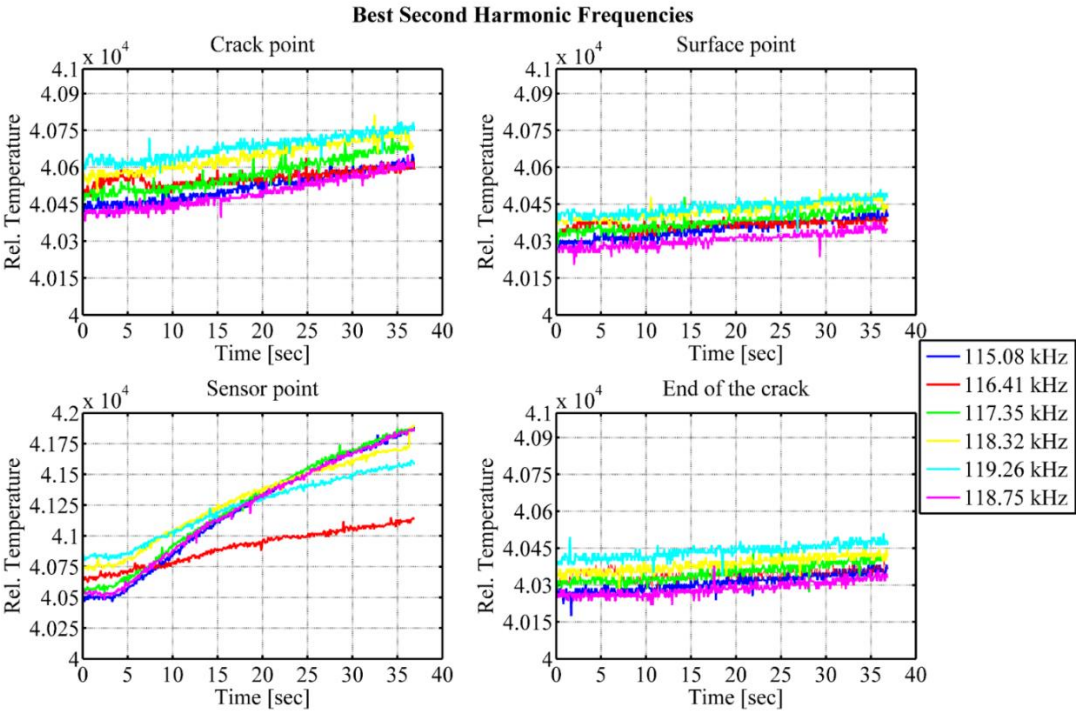

Figure 5.24: best (in terms of amplitude) 2nd harmonic ($2f_0$) frequencies relative (arbitrary units) temperature profiles for positions at the crack point, surface point, sensor point and end of the crack.

The thermal gradients for each frequency and position are highlighted in Figure 5.25. The highest thermal gradients refer to the frequencies that provided the greatest average 2nd harmonic responses over the inspected region with the exception of 115,859 Hz. Although, local frequency response

around the cracked region shows that the largest 2nd harmonic in terms of frictional heating is in fact at 115,859 Hz. This demonstrates that the combination and interaction between f_0 and the nonlinear vibration modes ($2f_0$) near the crack interface can have a large effect on the generation of heat, and ultimately the effectiveness of the thermosonic method.

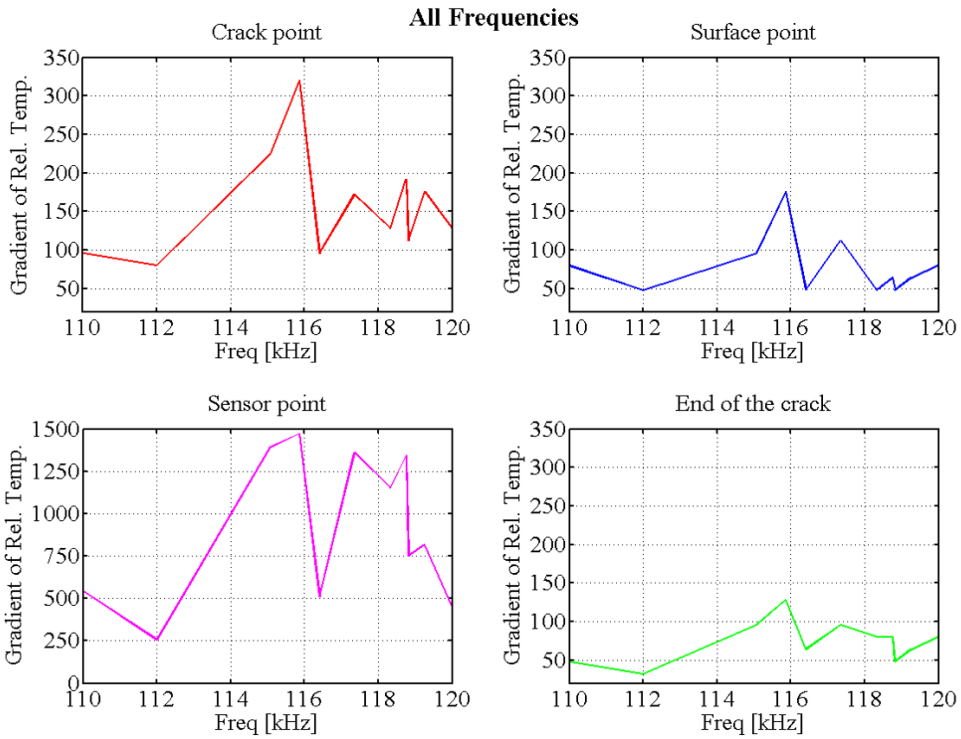

Figure 5.25: relative (arbitrary units) thermal gradients for various frequencies tested for positions at the crack point, surface point, sensor point and end of the crack.

In order to assess the effect of nonlinearity around the cracked region, β_{ratio} (Figure 5.26 (b), blue line, normalised) was calculated by determining the ratio $\beta_{damaged\ region}/\beta_{undamaged\ region}$ (Figure 5.26 (a)), it is possible to evaluate which frequency gives rise to the largest nonlinearity near the cracked area relative to the average velocity over the total examined area. By comparing the β_{ratio} to the relative temperature profile (normalised) it is clear that the production of nonlinearities are in line with the heat generated at the cracked region.

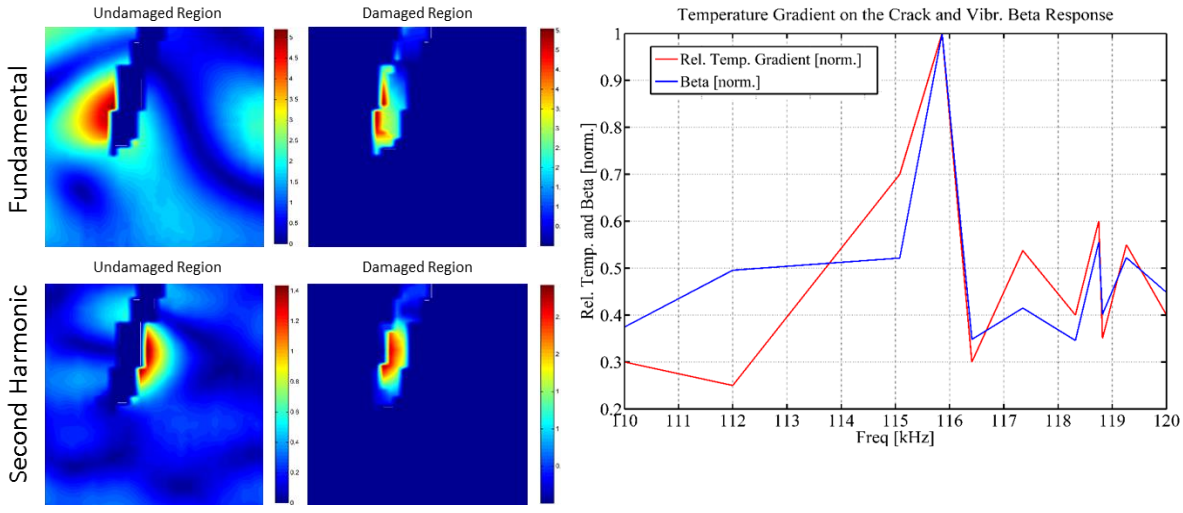

Figure 5.26: damaged and undamaged regions (excited at 115,859Hz) selected for the assesssment of the nonlinear parameter β, (b) relative (arbitrary units) temperature gradient at the crack point vs. normalised beta ratio β_{ratio}.

5.2.6 Conclusion

This work utilised a sonic thermography technique to evaluate the frictional heating in the context the 2nd harmonic generation in cracked isotropic sample. The results showed that the greater the production of the 2nd harmonic near a cracked region the greater the generation of heating through sonic excitation. As was expected, the fundamental frequency excitation of damaged regions resulted in greater heat generation than that produced by the 2nd harmonic effects. However, more importantly, the combination of linear and nonlinear effects within the heating process can have a great influence on overall heat production and thus enhancing the probability of damage detection.

5.3 Thermosonic NDT Method for the Evaluation of BVID in Composite Stiffener Panel by means of Narrow Sweep Excitation

Building on the techniques developed in Sections 5.1 and 5.2, this work focused on developing a nonlinear sonic thermography method applicable to complex aerospace components such as stiffener panels. These structures play an integral role in aerospace applications and include fuselages, control surfaces, spar webs etc. Stiffener panels, especially when incorporated as part of aircraft exterior, are particularly prone to BVID with reliable detection of internal damage being impeded by its structural complexity. This is further addressed in the following Section.

5.3.1 Introduction

As explained in Chapter 1.1.2, the assessment of laminated composite materials subjected to LVI damage can be challenging as there may be very little visually discernible surface damage, while large areas of intra- and inter-laminar cracks (delaminations) may occur under the surface which can significantly reduce the strength of the material. This type of damage is generally referred to as BVID and can be caused during manufacturing as well as in service. Due to the hidden nature of BVID, composite materials must be regularly inspected. Furthermore, due to the ever increasing size of the composite structures, inspection should be rapid and cover large areas. There is a significant interest within the industry for thermosonic NDT methods due to their ability to satisfy these requirements [254]. However, as emphasised in Section 5.2.1, one of the major difficulties facing the ultrasonic thermography is associated with the repeatability of testing results which is typically impeded by the intrinsically stochastic physical behaviour governing the heat generation process in vibrating defects [250]. It was shown that heat generation is increased when exciting at certain resonance frequencies [255] but the determination of these frequencies is difficult and the repeatability is low. Moreover, several studies have shown that certain excitation frequencies may in fact terminate heat generation at the crack or damage interface due to an increase of compressive stresses which lock the interface with static friction [256].

According to the experimental evidence [203, 257], the heat generation in damaged regions can be linked to three mechanisms: (i) frictional rubbing of crack-face contact regions, (ii) elasto-plastic deformations in the crack or damage zone, and (iii) viscoelastic dissipation at stress concentrations (around delaminations and other defects) in certain materials. Indeed, the kinematics of the delaminated regions caused by the presence of small stresses exerted by the ultrasonic waves can result in frictional rubbing of contact regions of damage interfaces and viscoelastic losses (hysteresis) during the loading and unloading cycles of ultrasound excitation. Frictional heating is dependent on

the three main factors: the coefficient of friction, contact pressure and relative sliding velocity. Thus, the heating mechanism can be assumed to result from a combination of frictional heating due to "rubbing" (in-plane motion) between the rough surfaces of the delamination zone as well as "clapping" (out-of-plane motion) of delamination regions. According to tribologists [258], the frictional energy dissipated as heat is conducted into the contacting bodies, where surface and near-surface temperatures can change the structural properties of the sliding materials which ultimately results in wear. For the purpose of this work, it was assumed that due to the material properties (high melting points) of the given composite component and relatively low amplitude of the applied excitation, heating caused by friction from ultrasound stimulation did not result in any melting, softening or further damage to the material.

In addition to frictional heating, a local stiffness decrease at the damage location can result in localised temperature rise, and therefore, the conversion of mechanical energy into heat can be evaluated using the theory of thermoelasticity (see Chapter 3.4.1.3).

The method developed herein relies on the acousto-ultrasonic stimulation of damaged regions, whereby the excitation frequencies are determined by following on from the principles of classical and nonclassical nonlinear ultrasound techniques discussed in the preceding chapters. The excitation frequencies are considered to be damage-specific resonance frequencies also known as local defect resonance (LDR) which excite and heat the damaged regions [214]. The process aims to identify the damage-specific excitation frequencies that enhance the "clapping/rubbing" phenomena in defects (e.g. cracks, delaminations), thereby generating heat that can be observed using an infrared (IR) camera. It has been experimentally shown that in order to attain the maximum acoustic wave-defect interaction, the concept of LDR should be used [259]. Using this concept, a strong wave-defect interaction was confirmed by a resonance-induced rise of local temperature of the defect. The LDR frequency behaviour of a single horizontal near-surface delamination was shown to be dependent on the resonance of the material layer above the defect (thickness d) and can be analytically estimated as [260]

$$\boldsymbol{f}_{LDR} \cong \frac{\boldsymbol{3.2d}}{\boldsymbol{2r^2}}\sqrt{\frac{\boldsymbol{E}}{\boldsymbol{12\rho(1-\nu^2)}}}, \qquad \textbf{(5.11)}$$

where r is the radius, E is the Young's Modulus, ρ is the density of the material and ν is Poisson's ratio. Initially, an experimental nonlinear ultrasound method was used to determine the LDR to evaluate multiple BVIDs in the stiffener panel. Given that the production of further harmonics can be related to damaged regions, the 2nd harmonic was measured over a range of frequencies for the given test piece in order to determine the frequencies that gave rise to the largest 2nd harmonic amplitudes. This indicated which excitation frequency gave the highest levels of "clapping/rubbing" at the damaged

regions, and thus enabling heating. These frequencies were then evaluated by measuring the relative temperature rise at the centre of the damaged regions. This method relies on knowing the location of damage, and as such is not applicable to post-manufacturing or in-service testing. This is primarily due to the fact that in reality, with an unknown defect/damage geometry and location, the determination of the LDR is problematic. Further adding to this difficulty is the complexity of composite failure modes and composite structure topologies (such as a curved stiffener panel with multiple layers oriented at different angles). In this study, an ultrasonic C-scan inspection of several LVI damage locations revealed multiple delaminations of various sizes throughout the thickness of the component which is characteristic to BVID. Indeed, the complexity of the LVI-induced through-the-thickness damage distribution was observed in the study of helicoidal composites in Chapter 3. Therefore, an experimental methodology was developed herein which does not require the determination of the LDR. Instead, the stiffener panel can be stimulated by the repeated sweep excitation over a narrow frequency band, thereby exciting multiple LDR frequencies and promoting an effective heating of the damaged regions. In order to further evaluate the experimental results, a fully coupled structural-thermal 3D FEA model was developed using LS-DYNA® allowing to qualitatively assess the dynamic mechanical and thermal response of the structure driven by the harmonic loading. The modelling approach incorporated the devised orthotropic nonlinear elastic constitutive model presented in Chapter 5.1 was used in this study to represent the damaged regions in FEA simulations of the stiffener panel.

5.3.2 Experimental Setup

The impacted sample was a composite stiffener panel with a width of 577 mm, length of 797 mm and thickness of 5.5 mm. The sample consisted of three stiffeners running the whole length of the panel. Four areas of BVID were present: 2 between stiffeners 1 and 2; and 2 between stiffeners 2 and 3. This study focused on damage zones A, B and C. BVID were introduced by LVI testing using an impact energy of 10-15 J. Figure 5.27 shows the modelled stiffener panel, while Figure 5.28 shows the damage locations (A, B and C), stiffener locations and the area evaluated using the LDV.

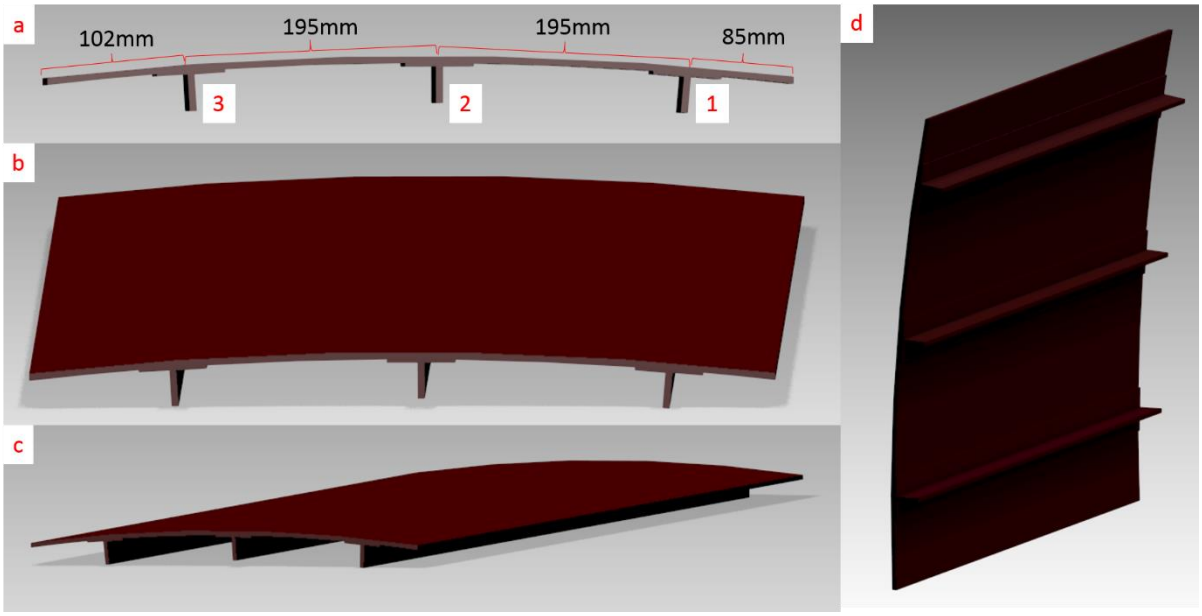

Figure 5.27: modelled stiffener panel: (a) side view with stiffener locations, (b) side and top view, (c) isometric view and (d) bottom view.

Figure 5.28 presents the damage evaluation results found by using a phased array C-scan system comprised of an array of 64 piezoelectric elements. Four methods were used to evaluate the damage regions: time of flight and amplitude (TOF + AMP), AMP, TOF and colour TOF. It is evident that substantial delamination occurred at the specified locations. Using these results it is possible to assess the size of the delaminated regions. Using the coordinate system shown in Figure 5.28, with the top left corner of the panel having coordinates in mm (0,0) and the bottom right (577,797) the position of the damage regions are: A (180,180), B (382,310), C (195,547) and D (367,115). The piezoelectric transducer was placed at locations P1 (42.5,40), P2 (127.5,40) and P3 (322.5,40).

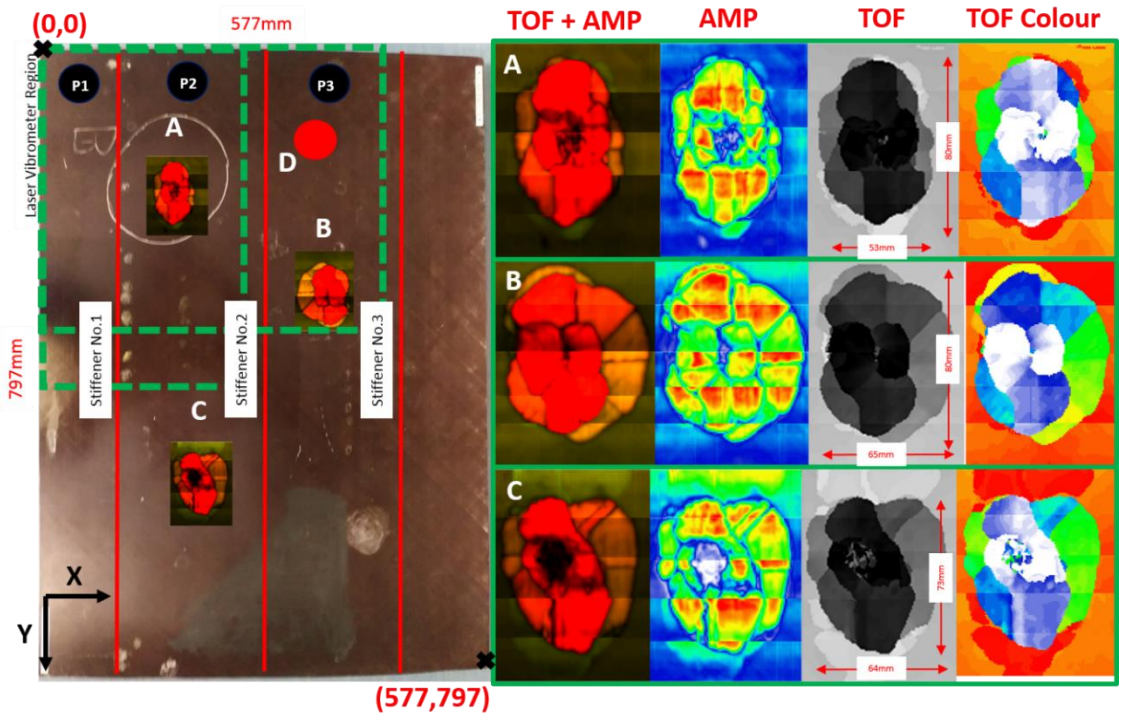

Figure 5.28: summary of composite stiffener panel dimensional characteristics and the damage assessment of BVID regions using ultrasonic phased array C-scan.

A waveform generator (TTi-TGA12104) was connected to an amplifier (Piezoshaker-Amplifier HVA-DB100, includes vacuum pump) and piezoelectric transducer (Piezoshaker PS-X-03-6/1000) in order to provide excitation ranging from 20 kHz to 30 kHz at 200 V. A vacuum pump and sucker attachment was used to attach the transducer to the test samples. The infrared camera used was a mid-wavelength infrared device (CEDIP Jade 3 MWIR 3-5 µm) that uses an electrically cooled indium antimonide detector and has a frame rate of up to 150 Hz, a resolution of 320 x 256 pixels (vertical x horizontal) average NeDT of 30 mK. A single frequency sinusoidal continuous wave form was generated and used to excite the damage regions for the LDR tests while thermal images were recorded by the camera. A narrow sweep excitation between 20 kHz - 30 kHz was used to evaluate the ability of the method. The overall instrumentation setup was virtually identical to the one used in the previous chapter (Figure 5.9).

5.3.3 Structural-Thermal FEA Model

5.3.3.1 Numerical Procedure

In order to model a dynamic mechanical and thermal response of the structure driven by the harmonic loading, a coupled structural-thermal 3D FEA was performed. Different numerical integration schemes were used for solving the structural and thermal models. The structural simulation steps were performed using the methodology outlined in 2.5. The constitutive model accounted for the mechanical as well as thermal strains driven by the elastic deformation. The total strains were integrated in time and the principle strain components include local thermal strains due to thermal expansion of the finite elements

$$\varepsilon_{k+1}^{m} = \varepsilon_{k}^{m} + \alpha^{T,m}\Delta T_{k}\,, \tag{5.12}$$

where ε_{k}^{m} denotes the total element strain components in principle material directions at the time step *k* (i.e. the current state) with m = 1, 2, 3, $\alpha^{T,m}$ are the coefficients of linear thermal expansion and ΔT_{k} is a temperature increment at a current simulation step *k*. The temperature change is calculated based on the thermoelastic theory (Equation 2) for homogeneous orthotropic elastic body under adiabatic conditions [261]

$$\Delta T_{k} = \frac{T_{k}}{\rho C_{p}} \sum_{m=1}^{m=3} \alpha^{T,m}\Delta\sigma_{k}^{m}\,, \tag{5.13}$$

where C_p is specific heat, $\Delta\sigma_{k}^{m}$ is the stress increment in the principle material direction, T_{k} is the absolute temperature at the current time step and other terms have their usual meaning; note that at the initial time step T_{k} is a prescribed variable and was set to 20 °C in this analysis.

The total temperature is then updated according to

$$T_{k+1} = T_{k} + \Delta T_{k}\,. \tag{5.14}$$

Subsequently, T_{k+1} is used as an input to the thermal solver (i.e $T_{k+1} = T_{n}$) which outputs the new value of temperature T_{n+1} for each finite element based on heat conduction which is then used as a current temperature $T_{n+1} = T_{k}$ during next structural time step.

In the coupled solver configuration, a structural step is solved first with a subsequent thermal step for which a fully implicit backward difference method was employed; this is a recursive process until the specified termination time is reached. In the devised model, the harmonic excitation of the structure resulted in the generation of internal strains and stresses which in turn produced the associated temperature gradients. Therefore, the purpose of the thermal step was to compute the transient heat

transfer caused by the simulated thermos-elastic effect. In 3D continuum, the generalised heat conduction equation is [55]

$$\rho C_p \frac{\partial T}{\partial t} = \nabla \cdot \mathbf{q} + Q\,, \tag{5.15}$$

where T is the temperature field, Q is the internal heat generation per unit volume and **q** is the heat flux vector defined in vector and indicial notation as:

$$\mathbf{q} = -\mathbf{k} \cdot \nabla T \;\text{ or }\; q_i = -k_{ij} \frac{\partial T}{\partial x_j}\,, \tag{5.16}$$

where **k** is the thermal conductivity tensor of order two; Eq. (5.16) is the well-known Fourier's heat conduction law and can be discretised numerically using the finite element method as follows [55]

$$T_{n+1} = \left(\frac{\mathbf{C}_n}{\Delta t} + \mathbf{H}_n \right)^{-1} \left[\mathbf{F}_n + T_n \frac{\mathbf{C}_n}{\Delta t} \right], \tag{5.17}$$

where $\boldsymbol{C}$, $\boldsymbol{H}$ and $\boldsymbol{F}$ are the global heat capacity matrix, conductivity matrix and thermal force vector respectively and are equal to a summation of their respective element matrices over the total number of elements in the finite element domain and n denotes the numerical simulation step with $n = 1, 2, 3, \ldots$. A fully implicit numerical scheme was used to solve Eq. (5.17). LS-DYNA® performs time integration using a generalised trapezoidal method which is unconditionally stable [55]. With heat transfer taking place on a longer time scale than the mechanical deformation and therefore the thermal time step can be allowed to be much larger than that of a mechanical time step - for this work, 50 times larger time step was used for the thermal analysis yielding adequate results.

5.3.3.2 FEA Model Setup

The constitutive model was implemented in LS-DYNA® using the User Defined Material (UMAT) modelling interface as described in Section 5.1.3. The skin and the stiffeners of the CFRP panel consisted of 16 plies arranged in quasi-isotropic layup [0/90/-45/+45]2s which were modelled ply-by-ply with 1 finite element through the thickness of each layer. Figure 1 shows the FE model of the stiffener panel with nonlinear material model applied to areas corresponding to the impact damage evaluated by the phased array C-scan during the physical experiment idealised into circular regions. The geometry of the stiffener panel was meshed using fully integrated 8-node solid elements. In present analysis, the maximum frequency of interest was of the order of 50 kHz yielding a sampling rate of 1 MHz in case 20 points per wave length are desired. This information combined with the elastic properties of CFRP material resulted in an optimum element size of 2.5 mm. However, to achieve further increase in spectral resolution, an element size of 1.5 mm was used to discretise the geometry.

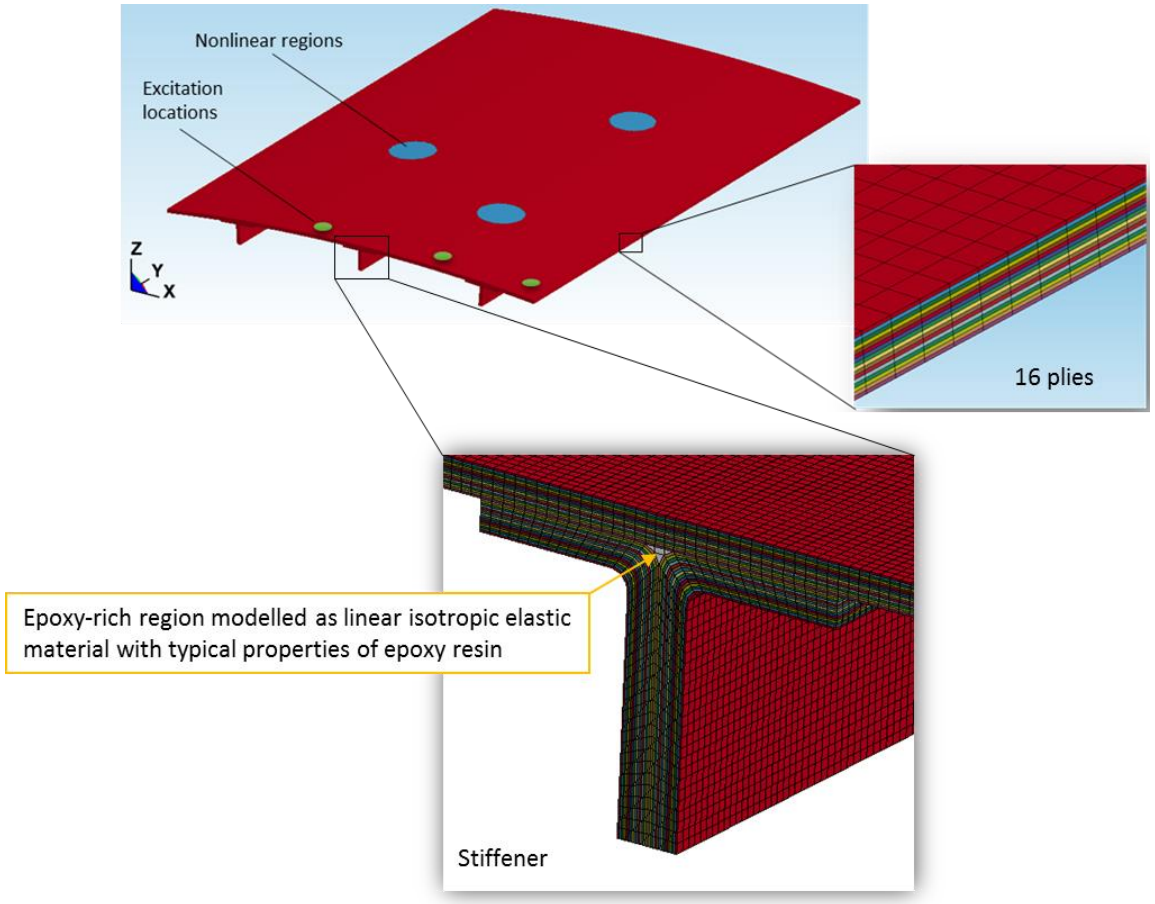

Figure 5.29: FE mesh

The same material model was applied to all regions of the FE mesh with the only difference being the nonlinear parameter β which was set to a non-zero value only for the nonlinear response areas of the model. With $\beta = 0$ the bulk of the mesh behaved as linear orthotropic elastic thermal material; $\beta > 0$ was specified for the damaged regions locally yielding a nonlinear response. Instead of attempting

to determine this parameter experimentally, a sensitivity analysis was carried out in order to identify a suitable value. If β is too small, no significant nonlinearities may arise from the model, whereas large value of β can lead to numerical instabilities causing the simulation to fail. Although computationally expensive, the latter may be mitigated by scaling down the time step size using *CONTROL_TIMESTEP [79] card within LS-DYNA® input deck. The values of β in the region of 1e-2 to 1e-4 worked sufficiently well in the current model with the critical time step size pre-multiplied by the factor of 0.5 aiding the stability of the model. However, the level of nonlinear spectral response depends not only on the values of the classical nonlinear parameters but also on the size of the nonlinear regions and the amplitude of the applied harmonic loading. A simple sinusoidal load was applied to the excitation nodes covering the area of the contact transducer used in the experimental setup

$$F(t) = Q_0 sin(2\pi f_0 t), \quad \textbf{(1)}$$

where Q_0 is the excitation amplitude, which was set to 50N, and f_0 is the excitation frequency set to 22.5kHz. An excitation of 20 ms was applied at the start of the simulation with the wave propagation simulated for further 10 ms.

The numerical problem was specified as a coupled structural-thermal analysis using the card *CONTROL_SOLUTION with thermal solver settings provided in *CONTROL_THERMAL_SOLVER and *CONTROL _THERMAL_TIMESTEP. This way, mechanical strains and stresses were evaluated by the structural module, with adiabatic heat generation arising from the constitutive relationship, while the heat transfer within the FE domain was taken into account using the thermal solver. No heat transfer to the environment was considered.

ρ (g/cm^3)	E_1 (GPa)	E_2 (GPa)	E_3 (GPa)	G_{12} (GPa)	G_{23} (GPa)	G_{13} (GPa)	ν_{12}	ν_{23}	ν_{13}
1.56	121	8.6	8.6	4.7	3.1	4.7	0.27	0.4	0.27

$\alpha_{T,1}$* (C°$^{-1}$)	$\alpha_{T,2}$* (C°$^{-1}$)	$\alpha_{T,3}$* (C°$^{-1}$)
-4.7e-7	3e-5	3e-5

*** Coefficients of thermal expansion at reference temperature of 20° C**

Table 5-6: material properties used in the structural-thermal FEA model of the CFRP stiffener panel.

5.3.4 LDR determination for Nonlinear Ultrasound Stimulated Thermography

Two piezoelectric transducers were used to determine the LDR, the excitation transducer was located at Position 1 (P1 (dark color), PZT-Panametrics NDT X1020 100 kHz 515345) while the signal was captured at Position 2 (P2 (dark color), PZT-Panametrics V101 0.5 MHz 707718), refer to Figure 5.30. The waveform generator was used to generate the sweep signal at the transducer 1, while sensor 2 was connected to an oscilloscope (Picoscope 4244) and PC.

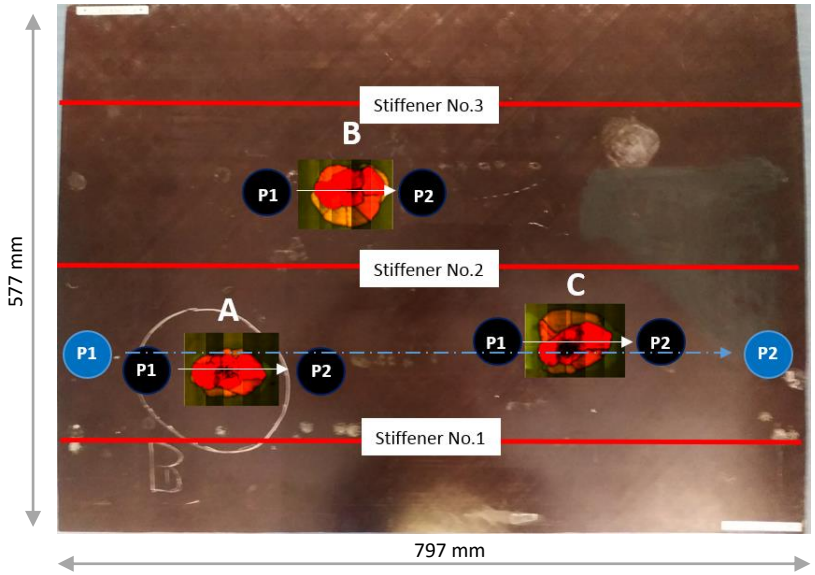

Figure 5.30: location of piezoelectric transducers for LDR frequency evaluation.

A frequency sweep was conducted using the range of 20 kHz - 30 kHz in order to determine the LDR frequencies corresponding to each damage location. The excitation transducer sending a sweep function was placed at position P1 (black), while the receiving one was located at P2 (black) – see Figure 5.30. Successively, this procedure was repeated at each damage region (i.e. A, B and C). The LDR frequencies were identified as the fundamental frequencies that corresponded to the largest generation of the 2nd harmonic in the response spectrum. In other words, in the analysis of the frequency response (blue line of Figure 5.31), the 2nd harmonic frequencies with the largest amplitude were identified first, while the fundamental frequencies that generated them were marked as LDRs. Subsequently, the LDR frequencies were used when conducting further testing. Figure 5.31 below shows the frequency response for the three damaged regions (i.e. A, B and C), while Table 5-7 shows the fundamental frequencies associated with the largest 2nd harmonic response selected. Figure 5.31 also shows the 3rd harmonic response, although it was not of primary interest in this study as its amplitude was comparatively low.

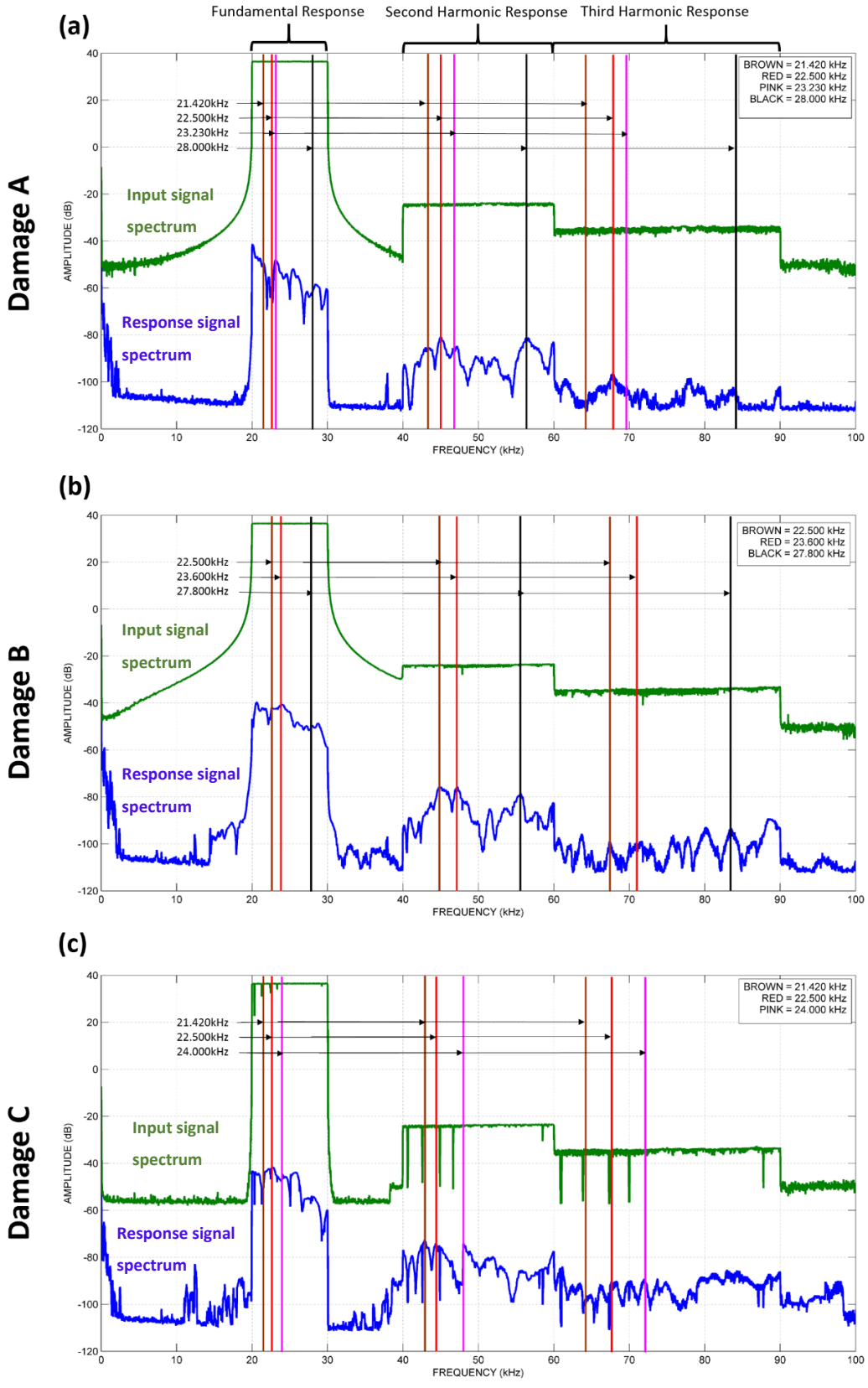

Figure 5.31: frequency selection process according to the 2nd harmonic amplitude for damage A, B and C.

The raw input signal to the transducer (directly from the amplifier) is shown in green, while the captured response received at P2 locations on the stiffener panel are shown in blue (material

resonance). When reviewing the peak responses of the 2nd harmonic, it can be observed that these frequencies do not necessarily relate to the highest fundamental frequency response (material resonance), thus they can be considered to be LDR-related frequencies. The third harmonic responses of the highest second harmonic responses have also been highlighted in the figure. The vertical colored bands refer to the selected excitation frequencies for the fundamental, second and third harmonics; for example in Figure 5.31 (a), the first brown line from the left refers to 21.420 kHz (the fundamental frequency), the second brown line (to the right) refers to 42.840 kHz (2 x 21.420 kHz, the 2nd harmonic) and the third brown line refers to 64.260 kHz (3 x 21.420 kHz, the 3rd harmonic). Table 5-7 summarises the fundamental frequencies which lead to the generation of the highest 2nd harmonic amplitude.

Damage A (kHz)	Damage B (kHz)	Damage C (kHz)
21.420	22.500	21.420
22.500	23.600	22.500
23.230	27.800	24.000
28.000		

Table 5-7: top frequencies according to the highest 2nd harmonic.

5.3.5 Ultrasonic Wave Propagation in Stiffener Panel

Figure 5.32, Figure 5.33 and Figure 5.34 display the wave propagation over time at 22.5 kHz for the three excitation positions (refer to Figure 5.28) obtained experimentally (LDV) and computationally (LS-DYNA®). The figures show the effect of the stiffener on the direction and symmetry (long parallel waves generated) of the wave. There is a clear reduction in the amplitude of the wave as it passes the stiffener (red line), this can be seen for piezo positions P1, P2 and P3. This reduction in amplitude has a direct effect on the ability of the wave to heat damaged regions, due to the reduction of stress in these regions. For piezo locations 1 and 3, the position of damage A can be visually identified by observing the discontinuities in the wave front. Although, after a short period of time it becomes difficult to discern the position of the damage as the combined effect of ultrasonic wave reflection, scattering and the appearance of standing waves arising from the natural vibration of the structure becomes more prominent.

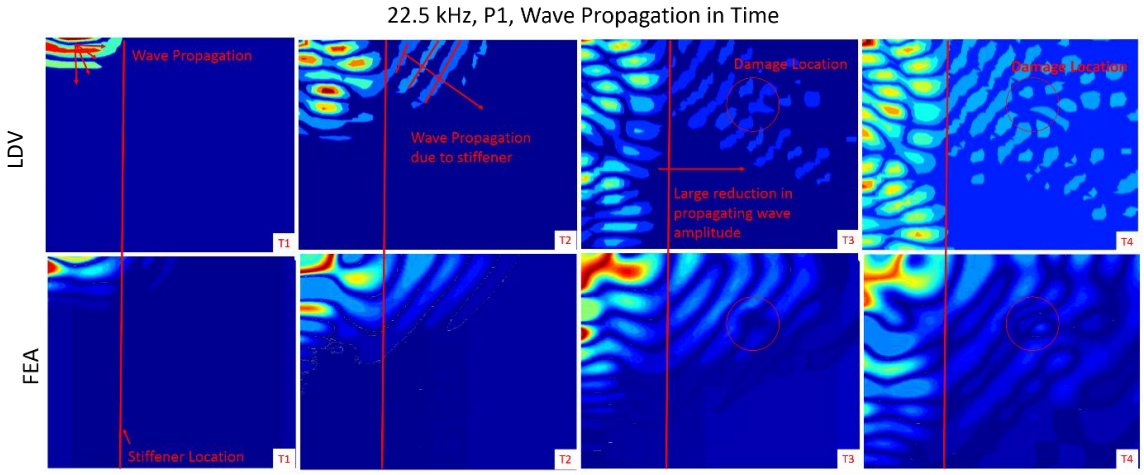

Figure 5.32: propagation of wave from position 1 (22.5 kHz excitation, out-of-plane displacement) at four consecutive points in time.

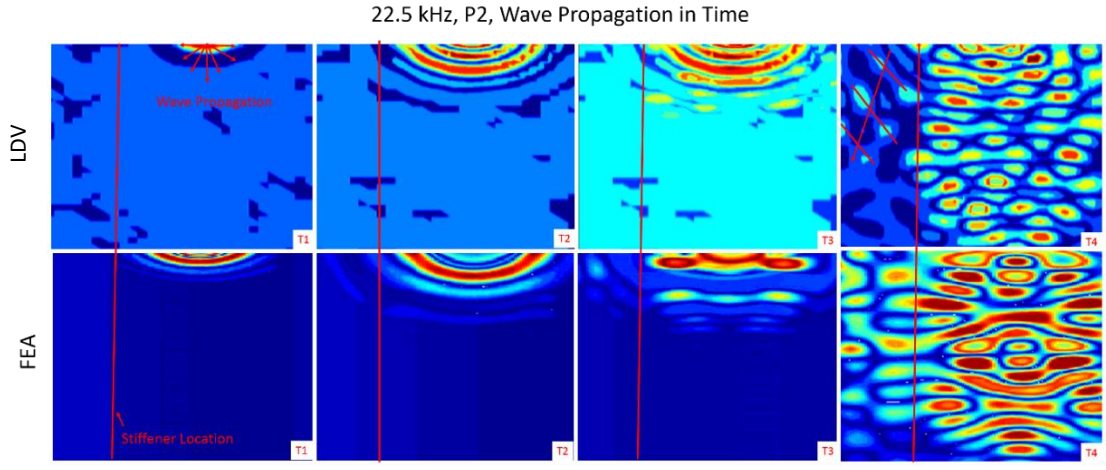

Figure 5.33: propagation of wave from position 2 (22.5 kHz excitation, out-of-plane displacement) at four consecutive points in time.

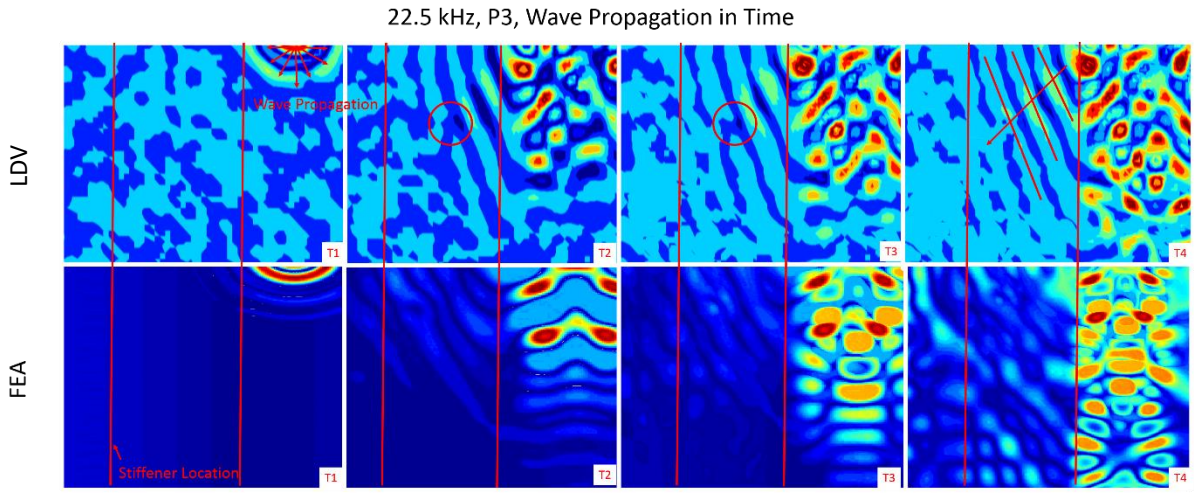

Figure 5.34: propagation of wave from position 3 (22.5 kHz excitation, out-of-plane displacement) at four consecutive points in time.

5.3.6 Modal Analysis of the Stiffener Panel

In order to computationally investigate the free vibration response of the structure, a modal analysis was performed using an implicit solver capability of LS-DYNA® with Figure 5.35 showing the results displayed as contours of out-of-plane displacement plotted for selected resonant frequencies in the range of 20 kHz to 30 kHz. Observing the vibration patterns, it is evident that various structural components are excited at different frequencies. This qualitatively confirms the importance of correct frequency selection. Considering the complexity of the stiffener panel and the frequency selected, it is possible to stimulate a sample at frequency that excites merely the individual sections between stiffeners. For example, according to the modal analysis: 22,508 Hz leads to a more pronounced displacement amplitude between stiffener 1 and 2; 22,620 Hz excites the structure between stiffeners 2 and 3, while 22,466 Hz excites to the right of stiffener 3. This effect suggests that multiple frequencies should be considered in order to ensure that the devised method sufficiently stimulates all regions of the panel. One of the big issues relating to the sonic thermography techniques is the generation of sufficient energy to cause heating at defect and damage regions. By understanding the deformation of the structure at various frequencies, it is possible to reduce the excitation energy required to sufficiently excite and generate heat in these regions.

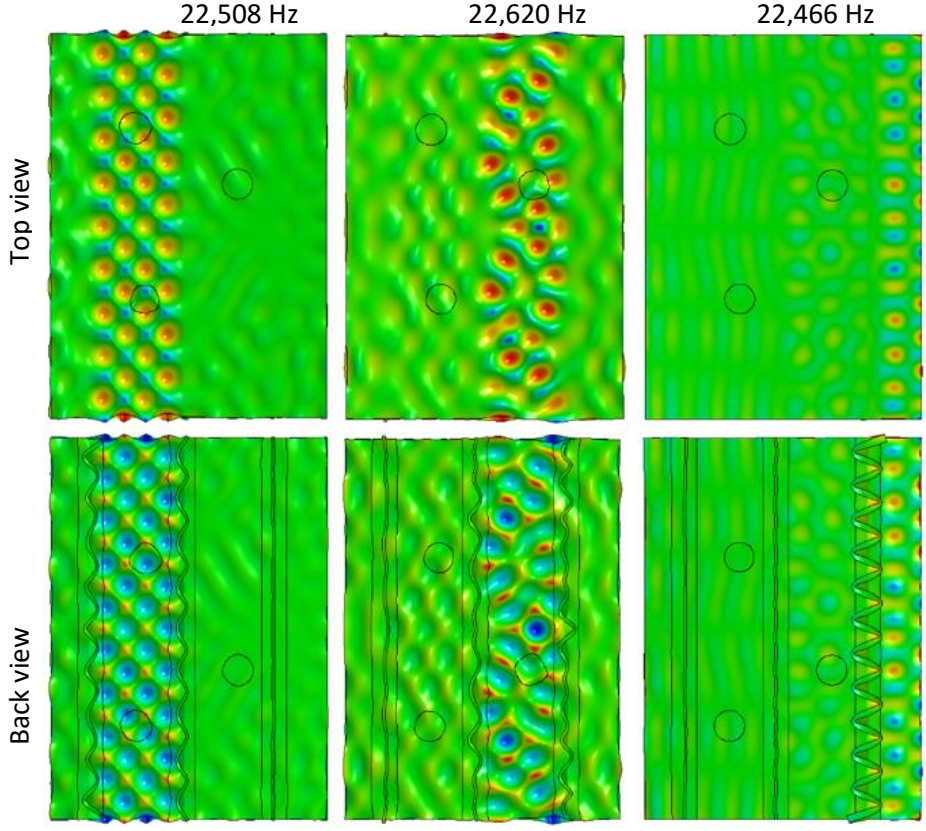

Figure 5.35: Modal FEA – contours of out-of-plane displacement.

5.3.7 Nonlinear Ultrasound Stimulated Thermography using LDR

Figure 5.36 shows the general format for the present test method. The vertical red lines indicate the position of the stiffeners (1, 2 and 3 from the left), while the dashed green lines show the two areas evaluated using the LV. The capability of the technique was evaluated using the LDR frequencies determined from the sweep analysis of the damaged regions (Figure 5.31).

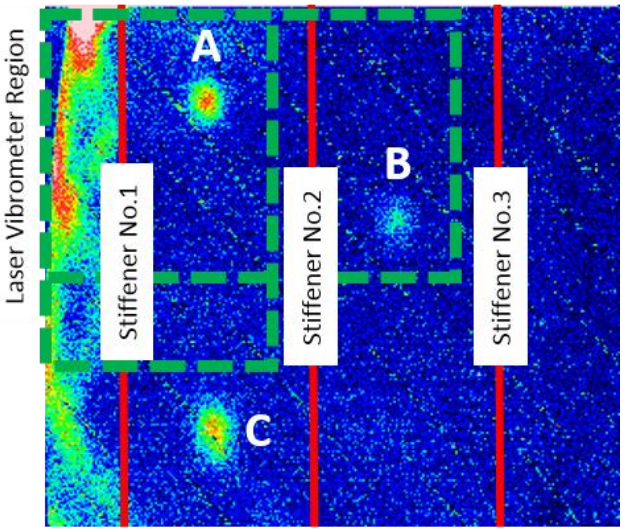

Figure 5.36: an image of temperature distribution using IR camera; note the stiffener and damage locations.

Figure 5.37, Figure 5.38 and Figure 5.39 show the results for frequencies 21.42 kHz, 22.5 kHz and 23.23k Hz respectively. The thermographic images of the BVID demonstrates that the heating was mainly produced in the core part of the delamination which can be further confirmed by comparing the location of heating to the ultrasonic phased array C-scan results (Figure 5.28). Heating of the BVID is clearly dependent on: (i) the excitation position (P1, P2 and P3) as suggested by the modal analysis results, (ii) the frequency of excitation, and (iii) the distance between the piezo transducer and the damaged region. Heating of damaged regions is amplified when excitation takes place on the same section of the stiffener panel, while heating is reduced when the excitation location and damage region is separated by a stiffener. This reduction of heating due to the presence of the stiffeners is clearly visible and confirmed by the wave propagation results from the previous Section (Figure 5.32, Figure 5.33 and Figure 5.34).

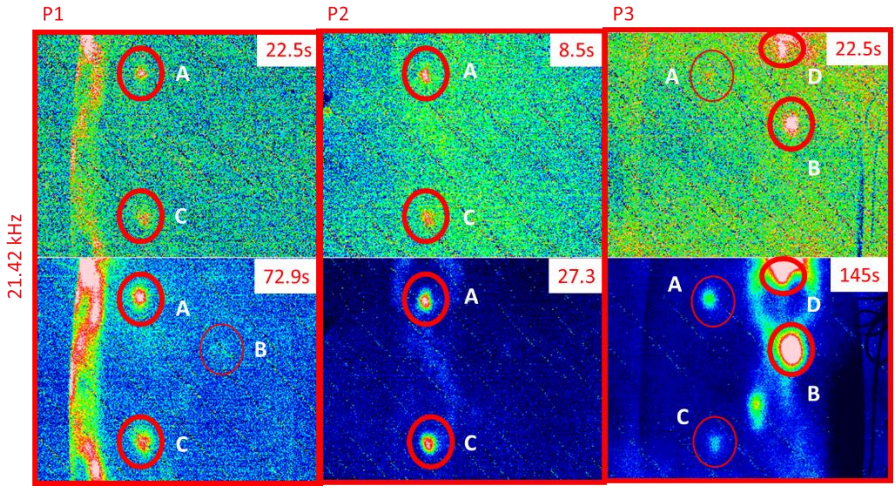

Figure 5.37: thermal imaging results using three piezoelectric transducer locations (P1, P2 and P3) at various excitation durations (21.42 kHz)

Figure 5.38 shows the raw and background subtracted images along with the smoothed images of the thermal response during ultrasound excitation. It can be seen that damages B and D become clearer when the images are smoothed. The thermal images captured using the infra-red camera were processed using a *background subtraction*[17] method.

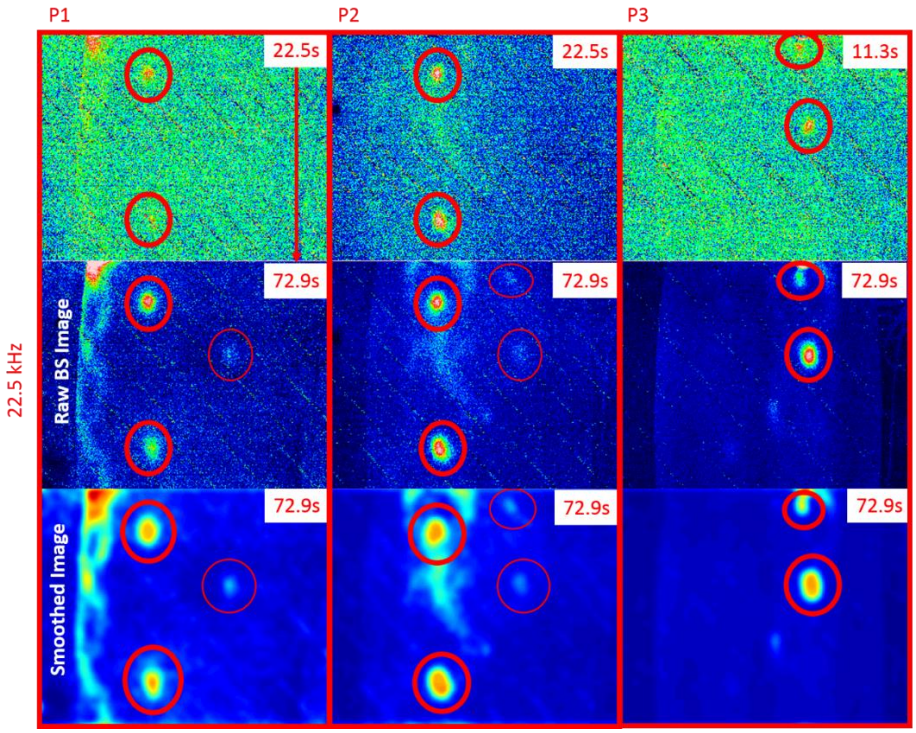

Figure 5.38: thermal imaging results using three piezoelectric transducer locations (P1, P2 and P3) at various excitation durations (22.5 kHz)

[17] In present context, background subtraction refers to an image processing technique performed by subtracting the image obtained in the reference configuration (before ultrasonic excitation) from the current one (after or during the ultrasonic excitation of the test piece).

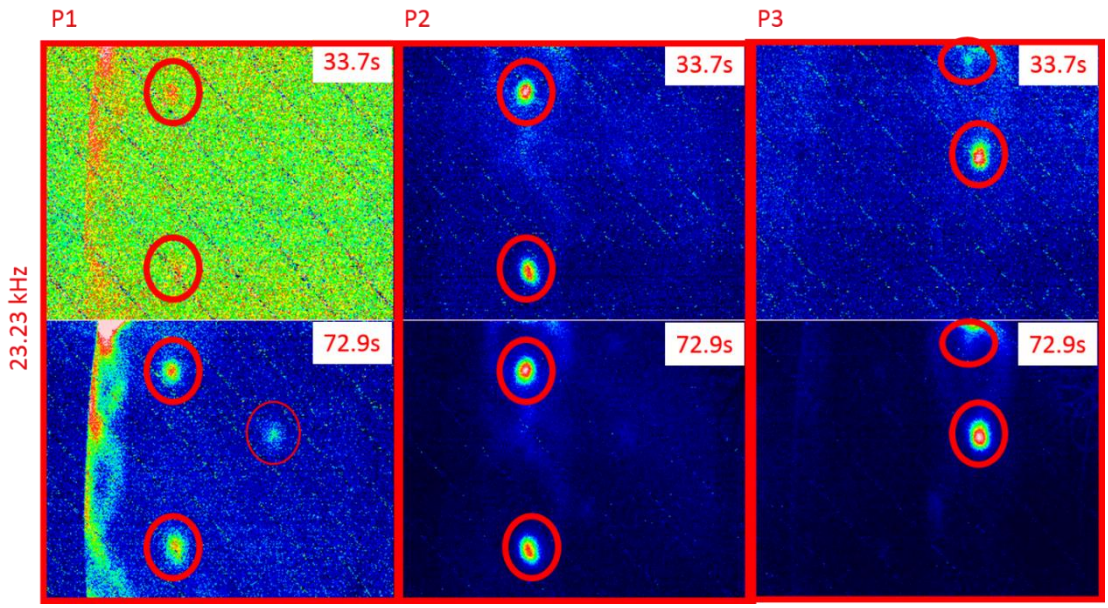

Figure 5.39: thermal imaging results using three piezoelectric transducer locations (P1, P2 and P3) at various excitation durations (23.23 kHz)

5.3.8 Nonlinear Ultrasound Stimulated Thermography using Narrow Sweep Excitation

Following the modal analysis and the LDR testing from the previous Section, it is clear that an alternative method should be used to improve detection capabilities of the nonlinear thermosonics method. It was seen previously that stiffeners restrict the waves from propagating with sufficient energy past them and combined with the difficulty in determining the LDR frequencies results in impaired effectiveness of such methods to be used for real world applications. The methodology which focuses on exciting a narrow frequency band using a sinusoidal sweep function provides various advantages to the direct LDR methods: (i) large areas can be evaluated by understanding the general frequency response of the material (setup shown in Figure 5.30, P1 to P2 (blue)) and (ii) excitation is more likely to excite multiple LDR frequencies due to the sweep methodology. The devised testing methodology involved exciting the structure between 20 kHz to 30 kHz with a sweep duration of 40 s repeated three times (total excitation time of 120 s). This was experimentally found to be an optimum scenario. If the stimulation duration is too short, no sufficient heating may be generated that can be resolved by the thermal camera. On the contrary, a very long duration may lead to the extensive heating of the whole specimen diminishing the thermal contrast required for the defects to be discerned. Generally, the excitation duration is dependent on the thickness of the structure, its thermal inertia (thermal diffusivity – see Chapters 3.2.5-0), the environmental conditions during the test and the equipment being used (e.g. transducer, IR camera etc.).

Figure 5.40 represents the temperature rise (blue line) vs. the frequency response (f_0 – black line, and $2f_0$ -red line, 20 kHz to 30 kHz) using arbitrary units as merely the trends of the curves were of interest in this study. Figure 5.40 (a) displays the amplitude of the frequency response obtained with a transducer at location P2 of damage A (see Figure 5.30 – damage A P2 (black)) along with the temperature rise indicated by a blue line acquired by averaging the temperature rise at several points on the surface of damage location A. As outlined earlier, the excitation frequency was swept continuously three times from 20 kHz to 30 kHz, and therefore, the 2nd harmonic ($2f_0$) response was observed at 40 kHz - 60 kHz. It can be seen that there is a clear correlation between the peaks of the 2nd harmonic and heating, while the heating profile followed the fundamental response in a somewhat more inferior fashion, although, f_0 should not be ignored as it generally leads to a large contribution to the heating of damaged regions which will be addressed later on.

Figure 5.40 (b) shows the general material response between stiffener 1 and 2 from one end of the panel to the other (see setup in Figure 5.30 – P1-P2 (blue)). Although, there are clear differences in the second harmonic responses between (a) and (b), there is still a good correlation between high harmonic responses and the generation (increase) in temperature at damage A.

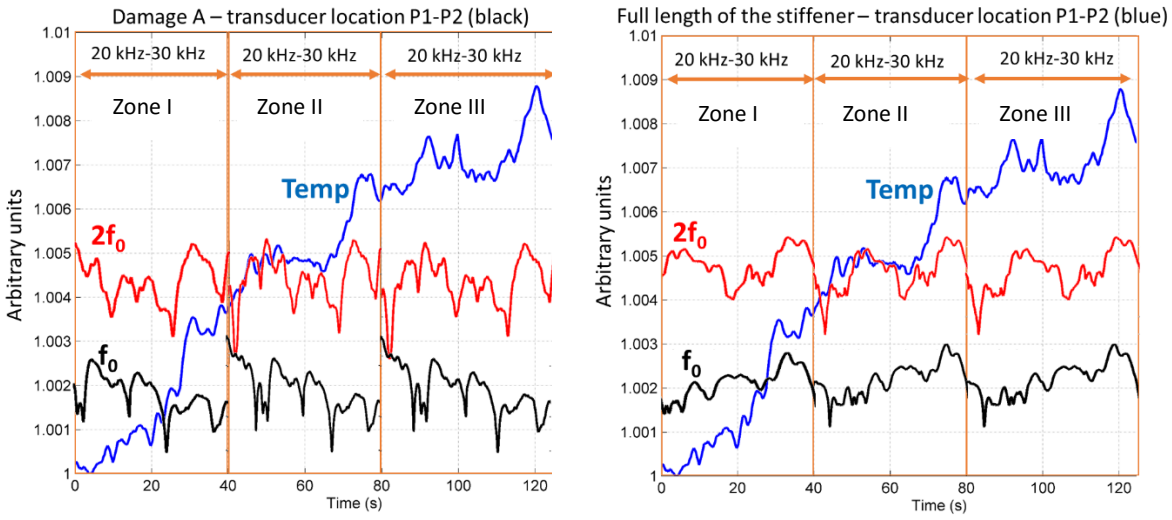

(a) (b)

Figure 5.40: temperature profile (blue line) during the three consecutive frequency sweep excitations compared with the fundamental (black line) and the 2nd harmonic response (red line) at damage region A (a) and between the stiffener panels 1 and 2 (b) ; sweep range 20k Hz - 30 kHz.

Figure 5.41 shows the results obtained using the outlined methodology. It is evident that damage locations A, B and C are clearly visible using the IR camera while exciting from transducer position 1 (P1). These results show the ability and effectiveness of the method to excite multiple damage regions separated by multiple stiffener panels. Figure 5.38 (22.5 kHz, LDR) displayed similar results in that the three damage locations were visible when exciting from P1, although, the determination of the excitation frequency required prior knowledge of the damage location. Other LDR frequencies highlighted in the previous Section were not effective in determining the damage locations when exciting from positions separated by stiffeners. This can be explained by the modal analysis results which indicated that various frequencies excite different areas between the stiffeners.

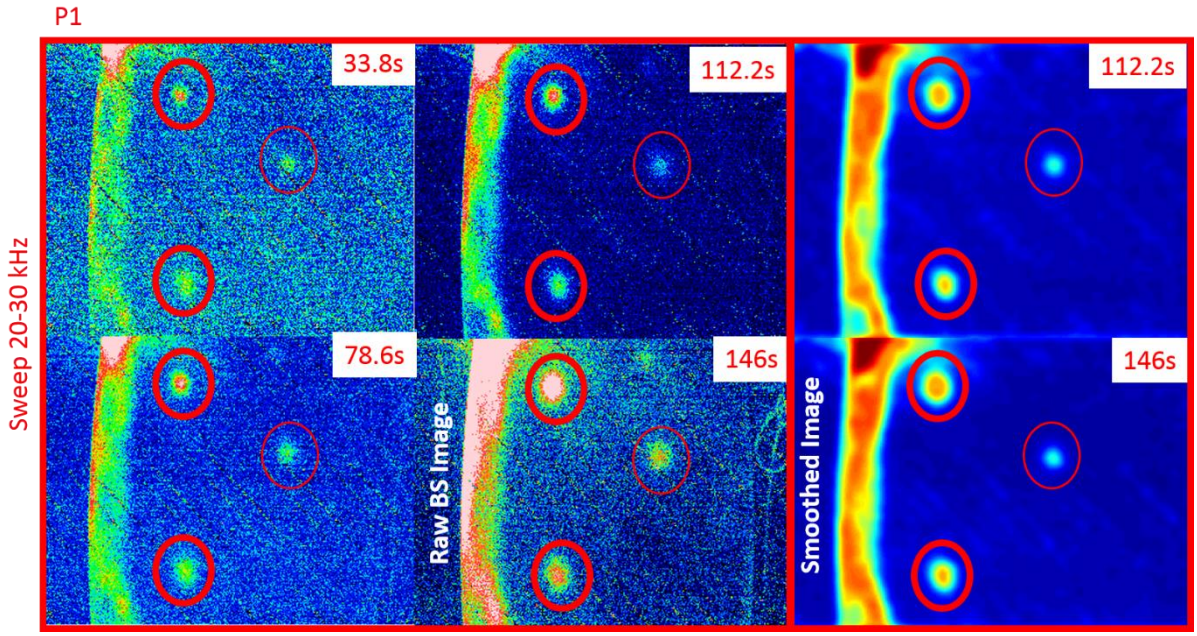

Figure 5.41: the thermal imaging results using transducer position (P1) while conducting a sweep (20 kHz - 30 kHz).

5.3.9 Further Investigation of the Nonlinear Thermosonic Response

The generation of the fundamental frequency and further harmonics (2nd and 3rd) were evaluated using a LDV for the various testing positions P1 (Figure 5.42), P2 (Figure 5.43) and P3 (Figure 5.44). Figure 5.42 and Figure 5.43 show that there is a clear generation of the fundamental, second and third harmonics at the damaged region clearly shown by the high amplitude response to the right of stiffener 1, exactly at location of damage A. This confirms that the frequency selection process led to the determination of the harmonics that related to the LDR frequencies. Furthermore, heating to the left of the stiffener 1 follows a shape that is similar to that produced by the fundamental, second and third harmonic responses.

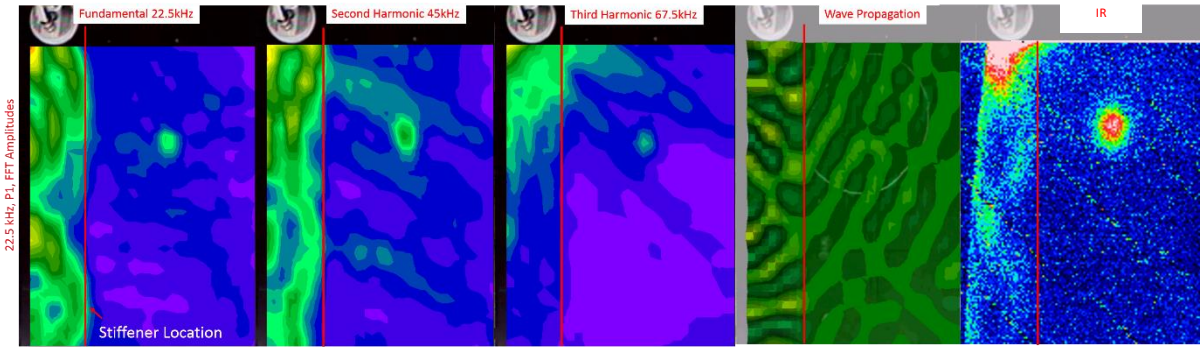

Figure 5.42: amplitudes of the fundamental and harmonic components of the frequency response spectrum obtained using LDV, a snapshot of wave propagation obtained via LDR, thermal image acquired with IR camera; transducer position 1 (22.5 kHz excitation).

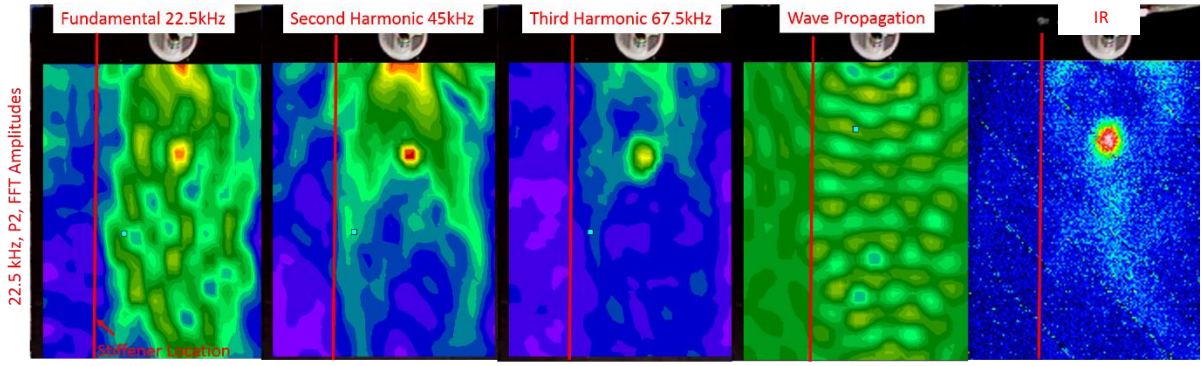

Figure 5.43: amplitudes of the fundamental and harmonic components of the frequency response spectrum obtained using LDV, a snapshot of wave propagation obtained via LDR, thermal image acquired with IR camera; transducer position 2 (22.5 kHz excitation).

Unlike excitation positions P1 and P2, P3 did not exhibit large harmonic (2nd and 3rd) responses between stiffener 1 and 2 but did exhibit large harmonic responses to the right of stiffener 2. When comparing the IR image to the production of harmonics (LDV), only damage B and D could be clearly seen, this suggests that further harmonic excitation of the damage region provides significant heating and can be a significant factor in damage detection. The reduction of heating at damage A (P3) is a

direct effect of the reduction in the propagating wave amplitude between stiffener 1 and 2 which is visualised in the wave propagation image (Figure 5.44) and ultimately results in a reduction in the production of the 2nd and 3rd harmonics.

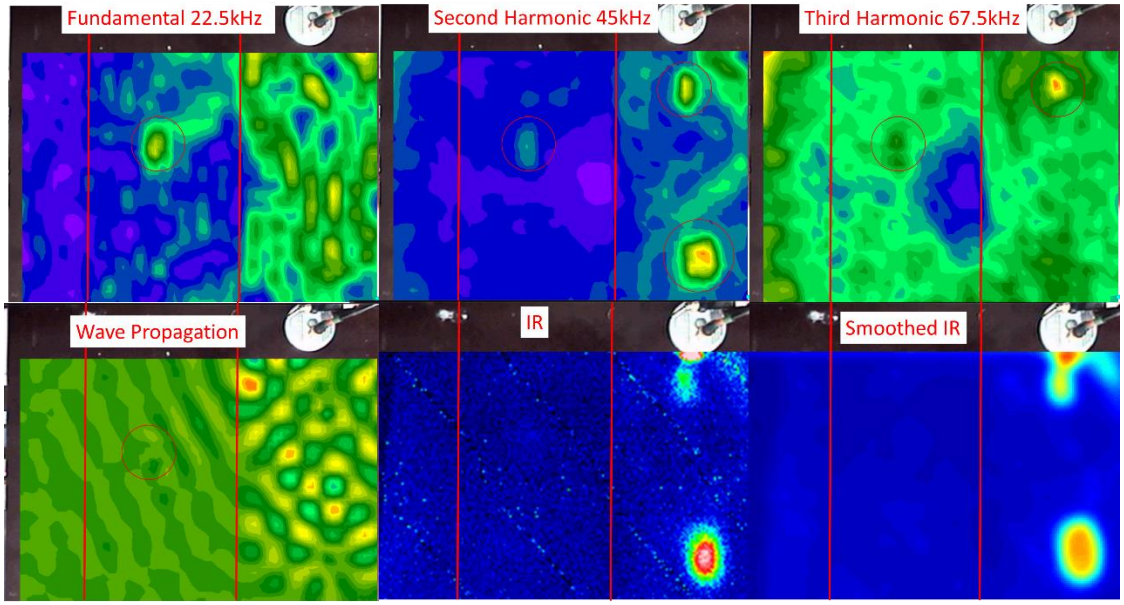

Figure 5.44: amplitudes of the fundamental and harmonic components of the frequency response spectrum obtained using LDV, a snapshot of wave propagation obtained via LDR, thermal image acquired with IR camera; transducer position 3 (22.5 kHz excitation).

Figure 5.45 shows a temperature distribution on the surface of the stiffener panel as calculated by the coupled structural-thermal FEA model. According to Eq. (5.13), the heating was calculated based on the principle elastic stresses at finite elements. It is evident from the figure that there were localised regions of elevated temperature at the locations where nonlinear constitutive model was introduced (highlighted by dashed circles). When the constant of nonlinearity (β) was set to zero, no distinct temperature rise was produced at those locations. This signifies a link between the generation of the 2nd harmonic and the heat. Increasing the β parameter led to a nonlinear change in stiffness coefficients which subsequently resulted in the damage-localised stress increase leading to the generation of heat in the corresponding finite elements. The heating pattern was also dependent on the excitation location. However, no colour maps are present in this study as no attempt was made to quantitatively compare the results.

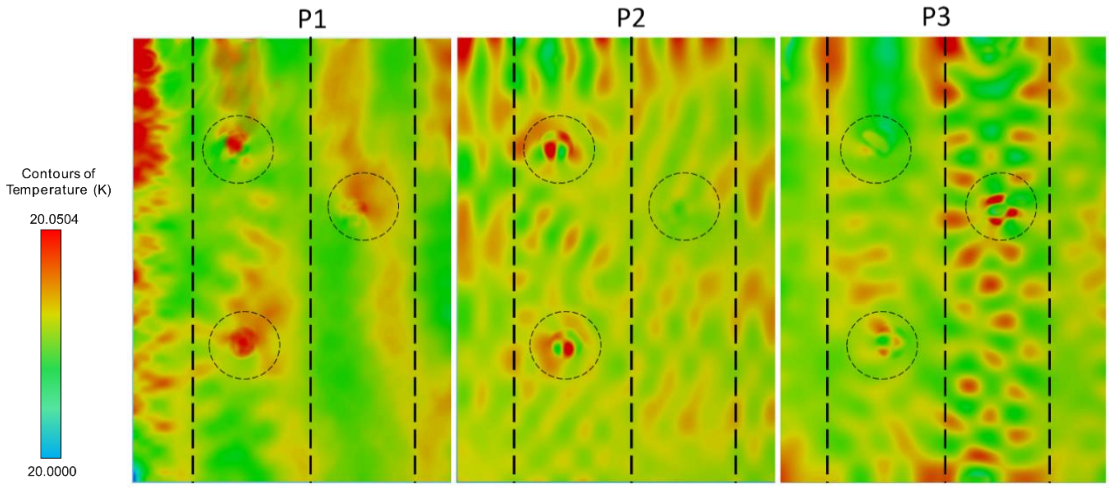

Figure 5.45: temperature distribution (FEA) on the surface of the stiffener panel at various excitation positions at final simulation step (22.5 kHz).

Next, the frequency and thermal response data when exciting at LDR was taken along the line in between the stiffeners 1 and 2 and therefore covering the damage locations A and C – see Figure 5.46. Figure 5.46 (a) and (b) highlights the difference in the voltage amplitude between the fundamental and the second harmonic for damage A and C. As can be expected, the overall amplitude of the fundamental is much larger than that produced by the second harmonic response, whereas the second harmonic, exciting at LDR, only excites the damage regions. Comparing the LDV results to the IR temperature profile (Figure 5.46 (c)), it is clear to see that the general heating (in areas other than the damage region) is driven by the fundamental frequency. This becomes clear as there is a thermal ridge that is evident in the fundamental LDV results as well as the thermal temperature profile.

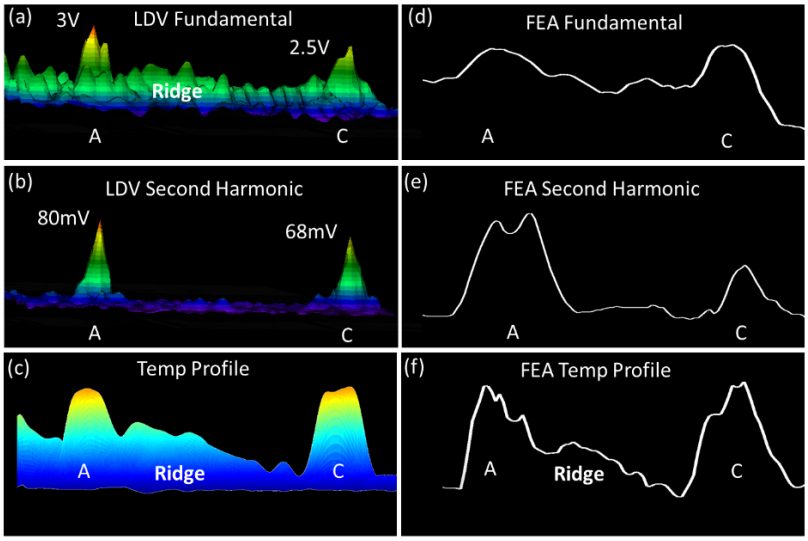

Figure 5.46: fundamental harmonic amplitude covering damage A and C ((a) – LDV, (d)-FEA), second harmonic amplitude for damage A and C ((b) – LDV, (e)-FEA), thermal profile ((c) – IR, (f)-FEA); the excitation was performed at the LDR frequency 22.5 kHz.

Figure 5.47 highlights the fact that this ridge is the result of the fundamental frequency response of the material, rather than heating due to the nonlinear material LDR frequency. Following on from the results shown in Figure 5.44, this confirms that the nonlinear frequency response at LDR causes significant heating that in that case was the critical factor in not detecting damage A (when exciting from transducer P3). Thus, as was hypothesised, due to the increase in heating at LDR (determined using the principles of nonlinear ultrasound) the required wave energy needed to cause heating is reduced.

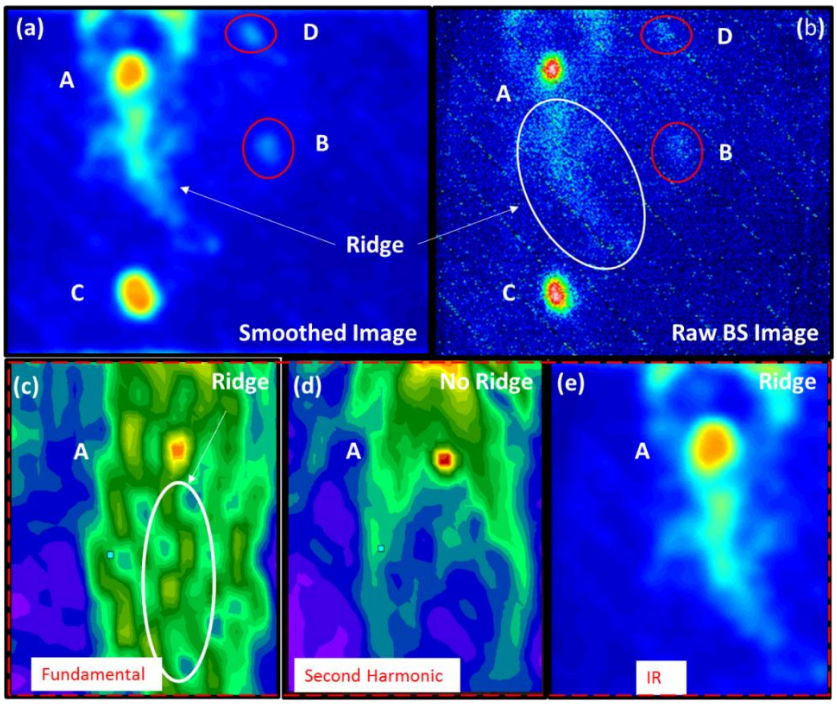

Figure 5.47: (a) smoothed IR image, (b) raw background subtracted IR image, (c) fundamental frequency response (LDV), (d) second harmonic frequency response (LDV), (e) smoothed IR image near damage A; all results obtained using 22.5 kHz excitation applied for 72.9 s.

Figure 5.48 (a) and (b) below, highlights the difference in the velocity response between the fundamental and second harmonic for damage A. The amplitude of the fundamental is much larger than that produced by the second harmonic response, which again is expected and follows the voltage results from Figure 5.46.

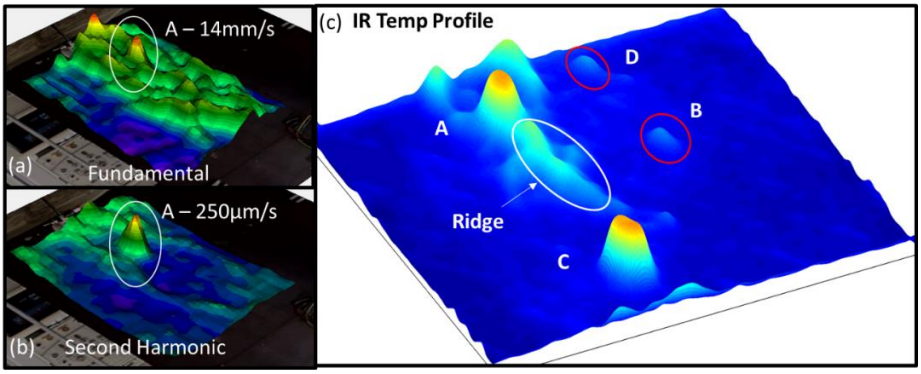

Figure 5.48: 3D representation of Damage A for the Fundamental (a) and Second Harmonic (b) in terms of velocity, (c) NUST smoothed temperature profile for the whole stiffener panel with damage A, B, C and D.

5.3.10 Conclusion

A complex composite stiffener panel was assessed using a structural-thermal FEA model and a nonlinear ultrasound stimulated thermography method. It was experimentally evaluated using a LDV and IR camera in order to detect the propagation of waves and structural vibration resulting in the heat generation with the aim of locating BVID. Two methodologies were qualitatively evaluated: (i) the local defect resonance (LDR) and (ii) the proposed nonlinear narrow sweep excitation. The ability of the LDR to excite the damage regions efficiently was observed and confirms other research studies that found similar trends. However, the determination of the LDR remains one of the major issues, which in most cases is not feasible without prior knowledge of damage location and/or size.

Given a highly dependent nature of the structure and damage regions on the frequency of excitation, this work provides an alternative method based on the ultrasonic stimulation of the structure using a narrow frequency sweep which was shown to lead to the determination of the damage locations. By understanding which frequency range gives rise to the highest nonlinear harmonic responses in the material and exciting at the corresponding fundamental frequency range, this method increases the probability of single or multiple damage excitation and heating. However, it is important to note that the proposed technique still requires a considerable amount of operator's judgment when selecting a transducer type, bandwidth and input power which were not fully addressed in this study.

FEA Modal analysis results suggested that for the present structure, evaluation and localisation of damage regions using a single frequency excitation becomes very difficult for a structural component featuring multiple stiffeners. The experimental methodology was also shown to aid the heating of the damage regions separated by the stiffeners due to the fact that the transfer of wave energy throughout the structure is impeded by the presence of the stiffeners and can vary widely dependent on the frequency.

A coupled structural-thermal FEA model of stiffener panel was developed with material behaviour of damaged regions modelled utilising the nonlinear orthotropic elastic material model developed in Chapter 5.1 which is based on the classical nonlinear theory. While there is generally a number of physical mechanisms that could be driving the generation of heat in the presence of material flaws such as sliding and clapping contact at the crack interface, in the present FEA model, the transient temperature generation was assumed to be exhibited merely by the mechanical stress. This behaviour was implemented into the constitutive model based on the classical thermoelastic theory. Subsequently, the FEA simulations predicted the generation of the 2^{nd} harmonic as well as the temperature rise corresponding to the damaged regions of the finite element mesh represented by the nonlinear material model.

5.4 NDE Method based on the Generation of Subharmonic Frequencies in Single Lap Adhesive Joints

Stiffener panels considered in the previous Section can also fail by debonding at the stiffener-skin interface, which can occur as a result of large out-of-plane displacements driven by buckling [262]. Indeed, as vast majority of composite components are adhesively bonded, debonding of stiffeners and other components is a significant concern in the development and use of composites in aerospace structures [263]. In this work, a NDT/NDE method addressing this issue is presented.

5.4.1 Introduction

There are a number of structural applications where the only feasible method of joining components together is by means of an adhesive. This approach presents several advantages in terms of cost and ease of manufacturing, light weight, optimum stress distribution in the bonded region, and the ability to join dissimilar materials. While the in-service behaviour of the mechanical fasteners (e.g. rivets, bolts, screws etc.) and welds has been well understood, the same cannot be said about the adhesive joints. Partial disbonds and voids are typical defect types characteristic to the bonded structures. In the past several decades, a considerable research effort focused on investigating their effects on the bond strength, the dynamic response of the adhesive joints, and the development of the appropriate nondestructive evaluation (NDE) techniques for detection, localisation and sizing of the bond related defects. Indeed, with growing design complexities, reliable NDE methods are required for disbond detection and evaluation in situations when a direct physical access to a component for inspection may not be possible (e.g. internal structure of an aircraft wing). Traditional linear acousto-ultrasonic testing NDE inspection techniques typically involve detecting the reflection and scattering of primary waves at material discontinuities [264] with subsequent imaging of signal amplitude and phase. As the frequency response of a structure changes in the presence of disbonds/voids [265], acoustic emission (AE) and the level of damping can also be used as a measure of bond strength [266, 267]. A disbond present in a structure is generally termed in literature as a kissing bond, which is characterised by the two compressed but otherwise unbounded surfaces [268]. The resulting change in stiffness and acoustic impedance in the vicinity of kissing bonds is typically very small and therefore little or no energy is reflected for the detection using the standard linear pulse-echo approach [269]. Therefore, the effectiveness of the linear techniques is limited in cases when a crack or disbond is fully/partially closed due to a closure stress or oxide films [159].

It was previously shown that the 2nd harmonic presence in the response spectrum of the medium subjected to a single tone acousto-ultrasonic excitation can be used as a signature of defect/damage presence. However, the utility of the second order harmonic amplitude for damage characterisation of materials is principally associated with the media that manifest classical nonlinear behaviour [188] that can originate at the micro scale. While classical and nonclassical NEWS methods were demonstrated to be effective in certain conditions, it is important to note that many materials, including the substrate (e.g. aluminium or composite plates) and the adhesive itself, can exhibit the aforementioned classical nonlinear behaviour even in a defect free state. Indeed, it is well known that a wave propagating through a fluid such as water attains second and higher order harmonics. Moreover, the signal-to-noise ratio (SNR) of defect generated harmonics is typically very low as the equipment (e.g. waveform generators, amplifiers, transducers etc.) also produces these nonlinear effects [159]. This leads to an essential requirement for any NDE method based on the nonlinearity measurement to be capable of reliably discerning between the inherent system nonlinearity (e.g. due to instrumentation) and the defect related one (e.g. CAN).

In present study, an analytical description of nonlinear elastic effects with emphasis on subharmonic generation associated with fully contact nonlinear LDR is provided considering a plate in bending subjected to a harmonic point load. The analytical model qualitatively indicated the generation of higher harmonics and the combination frequencies corresponding to the nonlinear intermodulation of the driving and the LDR frequencies, namely f_0 and f_d respectively. Subsequently, a single lap joint (SLJ) structure comprised of two isotropic plates partially joined with an adhesive was considered in the experimental and numerical campaign. The aim was to identify f_d of the debonded region and use the subharmonic component of the combination frequencies to perform nonlinear sensing and imaging of the defect. The numerical modelling was performed by means of commercial finite element analysis (FEA) software LS-DYNA® incorporating user defined cohesive elements representing the disbond, while an experimental validation utilised piezoelectric transducers and LDV.

5.4.2 Analytical Modelling

5.4.2.1 1-D Approach – Anharmonic Oscillator

As mentioned earlier, the LDR can enhance the efficiency of classical nonlinear response (e.g. higher harmonic generation and wave mixing) of the defects via local vibration amplification even at moderate levels of input signal. However, there are other dynamic nonlinear phenomena that are characteristic to resonant defects which include nonlinear resonance, subharmonics generation [179, 180], parametric (amplitude-dependent) resonance [188] and self-modulation [180]. To analytically demonstrate the existence of these effects and their respective spectral components, it is assumed that the damaged region manifests both resonance and nonlinear properties and therefore can be defined as an anharmonic (nonlinear) oscillator. Following the formulation and notation of Landau and Lifshitz [188], the equation of motion for an nonlinear oscillator in one dimension can be stated as

$$\ddot{x} + 2\lambda\dot{x} + \omega_0^2 x = \frac{Q_0}{m}\cos f_0 t - \xi x^2, \qquad \textbf{(5.18)}$$

where x is displacement, λ is a damping coefficient, Q_0 and f_0 are the amplitude and frequency of the excitation force, m is the structural mass; ω_0 is the resonant angular frequency of the system in absence of friction (damping), driving forces and the nonlinear term; ξx^2 is the second order nonlinear term of the anharmonic oscillator with its respective coefficient (constant) ξ. Assuming the driving force is reasonably small and the nonlinear terms are much smaller than the linear one, a well-known perturbation method can be used by seeking a solution to Eq. (5.18) in a form of a series of successive approximations

$$x = x^{(1)} + x^{(2)}, \qquad \textbf{(5.19)}$$

where $x^{(1)} = A(f_0)\cos f_0 t$ is a harmonic function of amplitude A representing a solution to the linear case in absence of damping, the driving force and the nonlinear terms. Setting $f_0 = 2\omega_0 + \varepsilon$ with small ε (i.e. driving frequency near double the resonant value), Eq. (5.18) can be solved resulting in a condition for subharmonic resonance with the solution comprising subharmonic frequency outputs: $\omega = nf_0 / 2$ (n=1, 2, 3, …) [270].

5.4.2.2 2D Approach – Nonlinear Flexural Waves

Following the formulation for an anharmonic oscillator expressed by Eq. **(5.18**) in the absence of in-plane and thermal forces and excluding effects of damping, a nonlinear equation of motion governing the bending of thin (span-to-thickness ratio greater than 10) homogeneous isotropic plates of length *a* and width *b* subjected to a sinusoidal transverse force q can be stated as follows

$$D\left(\frac{\partial^4 w_0(x,y,t)}{\partial x^4}+2\frac{\partial^4 w_0(x,y,t)}{\partial x^2\partial y^2}+\frac{\partial^4 w_0(x,y,t)}{\partial y^4}\right)+I_0\frac{\partial^2 w_0(x,y,t)}{\partial t^2}+ \\ -q(x,y,t)+q^{NL}(\xi,x,y,t)=0, \tag{5.20}$$

where D is the bending/flexural rigidity of the plate, w_0 is the transverse (out-of-plane) displacement which is a function of (x,y) coordinates and the time variable t, I_0 is the mass moment of inertia, q^{NL} is a nonlinear force term which can be a sum of quadratic and cubic terms as in Eq. **(5.19**) , although, only the second order one (q^{II}) was considered in this study

$$q^{NL}(\xi,x,y,t)=q^{II}(\xi,x,y,t), \tag{5.21}$$

where ξ is the second order nonlinear coefficient (constant). Assuming that $q^{NL}<<q$ and setting the boundary conditions of a simply supported plate at all four edges and initial conditions such that $w_0(x,y,0)=0$ and $\partial w_0(x,y,0)/\partial t=0$ are zero, a first order perturbation theory can be used to solve Eq. (5.20) in the form

$$w_0(x,y,t)=w_0^{(1)}(x,y,t)+\xi w_0^{(2)}(x,y,t). \tag{5.22}$$

Assuming a harmonic input $Q_0\cos(2\pi f_0 t)$ as a point source at (x_0,y_0) having an amplitude Q_0 and the driving frequency f_0, the solution of the linear inhomogeneous problem can be obtained via series expansion of the transverse deflection $w_0^{(1)}(x,y,t)$ and load $q(x,y,t)$ for $t\geq 0$ which is known as the Navier solution method

$$w_0^{(1)}(x,y,t)=\sum_{n=1}^{\infty}\sum_{m=1}^{\infty}A^I L_1\sin(\alpha x)\sin(\beta y), \tag{5.23}$$

where $L_1=\cos(2\pi f_0 t)-\cos(2\pi f_{mn}t)$, $A^I=Q_0/\pi^2 abI_0\left(f_{mn}^2-f_0^2\right)$, $\alpha=m\pi/a$, $\beta=n\pi/b$ and

f_{mn} is a series of resonant frequencies for simply supported plate with $m,n=1,2,3,\ldots$. The particular linear solution corresponds to the steady state oscillation of the plate at the frequency f_0 of the excitation force. Similarly, taking f_d as the LDR frequency associated with the defect at the location (x_d, y_d) and assuming an expansion of the nonlinear out-of-plane displacements and transverse loads, the second order ($w_0^{(2)}$) nonlinear solutions can be obtained in the form shown by Eq. (5.24)

$$w_0^{(2)}(x,y,t)=\sum_{n=1}^{\infty}\sum_{m=1}^{\infty}\left[\frac{\overline{A}^{II}}{2}(S_1+S_2+S_3+S_4)\right]\sin(\alpha x)\sin(\beta y), \qquad \textbf{(5.24)}$$

where $A^{II}=\left[Q_0\sin(\alpha x_d)\sin(\beta y_d)/\pi^2 abI_0\left(f_d^2-f_0^2\right)\right]^2$ with $\overline{A}^{II}=A^{II}/I_0$.

S terms in Eq. (5.24) correspond to a number of nonlinear elastic phenomena associated with the local resonance at the defect location and can be defined as follows

$$S_1=\frac{\left[1-\cos(2\pi f_{mn}t)\right]}{2\pi^2 f_{mn}^2}, \qquad \textbf{(5.25)}$$

$$S_2=\frac{\cos(2\pi f_{mn}t)-\cos(4\pi f_0 t)}{4\pi^2\left(4f_0^2-f_{mn}^2\right)}, \qquad \textbf{(5.26)}$$

$$S_3=\frac{\cos(2\pi f_{mn}t)-\cos(4\pi f_d t)}{4\pi^2\left(4f_d^2-f_{mn}^2\right)}, \qquad \textbf{(5.27)}$$

$$S_4=\frac{2\left[\cos\left[2\pi(f_0\pm f_d)t\right]-\cos(2\pi f_{mn}t)\right]}{\left[(2\pi f_0\pm 2\pi f_d)^2-4\pi^2 f_{mn}^2\right]} \qquad \textbf{(5.28)}$$

Of particular interest to this work is the term S_4 (Eq. (5.28)) containing the combination frequencies ($f_0\pm f_d$) which gives rise to the generation of sub-harmonic frequency (f_0-f_d) in case f_0 is chosen such that f_0 =2 f_d . In other words, exciting a sample at double of LDR frequency corresponding to the disbond should lead to the generation of sidebands at f_0-f_d and f_0+f_d . The former is of primary interest in this study as the subharmonic components in the spectrum are less susceptible to the instrumentation effects.

5.4.3 Experimental Setup and Procedure

The single lap joint (SLJ) samples were manufactured using two aluminium plates partially joined by the adhesive (Table 5-8). Prior to bonding, the joint surfaces were polished with emery paper and cleaned with acetone; the procedure advised by the manufacture was followed for the application of the adhesive. The nominal thickness of the applied adhesive was 0.15 mm. Artificial defects in the form of disbonds (voids) were introduced by careful application of the adhesive and placing a Teflon sheet in the desired debonded region during the manufacturing process. Afterwards, the samples were inspected using an ultrasonic C-scan method in order to ensure that the samples conformed to the specification set for the debonded area. In the experimental setup, two piezoelectric (PZT) transducers were bonded to the surface of the samples in order to generate and receive the acousto-ultrasonic waves. The dimensions and the material properties of the test samples are shown in Figure 5.49 and Table 5-8 respectively.

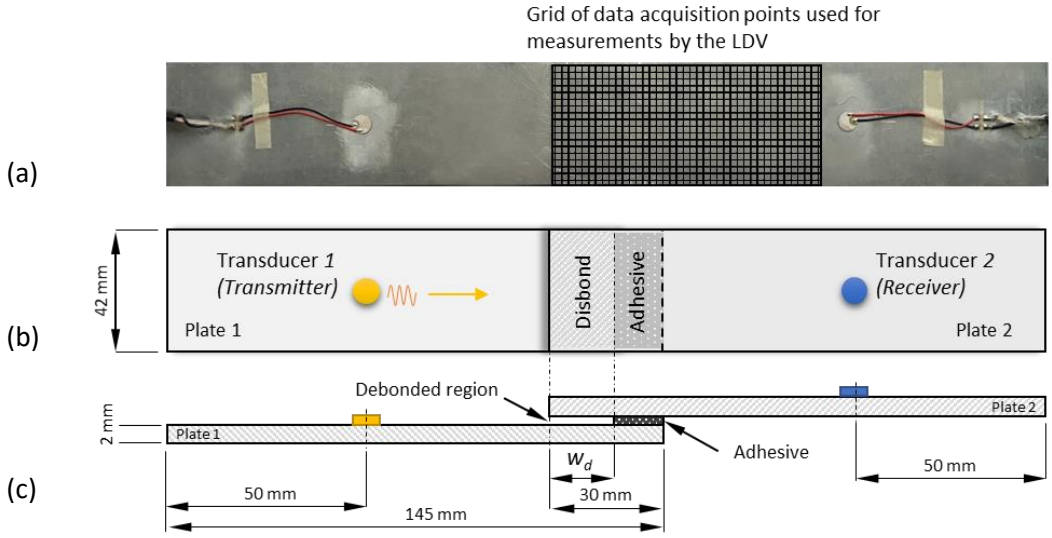

Figure 5.49: (a) a photograph of one of the actual SLJ samples with an overlaid grid of data points as used in the laser-Doppler vibrometer (LDV) experiments, (b) and (c) are the schematics of the top and side views with the specified dimensions.

	Young's modulus (GPa)	Mass density (g/cm^3)	Poisson's ratio
Aluminium (6061) plate	71	2.77	0.33
Araldite 2012A adhesive	1.654	1.17	0.3

Table 5-8: material properties.

The experimental campaign aimed at evaluating the presence of the disbond and its location by harmonically exciting the sample with piezoelectric (PZT) transducer 1 and analysing the spectral

response. A number of samples were manufactured with different widths (w_d) of debonded areas. The specifications of the samples is provided in Table 5-9.

No.	Number of samples	Recess (disbond) width w_d (mm)
1	3	0 (fully bonded)
2	3	10
3	3	20

Table 5-9: specification of the recess areas used in SLJ samples.

In the present methodology, two testing procedures were carried out. The first one (refer to Figure 5.50(a)) involved capturing the response at the receiving PZT (transducer 2) without the use of the laser-Doppler vibrometer (LDV). A range of frequencies in the range from 10 kHz to 40 kHz with an increment of 5 Hz were transmitted from PZT 1 and the response was captured with PZT 2. At each frequency, a continuous sinusoidal wave of 3 seconds in duration and an amplitude of 50 V_{pp} (Volts peak-to-peak) was sent to PZT 1 five times and the corresponding averaged frequency spectrum response was recorded. The choice of input voltage is crucial for the successful generation of subharmonics. As stated by several authors [178], the subharmonics tend to exhibit a "threshold behaviour" which is characterised by a substantial increase in amplitude of subharmonic spectrum component after a certain input amplitude is exceeded. The excitation amplitude of 50 V_{pp} used in this study, which is similar to the level reported in literature [157, 179], was set by gradually increasing the excitation amplitude until the subharmonic level becomes constant.

A programme was written in LabVIEW software that interfaced between the PC and the waveform generator which allowed to automate the process of sending and acquiring the signals. This process could have been performed using the LDV which operates based on the principles of Doppler-effect and sensing the frequency shift of back scattered light from a moving surface. However, due to the limitations of the LDV software, implementing the automation procedure proved challenging. Moreover, the testing procedure that involves the PZT transducers without the use of LDV is more affordable and practical solution in terms of real world applications as the LDV equipment is a high cost asset and requires a direct line of sight with a test component.

LDV setup as shown in Figure 5.50(b) was used to capture the vibration velocity of the surface of the specimens.

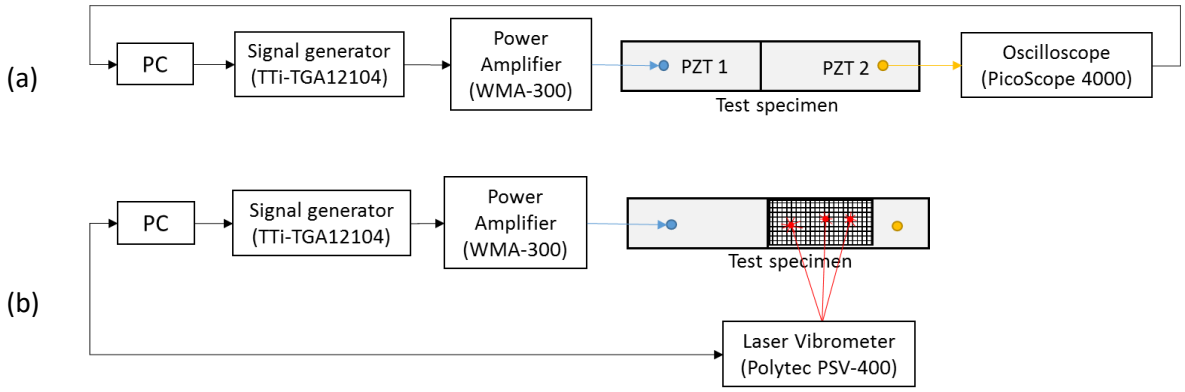

Figure 5.50: (a) test setup with piezoelectric transducers and (b) the LDV.

5.4.4 Numerical Model

In this study, a commercial FEA code LS-DYNA®® was used to perform a structural modal and dynamic analyses. In the modal analysis, the eigenvalues and their corresponding eigenfunctions were extracted which are associated with the natural frequencies and modes of free vibration of the structure. Hence, each possible resonance frequency with the corresponding vibration pattern can be plotted allowing an LDR frequency to be readily identified.

The dynamic part aimed at stimulating a wave propagation phenomena mimicking the experimental setup presented earlier. Figure 5.51 presents a computational domain (finite element (FE) mesh) used for the analysis.

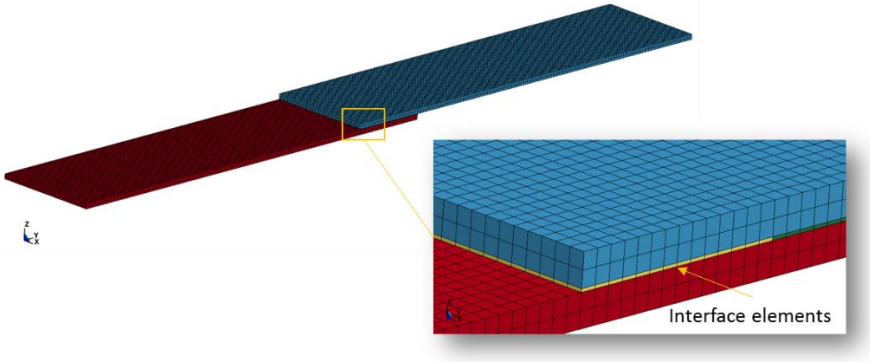

Figure 5.51: FE mesh.

Both the aluminium plates and the adhesive were modelled as isotropic elastic materials with the properties displayed in Table 5-8, whereas the disbond was modelled using a more special treatment.

While in the physical experiments, the dynamic interaction was allowed by contact between the upper and lower surfaces (i.e. kissing bond) of the plates in the overlapping area with no adhesive on (i.e. the debonded area), the interface (cohesive) elements represented this interaction in the numerical domain for the purpose of dynamic analysis. In the cohesive element formulation, the separation (relative displacement) between the upper and lower surface of the element is resisted by a nonlinear force-displacement relationship. Essentially, cohesive elements act as nonlinear springs connecting the opposing surfaces; instead of strains, the deformation is in terms of the relative displacements between the upper and lower surfaces of the element interpolated to the Gauss integration points; the force per unit area (traction) is used in the formulation. Cohesive zone models (CZM) are typically used for analysis of bonded structures such as composite panels where the crack path is known a priori and can be used to simulate a separation of the two adjacent layers (i.e. delamination). In this study, the cohesive element formulation with a bilinear traction-displacement relationship was implemented by means of a user defined cohesive material model interface of LS-DYNA® in order to represent a nonlinear contact behaviour in the disbond. An alternative method could be to use one of the contact algorithms of LS-DYNA® to simulate the interaction between the plates. However, no user defined capability currently exists for this purpose and all built-in contact algorithms are represented as linear springs.

In the cohesive element formulation, the tractions are calculated in the local coordinate system on the mid-surface defined half way between the upper and lower nodes (i.e. node pairs 1-5, 2-6, 3-7, 4-8 – refer to Figure 5.52 below).

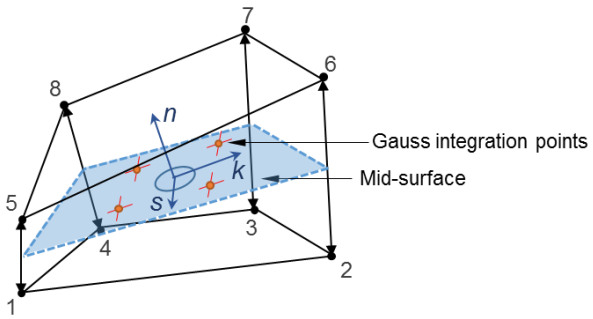

Figure 5.52: a schematic view of an 8-node cohesive finite element.

The relative displacements at an integration point at the of the element can be defined as follows

$$\Delta u = R^T \sum_{i=1}^{4} N_i(s,k)\Delta x_{i+4,i} - R_0^T \sum_{i=1}^{4} N_i(s,k)\Delta X_{i+4,i}, \quad \text{for i=1 to 4,} \qquad \textbf{(5.29)}$$

where *s*, *k* and *n* denoting the local coordinates, where components *s* and *k* are in-plane of the cohesive surface and *n* is normal to the plane; $\Delta x_{i+4,i}$ and $\Delta X_{i+4,i}$ are the coordinates in the current and the reference (initial) configurations respectively with subscripts referring the node pairs; R^T and R_0^T is a transpose of a rotation matrix from local to a global coordinate system in the current and the

initial configuration respectively; N is a matrix of element shape functions which in the case of the present cohesive elements are linear interpolating functions used to calculate continuous fields (e.g. displacements) from discrete nodal displacements. Once the displacements are known, the tractions can be calculated as follows

$$\begin{Bmatrix} t_s^c \\ t_k^c \\ t_n^c \end{Bmatrix} = \begin{bmatrix} E_s & 0 & 0 \\ 0 & E_t & 0 \\ 0 & 0 & E_n \end{bmatrix} \begin{Bmatrix} \Delta u_s \\ \Delta u_k \\ \Delta u_n \end{Bmatrix}, \quad \textbf{(5.30)}$$

where t_s^c and t_t^c are in-plane tractions (N/mm^2), and t_n^c is normal traction (N/mm^2) – superscript is used to avoid confusion between the tractions associated with the cohesive and standard finite elements; E_s and E_t are the in-plane and the normal element stiffness (N/mm^3) respectively; Δu are the relative displacements (mm) at an integration point. The kissing bond was assumed to be dependent only on the normal stiffness [135, 181] (i.e. only "clapping" and no "rubbing" phenomena), and therefore, the shear components E_s and E_t were set to zero. Similarly to the reported mechanical diode crack models [271, 272], the following traction-displacement relationship was implemented

$$t_n^c = \begin{cases} 0 & \Delta u_n \geq 0 \\ E_{n1}\Delta u_n + E_{n2}\Delta u_n^2 & \Delta u_n < 0 \end{cases}, \quad \textbf{(5.31)}$$

where E_{n1} and E_{n2} were set to 5 x 10^3 (N/mm^3) and 3 x 10^3 (N/mm^3) respectively based on the coefficients reported by [181]. According to Eq. (5.31), there is zero stiffness when the plates are moving apart and nonlinear stiffness when the plates are moving closer together which is graphically represented in Figure 5.53 below.

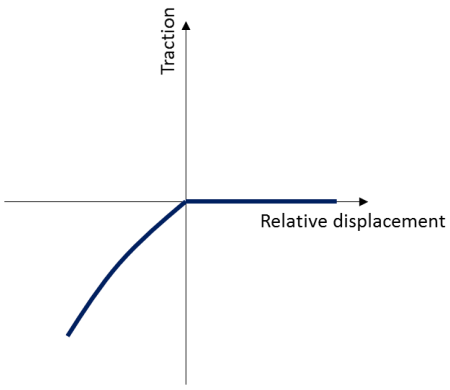

Figure 5.53: bilinear traction-displacement law used to represent the stiffness of the cohesive elements.

Subsequently, the nodal forces are obtained by integrating the tractions over the mid-surface of the cohesive element using 2 x 2 Gauss integration points and rotating them into the global coordinate system

$$\mathbf{F}^{coh} = \sum_{e=1}^{n_{el}} \mathbf{L}_e^T \left[\mathbf{R} \int_{\Gamma_e^c} \mathbf{t}^c \mathbf{N} d\Gamma \right], \tag{5.32}$$

where Γ_e^c is the boundary of the cohesive element; $\mathbf{t}^c$ is the vector of traction forces per unit area in the element coordinate system; $\mathbf{L}_e$ is the Boolean connectivity matrix which is used to collect the element forces into a global force matrix.

The governing Eq. (2.27) as described in Chapter 2.5.1 can be modified to include a matrix of cohesive forces.

$$\mathbf{M\ddot{u}} = \mathbf{F}^{ext} - \mathbf{F}^{int} - \mathbf{F}^{coh}, \tag{5.33}$$

where $\mathbf{\ddot{u}}$ is the second time derivative of the global displacement vector

Therefore, a choice of element size for finite element mesh is very important. Material parameters and the size of finite elements directly affect the critical time step size. In present analysis, the maximum frequency of interest was of the order of 50 kHz which leads to a sampling rate of 2 Msps (megasamples per second) as 40 points per wavelength were chosen. This information combined with the elastic properties of aluminium material yielded an element size of 3.1mm for an 8-node fully integrated finite element. To achieve further increase in spectral resolution, an element size of 1 mm was used for the mesh of the aluminium plates. Free-free boundary conditions were used as it better represented the experimental setup. The loading was applied as harmonic force acting on the area of the nodes representative of the area of the PZT

$$F(t) = \bar{t}_z = Q_0 \sin(2\pi f_0 t), \tag{5.34}$$

where $\bar{t}_z$ is the force acting in the normal (z) direction which is prescribed on the nodes representing the PZT as shown in Figure 5.54; Q_0 is the excitation amplitude, f_0 is the fundamental frequency of the excitation and t is a time variable.

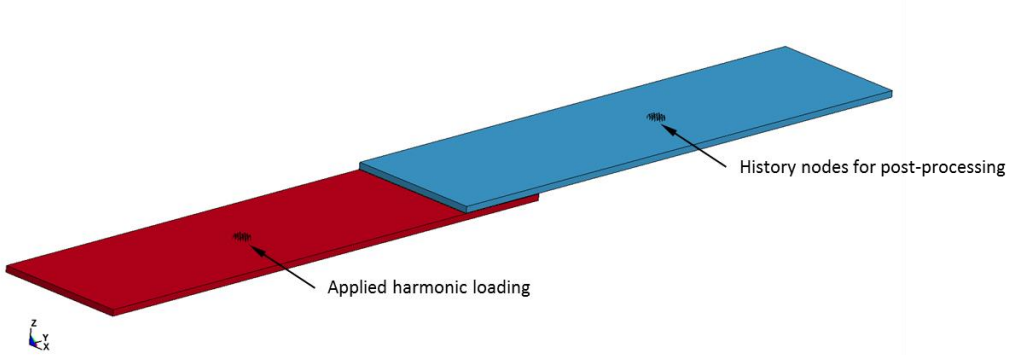

Figure 5.54: position of the loading and history nodes as used in the numerical analysis.

The out-of-plane displacement and velocity values were recorded during the simulation at the history nodes shown in Figure 5.54. The history data was averaged among these nodes in the post-processing step.

5.4.5 Results and Discussion

While an LDR frequency (f_d) can be analytically obtained for several types of internal defects by making certain assumptions about their geometry [212], no analytical expression yet exists so that the LDR can be readily calculated for an arbitrary defect type or a disbond featuring in the present study. Through modal analysis using LS-DYNA®, a natural frequency associated with the mode of vibration that displayed an apparent interaction in the debonded region was identified and used as f_d. The corresponding flexural modal shape of a sample with a recess (disbond) width w_d of 20 mm is shown in Figure 5.55. A flexural mode of vibration was chosen as previous research efforts indicated a possible correlation between the subharmonic generation and the flexural mode in an aluminium sample with a fatigue crack [179].

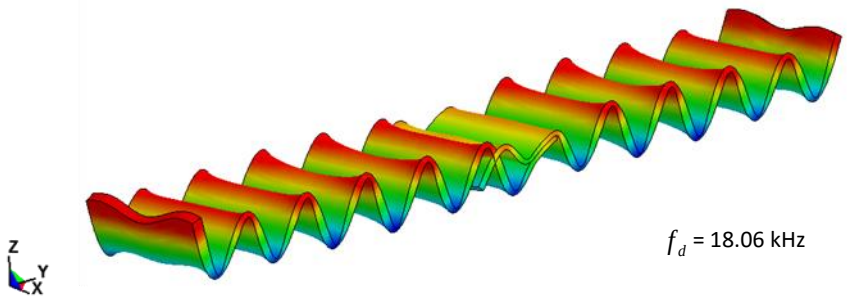

Figure 5.55: a flexural mode shape of vibration as predicted by modal FEA (LS-DYNA®).

Guided by the LDR frequency (f_d) determined from the FEA, the first part of the experimental campaign aimed at identifying the frequency corresponding to the same mode of vibration in a

physical sample. The results of the frequency sweep along with the corresponding 2nd harmonic ($2f_0$) response at each excitation frequency are plotted in Figure 5.56.

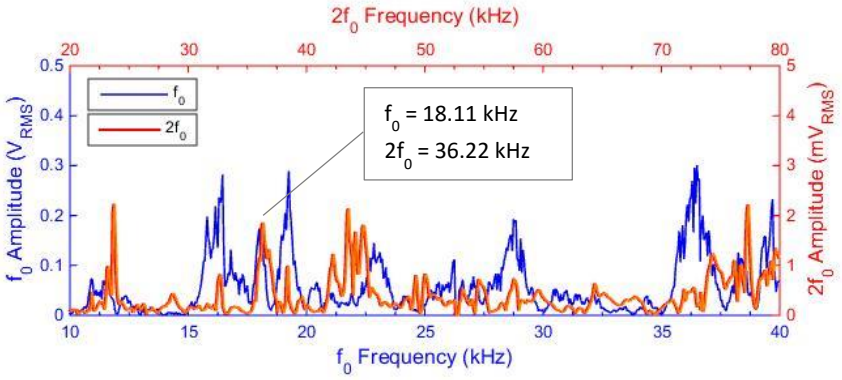

Figure 5.56: fundamental and 2nd harmonic frequency response of the sample with w_d of 20 mm.

As it can be seen from Figure 5.56(a), a clear amplitude peak of the fundamental and its 2nd harmonic frequency was observed at f_0 = 18.11 kHz which is in close spectral proximity to its numerically obtained counterpart (i.e. 18.06 kHz). Experimentally obtained time averaged spectrum is shown in Figure 5.57(a), whereas the frequency domain of nodal velocities acquired in the numerical wave propagation analysis is displayed in Figure 5.57(b).

(a)

(b)

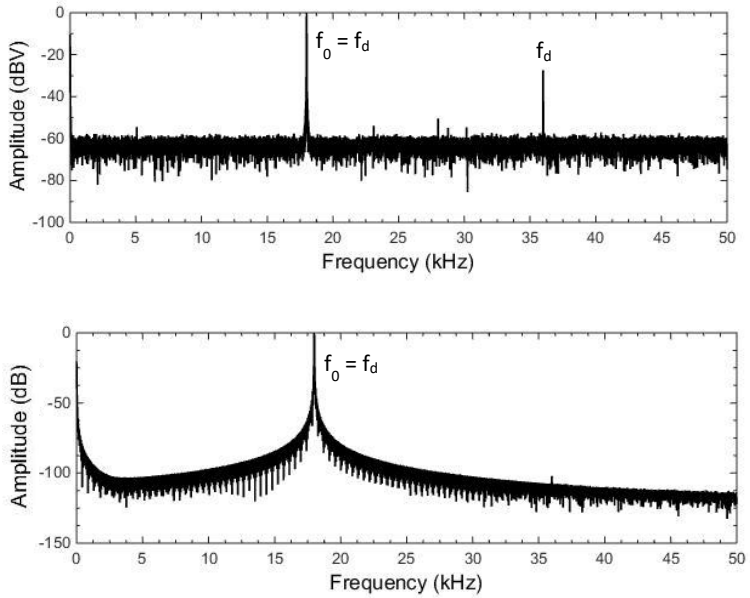

Figure 5.57: fundamental-normalised frequency response spectrum obtained (a) experimentally (PZT) and via (b) numerical simulation (LS-DYNA®).

In order to verify that the experimentally obtained response at 18.11 kHz was indeed associated with the flexural mode, a LDV was used to measure the out-of-plane velocity at the surface of the sample while exciting the sample at f_0 = 18.11 kHz. The plot of the vibration amplitude recorded by the LDV is presented in Figure 5.58(b).

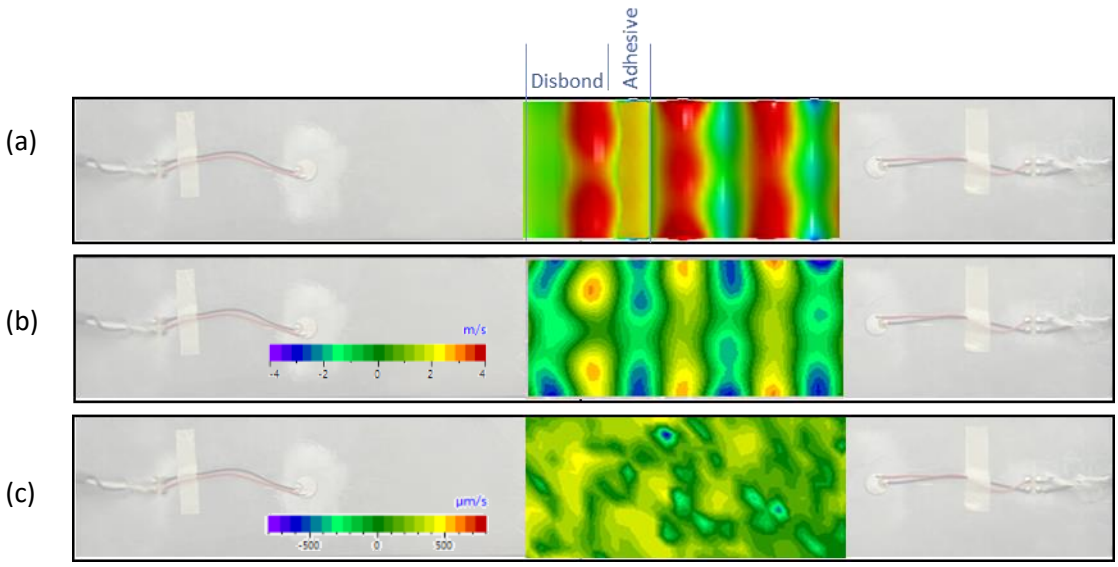

Figure 5.58: (a) numerically (LS-DYNA®) obtained out-of-plane displacement of the sample signifying a flexural mode at 18.06 kHz; (b) experimental (LDV) results – amplitude of the driving vibration velocity at f_0 = 18.11 kHz and (c) the amplitude of its spectral component at $2f_0$ = 36.22 kHz.

Subsequently, the existence of the flexural mode at f_0 = 18.11 kHz was experimentally confirmed which correlates well with the out-of-plane response obtained numerically via modal analysis (Figure 5.58(a)). The plot of the 2nd harmonic amplitude (Figure 5.58(c)) of the frequency spectrum for the corresponding f_0 does not clearly indicate the presence of the disbond, although, a moderate increase in the vibration amplitude can be observed in its vicinity. According to the analytical model, a subharmonic frequency component $f_0 - f_d$ should exit at $f_0 = 2f_d$ = 36.22 kHz in case 18.11 kHz is in fact f_d corresponding to the LDR frequency associated with the disbond. This was confirmed by plotting the subharmonic response $0.5f_0$ for each fundamental frequency of excitation f_0, which was obtained following the first experimental setup involving the two PZT transducers; the outcome is displayed in (Figure 5.59).

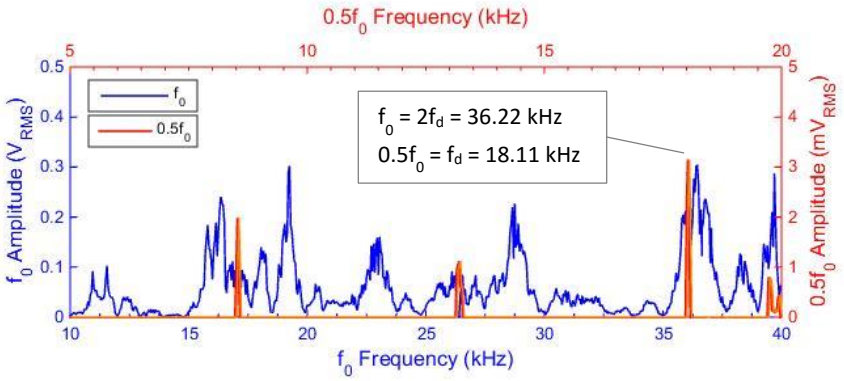

Figure 5.59: fundamental and subharmonic frequency response of the sample with w_d of 20 mm.

Experimentally obtained time averaged frequency spectrum is shown in Figure 5.60(a), whereas the frequency domain of nodal velocities acquired in the numerical wave propagation analysis is displayed in Figure 5.60(b).

(a)

(b)

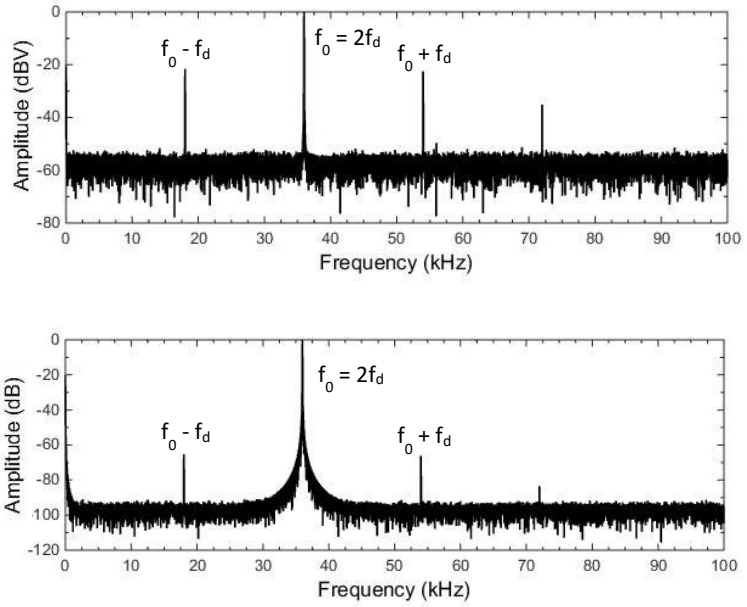

Figure 5.60: fundamental-normalised frequency response spectrum obtained (a) experimentally (PZT) and via (b) numerical simulation (LS-DYNA®).

Evidently, both the experimentally and computationally attained frequency responses of the sample under the excitation frequency of $2f_d$ contained the combination frequencies ($f_0 \pm f_d$) predicted by the analytic model. Furthermore, Figure 5.59 shows that in comparison to the 2nd harmonic response (Figure 5.56), there is only a small number of peaks associated with the subharmonic frequencies. This may be explained by the fact that the 2nd harmonic generation is a more frequent and common nonlinear phenomenon occurring at a broad range of frequencies and indeed often produced by the instrumentation itself. In this respect, the subharmonic response can be more advantageous and provided a clear localisation of the debonded region during the subsequent LDV experiments as presented in Figure 5.61.

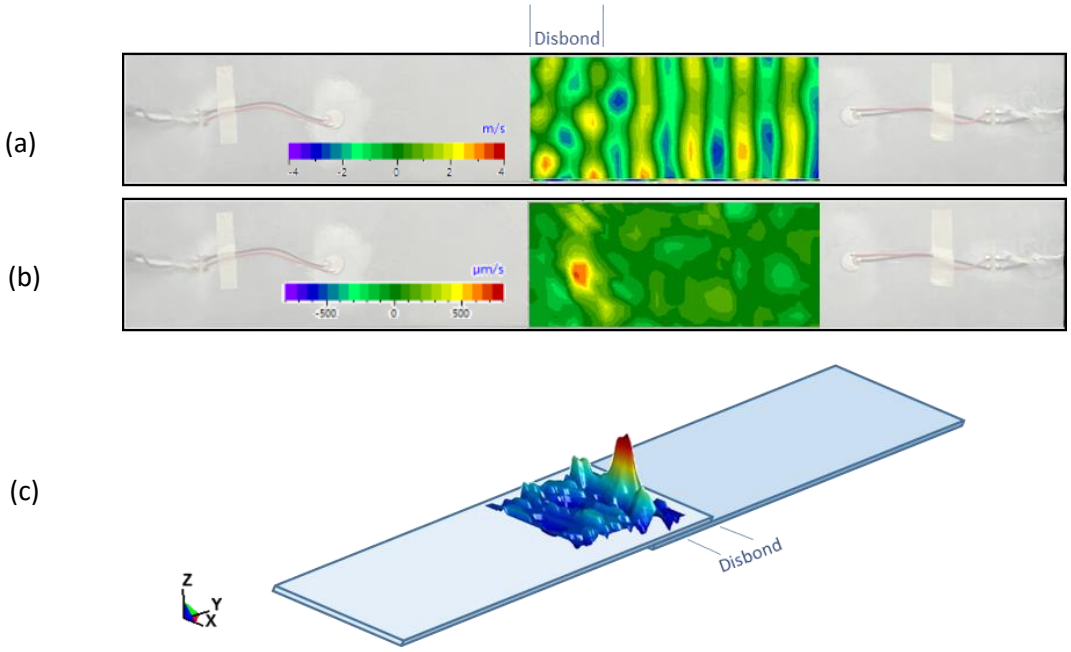

Figure 5.61: (a) experimental (LDV) results – amplitude of the vibration velocity at $f_0 = 2f_d$ = 36.22 kHz and (b) the amplitude of its spectral component at $0.5f_0$ = 18.11 kHz which is also $f_0 - f_d = f_d$; (c) a 3D surface plot of $0.5f_0$ amplitude obtained via LDV experiments.

The experimental and numerical procedures were repeated using samples and computational models with various disbond widths (see Table 5-9). The corresponding results are shown in Figure 5.62.

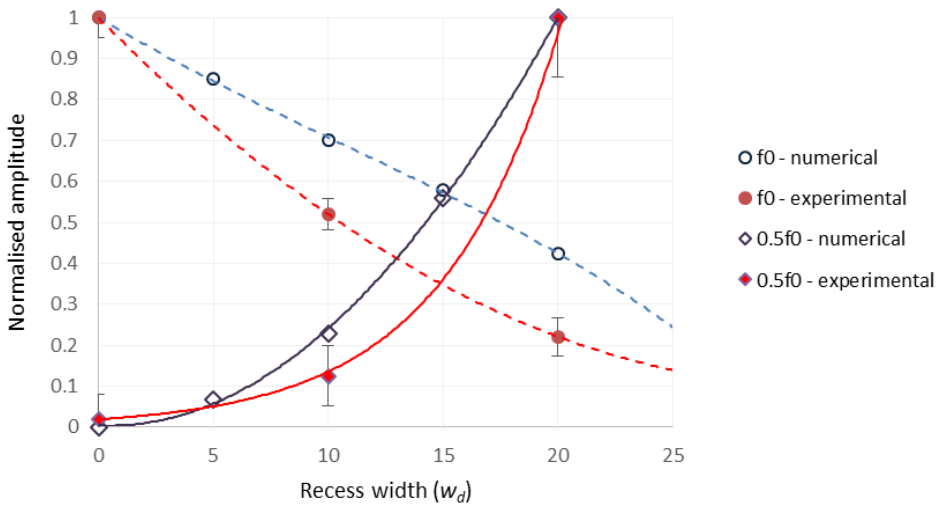

Figure 5.62: amplitude of the driving and the subharmonic frequency response at the excitation frequency of $2f_d$ normalised to the maximum value for each series of results; error bars represent standard deviation.

As expected, the amplitude of the driving frequency in the received signal reduced with increasing disbond width as less energy propagates into the other aluminium plate of the SLJ sample. On the contrary, the subharmonic amplitude increased with increasing recess width of the debonded region. This further confirm the dependence of the subharmonic generation on the extent of the disbond. Although the input signal amplitude was kept constant in the experimental and numerical studies, the

production of subharmonics is known to be strongly dependent on the input amplitude [178] and may need to be adjusted in other testing scenarios. The discrepancies between the numerical and experimental results can be explained by a multitude of factors and assumptions adopted for the computational approach. For example, no damping was used in the developed FEA model as it was not essential for the qualitative nature of the study.

5.4.6 Conclusion

A two dimensional analytical model based on a nonlinear oscillator was provided considering flexural waves in plates. The analytical model qualitatively indicated the generation of higher harmonics and the combination frequencies corresponding to the nonlinear intermodulation of the driving and the defect resonance frequencies. Subsequently, an isotropic single lap joint structure containing a disbond was considered in the experimental and numerical campaign. The LDR associated with the debonded region was identified via modal analysis, which was experimentally confirmed using surface-bonded piezoelectric transducers and LDV. Furthermore, it was confirmed that an effective subharmonic sensing can be achieved by exciting the sample at twice the value of a natural frequency and in this case, the flexural (natural) mode of vibration. Subsequently, the nonlinear imaging of the defect using subharmonic spectral component was successfully performed. Furthermore, a numerical model of partially bonded single lap joint was devised using a finite element analysis (FEA) software LS-DYNA® with user defined cohesive elements representing the disbond. The cohesive model incorporating bilinear stiffness relationship in the debonded region successfully predicted the generation of subharmonic frequencies in presence of the defect.

5.5 Development of Nonlinear Ultrasonic Phased Array C-Scan Imaging System

5.5.1 Introduction

The previous Sections looked at NEWS techniques involving sensing and imaging of the subharmonics and higher harmonics in the response spectrum of a material subjected to a single frequency harmonic input. In traditional NDT, the excitation is typically performed using a single monolithic piezoelectric transducer. However, advances in computing power and memory have been driving the use of ultrasonic phased arrays, which were briefly addressed in Chapter 3.2.3, in industrial NDT [273] and medical applications [274]. This approach offers flexibility in terms of the resulting wavefront, which can be translated, focused and steered in a user defined manner by having individually controlled parallel transmission circuits. This is achieved by setting the delay laws governing the staggered firing (transmission) of array elements. Some of the conventional ultrasonic phased array B-scan modes are: plane, focused and sector. A mover novel approach is referred to as *total focusing method* (TFM) [275]. Figure 5.63 schematically illustrates these modes.

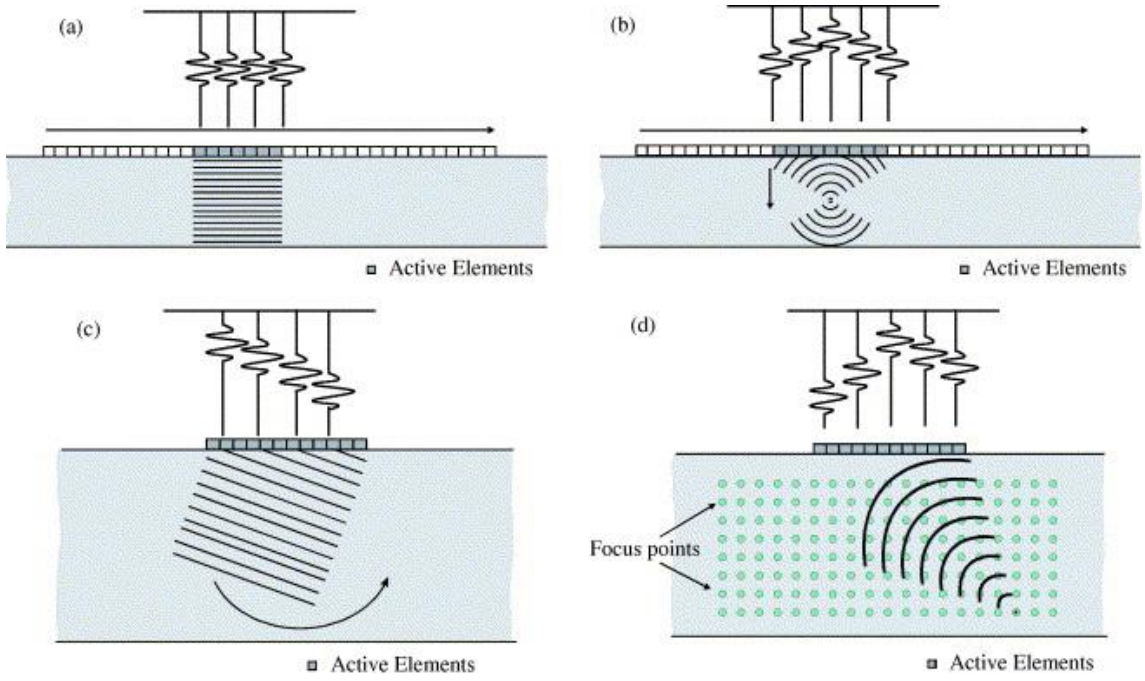

Figure 5.63: (a) plane B-scan, (b) focused B-scan, (c) sector B-scan and (d) TFM; reproduced from [276].

In plane B-scan mode, a group of adjacent elements, called aperture, are fired simultaneously which allows to introduce more acoustic energy into the specimen, thereby increasing the lateral resolution and increasing the sensitivity compare to transmitting with merely one element. The time domain signal is received by all elements in the active aperture and summed to form a single A-scan (time domain signal). The performance of this approach is equivalent to that of a single plane monolithic transducer of the identical size as the aperture. Subsequently, the active aperture is electronically

translated (shifted) along the length of the array and repeating the outlined transmission-reception process, with the resulting collection of A-scans combined into a final B-scan image.

Similar approach can be applied for focusing and to obtain a sector scan, which is equivalent of using curved transducers, lenses or wedges with monolithic piezoelectric probes. However, the TFM-based B-scan is qualitatively and quantitatively different from the aforementioned scanning modes and is performed in the post-processing step on the data captured with the full matrix of the array [275]. In the *full matrix capture* (FMC) approach, a complete set of raw A-scans is obtained by considering all combinations of transmitting and receiving elements. It typically involves firing at one element and capturing at all array elements, and sequentially shifting through all elements repeating the process. Subsequently, the gathered FMC data can be processed offline by focusing at every point in the user defined grid of points, as shown in Figure 5.63(c), achieving a TFM scan. The summation of the image intensity is performed at each point taking into account every possible transmitter-receiver couple, thereby fully utilising the information available for each point [276]. Compared to other scanning modes, the advantages of the TFM include enhanced resolution and sensitivity to smaller defects. However, it requires specialised hardware and is very demanding in terms of computer power and processing time. Another drawback is a relatively low SNR associated with the fact that merely one element is used for transmitting. Although, this is somewhat offset by the averaging effect introduced in the TFM. Holmes *et al.* [276] reported a 18 dB decrease in SNR for the TFM results reconstructed from FMC data relative to the results obtained by simultaneous firing all 64 elements of the phased array; an increase in SNR by 13 dB was obtained by taking 20 averages (averaging the data from 20 successive acquisitions) in the FMC procedure [276]. A good description of the outlined techniques and mathematical algorithms for obtaining the final B-scan image is provided by Holmes *et al.* [276].

Whilst the aforementioned techniques were generally explained in the context of linear ultrasound, they can also be applied in the nonlinear regime. Indeed, the use of nonlinear ultrasonic B-scan phased array imaging has been an active field of research in medical applications with the corresponding technique generally referred to as *harmonic imaging* [277]. The underlying principles of the origin of the nonlinearities are largely equivalent to what was already addressed in Chapter 3.4 and can be explained from a perspective of local pressure change caused by a propagating sound wave. A localised pressure increase of the travelling wavefront results in a local increase in temperature and consequently an increase in the local speed of sound (considering a compressible material). Hence, the wave propagates faster during its higher pressure phase than lower one, meaning that that the peaks of a plane sinusoidal single frequency wave would travel faster than the toughs. This self-distortion of a sinusoidal wave can lead to a sawtooth like wave, with wave energy being transferred from the fundamental frequency of transmission to higher harmonics. Mathematically, this can be

explained by considering the wave equation (Eq. (3.16)) and expanding the density term using a Taylor series expansion leading to a nonlinear equation of state (EOS) relating pressure to density as opposed to introducing the nonlinearity at the constitutive level (Eq. (3.24)). Subsequently, this approach leads to a Westervelt equation that accounts for the 2nd order nonlinearity, or its simplified form, termed Burgers' equation, which considers the nonlinear wave propagation in 1D [278]. A more comprehensive equation of nonlinear propagation of directional sound beams is provided by Khokhlov-Zabolotskaya-Kuznetsov (KZK) equation which accounts for the combination of nonlinearities, diffraction and absorption effects [279]. In medical sonography, the nonlinear properties of ultrasound offer improved imaging possibilities in tissue characterisation and particularly in enhanced ultrasound contract imaging. The latter technique involves injecting a contrast agent containing micro-bubbles into a patient's blood stream, which increases the acoustic impedance of the blood and therefore enhances the sensitivity of the linear imaging methods. Moreover, exciting at certain frequencies (typically between 1-10 MHz), the micro-bubbles start to resonate and oscillate in a nonlinear manner, thus transferring the energy of the fundamental frequency of excitation into higher harmonics, making it possible to perform harmonic imaging by displaying the amplitude of $2f_0$, $3f_0$, $4f_0$, $5f_0$, etc. [277, 280]. However, the main difficulty with the harmonic imaging in medical applications is associated with the fact that all soft tissues produce nonlinear response characterised by wave distortion and the presence of superharmonics in the response spectrum. This led to the ongoing research effort in the development of specialised transducers [281, 282] that can be inherently more sensitive to micro-bubble related frequencies by design.

In industrial NDT, there is also a number of published techniques aimed at performing the nonlinear phased array imaging. Yamanaka *et al.* [283] proposed a technique for subharmonic ($0.5f_0$) phased array imaging of closed cracks hypothesising an analogy between the effects associated with the micro-bubbles and closed cracks, although merely partially verified results were presented. Most recently, Ouchi *et al.* [284] used surface acoustic waves (SAW) to perform subharmonic (~5 MHz) imaging of the fatigue and corrosion-related cracks in aluminium and steel samples using a phased array transducer excited at 10 MHz 150 V. The resulting B-scan showed that the linear method produced a clearer image for the fatigue sample, while the subharmonic component was more sensitive to the corrosion crack [284]. Potter *et al.* [273] reported another interesting nonlinear phased array imaging technique that relies on the aforementioned FMC and TFM approaches. They hypothesised that as the absolute acoustic power injected into the material is higher during the physical focusing than during the reconstruction of the equivalent focusing in the TFM, there should be a lager acoustic energy transfer from the fundamental to other frequencies due to various nonlinear phenomena at the focal point in the former case. They further hypothesised that the relative

differences in the acoustic energy at a focal point using both methods are driven by the nonlinear losses local to that point [273]. Hence, their technique involves a parameter that is used as a measure of the acoustic nonlinearity at the focal point by comparing the relative energy of the transmission frequency band in both the physical focusing and in the TFM [273]. Hence, their approach does not depend on the amplitude of the particular component of sub and higher harmonics present in the response spectrum but rather considers the reduction of the fundamental frequency, which is assumed to be more severely affected by the local nonlinearities in physical focusing than in the focusing reconstructed from the FMC data. Interestingly, through the experimental work, involving a fatigued aluminium sample and a phased array probe of 64 elements (excited at 5 MHz), they showed that the developed nonlinear phased array imaging method successfully captured the presence of the crack by plotting the intensity of the devised nonlinear indicator in the form of a B-scan, whereas the linear technique was not effective. However, the main disadvantage of the method is the computer processing time which can span hours depending on the hardware. Also, the applicability of the technique to more complex structures and damage types have not been considered yet.

Whilst several nonlinear phased array B-scan techniques were discussed, there is little evidence development attempts involving its C-scan counterpart. As described in Chapter 3.2.3, the C-scan images can be obtained by post-processing a collection of B-scans acquired by translating the probe over the surface of the test specimen. Therefore, this work focused on the development of a nonlinear ultrasonic C-scan phased array system capable of continuously imaging and monitoring the nonlinear signature in a given aerospace complex components.

5.5.2 Hardware Setup and Capabilities

The motorised modular scanning system was build comprised of an aluminium profile structure, stepper motors, fully encoded in 3 axes, control module with LCD (Arduino based) and power supply module – Figure 5.65 schematically shows the system layout.

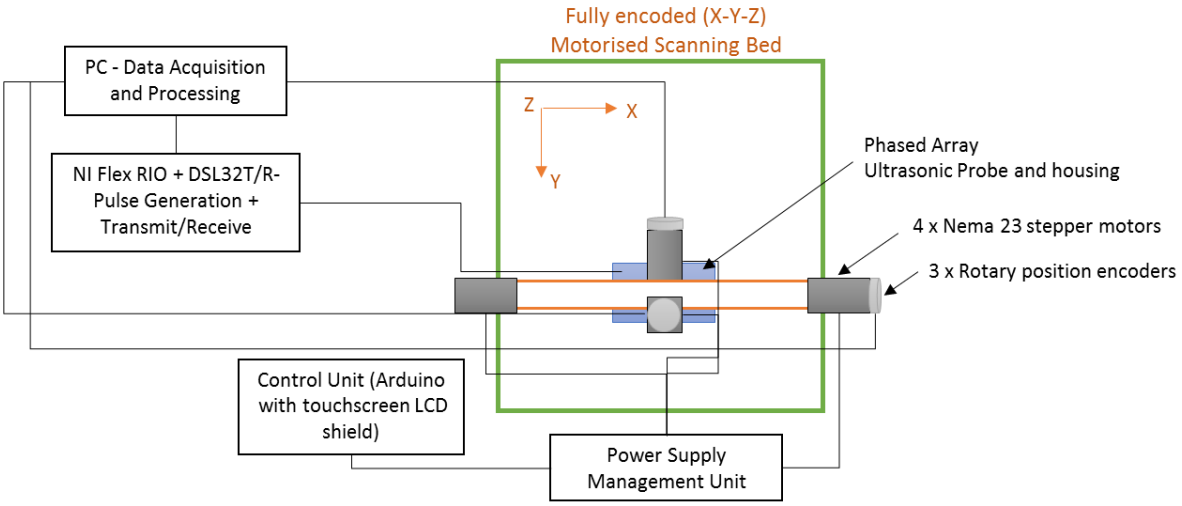

Figure 5.64: a schematic of the main components of the developed phased array scanning system.

The system was constructed to meet the requirements outlined in Figure 5.10.

Scanning Area	600 x 600 mm
Optimum Scanning Rate	800 cm^2/min
Allowable Sample Thickness	2-20 mm
Modular Transducer Attachment	YES
Immersion Scanning Possible	YES

Table 5-10: general characteristics of the scanning system.

The images of the actual scanner and the phase array probe holder is shown in Figure 5.65.

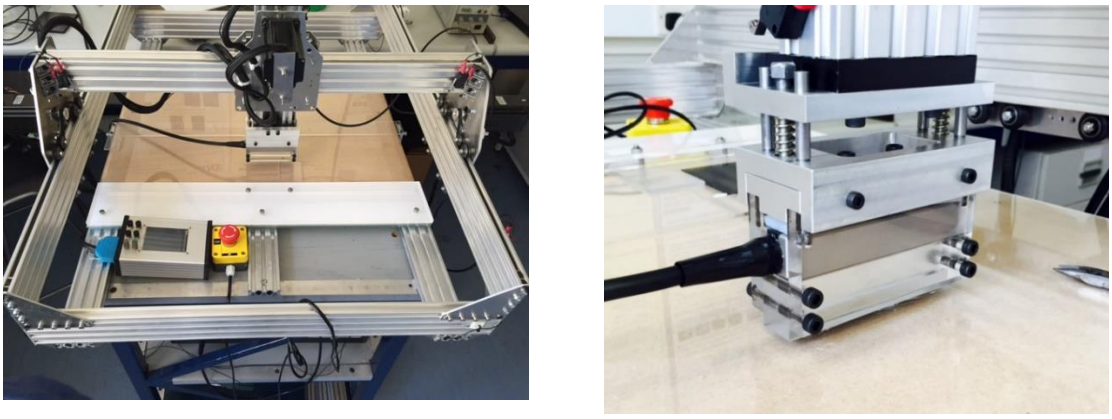

(a) (b)

Figure 5.65: (a) a modular nonlinear phased array scanning system and (b) transducer attachment housing.

The design allows for quick fitting of a variety of sensors and transducers to be used as a scanning tool. In the present setup, a 5 MHz (50% -6 dB) phased array sensor (128 elements) was used. The signal generation/processing hardware setup is comprised of National Instruments (NI) FlexRIO system along with multi-channel pulsers, receivers and digitisers required in order to enable a number of ultrasonic data acquisition and processing functions. The hardware incorporated the following:

- 2 x FlexRio Modules – 32 Channels (high performance I/O module)
- 1 x NI5752 – 32 Channels 12bit (Digitizer/Oscilloscope)
- 1 x DSL32T – 32 Channels (Pulser – provides independent control over 32 tri-level high voltage Pulsers)
- 1 x DSL32R – 32 Channels (Receiver – provides transmit-receive protection followed by low noise pre-amplification, directly coupled to NI5752).

The phased array system housed in the NI-PXI chassis is shown in Figure 5.66(b), while the phased array transducer is depicted in Figure 5.66(b).

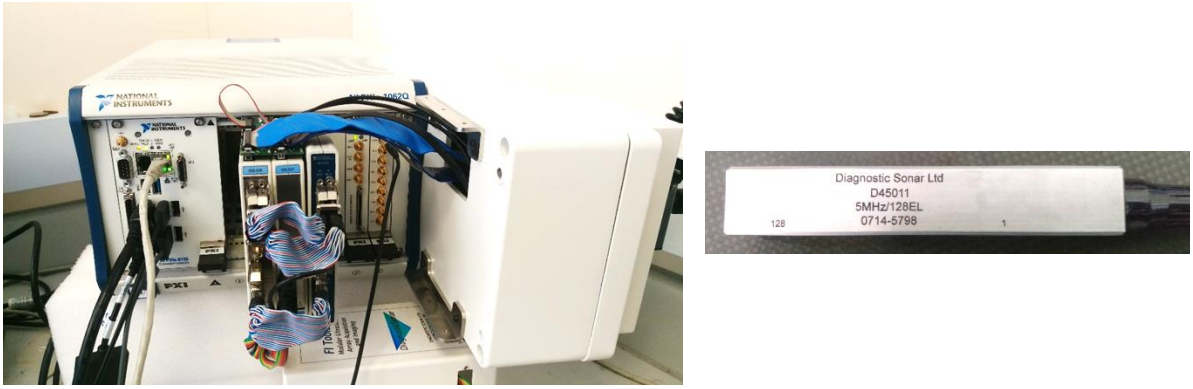

(a) phased array system assembled in the NI-PXI chassis (b) 128-element phase array probe

Figure 5.66: system components.

The phased array system allows for a high level of flexibility in terms of hardware and software support. The hardware side is fully upgradable as it utilises an industry standard PXI bus, while the software is implemented in NI LabVIEW and as a standard allows a plane scan, focused scan, steered scan, FMC and the ability to capture raw data for all methods which allows the development of nonlinear imaging techniques. Furthermore, the capabilities of a multi-element motorised system provide a much higher level of consistency in data acquisition, accuracy and speed in terms of damage assessment compared with single element transducers. The system provides sufficient amount of raw data to image nonlinear responses for damaged regions for complex aerospace structures.

The system requires a number of inputs, defined below, in order to correctly setup the test:

- Excitation frequency (2.5-7.5 MHz)
- Selection of the number of transmission and receiving elements
- Probe dimensions and information
- Wedge dimensions and information
- Number of excitation cycles (up to 10) and phase adjustments
- Speed of sound
- Beam focus depth (automated focal law adjustments)
- Voltage (0-150V)
- Gain adjustments
- Low Pass and High Pass filters

In the developed modular nonlinear phased array system, the collection of raw data from test samples and postprocessing the results is largely autoamted allowing to evaluate the damage in real time and offline. Various nonlinaer paramters were considered and compaured against the standard linear C-scan resuts. Table 5-11 below sumarasise the developed C-scan techiques.

Imaging method	**Parameter plotted**
Standard C-Scan	Amplitude of the time signal
Fundamental	A_0 - FFT amplitude of f_0 across the data set
2nd Harmonic	A_2 - FFT amplitude of $2f_0$ across the data set
3rd Harmonic	A_3 - FFT amplitude of $3f_0$ across the data set
Sub-Harmonic	$A_{0.5}$ - FFT amplitude of $0.5f_0$ across the data set
Beta	A_2/A_0^2
Gamma	A_3/A_0
Sub-Parameter	$A_{0.5}/ A_0$

Table 5-11: a number of devised linear and nonlinear imaging techniques that can be used with the specified phased array probe.

The aforementioned techniques were implemented as post-processing tools that operate on the raw time-domain data. The fast Fourier transform (FFT) is performed on the A-scans acquired for each point and the amplitude of the corresponding frequency component of interest is obtained.

5.5.3 Preliminary Results

Using the nonlinear imaging techniques defined in Table 5-11, the three laminates, including the helicoidal one subjected to LVI events presented in Chapter 4.3.4.2, were evaluated. Figure 5.67, Figure 5.68 and Figure 5.69 show the non-smoothed, nonfiltered results obtained using the excitation frequency of f_0 = 5 MHz with a sampling rate of 40 Ms and the voltage of 150 V_{pp}.

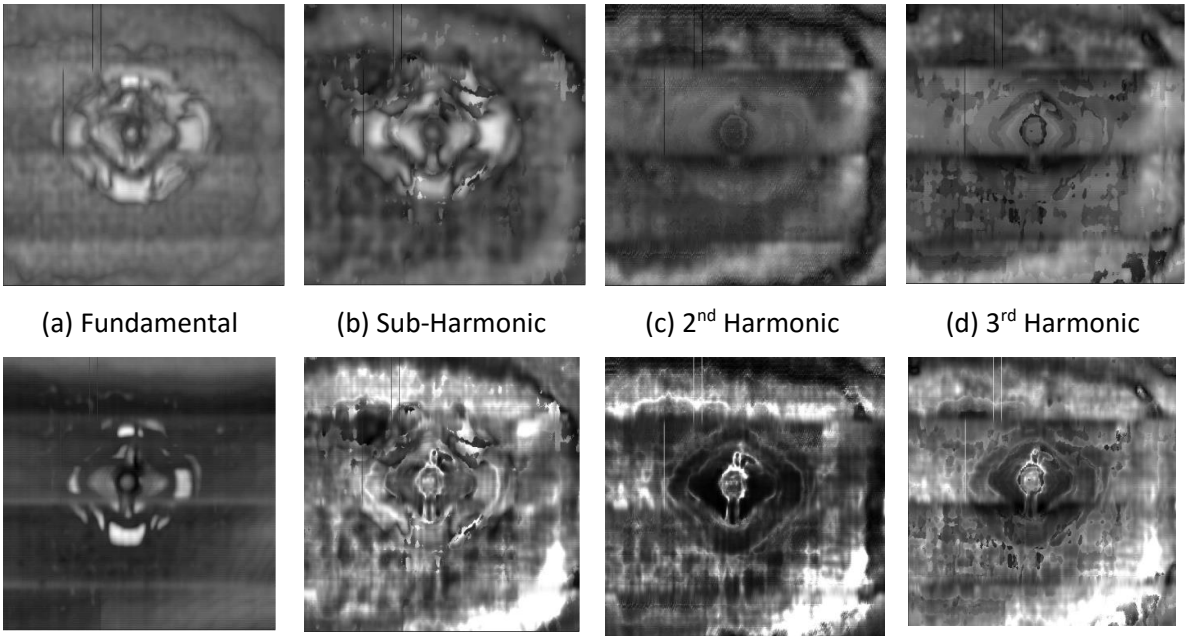

(a) Fundamental (b) Sub-Harmonic (c) 2nd Harmonic (d) 3rd Harmonic

(e) Linear C-scan (f) Sub-Parameter (g) Beta (h) Gamma

Figure 5.67: the results of phased array imaging for a cross-ply laminate with BVID.

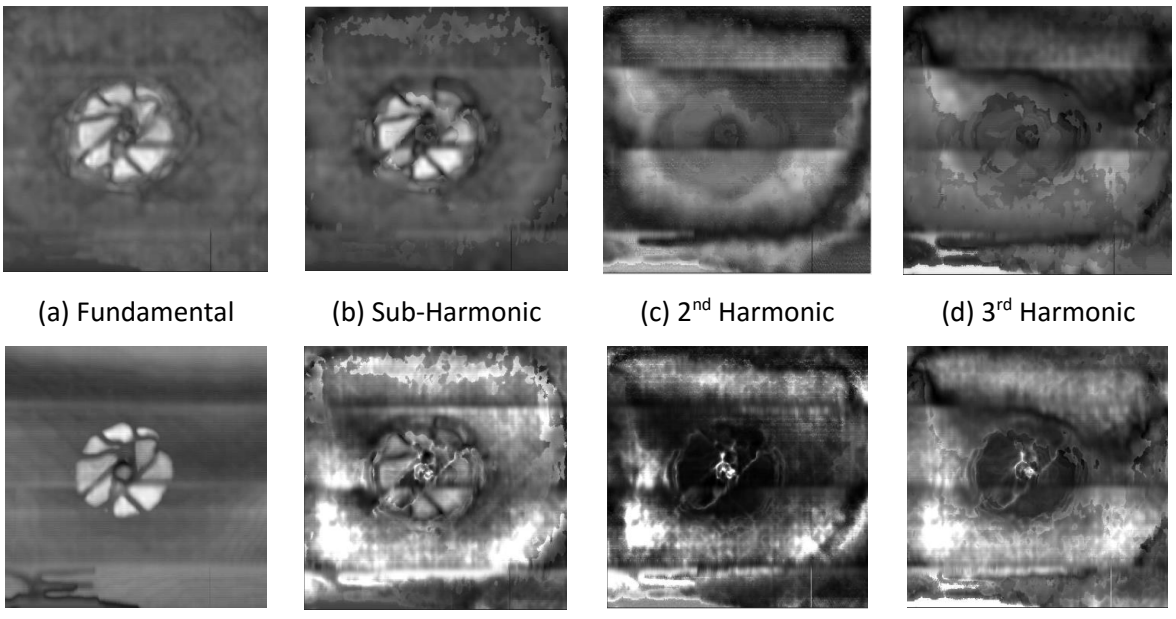

(a) Fundamental (b) Sub-Harmonic (c) 2nd Harmonic (d) 3rd Harmonic

(e) Linear C-scan (f) Sub-Parameter (g) Beta (h) Gamma

Figure 5.68: the results of phased array imaging for a quasi-isotropic laminate with BVID.

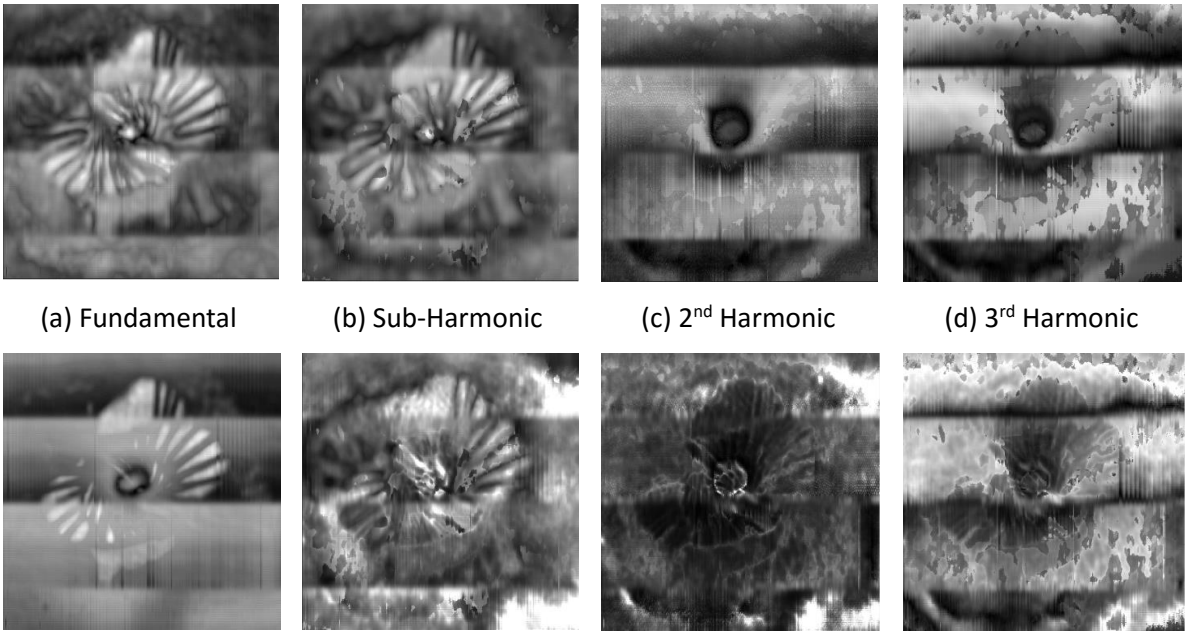

(a) Fundamental (b) Sub-Harmonic (c) 2nd Harmonic (d) 3rd Harmonic

(e) Linear C-scan (f) Sub-Parameter (g) Beta (h) Gamma

Figure 5.69: the results of phased array imaging for a helicoidal laminate with BVID.

Although it is evident that in most cases the linear/fundamental technique provided the clearest results, the C-scans of the subharmonic amplitude and sub-parameter showed in several cases a better contrast with clearer details than observable in the linear case. Furthermore, Figure 5.69 (c-d) indicated a significant contrast in the immediate locality of the impact zone for the helicoidal laminate using the 2nd and 3rd harmonic amplitudes.

5.5.4 Conclusion

Various phased array methods, including FMC and TFM along with interdisciplinary applications, have been introduced. A phased array effectively acts as a pulse-echo ultrasonic system containing an array of transducers referred to as elements. By varying the delay between the firing of adjacent elements, the resulting ultrasonic beam can be shaped. This allows to perform multiple measurements without repositioning of the sensor, and by motorising/automating the scanning process, enables eliminating the alignment/coupling variability that can mask the highly sensitive nonlinear signals. The nonlinear phased array C-scan system was developed, whereby several nonlinear imaging indictors were utilised. The preliminary results showed some promising characteristics and it is envisioned that these methods would lead to enhanced damage detection and nonlinearity localisation, especially by combing the various approaches.

6 Concluding Remarks and Future Work

There are numerous examples found in nature of structurally advanced multifunctional materials which has resulted in a significant research effort in recent years in an attempt to provide a basis for new and improved synthetic damaged-tolerant armour materials. In this thesis, a helicoidal or Bouligand structure typical to the impact resistant dactyl clubs of mantis shrimp was to some extent mimicked in the design of impact resistant composite layups. It is worth noting that while some research evidence in support of Bouligand stacking configurations exists, there is not yet clear indication that any composite utilising industry is using or seriously considering the use of such layups for real world applications. This is partly due to the manufacturing complexity involved in using the non-standard inter-ply angles but also due to the lack of research knowledge associated with performance of twisted composite architectures. Therefore, it is envisioned that the outcome of this research will lead to further studies and pave the way for the helicoidal laminates being used, in combination with their classical counterparts, for example, in aircraft radome, fuselage, leading edge protection and other applications requiring damage tolerance.

Another aspect, which is important to the damage tolerance approach, is a capability to detect damage or defects in structural components before they become a threat to the aircraft safety and performance. Whilst the linear ultrasound techniques have been successfully applied for several decades in order to detect the structural discontinuities characterised by significant impedance sources, they are not effective in evaluating structural damage at micro level such as closed cracks in metallic and composite components. Hence, several nonlinear ultrasonic techniques involving higher harmonics and subharmonics as signatures of the structural defect presence have been considered and evaluated using both experimental and numerical methods. The following Section summarises some of the original contributions, while several proposals for future work are provided in the last Section that concludes this thesis.

6.1 Original Contributions

- A study of damage resistance of angle-ply laminates arranged in bio-inspired helicoidal layups was carried out. The presented work is more complete than other research efforts published in literature and considered various impact energies, plate size, different rotation angles, and layup symmetry/balance. The advanced FEA approach by means of LS-DYNA® and MAT162 allowed a more qualitative and quantitative assessment of the dynamic performance and residual strength of the helicoidal composites.

- A constitutive nonlinear orthotropic elastic model was implemented and validated using a commercial FEA software LS-DYNA®. The model allows simulating the 2nd harmonic generation characteristic of the materials containing arbitrary damage or defects.

- An extensive experimental study considering the generation of the 2nd harmonic and heating at the crack interface in a fatigued sample was carried out by means of LDV and IR camera equipment. It indicated that a more reliable damage detection can be achieved by evaluating the combined response associated with the linear, nonlinear ultrasonic and thermal effects.

- A novel narrow sweep excitation nonlinear thermosonic method, which requires no prior knowledge of defect/damage locations, was suggested and qualitatively assessed. This method showed that the NDE process could be simplified while increasing the probability of detection by considering the presence of the 2nd harmonic in the response spectrum during the frequency selection process. The devised experimental technique was successfully applied on a complex composite stiffener panel with multiple BVIDs. A fully coupled structural-thermal FEA model capable of simulating the 2nd harmonic generation and the heating of the structure was also developed.

- An analytical model combining the anharmonic oscillator and flexural response of thin plates was adopted. Following the prediction of the model, a NDT/NDE method based on the generation of the subharmonic frequency for detection/imaging of disbonds in single lap joints using fully contact (via bonded piezoelectric transducers) and noncontact (LDV) instrumentation was developed and evaluated. The technique was further validated by the devised FEA model, whereby the nonlinear dynamic behaviour of the disbond was represented using a cohesive zone model.

- A nonlinear imaging phased array C-scan system was developed. A number of nonlinearity indicators were used for C-scan imaging of samples subjected to LVI. This presents a first step in developing a C-scan capable of localising the nonlinearities within a structural component.

6.2 Scope for Future Work

To conclude this thesis, a discussion of the future work considering each chapter of results is provided next.

In Chapter 3, the CFRP layups inspired by the internal structure of dactyl clubs of mantis shrimp were considered mimicking merely the helicoidal arrangement associated with the periodic phase of the clubs. However, the physical structure of the club was shown to be considerably complex featuring a stiff and strong impact layer followed by the periodic zone. This could be replicated in the experimental and/or numerical work, for instance, by manufacturing a laminate consisting of a titanium or steel layer (on the impact face) followed by the helicoidal CFRP lamination sequence underneath. Furthermore, the specimen can be manufactured as a hemispherical multi-featured structure driven by the cross-sectional topology of the dactyl club. The combined effect of these attributes could result in a superior impact-resistant structure. The FEA methodology developed in present work could be used for further numerical analysis and can involve LVI events at oblique angles given the stochastic nature of most FOD events.

In Chapter 5.1, the implemented nonlinear material model was applied to study an acoustic response of a fatigued sample. In future work, it can be applied to more complex components with other damage types.

Furthermore, the study of the 2^{nd} harmonic and heat generation in the vicinity of a crack in a fatigued sample presented in Chapter 5.2 can be expanded by evaluating the frictional work which can be calculated by means of Eq. (3.34). This can allow to attain further understanding of the relationship between various eigenmodes of vibration, heating and the generation of harmonics. Ultimately, this can guide the development of very effective and reliable thermosonic NDT techniques. However, the frictional heating is highly dependent on the normal force between the cracked surfaces. Whilst the experimental evaluation of this force is not feasible as no sensing equipment can penetrate the closed crack surfaces without altering the system, the resultant crack interface forces can be obtained numerically via FEA (wave propagation or frequency domain analysis). However, this would require a very high fidelity FEA modelling of the crack surface interaction – a detailed FE mesh can be obtained by high definition CT scan of the crack revealing its internal structure. Subsequently, the frictional work can be estimated and plotted against natural frequencies.

The numerical approach of coupled structural-thermal FEA modelling developed in Chapter 5.3, can be used to simulate the harmonic and thermal response of complex aerospace components. Subsequently, this data can serve as a baseline aiding effective NDT/NDE. Moreover, the suggested thermosonic technique by means of narrow sweep excitation should be evaluated on other large scale components and the actual aircraft considering in-service conditions.

In Chapter 5.4, an NDT/NDE method based on the subharmonic generation was presented. The analytical model considered flexure of isotropic rectangular plates. However, the governing Eq. (5.20) is almost identical to the plate bending equation for composite plates (Eq. (2.24)). The major difference is that the latter case involves several bending stiffness terms (D_{ij}) but this would not qualitatively change the combination frequencies obtained for the isotropic case, and therefore, the adopted approach is generally applicable to orthotropic plates as well. Thus, in future work, it can be readily applied to composite structures containing various damage types. Moreover, the analytical method can be expanded to include 3rd order nonlinearity yielding further combination frequencies which can be numerically and experimentally evaluated using the devised experimental and numerical approach.

The nonlinear C-scan developed in Chapter 5.5 can be enhanced by developing and implementing other nonlinear imaging techniques.

Appendix

A. Fundamentals of Composites

Composites are distinct from other materials such as metals and it is important to define the terms associated with this difference. Metals such as aluminium or titanium are considered *homogeneous isotropic* materials. In an isotropic body, the material properties are the same in all directions at a point and the medium is said to be homogeneous if the material properties are the same / uniform throughout the body, independent of the position. Moreover, resin matrix is also considered a homogeneous and isotropic. In an *anisotropic* body, the material properties are direction-dependent; fully anisotropic material has different material properties in all directions. A medium is called *heterogeneous* if its material properties vary with position in the body. A material can generally be an isotropic or anisotropic and homogeneous or heterogeneous. However, most composite materials are inherently heterogeneous and anisotropic in nature. A typical example of such a composite laminate, which was used this study, is comprised of layers of *unidirectional* (UD) carbon fibre plies stacked on top of each other at different orientation angles relative to the neutral axis as shown schematically in Figure 6.1.

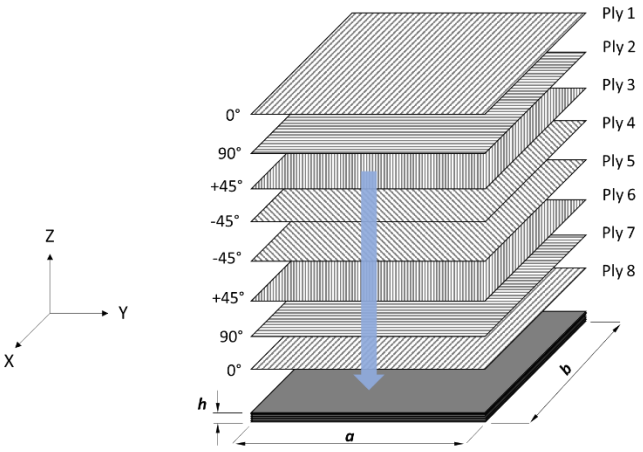

Figure 6.1: a schematic representation of a quasi-isotropic laminate layup.

UD composite material is usually supplied as a resin pre-impregnated tape, which is called *prepreg* for brevity, and is a typical example of a composite ply or lamina with fibres orientated in a single direction. Fibres are the primary load carrying constituents with the matrix supporting and bonding them together in a desired orientation. The matrix also acts as a load transferring and environmental resistance mechanism. The sequence in which the plies are stacked is referred to as *lamination scheme* (LS) or stacking sequence and determines the overall strength and stiffness of the laminate. The LS is denoted by [α/β/γ/δ/ε/…] where α is the orientation of the first ply and the plies are counted from top to bottom as shown in Figure 6.1. A general laminate considered in this study is termed *angle-ply*

laminate and consists of UD plies stacked at angles in the range of -90° ≤ θ ≤ 90° with the angle between the adjacent plies denoted as *rotation angle* or *pitch angle*; unless otherwise stated it has all layers of the same thickness and material. A traditional LS used in aerospace industry is called *quasi-isotropic* and characteristically consists of 0°, 90°, +45°, -45° or 0°, 60°, -60° angles. To some extent it mimics isotropic material properties – quasi-isotropic laminates exhibit *in-plane isotropy*. Another special type of LS is called *cross-ply* which only consists of layers stacked at 90° relative to each other – e.g. [0/90/0/90]. However, plies can be stacked in other various sequences and there are a number of technical terms associating the behaviour of the laminate with a particular type of LS. A laminate is qualified as *balanced* if for every layer in the laminate there exists somewhere in the laminate an identical (in terms of material and thickness) layer but of opposite fibre orientation. A *symmetric* composite layup is one for which LS is symmetric about the mid-plane of the laminate, and they are identified by a subscript 'S' following the description of the LS– e.g. stacking sequence $[0/90]_S$ has layers grouped as follows: 0°, 90°, 90°, 0°.

A laminate coordinate system with corresponding stress components is shown schematically in Figure 6.2.

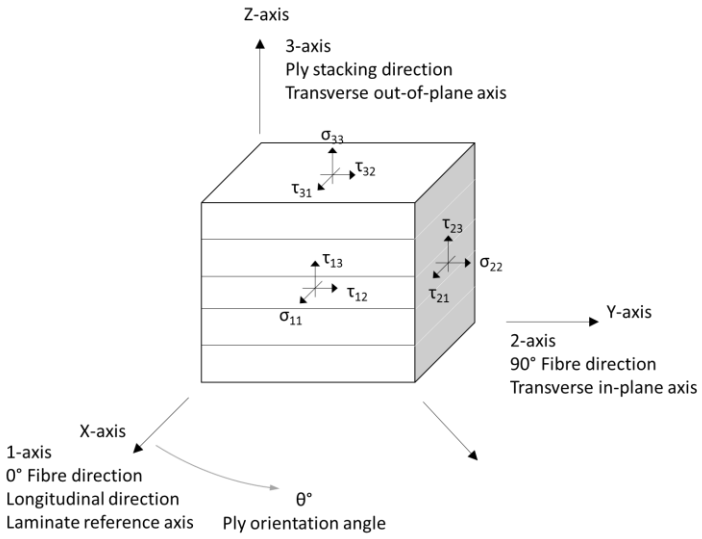

Figure 6.2: laminate coordinate system describing the principal material directions using notations (X Y Z) for the laminate and (1 2 3) for the plies for the axes.

The anisotropy of composite materials means that there are many variables governing its mechanical behaviour. In fact, a fully anisotropic material has 21 independent material stiffness components. The stress-strain relationship for such a material can be described using a *linear constitutive model* for infinitesimal deformation which is traditionally referred to as the *generalised Hook's law*

$$\boldsymbol{\sigma} = \mathbf{C}\colon \boldsymbol{\varepsilon}, \qquad \sigma_{ij} = C_{ijkl}\varepsilon_{kl} \tag{6.1}$$

In Eq. (6.1), the version of the stress-strain relationship is presented in a *tensorial (Kelvin) notation*, where $\boldsymbol{\sigma}$ and $\boldsymbol{\varepsilon}$ are *stress and strain 2nd order tensors* respectively and $\mathbf{C}$ is termed a *stiffness tensor (4th order)*. This constitutive relationship can be written in a more convenient form which is referred to as a contracted notation, *engineering notation* or *Voigt notation*

$$\{\sigma\} = [C]\{\varepsilon\}, \qquad \sigma_i = C_{ij}\varepsilon_j \quad , \tag{6.2}$$

Where the stress and strain is written as a column vector with components denoted using curly brackets or identified by a single subscript; C is no longer a tensor but a square *stiffness matrix* denoted by the square brackets or the two indices. Most material testing is performed with known loads or stresses and therefore it is convenient to rewrite Equation (6.2 in terms of strains:

$$\{\varepsilon\} = [S]\{\sigma\} \tag{6.3}$$

Where, $[S] = [C]^{-1}$ and is termed a *compliance matrix*. The form of the stress-strain relationship used in a particular Section of this thesis depends on its utility in aiding the explanation of the relevant concepts.

Most composite laminates including the ones considered in this work are classed as *orthotropic*, which can be considered as a special case of anisotropic behaviour. An orthotropic material is characterised by the existence of three mutually orthogonal planes of *material symmetry [46]*. Due to this symmetry and the symmetry of the stress and the stiffness tensors, the number of independent material coefficient components for such materials is reduced to 9 ($E_1, E_2, E_3, G_{12},\ G_{23}, G_{13}, \nu_{12},\ \nu_{23}, \nu_{13}$ – where, E is Young's modulus, G is the shear modulus and ν is the Poisson's ratio). Therefore, a strain-stress relationship shown in Equation (6.3 can be explicitly stated for an orthotropic material as

$$\begin{Bmatrix} \varepsilon_1 \\ \varepsilon_2 \\ \varepsilon_3 \\ \varepsilon_4 \\ \varepsilon_5 \\ \varepsilon_6 \end{Bmatrix} = \begin{bmatrix} \frac{1}{E_1} & -\frac{\nu_{21}}{E_2} & -\frac{\nu_{31}}{E_3} & 0 & 0 & 0 \\ -\frac{\nu_{12}}{E_1} & \frac{1}{E_2} & -\frac{\nu_{32}}{E_3} & 0 & 0 & 0 \\ -\frac{\nu_{13}}{E_1} & -\frac{\nu_{23}}{E_2} & \frac{1}{E_3} & 0 & 0 & 0 \\ 0 & 0 & 0 & \frac{1}{G_{23}} & 0 & 0 \\ 0 & 0 & 0 & 0 & \frac{1}{G_{13}} & 0 \\ 0 & 0 & 0 & 0 & 0 & \frac{1}{G_{12}} \end{bmatrix} \begin{Bmatrix} \sigma_1 \\ \sigma_2 \\ \sigma_3 \\ \sigma_4 \\ \sigma_5 \\ \sigma_6 \end{Bmatrix}, \tag{6.4}$$

where

$$\begin{aligned} \sigma_1 = \sigma_{11},\ \sigma_2 = \sigma_{22},\ \sigma_3 = \sigma_{33},\ \sigma_4 = \sigma_{23},\ \sigma_5 = \sigma_{13},\ \sigma_6 = \sigma_{12} \\ \varepsilon_1 = \varepsilon_{11},\ \varepsilon_2 = \varepsilon_{22},\ \varepsilon_3 = \varepsilon_{33},\ \varepsilon_4 = 2\varepsilon_{23},\ \varepsilon_5 = 2\varepsilon_{13},\ \varepsilon_6 = 2\varepsilon_{12}\ . \end{aligned} \tag{6.5}$$

The nine mechanical properties of a given laminate material can be evaluated experimentally through material testing or by means of one of *micro-mechanical* theories available in literature [46], which allows to calculate the macroscopic laminate properties from the known properties of its constituents considering the volume fractions of the fibres and the matrix. An advantage of this approach is that it is purely analytical and does not require the physical material testing to determine the properties of a ply. In general, composite laminates are usually analysed at three scales: micro, ply, and laminate level. As it can be seen from Figure 6.2, micro level deals with the analysis of fibres, matrix and the interface on the scale of individual fibres. The response of a laminate as a whole is considered at the *macroscopic* level, whereas the analysis length scale between micro and macro level is generally referred to as *mesoscopic* level.

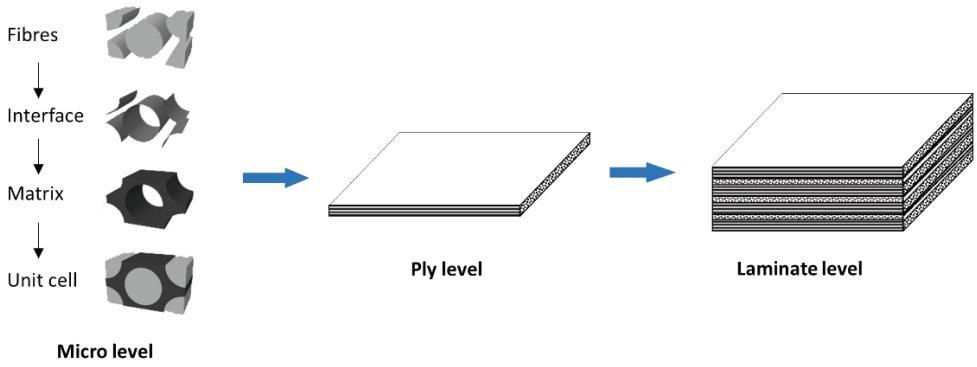

Figure 6.3: different physical scales considered in analysis of composite plates.

Bibliography

[1] G. Hellard. (2008, 01/12/2015). *Composites in Airbus*. Available: https://www.airbusgroup.com/dam/assets/airbusgroup/int/en/investor-relations/documents/2008/presentations/GIF2008/gif2008_workshop_composites_hellard.pdf

[2] MailOnline. (2009, 01/12/2015). *Bird strike! The moment 200 starlings were sucked into passenger jet engine on take-off*. Available: http://www.dailymail.co.uk/news/article-1217035/Bird-strike-The-moment-200-starlings-sucked-passenger-jet-engine-off.html

[3] S. E. W. Richard A. Dolbeer, John R. Weller, Amy L. Anderson, Michael J. Begier, "Wildlife Strikes to Civil Aircraft in the United States, 1990–2014," FAA, USDA 21, 2015.

[4] CAA. (2013, 01/12/2015). *Number Of Reported Uk Birdstrikes 2011-2013*. Available: http://www.caa.co.uk/docs/2008/srg_aats_ukbirdstrikes_2011-2013.pdf

[5] ICAO. (2015, 01/12/2015). *Technology Standards of Environmental Protection*. Available: http://www.icao.int/environmental-protection/Pages/technology-standards.aspx

[6] E. Phil and C. Soutis, *Polymer composites in the aerospace industry*: Elsevier, 2014.

[7] K.-Y. Jhang, "Applications of nonlinear ultrasonics to the NDE of material degradation," *Ultrasonics, Ferroelectrics, and Frequency Control, IEEE Transactions on,* vol. 47, pp. 540-548, 2000.

[8] R. Talreja, "Internal variable damage mechanics of composite materials," *Yielding, damage, and failure of anisotropic solids,* pp. 509-533, 1987.

[9] X. Jia, G. Chen, Y. Yu, G. Li, J. Zhu, X. Luo*, et al.*, "Effect of geometric factor, winding angle and pre-crack angle on quasi-static crushing behavior of filament wound CFRP cylinder," *Composites Part B: Engineering,* vol. 45, pp. 1336-1343, 2013.

[10] M. D. Rhodes, J. G. Williams, and J. H. Starnes, "Low-velocity impact damage in graphite-fiber reinforced epoxy laminates," *Polymer Composites,* vol. 2, pp. 36-44, 1981.

[11] J. Degrieck and R. Dechaene, "Real time recording of transverse impact experiments on composite laminates," in *IN: Composites evaluation; Proceedings of the Second International Conference on Testing, Evaluation and Quality Control of Composites-TEQC 87, Guildford, England, Sept. 22-24, 1987 (A88-55455 24-24). Sevenoaks, England and Stoneham, MA, Butterworths, 1987, p. 61-68.*, 1987, pp. 61-68.

[12] P. Hine, B. Brew, R. Duckett, and I. Ward, "The fracture behaviour of carbon fibre reinforced poly (ether etherketone)," *Composites Science and technology,* vol. 33, pp. 35-71, 1988.

[13] M. W. Czabaj and J. G. Ratcliffe, "Comparison of intralaminar and interlaminar mode I fracture toughnesses of a unidirectional IM7/8552 carbon/epoxy composite," *Composites Science and Technology,* vol. 89, pp. 15-23, 2013.

[14] L. T. Drzal, P. Herrera-Franco, and H. Ho, "Fiber-matrix interface tests," *Comprehensive Composite Materials: Test Methods, Nondestructive Evaluation and Smart Materials,* vol. 5, pp. 71-111, 2000.

[15] R. Krueger, "The Virtual Crack Closure Technique: History," *Approach and Applications", NASA, Hampton, USA, ICASE Report,* vol. 10, p. 2002, 2002.

[16] D. Hull and Y. B. Shi, "Damage mechanism characterization in composite damage tolerance investigations," *Composite Structures,* vol. 23, pp. 99-120, 1993.

[17] R. Krueger, M. K. Cvitkovich, T. K. O'Brien, and P. J. Minguet, "Testing and analysis of composite skin/stringer debonding under multi-axial loading," *Journal of Composite Materials,* vol. 34, pp. 1263-1300, 2000.

[18] J. R. Tarpani, M. T. Milan, D. Spinelli, and W. W. Bose, "Mechanical performance of carbon-epoxy laminates. Part II: quasi-static and fatigue tensile properties," *Materials Research,* vol. 9, pp. 121-130, 2006.

[19] R. E. Swain, C. E. Bakis, and K. L. Reifsnider, "Effect of Interleaves on the Damage Mechanisms and Residual Strength of Notched Composite Laminates Subjected to Axial Fatigue Loading,"

in *Composite Materials: Fatigue and Fracture, Fourth Volume*, ed: ASTM International, 1993, pp. 552-552-23.

[20] J. Cook, J. Gordon, C. Evans, and D. Marsh, "A mechanism for the control of crack propagation in all-brittle systems," in *Proceedings of the Royal Society of London A: Mathematical, Physical and Engineering Sciences*, 1964, pp. 508-520.

[21] B. Harris, A. Chen, S. Coleman, and R. Moore, "Residual strength and toughness of damaged composites," *Journal of materials science,* vol. 26, pp. 307-320, 1991.

[22] "ASTM D3039 / D3039M Test Method for Tensile Properties of Polymer Matrix Composite Materials," ed: ASTM International, 2006.

[23] "ASTM D5379 / D5379M Test Method for Shear Properties of Composite Materials by the V-Notched Beam Method," ed: ASTM International, 2012.

[24] "ASTM D2344 / D2344M Test Method for Short-Beam Strength of Polymer Matrix Composite Materials and Their Laminates," ed: ASTM International, 2013.

[25] A. International, "ASTM D3410 / D3410M Test Method for Compressive Properties of Polymer Matrix Composite Materials with Unsupported Gage Section by Shear Loading," ed: ASTM International, 2008.

[26] I. C. Graham Barnes, Richard Roberts, Daniel O. Adams, David M. Garner, "Crash Safety Assurance Strategies For Future Plastic And Composite Intensive Vehicles (Pcivs)," U.S. Department of Transportation, Research and Innovative Technology Administration2010.

[27] G. Milliron, "Lightweight Impact-Resistant Composite Materials: Lessons from Mantis Shrimp," ed, 2012.

[28] "ASTM D7137 / D7137M Test Method for Compressive Residual Strength Properties of Damaged Polymer Matrix Composite Plates," ed: ASTM International, 2012.

[29] M. O. W. Richardson and M. J. Wisheart, "Review of low-velocity impact properties of composite materials," *Composites Part A: Applied Science and Manufacturing,* vol. 27, pp. 1123-1131, // 1996.

[30] S. Abrate, "Impact on laminated composite materials," *Appl Mech Rev,* vol. 44, pp. 155-90, 1991.

[31] T. Nicholas, "Material behavior at high strain rates," *Impact dynamics,* pp. 277-332, 1982.

[32] W. J. Cantwell and J. Morton, "The impact resistance of composite materials — a review," *Composites,* vol. 22, pp. 347-362, 1991/09/01 1991.

[33] A. Ahmed and L. Wei, "The Low-Velocity Impact Damage Resistance Of The Composite Structures-A Review," *Rev. Adv. Mater. Sci,* vol. 40, pp. 127-145, 2015.

[34] D. Liu and L. E. Malvern, "Matrix cracking in impacted glass/epoxy plates," *Journal of Composite Materials,* vol. 21, pp. 594-609, 1987.

[35] P. Robinson and G. Davies, "Impactor mass and specimen geometry effects in low velocity impact of laminated composites," *International Journal of Impact Engineering,* vol. 12, pp. 189-207, 1992.

[36] G. Davies, X. Zhang, G. Zhou, and S. Watson, "Numerical modelling of impact damage," *Composites,* vol. 25, pp. 342-350, 1994.

[37] S. Timoshenko, J. Goodier, and H. N. Abramson, "Theory of elasticity," *Journal of Applied Mechanics,* vol. 37, p. 888, 1970.

[38] G. Dorey, "Impact damage in composites—development, consequences and prevention," in *Proc. of ICCM*, 1987, pp. 3.1-3.26.

[39] J. Helfinstine, "Charpy impact of unidirectional graphite/aramid/epoxy hybrid composites," in *Composite Materials: Testing and Design (Fourth Conference), ASTM STP*, 1972, pp. 375-388.

[40] "ASTM D7136 / D7136M-15, Test Method for Measuring the Damage Resistance of a Fiber-Reinforced Polymer Matrix Composite to a Drop-Weight Impact Event," ed. www.astm.org: ASTM International, 2015.

[41] B. Chandra Ray and D. Rathore, "A Review on Mechanical Behavior of FRP Composites at Different Loading Speeds," *Critical Reviews in Solid State and Materials Sciences,* vol. 40, pp. 119-135, 2015.
[42] I. M. Daniel and R. H. LaBedz, "Method for compression testing of composite materials at high strain rates," *Compression testing of homogeneous materials and composites, ASTM STP,* vol. 808, pp. 121-139, 1983.
[43] I. Hall and M. Guden, "High strain rate testing of a unidirectionally reinforced graphite epoxy composite," *Journal of materials science letters,* vol. 20, pp. 897-899, 2001.
[44] G. Caprino, "Residual strength prediction of impacted CFRP laminates," *Journal of Composite Materials,* vol. 18, pp. 508-518, 1984.
[45] C. Cazeneuve and J. Maile, "Study of the behaviour of carbon fibre composites under different deformation rates," in *J. Phys. Colloque C5*, 1985, pp. 551-556.
[46] J. N. Reddy and J. N. Reddy, *Mechanics of laminated composite plates and shells : theory and analysis*, 2nd ed. Boca Raton, FL ; London: CRC Press, 2004.
[47] M. E. Tuttle, *Structural analysis of polymeric composite materials*: CRC Press, 2012.
[48] M. J. Hinton, A. S. Kaddour, and P. D. Soden, *Failure criteria in fibre reinforced polymer composites: the world-wide failure exercise*: Elsevier, 2004.
[49] P. Soden, M. Hinton, and A. Kaddour, "A comparison of the predictive capabilities of current failure theories for composite laminates," *Composites Science and Technology,* vol. 58, pp. 1225-1254, 1998.
[50] A. Kaddour, M. Hinton, P. Smith, and S. Li, "A comparison between the predictive capability of matrix cracking, damage and failure criteria for fibre reinforced composite laminates: Part A of the third world-wide failure exercise," *Journal of Composite Materials,* vol. 47, pp. 2749-2779, 2013.
[51] S. Heimbs, S. Heller, P. Middendorf, F. Hähnel, and J. Weiße, "Low velocity impact on CFRP plates with compressive preload: Test and modelling," *International Journal of Impact Engineering,* vol. 36, pp. 1182-1193, 2009.
[52] S. Heimbs, T. Bergmann, D. Schueler, and N. Toso-Pentecôte, "High velocity impact on preloaded composite plates," *Composite Structures,* vol. 111, pp. 158-168, 5// 2014.
[53] B. Gama, T. Bogetti, and J. Gillespie, "Impact, damage and penetration modeling of thick-section composites using LS-Dyna MAT162," *Advances in composite materials,* vol. 1, pp. 83-102, 2012.
[54] B. N. Parlett and D. S. Scott, "The Lanczos algorithm with selective orthogonalization," *Mathematics of computation,* vol. 33, pp. 217-238, 1979.
[55] J. O. Hallquist, "LS-DYNA theory manual," *Livermore Software Technology Corporation (LSTC),* vol. 3, 2006.
[56] (01/01/2016). *Neue Materialmodelle für Composites in LS-DYNA*. Available: http://www.dynamore.de/en/downloads/infodays/dokumente/2013-composites/newmaterials
[57] (01/01/2016). *Properties & Limits: Review of Shell Element Formulations*. Available: https://www.dynamore.de/de/download/papers/2013-ls-dyna-forum/documents/review-of-shell-element-formulations-in-ls-dyna-properties-limits-advantages-disadvantages
[58] M. Andersoon and P. Liedberg, "Crash behavior of composite structures," *A CAE benchmarking study [Master's thesis in Applied Mechanics]. Chalmers University of Technology. Göteborg, Sweden,* 2014.
[59] (01/01/2016). *Mantis Shrimp - Deadly Clown Colored Creature*. Available: http://www.factzoo.com/invertebrates/mantis-shrimp-deadly-clown-colored-creature.html
[60] D. B. Z. Gama, "A Progressive Composite damage Model for Undirectional and Woven Fabric Composites, MAT162 Composite DMG MSC," Materials Sciences Corporation & University of Delaware Center for Composite Materials2014.

[61] Z. Hashin, "Failure criteria for unidirectional fiber composites," *Journal of applied mechanics,* vol. 47, pp. 329-334, 1980.
[62] J. B. Jordan, C. J. Naito, and B. Z. G. Haque, "Progressive damage modeling of plain weave e-glass/phenolic composites," *Composites Part B: Engineering,* vol. 61, pp. 315-323, 2014.
[63] J. Xiao, B. Gama, and J. Gillespie, "Progressive damage and delamination in plain weave S-2 glass/SC-15 composites under quasi-static punch-shear loading," *Composite Structures,* vol. 78, pp. 182-196, 2007.
[64] A. Matzenmiller, J. Lubliner, and R. Taylor, "A constitutive model for anisotropic damage in fiber-composites," *Mechanics of materials,* vol. 20, pp. 125-152, 1995.
[65] (01/01/2016). *Composites in technical applications*. Available: http://www.composite-simulation.de/content/download/haufe.pdf
[66] "LS-DYNA Aerospace Working Group Modeling Guidelines Document," 2012.
[67] (01/01/2016). *LS-DYNA® Aerospace Working Group (AWG)*. Available: http://awg.lstc.com/
[68] L. Kachanov, "Time of the rupture process under creep conditions," *Isv. Akad. Nauk. SSR. Otd Tekh. Nauk,* vol. 8, pp. 26-31, 1958.
[69] L. Kachanov, *Introduction to continuum damage mechanics* vol. 10: Springer Science & Business Media, 2013.
[70] M. Yazdchi, S. Valliappan, and W. Zhang, "A continuum model for dynamic damage evolution of anisotropic brittle materials," *International journal for numerical methods in engineering,* vol. 39, pp. 1555-1583, 1996.
[71] K. V. Williams, R. Vaziri, and A. Poursartip, "A physically based continuum damage mechanics model for thin laminated composite structures," *International Journal of Solids and Structures,* vol. 40, pp. 2267-2300, 2003.
[72] A. Forghani, M. Shahbazi, N. Zobeiry, A. Poursartip, and R. Vaziri, "6 - An overview of continuum damage models used to simulate intralaminar failure mechanisms in advanced composite materials A2 - Hallett, Pedro P. CamanhoStephen R," in *Numerical Modelling of Failure in Advanced Composite Materials*, ed: Woodhead Publishing, 2015, pp. 151-173.
[73] K. V. Williams and R. Vaziri, "Application of a damage mechanics model for predicting the impact response of composite materials," *Computers & Structures,* vol. 79, pp. 997-1011, 2001.
[74] P. Maimí, P. P. Camanho, J. Mayugo, and C. Dávila, "A continuum damage model for composite laminates: Part I–Constitutive model," *Mechanics of Materials,* vol. 39, pp. 897-908, 2007.
[75] P. Maimí, P. P. Camanho, J. Mayugo, and C. Dávila, "A continuum damage model for composite laminates: Part II–Computational implementation and validation," *Mechanics of Materials,* vol. 39, pp. 909-919, 2007.
[76] L. Mishnaevsky and P. Brøndsted, "Micromechanical modeling of damage and fracture of unidirectional fiber reinforced composites: A review," *Computational Materials Science,* vol. 44, pp. 1351-1359, 2009.
[77] P. Liu and J. Zheng, "Recent developments on damage modeling and finite element analysis for composite laminates: a review," *Materials & Design,* vol. 31, pp. 3825-3834, 2010.
[78] C. G. Davila and P. P. Camanho, "Decohesion elements using two and three-parameter mixed-mode criteria," 2001.
[79] "LS-DYNA Keyword User's Manual," LSTC, www.lstc.com2014.
[80] R. de Borst and J. J. Remmers, "Computational modelling of delamination," *Composites Science and Technology,* vol. 66, pp. 713-722, 2006.
[81] ASTM, "Test Method for Fracture Strength in Cleavage of Adhesives in Bonded Metal Joints," ed: ASTM International, 2012.
[82] T. Belytschko, W. K. Liu, B. Moran, and K. Elkhodary, *Nonlinear finite elements for continua and structures*: John Wiley & Sons, 2013.
[83] (01/01/2016). Available: http://www.matthewpais.com/Home
[84] I. Polmear, "Light metals: from traditional alloys to nanocrystals," *Elsevier, Oxford,* 2006.

[85] S. Xiao and T. Belytschko, "A bridging domain method for coupling continua with molecular dynamics," *Computer methods in applied mechanics and engineering,* vol. 193, pp. 1645-1669, 2004.
[86] C. McVeigh and W. K. Liu, "Multiresolution continuum modeling of micro-void assisted dynamic adiabatic shear band propagation," *Journal of the Mechanics and Physics of Solids,* vol. 58, pp. 187-205, 2010.
[87] K.-A. Van Den Abeele, P. A. Johnson, and A. Sutin, "Nonlinear elastic wave spectroscopy (NEWS) techniques to discern material damage, part I: nonlinear wave modulation spectroscopy (NWMS)," *Research in nondestructive evaluation,* vol. 12, pp. 17-30, 2000.
[88] M. Meo and G. Zumpano, "Nonlinear elastic wave spectroscopy identification of impact damage on a sandwich plate," *Composite Structures,* vol. 71, pp. 469-474, 2005.
[89] G. Zumpano and M. Meo, "Damage localization using transient non-linear elastic wave spectroscopy on composite structures," *International Journal of Non-Linear Mechanics,* vol. 43, pp. 217-230, Apr 2008.
[90] Y. Hung, Y. S. Chen, S. Ng, L. Liu, Y. Huang, B. Luk*, et al.*, "Review and comparison of shearography and active thermography for nondestructive evaluation," *Materials Science and Engineering: R: Reports,* vol. 64, pp. 73-112, 2009.
[91] Y. Hung, "Applications of digital shearography for testing of composite structures," *Composites Part B: Engineering,* vol. 30, pp. 765-773, 1999.
[92] (2012, 01/12/2015). *Advanced Calculator - User's Manual*. Available: http://www.olympus-ims.com/en/.downloads/download/?file=285214785&fl=en_US
[93] (2015, 01/12/2015). *Phased Array Linear Scans*. Available: http://www.olympus-ims.com/en/ndt-tutorials/instrumententation/sscan/
[94] (01/12/2015). *ThermoWorks Emissivity Table*. Available: http://www.thermoworks.com/emissivity_table.html
[95] S. M. Shepard, "Flash thermography of aerospace composites," in *IV Conferencia Panamericana de END Buenos Aires*, 2007.
[96] X. Maldague, *Advances in signal processing for nondestructive evaluation of materials* vol. 262: Springer Science & Business Media, 1994.
[97] S. M. Shepard, "Understanding flash thermography," *Materials evaluation,* vol. 64, pp. 460-464, 2006.
[98] D. Bates, G. Smith, D. Lu, and J. Hewitt, "Rapid thermal non-destructive testing of aircraft components," *Composites Part B: Engineering,* vol. 31, pp. 175-185, 2000.
[99] D. P. Almond and P. Patel, *Photothermal science and techniques* vol. 10: Springer, 1996.
[100] L. Favro, X. Han, Z. Ouyang, G. Sun, and R. Thomas, "Sonic IR imaging of cracks and delaminations," *Analytical Sciences/Supplements,* vol. 17, pp. s451-s453, 2002.
[101] J. Rantala, D. Wu, and G. Busse, "Amplitude-modulated lock-in vibrothermography for NDE of polymers and composites," *Research in Nondestructive Evaluation,* vol. 7, pp. 215-228, 1996.
[102] T. Zweschper, A. Dillenz, G. Riegert, D. Scherling, and G. Busse, "Ultrasound excited thermography using frequency modulated elastic waves," *Insight-Non-Destructive Testing and Condition Monitoring,* vol. 45, pp. 178-182, 2003.
[103] M. Morbidini and P. Cawley, "Reliable crack detection in thermosonics NDE," in *REVIEW OF PROGRESS IN QUANTITATIVE NONDESTRUCTIVE EVALUATION: 34th Annual Review of Progress in Quantitative Nondestructive Evaluation*, 2008, pp. 536-543.
[104] U. Polimeno and D. P. Almond, "A compact thermosonic inspection system for the inspection of composites," in *Proc., Int. Conf. on Composite Materials*, 2009.
[105] I. Solodov, M. Rahammer, D. Derusova, and G. Busse, "Highly-efficient and noncontact vibro-thermography via local defect resonance," *Quantitative InfraRed Thermography Journal,* pp. 1-14, 2015.
[106] X. Han, V. Loggins, Z. Zeng, L. Favro, and R. Thomas, "Mechanical model for the generation of acoustic chaos in sonic infrared imaging," *Applied physics letters,* vol. 85, pp. 1332-1334, 2004.

[107] L. Favro, R. Thomas, X. Han, Z. Ouyang, G. Newaz, and D. Gentile, "Sonic infrared imaging of fatigue cracks," *International journal of fatigue,* vol. 23, pp. 471-476, 2001.
[108] T. Barden, D. P. Almond, S. G. Pickering, M. Morbidini, and P. Cawley, "Detection of impact damage in CFRP composites by thermosonics," *Nondestructive Testing and Evaluation,* vol. 22, pp. 71-82, 2007.
[109] M. Morbidini and P. Cawley, "A calibration procedure for sonic infrared nondestructive evaluation," *Journal of Applied Physics,* vol. 106, p. 023504, 2009.
[110] A. E. Lord Jr, "Acoustic emission," *Physical acoustics,* vol. 11, pp. 289-353, 2012.
[111] D. Jiles, "Review of magnetic methods for nondestructive evaluation (Part 2)," *NDT International,* vol. 23, pp. 83-92, 1990.
[112] J. W. Strutt, "On waves propagated along the plane surface of an elastic solid," *Proceedings of the London Mathematical Society,* vol. 17, pp. 4-11, 1885.
[113] H. Lamb, "On waves in an elastic plate," *Proceedings of the Royal Society of London. Series A, Containing papers of a mathematical and physical character,* vol. 93, pp. 114-128, 1917.
[114] A. E. H. Love, *Some problems of geodynamics*: Cambridge University Press, 2015.
[115] V. Giurgiutiu, *Structural health monitoring: with piezoelectric wafer active sensors*: Academic Press, 2007.
[116] J. Achenbach, *Wave propagation in elastic solids* vol. 16: Elsevier, 2012.
[117] I. A. Viktorov, *Rayleigh and Lamb waves: physical theory and applications*: Plenum press, 1970.
[118] J. Rose, K. Rajana, and M. Hansch, "Ultrasonic guided waves for NDE of adhesively bonded structures," *The Journal of Adhesion,* vol. 50, pp. 71-82, 1995.
[119] R. Chona, C. Suh, and G. Rabroker, "Characterizing defects in multi-layer materials using guided ultrasonic waves," *Optics and Lasers in Engineering,* vol. 40, pp. 371-378, 2003.
[120] A. H. Meitzler, "Mode coupling occurring in the propagation of elastic pulses in wires," *The Journal of the Acoustical Society of America,* vol. 33, pp. 435-445, 1961.
[121] A. H. Nayfeh, "The general problem of elastic wave propagation in multilayered anisotropic media," *The Journal of the Acoustical Society of America,* vol. 89, pp. 1521-1531, 1991.
[122] M. J. Lowe, "Matrix techniques for modeling ultrasonic waves in multilayered media," *Ultrasonics, Ferroelectrics, and Frequency Control, IEEE Transactions on,* vol. 42, pp. 525-542, 1995.
[123] J. McKeon and M. Hinders, "Lamb wave scattering from a through hole," *Journal of Sound and Vibration,* vol. 224, pp. 843-862, 1999.
[124] R. D. Mindlin, "Mathematical theory of vibrations of elastic plates," in *10th Annual Symposium on Frequency Control*, 1956, pp. 10-44.
[125] B. Tang and E. Henneke II, "Long wavelength approximation for Lamb wave characterization of composite laminates," *Research in Nondestructive Evaluation,* vol. 1, pp. 51-64, 1989.
[126] D. N. Alleyne and P. Cawley, "The interaction of Lamb waves with defects," *Ultrasonics, Ferroelectrics, and Frequency Control, IEEE Transactions on,* vol. 39, pp. 381-397, 1992.
[127] E. Moulin, J. Assaad, C. Delebarre, and D. Osmont, "Modeling of Lamb waves generated by integrated transducers in composite plates using a coupled finite element–normal modes expansion method," *The Journal of the Acoustical Society of America,* vol. 107, pp. 87-94, 2000.
[128] K. Diamanti, J. Hodgkinson, and C. Soutis, "Detection of low-velocity impact damage in composite plates using Lamb waves," *Structural Health Monitoring,* vol. 3, pp. 33-41, 2004.
[129] R. Seifried, L. J. Jacobs, and J. Qu, "Propagation of guided waves in adhesive bonded components," *NDT & E International,* vol. 35, pp. 317-328, 2002.
[130] P. K. Banerjee, *The boundary element methods in engineering* vol. 2: McGraw-Hill London, 1994.
[131] A. T. Patera, "A spectral element method for fluid dynamics: laminar flow in a channel expansion," *Journal of computational Physics,* vol. 54, pp. 468-488, 1984.

[132] S. Gopalakrishnan, A. Chakraborty, and D. R. Mahapatra, *Spectral finite element method: wave propagation, diagnostics and control in anisotropic and inhomogeneous structures*: Springer Science & Business Media, 2007.
[133] C. Willberg, S. Duczek, J. V. Perez, D. Schmicker, and U. Gabbert, "Comparison of different higher order finite element schemes for the simulation of Lamb waves," *Computer methods in applied mechanics and engineering,* vol. 241, pp. 246-261, 2012.
[134] I. Solodov, "Nonlinear Acoustic NDT: Approaches, Methods, and Applications," in *Proceedings NDT in Progress, 5th International Workshop of NDT Experts. Prague*, 2009.
[135] K.-Y. Jhang, "Nonlinear ultrasonic techniques for nondestructive assessment of micro damage in material: a review," *International journal of precision engineering and manufacturing,* vol. 10, pp. 123-135, 2009.
[136] J. W. S. B. Rayleigh, *The theory of sound* vol. 2: Macmillan, 1896.
[137] L. Brillouin, "Tensors in Mechanics and Elasficify," 1964.
[138] F. D. Murnaghan, *Finite deformation of an elastic solid*: Dover Publications Inc., 1951.
[139] A. Thuras, R. Jenkins, and H. O'Neil, "Extraneous frequencies generated in air carrying intense sound waves," *Bell System Technical Journal, The,* vol. 14, pp. 159-172, 1935.
[140] P. H. Carr, "Harmonic generation of microwave phonons in quartz," *Physical Review Letters,* vol. 13, p. 332, 1964.
[141] K. A. Van Den Abeele, P. Johnson, and A. Sutin, "Nonlinear elastic wave spectroscopy (NEWS) techniques to discern material damage, part I: nonlinear wave modulation spectroscopy (NWMS)," *Research in Nondestructive Evaluation,* vol. 12, pp. 17-30, 2000.
[142] L. Landau and E. Lifshitz, "Theory of Elasticity, 3rd," ed: Pergamon Press, Oxford, UK, 1986.
[143] A. Hikata, B. B. Chick, and C. Elbaum, "Dislocation contribution to the second harmonic generation of ultrasonic waves," *Journal of Applied Physics,* vol. 36, pp. 229-236, 1965.
[144] R. A. Guyer and P. A. Johnson, "Nonlinear mesoscopic elasticity: Evidence for a new class of materials," *Physics today,* vol. 52, pp. 30-36, 1999.
[145] J. H. Cantrell, "Fundamentals and applications of non-linear ultrasonic nondestructive evaluation," *Ultrasonic non-destructive evaluation,* vol. vol. 6, pp. p.363-434, 2004.
[146] D. Broda, W. J. Staszewski, A. Martowicz, T. Uhl, and V. V. Silberschmidt, "Modelling of nonlinear crack–wave interactions for damage detection based on ultrasound—A review," *Journal of Sound and Vibration,* vol. 333, pp. 1097-1118, 2/14/ 2014.
[147] J. Frouin, S. Sathish, T. E. Matikas, and J. K. Na, "Ultrasonic linear and nonlinear behavior of fatigued Ti–6Al–4V," *Journal of materials research,* vol. 14, pp. 1295-1298, 1999.
[148] P. Johnson, "New wave in acoustic testing," *Mater. World,* vol. 7, pp. 544-546, 1999.
[149] J. H. Cantrell and W. T. Yost, "Nonlinear ultrasonic characterization of fatigue microstructures," *International Journal of fatigue,* vol. 23, pp. 487-490, 2001.
[150] D. Hurley, D. Balzar, and P. Purtscher, "Nonlinear ultrasonic assessment of precipitation hardening in ASTM A710 steel," *Journal of Materials Research,* vol. 15, pp. 2036-2042, 2000.
[151] Y. Choi, K. Jhang, I. Park, and H. Kim, "Application of non-linear acoustic effect for evaluation of degradation of 2.25 Cr-1Mo steel," *Journal of the Korean Society for Nondestructive Testing,* vol. 22, pp. 170-176, 2002.
[152] I.-K. Park, H.-M. Kim, and K.-Y. Jhang, "Nondestructive Evaluation of Degraded 2.25 Cr-1Mo Steel and Estimation of Nonlinear Acoustic Effect using Bispectral Analysis," in *ASME 2003 Pressure Vessels and Piping Conference*, 2003, pp. 65-71.
[153] U. Polimeno, M. Meo, D. P. Almond, and S. L. Angioni, "Detecting low velocity impact damage in composite plate using nonlinear acoustic/ultrasound methods," *Applied Composite Materials,* vol. 17, pp. 481-488, 2010.
[154] V. E. Nazarov, L. A. Ostrovsky, I. A. Soustova, and A. M. Sutin, "Nonlinear acoustics of micro-inhomogeneous media," *Physics of the Earth and Planetary Interiors,* vol. 50, pp. 65-73, 1988.
[155] B. Sarens, B. Verstraeten, C. Glorieux, G. Kalogiannakis, and D. Van Hemelrijck, "Investigation of contact acoustic nonlinearity in delaminations by shearographic imaging, laser doppler

vibrometric scanning and finite difference modeling," *Ultrasonics, Ferroelectrics, and Frequency Control, IEEE Transactions on,* vol. 57, pp. 1383-1395, 2010.

[156] D. R. Johnson, K. Wang, and J.-S. Kim, "Investigation of the threshold behavior of subharmonics for damage detection of a structure with a breathing crack," in *SPIE Smart Structures and Materials+ Nondestructive Evaluation and Health Monitoring*, 2010, pp. 765032-765032-9.

[157] I. Solodov, "Resonant Acoustic Nonlinearity of Defects for Highly-Efficient Nonlinear NDE," *Journal of Nondestructive Evaluation,* vol. 33, pp. 252-262, 2014.

[158] A. Moussatov, Gusev, V., Castagnede, B., "Self Induced Hysteresis for Nonlinear Acoustic Waves in Cracked Material," *Physical Review Letters,* vol. 90, p. 124301, 2003.

[159] K. Yamanaka, T. Mihara, and T. Tsuji, "Evaluation of closed cracks by model analysis of subharmonic ultrasound," *Japanese journal of applied physics,* vol. 43, p. 3082, 2004.

[160] I. Solodov, J. Wackerl, K. Pfleiderer, and G. Busse, "Nonlinear self-modulation and subharmonic acoustic spectroscopyfor damage detection and location," *Applied physics letters,* vol. 84, pp. 5386-5388, 2004.

[161] I. Y. Solodov, "Ultrasonics of non-linear contacts: propagation, reflection and NDE-applications," *Ultrasonics,* vol. 36, pp. 383-390, 1998.

[162] T. P. Berndt and R. E. Green Jr, "Feasibility study of a nonlinear ultrasonic technique to evaluate adhesive bonds," in *Nondestructive Characterization of Materials VIII*, ed: Springer, 1998, pp. 125-131.

[163] S. Hirsekorn, "Nonlinear transfer of ultrasound by adhesive joints–a theoretical description," *Ultrasonics,* vol. 39, pp. 57-68, 2001.

[164] C. Brotherhood, B. Drinkwater, and S. Dixon, "The detectability of kissing bonds in adhesive joints using ultrasonic techniques," *Ultrasonics,* vol. 41, pp. 521-529, 2003.

[165] D. Yan, S. A. Neild, and B. W. Drinkwater, "Modelling and measurement of the nonlinear behaviour of kissing bonds in adhesive joints," *NDT & E International,* vol. 47, pp. 18-25, 2012.

[166] A. Klepka, W. Staszewski, R. Jenal, M. Szwedo, J. Iwaniec, and T. Uhl, "Nonlinear acoustics for fatigue crack detection–experimental investigations of vibro-acoustic wave modulations," *Structural Health Monitoring,* vol. 11, pp. 197-211, 2012.

[167] D. Yan, B. W. Drinkwater, and S. A. Neild, "Measurement of the ultrasonic nonlinearity of kissing bonds in adhesive joints," *NDT & E International,* vol. 42, pp. 459-466, 7// 2009.

[168] M. Rothenfusser, M. Mayr, and J. Baumann, "Acoustic nonlinearities in adhesive joints," *Ultrasonics,* vol. 38, pp. 322-326, 2000.

[169] M. Meo and G. Zumpano, "Nonlinear elastic wave spectroscopy identification of impact damage on a sandwich plate," *Composite structures,* vol. 71, pp. 469-474, 2005.

[170] V. E. Nazarov and A. M. Sutin, "Nonlinear elastic constants of solids with cracks," *The Journal of the Acoustical Society of America,* vol. 102, pp. 3349-3354, 1997.

[171] J. Greenwood and J. Williamson, "Contact of nominally flat surfaces," in *Proceedings of the Royal Society of London A: Mathematical, Physical and Engineering Sciences*, 1966, pp. 300-319.

[172] N.-Y. Kim, K.-Y. Jhang, T.-H. Lee, S.-Y. Yang, and Y.-C. Chang, "Reflection and transmission of acoustic waves across contact interfaces," *Journal of the Korean Society for Nondestructive Testing,* vol. 28, pp. 292-301, 2008.

[173] S. Biwa, S. Nakajima, and N. Ohno, "On the acoustic nonlinearity of solid-solid contact with pressure-dependent interface stiffness," *Journal of applied mechanics,* vol. 71, pp. 508-515, 2004.

[174] C. Pecorary and I. Solodov, "Non-classical nonlinear dynamics of solid interfaces in partial contact for NDE applications," *Universality of Non-Classical Nonlinearity with Application to NDE and Ultrasonics,* vol. 19, pp. 307-324, 2006.

[175] M. I. Friswell and J. E. Penny, "Crack modeling for structural health monitoring," *Structural Health Monitoring,* vol. 1, pp. 139-148, 2002.

[176] I. Y. Solodov, Korshak, B.A., "Instability, chaos and memory in acoustic-wave-crack interaction," *Physical Review Letters,* vol. 90, 2002.
[177] E. Ballad, S. Y. Vezirov, K. Pfleiderer, I. Y. Solodov, and G. Busse, "Nonlinear modulation technique for NDE with air-coupled ultrasound," *Ultrasonics,* vol. 42, pp. 1031-1036, 2004.
[178] Y. Ohara, T. Mihara, and K. Yamanaka, "Effect of adhesion force between crack planes on subharmonic and DC responses in nonlinear ultrasound," *Ultrasonics,* vol. 44, pp. 194-199, 2006.
[179] Z. Wang, W. Qu, and L. Xiao, "Nonlinear Ultrasonic Damage Detection for Fatigue Crack Using Subharmonic Component," in *EWSHM-7th European Workshop on Structural Health Monitoring*, 2014.
[180] I. Solodov, J. Wackerl, K. Pfleiderer, and G. Busse, "Nonlinear self-modulation and subharmonic acoustic spectroscopy for damage detection and location," *Applied Physics Letters,* vol. 84, pp. 5386-5388, 2004.
[181] S. Delrue and K. Van Den Abeele, "Three-dimensional finite element simulation of closed delaminations in composite materials," *Ultrasonics,* vol. 52, pp. 315-324, 2012.
[182] K. Yamanaka, Y. Ohara, M. Oguma, and Y. Shintaku, "Two-Dimensional Analyses of Subharmonic Generation at Closed Cracks in Nonlinear Ultrasonics," *Applied physics express,* vol. 4, p. 076601, 2011.
[183] C. Courtney, B. Drinkwater, S. Neild, and P. Wilcox, "Global crack detection using bispectral analysis," in *ECNDT, proceedings of the 9th European non destructive testing conference*, 2006.
[184] L. Straka, Y. Yagodzinskyy, M. Landa, and H. Hänninen, "Detection of structural damage of aluminum alloy 6082 using elastic wave modulation spectroscopy," *Ndt & E International,* vol. 41, pp. 554-563, 2008.
[185] L. Ostrovsky and P. Johnson, "Dynamic nonlinear elasticity in geomaterials," *Rivista del nuovo cimento,* vol. 24, pp. 1-46, 2001.
[186] A. Sutin and V. Nazarov, "Nonlinear acoustic methods of crack diagnostics," *Radiophysics and quantum electronics,* vol. 38, pp. 109-120, 1995.
[187] A. Moussatov, V. Gusev, and B. Castagnede, "Self-induced hysteresis for nonlinear acoustic waves in cracked material," *Physical review letters,* vol. 90, p. 124301, 2003.
[188] L. Landau and E. Lifshitz, "Classical mechanics," ed: Pergamon Press, Oxford, 1960.
[189] K.-A. Van Den Abeele, J. Carmeliet, J. A. Ten Cate, and P. A. Johnson, "Nonlinear elastic wave spectroscopy (NEWS) techniques to discern material damage, Part II: Single-mode nonlinear resonance acoustic spectroscopy," *Journal of Research in Nondestructive Evaluation,* vol. 12, pp. 31-42, 2000.
[190] P. Johnson, "The Universality of Nonclassical Nonlinearity (with Application to Nondestructive Evaluation and Ultrasonics)," *Springer New York,* vol. 12, pp. 30-31, 2006.
[191] J. A. TenCate, E. Smith, and R. A. Guyer, "Universal slow dynamics in granular solids," *Physical Review Letters,* vol. 85, p. 1020, 2000.
[192] G. A. Gist, "Fluid effects on velocity and attenuation in sandstones," *The Journal of the Acoustical Society of America,* vol. 96, pp. 1158-1173, 1994.
[193] J. Ortin, "Preisach modeling of hysteresis for a pseudoelastic Cu-Zn-Al single crystal," *Journal of applied physics,* vol. 71, pp. 1454-1461, 1992.
[194] I. Mayergoyz, "Hysteresis models from the mathematical and control theory points of view," *Journal of Applied Physics,* vol. 57, pp. 3803-3805, 1985.
[195] R. Guyer, K. McCall, and G. Boitnott, "Hysteresis, discrete memory, and nonlinear wave propagation in rock: A new paradigm," *Physical review letters,* vol. 74, p. 3491, 1995.
[196] A. Nowick and W. Heller, "Anelasticity and stress-induced ordering of point defects in crystals," *Advances in Physics,* vol. 12, pp. 251-298, 1963.
[197] L. Fletcher, "Recent developments in contact conductance heat transfer," *Journal of Heat Transfer,* vol. 110, pp. 1059-1070, 1988.

[198] B. Vick, M. J. Furey, and C. Kajdas, "An examination of thermionic emission due to frictionally generated temperatures," *Tribology Letters,* vol. 13, pp. 147-153, 2002.
[199] B. Vick and M. J. Furey, "A basic theoretical study of the temperature rise in sliding contact with multiple contacts," *Tribology International,* vol. 34, pp. 823-829, 2001.
[200] B. Vick and M. Ozisik, "Quasi-steady-state temperature distribution in periodically contacting finite regions," *Journal of Heat Transfer,* vol. 103, pp. 739-744, 1981.
[201] M. Shojaeefard, K. Goudarzi, and M. S. Mazidi, "Inverse heat transfer problem of thermal contact conductance estimation in periodically contacting surfaces," *Journal of Thermal Science,* vol. 18, pp. 150-159, 2009.
[202] A. Ovcharenko, M. Yang, K. Chun, and F. Talke, "Transient thermomechanical contact of an impacting sphere on a moving flat," *Journal of Tribology,* vol. 133, p. 031404, 2011.
[203] C. Homma, M. Rothenfusser, J. Baumann, and R. Shannon, "Study of the heat generation mechanism in acoustic thermography," in *Quantitative Nondestructive Evaluation*, 2006, pp. 566-573.
[204] D. Dowson, *History of tribology*: Addison-Wesley Longman Limited, 1979.
[205] B. B. Kang, "Excitation method for thermosonic non-destructive testing," Imperial College London, 2008.
[206] T. Emery and J. Dulieu-Barton, "Thermoelastic stress analysis of damage mechanisms in composite materials," *Composites Part A: Applied Science and Manufacturing,* vol. 41, pp. 1729-1742, 2010.
[207] P. Stanley and W. Chan, "Quantitative stress analysis by means of the thermoelastic effect," *The Journal of Strain Analysis for Engineering Design,* vol. 20, pp. 129-137, 1985.
[208] V. Ginzburg, "The theory of Luxemburg–Gorky effect," *Izvestiya Akademii Nauk SSR, Seriya Fizicheskaya,* vol. 12, p. 253, 1948.
[209] V. Zaitsev, V. Gusev, and B. Castagnede, "Luxemburg-Gorky effect retooled for elastic waves: A mechanism and experimental evidence," *Physical review letters,* vol. 89, p. 105502, 2002.
[210] F. Aymerich and W. Staszewski, "Experimental study of impact-damage detection in composite laminates using a cross-modulation vibro-acoustic technique," *Structural Health Monitoring,* 2010.
[211] S. Hirsekorn and P. P. Delsanto, "On the universality of nonclassical nonlinear phenomena and their classification," *Applied physics letters,* vol. 84, pp. 1413-1415, 2004.
[212] I. Solodov, J. Bai, and G. Busse, "Resonant ultrasound spectroscopy of defects: Case study of flat-bottomed holes," *Journal of Applied Physics,* vol. 113, p. 223512, 2013.
[213] G. De Angelis, M. Meo, D. P. Almond, S. G. Pickering, and S. L. Angioni, "A new technique to detect defect size and depth in composite structures using digital shearography and unconstrained optimization," *NDT & E International,* vol. 45, pp. 91-96, 2012.
[214] I. Solodov, "Local defect resonance (LDR): A route to highly efficient thermosonic and nonlinear ultrasonic NDT," in *40TH ANNUAL REVIEW OF PROGRESS IN QUANTITATIVE NONDESTRUCTIVE EVALUATION: Incorporating the 10th International Conference on Barkhausen Noise and Micromagnetic Testing*, 2014, pp. 1663-1670.
[215] U. G. K. Wegst and M. F. Ashby, "The mechanical efficiency of natural materials," *Philosophical Magazine,* vol. 84, pp. 2167-2186, 2004.
[216] U. G. K. Wegst, H. Bai, E. Saiz, A. P. Tomsia, and R. O. Ritchie, "Bioinspired structural materials," *Nat Mater,* vol. 14, pp. 23-36, 01//print 2015.
[217] W. Yang, I. H. Chen, J. McKittrick, and M. A. Meyers, "Flexible Dermal Armor in Nature," *Jom,* vol. 64, pp. 475-485, 2012.
[218] W. Yang, I. H. Chen, B. Gludovatz, E. A. Zimmermann, R. O. Ritchie, and M. A. Meyers, "Natural flexible dermal armor," *Adv Mater,* vol. 25, pp. 31-48, Jan 4 2013.
[219] G. M. Luz and J. F. Mano, "Biomimetic design of materials and biomaterials inspired by the structure of nacre," *Philos Trans A Math Phys Eng Sci,* vol. 367, pp. 1587-605, Apr 28 2009.

[220] Y. Bouligand, "Twisted fibrous arrangements in biological materials and cholesteric mesophases," *Tissue and Cell,* vol. 4, pp. 189-217, // 1972.
[221] S. N. Patek and R. L. Caldwell, "Extreme impact and cavitation forces of a biological hammer: strike forces of the peacock mantis shrimp Odontodactylus scyllarus," *J Exp Biol,* vol. 208, pp. 3655-64, Oct 2005.
[222] J. C. Weaver, G. W. Milliron, A. Miserez, K. Evans-Lutterodt, S. Herrera, I. Gallana*, et al.*, "The stomatopod dactyl club: a formidable damage-tolerant biological hammer," *Science,* vol. 336, pp. 1275-80, Jun 8 2012.
[223] L. K. Grunenfelder, N. Suksangpanya, C. Salinas, G. Milliron, N. Yaraghi, S. Herrera*, et al.*, "Bio-inspired impact-resistant composites," *Acta Biomater,* vol. 10, pp. 3997-4008, Sep 2014.
[224] M. M. Giraud, J. Castanet, F. J. Meunier, and Y. Bouligand, "The fibrous structure of coelacanth scales: A twisted 'Plywood'," *Tissue and Cell,* vol. 10, pp. 671-686, // 1978.
[225] M.-M. Giraud-Guille, "Twisted plywood architecture of collagen fibrils in human compact bone osteons," *Calcified tissue international,* vol. 42, pp. 167-180, 1988.
[226] B. Chen, X. Peng, C. Cai, H. Niu, and X. Wu, "Helicoidal microstructure of Scarabaei cuticle and biomimetic research," *Materials Science and Engineering: A,* vol. 423, pp. 237-242, 2006.
[227] T. Apichattrabrut and K. Ravi-Chandar, "Helicoidal composites," *Mechanics of Advanced Materials and Structures,* vol. 13, pp. 61-76, 2006.
[228] L. Cheng, A. Thomas, J. L. Glancey, and A. M. Karlsson, "Mechanical behavior of bio-inspired laminated composites," *Composites Part A: Applied Science and Manufacturing,* vol. 42, pp. 211-220, 2// 2011.
[229] N. H. Ngern, J. S. Shang, and V. B. Tan, "Impact Performance Of Biomimetic Helicoidal Composite Plates," 2015.
[230] J. Andersons and M. König, "Dependence of fracture toughness of composite laminates on interface ply orientations and delamination growth direction," *Composites Science and Technology,* vol. 64, pp. 2139-2152, 2004.
[231] F.-K. Chang and K.-Y. Chang, "A progressive damage model for laminated composites containing stress concentrations," *Journal of composite materials,* vol. 21, pp. 834-855, 1987.
[232] R. Borg, L. Nilsson, and K. Simonsson, "Modeling of delamination using a discretized cohesive zone and damage formulation," *Composites Science and Technology,* vol. 62, pp. 1299-1314, 2002.
[233] S. Sánchez-Sáez, E. Barbero, R. Zaera, and C. Navarro, "Compression after impact of thin composite laminates," *Composites Science and Technology,* vol. 65, pp. 1911-1919, 2005.
[234] A. Duarte, I. Herszberg, and R. Paton, "Impact resistance and tolerance of interleaved tape laminates," *Composite structures,* vol. 47, pp. 753-758, 1999.
[235] B. A. Gama and J. W. Gillespie, "Finite element modeling of impact, damage evolution and penetration of thick-section composites," *International Journal of Impact Engineering,* vol. 38, pp. 181-197, 2011.
[236] C. Lopes, S. Sádaba, C. González, J. LLorca, and P. Camanho, "Physically-sound simulation of low-velocity impact on fiber reinforced laminates," *International Journal of Impact Engineering,* 2015.
[237] B. W. Kim and A. H. Mayer, "Influence of fiber direction and mixed-mode ratio on delamination fracture toughness of carbon/epoxy laminates," *Composites Science and Technology,* vol. 63, pp. 695-713, 2003.
[238] V. C. Li, Y. Wang, and S. Backer, "Effect of inclining angle, bundling and surface treatment on synthetic fibre pull-out from a cement matrix," *Composites,* vol. 21, pp. 132-140, 1990.
[239] J. Tao and C. Sun, "Influence of ply orientation on delamination in composite laminates," *Journal of Composite Materials,* vol. 32, pp. 1933-1947, 1998.
[240] S. Vanaverbeke and K. Van Den Abeele, "Two-dimensional modeling of wave propagation in materials with hysteretic nonlinearity," *The Journal of the Acoustical Society of America,* vol. 122, p. 58, 2007.

[241] M. Scalerandi, V. Agostini, P. P. Delsanto, K. Van Den Abeele, and P. A. Johnson, "Local interaction simulation approach to modelling nonclassical, nonlinear elastic behavior in solids," *The Journal of the Acoustical Society of America,* vol. 113, p. 3049, 2003.
[242] F. Amerini and M. Meo, "Structural health monitoring of bolted joints using linear and nonlinear acoustic/ultrasound methods," *Structural Health Monitoring,* p. 1475921710395810, 2011.
[243] M. Amura, M. Meo, and F. Amerini, "Baseline-free estimation of residual fatigue life using a third order acoustic nonlinear parameter," *The Journal of the Acoustical Society of America,* vol. 130, p. 1829, 2011.
[244] G. Zumpano and M. Meo, "A new damage detection technique based on wave propagation for rails," *International journal of solids and structures,* vol. 43, pp. 1023-1046, 2006.
[245] F. Ciampa, E. Barbieri, and M. Meo, "Modelling of multiscale nonlinear interaction of elastic waves with three-dimensional cracks," *The Journal of the Acoustical Society of America,* vol. 135, pp. 3209-3220, 2014.
[246] P. Theocaris and D. Sokolis, "Spectral decomposition of the compliance fourth-rank tensor for orthotropic materials," *Archive of Applied Mechanics,* vol. 70, pp. 289-306, 2000.
[247] M. M. F. Ciampa, "Modelling of Multiscale Nonlinear Interaction of Elastic Waves with 3D Cracks," *Manuscript submitted to Journal of Acoustical Society of America,* 2013.
[248] J. Sarrate Ramos and A. Huerta, "An improved algorithm to smooth graded quadrilateral meshes preserving the prescribed element size," 2012.
[249] N. G. Meyendorf, H. Rösner, V. Kramb, and S. Sathish, "Thermo-acoustic fatigue characterization," *Ultrasonics,* vol. 40, pp. 427-434, 2002.
[250] M. Morbidini, P. Cawley, T. Barden, D. Almond, and P. Duffour, "Prediction of the thermosonic signal from fatigue cracks in metals using vibration damping measurements," *Journal of Applied Physics,* vol. 100, p. 104905, 2006.
[251] I. Solodov, M. Rahammer, D. Derusova, and G. Busse, "Highly-efficient and noncontact vibro-thermography via local defect resonance," *Quantitative InfraRed Thermography Journal,* vol. 12, pp. 98-111, 2015.
[252] ASTM, "ASTM E399 Test Method for Linear-Elastic Plane-Strain Fracture Toughness KIc of Metallic Materials," ed: ASTM International, 2015.
[253] ASTM, "ASTM E647 Test Method for Measurement of Fatigue Crack Growth Rates," ed: ASTM International, 2015.
[254] J. DiMambro, D. Ashbaugh, C. Nelson, and F. Spencer, "Sonic infrared (IR) imaging and fluorescent penetrant inspection probability of detection (POD) comparison," in *Review of progress in quantitative nondestructive evaluation*, 2007, pp. 463-470.
[255] K. Reifsnider, E. G. Henneke, and W. Stinchcomb, "The mechanics of vibrothermography," *Mechanics of nondestructive testing,* pp. 249-276, 1980.
[256] J. Lu, X. Han, G. Newaz, L. Favro, and R. Thomas, "Study of the effect of crack closure in sonic infrared imaging," *Nondestructive Testing and Evaluation,* vol. 22, pp. 127-135, 2007.
[257] J. Renshaw, J. C. Chen, S. D. Holland, and R. B. Thompson, "The sources of heat generation in vibrothermography," *NDT & E International,* vol. 44, pp. 736-739, 2011.
[258] B. Basu and M. Kalin, "Frictional Heating and Contact Temperature," *Tribology of Ceramics and Composites: A Materials Science Perspective,* pp. 60-69, 2011.
[259] I. Solodov, J. Bai, S. Bekgulyan, and G. Busse, "A local defect resonance to enhance acoustic wave-defect interaction in ultrasonic nondestructive evaluation," *Applied Physics Letters,* vol. 99, p. 211911, 2011.
[260] L. Shuyu, "Equivalent circuits and directivity patterns of air-coupled ultrasonic transducers," *The Journal of the Acoustical Society of America,* vol. 109, pp. 949-957, 2001.
[261] P. Stanley and W. Chan, "The application of thermoelastic stress analysis techniques to composite materials," *The Journal of Strain Analysis for Engineering Design,* vol. 23, pp. 137-143, 1988.

[262] C. Meeks, E. Greenhalgh, and B. G. Falzon, "Stiffener debonding mechanisms in post-buckled CFRP aerospace panels," *Composites Part A: Applied Science and Manufacturing,* vol. 36, pp. 934-946, 7// 2005.
[263] K. Stevens, R. Ricci, and G. Davies, "Buckling and postbuckling of composite structures," *Composites,* vol. 26, pp. 189-199, 1995.
[264] W. J. N. de Lima and M. F. Hamilton, "Finite-amplitude waves in isotropic elastic plates," *Journal of Sound and Vibration,* vol. 265, pp. 819-839, 8/21/ 2003.
[265] H. Nayeb-Hashemi and J. Rossettos, "Nondestructive Evaluation of Adhesively Bonded Joints by Acousto-Ultrasonic Technique and Acoustic Emission," 1997.
[266] W. Zhou, R. Liu, Z.-h. Lv, W.-y. Chen, and X.-t. Li, "Acoustic emission behaviors and damage mechanisms of adhesively bonded single-lap composite joints with adhesive defects," *Journal of Reinforced Plastics and Composites,* vol. 34, pp. 84-92, 2015.
[267] A. A. Khalil and A. N. Kagho, "Non-destructive testing of adhesively bonded joints using vibrational analysis," *International Journal of Adhesion and Adhesives,* vol. 11, pp. 121-127, 4// 1991.
[268] P. B. Nagy, "Ultrasonic classification of imperfect interfaces," *Journal of Nondestructive Evaluation,* vol. 11, pp. 127-139, 1992.
[269] K. Vine, P. Cawley, and A. Kinloch, "The correlation of non-destructive measurements and toughness changes in adhesive joints during environmental attack," *The Journal of Adhesion,* vol. 77, pp. 125-161, 2001.
[270] F. K. Kneubühl, *Oscillations and waves*: Springer Science & Business Media, 2013.
[271] G.-W. Kim, D. R. Johnson, F. Semperlotti, and K. Wang, "Localization of breathing cracks using combination tone nonlinear response," *Smart Materials and Structures,* vol. 20, p. 055014, 2011.
[272] K. Naito and T. Sugiura, "A possible mechanism causing subharmonics in ultrasonic testing of a closed crack," in *Ultrasonics Symposium (IUS), 2010 IEEE*, 2010, pp. 2392-2395.
[273] J. Potter, A. Croxford, and P. Wilcox, "Nonlinear ultrasonic phased array imaging," *Physical review letters,* vol. 113, p. 144301, 2014.
[274] M.-X. Tang, H. Mulvana, T. Gauthier, A. Lim, D. Cosgrove, R. Eckersley*, et al.*, "Quantitative contrast-enhanced ultrasound imaging: a review of sources of variability," *Interface Focus,* vol. 1, pp. 520-539, 2011.
[275] Ö. Oralkan, A. S. Ergun, J. A. Johnson, M. Karaman, U. Demirci, K. Kaviani*, et al.*, "Capacitive micromachined ultrasonic transducers: Next-generation arrays for acoustic imaging?," *Ultrasonics, Ferroelectrics, and Frequency Control, IEEE Transactions on,* vol. 49, pp. 1596-1610, 2002.
[276] C. Holmes, B. W. Drinkwater, and P. D. Wilcox, "Post-processing of the full matrix of ultrasonic transmit–receive array data for non-destructive evaluation," *NDT & E International,* vol. 38, pp. 701-711, 2005.
[277] G. M. Matte, P. L. Van Neer, M. G. Danilouchkine, J. Huijssen, M. D. Verweij, and N. De Jong, "Optimization of a phased-array transducer for multiple harmonic imaging in medical applications: frequency and topology," *Ultrasonics, Ferroelectrics, and Frequency Control, IEEE Transactions on,* vol. 58, pp. 533-546, 2011.
[278] P. N. Wells, "Ultrasonic imaging of the human body," *Reports on progress in physics,* vol. 62, p. 671, 1999.
[279] A. Rozanova-Pierrat, "Mathematical analysis of Khokhlov-Zabolotskaya-Kuznetsov (KZK) equation," 2006.
[280] S. Krishnan and M. O'Donnell, "Transmit aperture processing for nonlinear contrast agent imaging," *Ultrasonic imaging,* vol. 18, pp. 77-105, 1996.
[281] A. Bouakaz, F. ten Cate, and N. de Jong, "A new ultrasonic transducer for improved contrast nonlinear imaging," *Physics in medicine and biology,* vol. 49, p. 3515, 2004.

[282] M. Pasovic, M. Danilouchkine, G. Matte, A. F. van der Steen, O. Basset, N. de Jong*, et al.*, "Broadband reduction of the second harmonic distortion during nonlinear ultrasound wave propagation," *Ultrasound in medicine & biology,* vol. 36, pp. 1568-1580, 2010.

[283] K. Yamanaka, Y. Ohara, S. Yamamoto, and T. Mihara, "Ultrasonic evaluation of closed cracks using subharmonic/superharmonic phased array and a laser interferometer," in *4th Pan American Conference for NDT, Oct*, 2007, pp. 22-26.

[284] A. Ouchi, A. Sugawara, Y. Ohara, and K. Yamanaka, "Subharmonic phased array for crack evaluation using surface acoustic wave," *Japanese Journal of Applied Physics,* vol. 54, p. 07HC05, 2015.